

Universität Potsdam

---

---

**CRITICAL STATES OF SEISMICITY**

Modeling and data analysis

---

---

**Habilitationschrift**

zur Erlangung des akademischen Grades  
Doctor rerum naturalium habitatus (Dr. rer. nat. habil.)  
in der Wissenschaftsdisziplin Theoretische Physik

angenommen an der  
Mathematisch–Naturwissenschaftlichen Fakultät  
der Universität Potsdam

von  
Dr. Gert Zöller  
geboren am 25. Juli 1967  
in Lüdenscheid

Potsdam, im September 2005



# Contents

<b>1</b>	<b>Introduction</b>	<b>1</b>
<b>2</b>	<b>Conceptual models for seismicity</b>	<b>6</b>
2.1	Reid’s elastic rebound theory (1910): A model for the Parkfield segment? . . . . .	6
2.2	Spring-block systems and cellular automata . . . . .	8
<b>3</b>	<b>Modeling seismicity in real fault regions</b>	<b>10</b>
3.1	Fault geometry and model framework . . . . .	10
3.2	Plate motion . . . . .	12
3.3	Friction and coseismic stress transfer; quasidynamic approach . . . . .	13
3.4	Model algorithm . . . . .	16
3.5	Limits and parameters of the model . . . . .	17
3.6	Model extensions . . . . .	17
3.7	Data types . . . . .	20
<b>4</b>	<b>Results</b>	<b>21</b>
4.1	Frequency-size distributions . . . . .	21
4.2	Temporal occurrence of large earthquakes . . . . .	24
4.3	The stress field for different degrees of disorder . . . . .	24
4.4	Aftershocks and foreshocks . . . . .	26
4.5	Accelerating moment release . . . . .	30
4.6	Critical point analysis of seismicity in California . . . . .	32
<b>5</b>	<b>Summary and conclusions</b>	<b>38</b>
<b>6</b>	<b>Outlook</b>	<b>40</b>
	<b>Bibliography</b>	<b>41</b>

A	Self-organization of spatio-temporal earthquake clusters	49
B	Seismic quiescence as an indicator for large earthquakes in a system of self-organized criticality	59
C	Observation of growing correlation length as an indicator for critical point behavior prior to large earthquakes	64
D	The role of disorder and stress concentration in nonconservative fault systems	74
E	Detecting premonitory seismicity patterns based on critical point dynamics	93
F	A systematic test on precursory seismic quiescence in Armenia	100
G	A systematic spatiotemporal test of the critical point hypothesis for large earthquakes	120
H	On increase of earthquake correlation length prior to large earthquakes in California	125
I	Earthquake clusters resulting from delayed rupture propagation in finite fault segments	147
J	Emergence of a band-limited power law in the aftershock decay rate of a slider-block model	158
K	Quasi-static and quasi-dynamic modeling of earthquake failure at intermediate scales	163
L	The role of heterogeneities as a tuning parameter of earthquake dynamics	180
M	Aftershocks resulting from creeping sections in a heterogeneous fault	204
N	Earthquake activity related to seismic cycles in a model for a heterogeneous strike-slip fault	209

# Chapter 1

## Introduction

In 2003, the geophysicist Vladimir Keilis-Borok, director of the *International Institute of Earthquake Prediction Theory and Mathematical Geophysics* in Moscow issued an alarm for an upcoming earthquake of magnitude 6.4 or greater within a 12,440 square miles area of southern California that includes portions of the eastern Mojave Desert, Coachella Valley, Imperial Valley (San Bernardino, Riverside and Imperial Counties) and eastern San Diego County, during a time interval of nine months (January 5 - September 5, 2004). This prediction was based on previous observations of microearthquake patterns forming chains. Keilis-Borok and co-workers claimed to have predicted two earthquakes correctly by means of such chains – one in Hokkaido, Japan in September 2003 and the second in San Simeon, California in December 2003. However, the deadline of the recent forecast passed and no earthquake fitting the alarm occurred.

Apart from the social and the economic dimension, this failed prediction raises also basic scientific questions in earth sciences: Is a prediction of earthquakes solely based on the emergence of seismicity patterns reliable? In other words, is there a “magic parameter”, which becomes anomalous prior to a large earthquake? Is it necessary that such a parameter is based on a physical model? Are pure observational methods without specific physical understanding, like the pattern recognition approach of Keilis-Borok, also sufficient? Taking into account that earthquakes are monitored continuously only since about 100 years and the best available data sets (“earthquake catalogs”) cover only a few decades, it seems questionable to forecast earthquakes solely on the basis of observed seismicity patterns, because large earthquakes have recurrence periods of decades to centuries; consequently, data sets for a certain region include not more than ten large events making a reliable statistical testing questionable.

The relation between frequency and magnitude of earthquakes in a large seismically active region is given by the empirical Gutenberg-Richter law [GUTENBERG AND RICHTER, 1956]

$$\log N = bM - a, \quad (1.1)$$

where  $N$  is the frequency of earthquakes with magnitude equal to or greater than  $M$ ;  $a$  is a measure of the overall seismicity level in a region and the slope  $b$  is the Richter  $b$  value, which determines the relation between large and small earthquakes.

A key problem of the present work is the evaluation of the relevance of observed seismicity patterns. First, it is important to decide whether an observed pattern has a physical

origin or is an artifact, arising for example from inhomogeneous reporting or from man-made seismicity, like quarry blasts or explosions. Second, the non-artificial events have to be analyzed with respect to their underlying mechanisms. This leads to an inverse problem with a non-unique solution, which can be illustrated for the most pronounced observed seismicity pattern, the occurrence of aftershocks. It is empirically known that the earthquake rate  $\dot{N}$  after a large event at time  $t_M$  follows the modified Omori law [OMORI, 1894; UTSU *et al.*, 1995]

$$\dot{N} = \frac{c_1}{(c_2 + t - t_M)^p}, \quad (1.2)$$

where  $t$  is the time,  $c_1$  and  $c_2$  are constants, and the Omori exponent  $p$  is close to unity. In particular, aftershocks are an almost universal phenomenon; that is, they are observed nearly after each mainshock. The underlying mechanisms leading to aftershocks are, however, unknown. Various physical models have been designed in order to explain aftershock occurrence following Eq. (1.2). These models assume physical mechanisms including viscoelasticity [HAINZL *et al.*, 1999], pore fluid flow [NUR AND BOOKER, 1972], damage rheology [BEN-ZION AND LYAKHOVSKY, 2003; SHCHERBAKOV AND TURCOTTE, 2004], and special friction laws [DIETERICH, 1994]. The question, which mechanism is realistic in a certain fault zone, remains open. Detailed comparisons of observed and modeled seismicity with respect to the aftershock rate, the duration of aftershock sequences, the dependence on the mainshock size, and other features are necessary to address this problem. Additionally, the results from lab experiments on rupture dynamics, and satellite observations in fault zones, provide important constraints for the evaluation of such models.

Apart from aftershock activity, other seismicity patterns are well-known from observations, e.g. foreshocks [JONES AND MOLNAR, 1979], seismic quiescence [WYSS AND HABERMANN, 1988; HAINZL *et al.*, 2000b; ZÖLLER *et al.*, 2002], and accelerating seismic moment release [BUFE AND VARNES, 1993; JAUMÉ AND SYKES, 1999]. These patterns have been documented in several cases before large earthquakes. They occur, however, less frequent than aftershocks. For example, foreshocks are known to precede only 20-30% of large earthquakes [WYSS, 1997]. Therefore, their predictive power is questionable. Moreover, it is not clear whether or not these findings can be attributed to physical processes or to random fluctuations in the highly noisy earthquake catalogs. This problem can be addressed by using conceptual fault models which allow to simulate long earthquake sequences over at least 1000 years. If the models are to some extent physical, the occurrence of seismicity patterns can be studied with reasonable statistics. The main ingredients of such models are the geometry of a fault region, empirically known friction laws, quenched spatial heterogeneities, and stress and displacement functions in accordance to dislocation theory [CHINNERY, 1963; OKADA, 1992]. In order to allow for detailed studies of the relations between the imposed mechanisms and the observed seismicity functions, it is important that the number of adjustable parameters is limited. It is emphasized that these models do not aim to reproduce an observed earthquake catalog in detail. Instead, the main goal is to address questions like: Why is the Parkfield segment of the San Andreas fault characterized by relatively regular occurrence of earthquakes with magnitude  $M \approx 6$ , while on the San Jacinto fault in California the properties of earthquake occurrence are more irregular?

In nonlinear dynamics, conceptual models have a long tradition. The Lorenz equations [LORENZ, 1963], which are a set of three coupled ordinary differential equations, have been proposed to describe convection in a fluid layer heated from below and serve therefore as a model for mantle convection. In a certain range of parameters, they are an example for deterministic chaos [SPARROW, 1982]. In oceanography, low-dimensional box models have been used to simulate the thermohaline circulation and their stability [STOMMEL, 1961; RAHMSTORF, 2001]. These models include critical parameter ranges characterized by bifurcations. Theoretical ecology and population dynamics are also a research area, where models based on a small number of equations provide insights in the evolution of the population of a species [BLASIUS *et al.*, 1999].

Conceptual models for seismicity are mainly based on one or more solid blocks, which are driven by a plate over a rough surface. The plate and the blocks are connected with springs. This model can produce stick-slip motion of the blocks, where a slip event is considered to simulate an earthquake. The model setup allows to govern a wide range of complexity, beginning with a single-block model which produces periodic occurrence of earthquakes of uniform size, ending with a network of connected blocks leading to complex sequences of earthquakes with variable size. The latter model has been proposed by BURRIDGE AND KNOPOFF [1967]. In order to reduce the computational effort, i.e. solving coupled differential equations, the use of cellular automata became popular [OLAMI *et al.*, 1992; LOMNITZ-ADLER, 1999]. Mathematically, these models include maps instead of differential equations; physically, this corresponds to instantaneously occurring slip events, neglecting inertia effects. The main ingredients of such models are (1) external driving (plate motion), and (2) sudden change of system parameters (stress), when a critical value (material strength) is reached, followed by an avalanche of block slips (stress drop and co-seismic stress transfer during an earthquake). While the first process lasts for years to several decades, the second occurs on a time scale of a few seconds. The simplest model including these feature has been formulated by REID [1910] and is known as Reid’s *elastic rebound theory*; in terms of spring-block models, this corresponds to a single-block model with constant plate velocity. Accounting for spatial heterogeneity and fault segmentation, many interacting blocks, or fault segments, have to be considered. This leads to a spatiotemporal stress field instead of a single stress value. In general, the material strength will also become space-dependent. Such a model framework can be treated with the methodology of statistical physics similar to the Ising model or percolation models [MAIN *et al.*, 2004]. In this context, large earthquakes are associated with second-order phase transitions [SORNETTE, 2004]. The view of earthquakes as phase transitions in a system with many degrees of freedom and an underlying critical point, is hereinafter referred to as the “critical point concept”. It is interesting to note that the period before such a phase transition is characterized by a preparation process, or a “critical state”, e.g. in terms of growing spatial correlation length following a power law [BINNEY *et al.*, 1993]. However, depending on the parameters of a model, different scenarios are conceivable: the system trajectory can enter the critical state and the critical point frequently (“supercritical”) or it becomes never critical (“subcritical”). A case of special interest is the class of models showing *self-organized criticality* (SOC) [BAK, 1996], which have their origin in a simple cellular automaton model for a sandpile [BAK AND TANG, 1996]. Here, the system drives itself permanently in the vicinity of the critical point with almost scale-free characteristics. Consequently, each small event can grow into a large earthquake with

some probability.

A major part of the present work deals with the detection and the characterization of critical states of seismicity using a model of a segmented fault in a three-dimensional elastic half-space. The assumption of a critical point underlying the dynamics of seismicity is discussed with respect to applicability and limits for different realizations of the fault model. Although the model framework is conceptual, various realistic or physically motivated features are included. On the one hand, the current state of the model simulates all important seismicity patterns, which are known from observations. On the other hand, the model is simple enough to make simulations of thousands of years possible. This allows to study relations between patterns and underlying mechanisms as well as indicators for critical states in detail with a reasonable statistics. Synthetic seismicity has the advantage of providing access to hidden quantities, e.g. the stress field; moreover, data sets of arbitrary high quality can be generated. The combination of both, synthetic and observed seismicity, provides important insights in the understanding of seismicity patterns and their underlying mechanisms from various points of view.

Statistical features like the frequency-size distribution can be calculated with high precision. Despite the scaling behavior (Eq. (1.1)) for small and intermediate earthquakes, which is observed for all sets of model parameters, clear deviations become visible for large magnitudes. Such deviations are known from real catalogs, but their statistical significance is not clear in all cases. The model simulations suggest that deviations from scaling for strong earthquakes can be attributed to physical properties. One important property is the spatial disorder of brittle parameters of the fault. The presence of strong heterogeneities suppresses system-wide events with some probability, whereas such events can evolve more easily on smooth faults. The degree of quenched (time-independent) spatial heterogeneity turns out to be a key parameter for statistical and dynamical properties of seismicity. This includes the temporal regularity of mainshock occurrence, various aspects of stress and displacement field, and a spontaneous mode-switching between different dynamical regimes without changing parameters. It is interesting that the degree of heterogeneity can act as a tuning parameter that allows for a continuous change of the model dynamics between the end-member cases of supercritical and subcritical behavior. Such a dependence, which is observed also for other parameters, can be visualized in phase diagrams similar to the phase diagram for the different aggregate states of water. For increasing complexity of a model, the number of axis of the phase diagram, representing the relevant model parameters, will increase. The above mentioned question of distinguishing different faults like the Parkfield segment and the San Jacinto fault can be rephrased to the problem of assigning the faults to different points in such a diagram. An important step in this direction is the physical modeling of observed seismicity patterns like aftershocks (Eq. (1.2)), foreshocks, and the acceleration of seismic energy release before large earthquakes. The latter phenomenon which is known to occur over large regions including more than one fault, can be interpreted in terms of the approach towards a critical point. This view is supported by an observational study of the growth of the spatial correlation length which is a different aspect of the same underlying physics.

The present work is organized as follows: An overview of commonly used fault models is given in Chapter 2. It is also discussed, how these models are taken into account for the design of a more realistic fault model. In Chapter 3, the setup of the new fault model is described, with respect to the mathematical framework, the imposed physical mechanisms,



possible extensions, and the limits. The results of the simulations are presented and discussed in Chapter 4. The last part of this chapter is devoted to a critical-point analysis of the Californian earthquake catalog. The Appendices A to N include the publications of the author, which are related to the subject of this thesis. In order to avoid a redundant presentation, many results in the main body (Chapter 2 to 4) are given as links to Figures and Tables in the Appendices. Finally, it is emphasized that the Appendices contain more results than the main body, which deals predominantly with the critical point concepts for earthquakes.

## Chapter 2

# Conceptual models for seismicity

In this chapter, the most important conceptual fault models are introduced and discussed.

### 2.1 Reid's elastic rebound theory (1910): A model for the Parkfield segment?

The Parkfield segment of the San Andreas fault in California is one of the best monitored seismic regions in the world. The reason is that over a period of about hundred years beginning in 1857, earthquakes with magnitude  $M \approx 6$  occurred almost periodically with a period of about 22 years. An exception is the 1934 event, which followed 12 years after the last mainshock. The last event fitting this rule was observed in 1966 leading to a forecast for a subsequent earthquake in 1988. In order to detect possible precursors to this event, the so-called Parkfield experiment, including ground motion instruments, strainmeters, and GPS stations, has been installed. However, the next  $M6$  earthquake occurred on September 28, 2004 without any significant precursory phenomenon [LANGBEIN, *et al.*, 2005]. Despite this failure, Parkfield is still a synonym for a region with an overall regular occurrence of large earthquakes following the idea of REID [1910]. In this view, earthquakes occur after a stress accumulation resulting from tectonic plate motion over some decades, followed by a stress drop in a few seconds. If geological and geophysical parameters remain constant and the entire fault segment is assumed to slip during an earthquake, this model predicts a periodic occurrence of earthquakes.

Quantitatively, Reid's model can be described by a block with mass  $m$ , which is driven

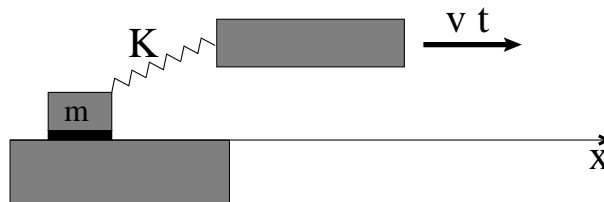


Figure 2.1: Sketch of a one-dimensional single-block model corresponding to Reid's elastic rebound theory.

with constant velocity  $v$  over a rough surface as shown in Fig. 2.1. If a velocity weakening friction law is imposed, the position of the block  $x(t)$  will evolve periodically in time and perform stick-slip motion, where slip events are interpreted as earthquakes. Mathematically,  $x(t)$  is a solution of Newton's equation

$$m\ddot{x} = K(vt - x) - f(\dot{x}), \quad (2.1)$$

where  $K$  is the spring constant and  $f(\dot{x})$  is the frictional force, which depends on the velocity  $\dot{x}$  of the block. Here, we assume to be in the regime of Hooke's law, where the stress  $\tau$  in the spring is proportional to the strain  $\varepsilon = \Delta l/l$  of the spring;  $l + \Delta l$  is the current length of the spring, and  $l$  is the equilibrium length. The actual position  $x$  is called the displacement of the block. The main features of this model are summarized in Fig. 2.2. The stress function is periodic, the displacement is a staircase function, and the slip events (earthquakes) occur also periodically. The sequence of  $M6$  earthquakes on the Parkfield segment is shown in Fig. 2.3.

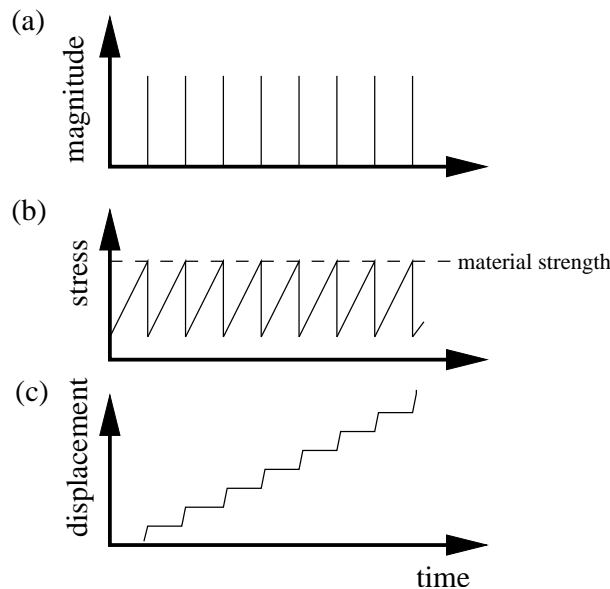


Figure 2.2: Summary of main features of the single-block model (Fig. 2.1): (a) magnitude, (b) stress, and (c) displacement as a function of time.

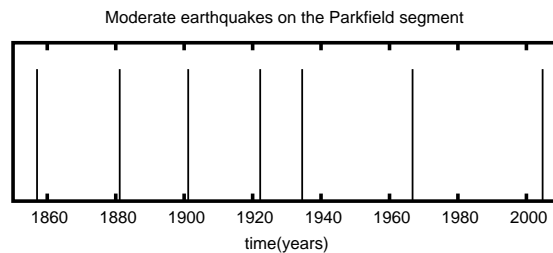


Figure 2.3: Sequence of moderate earthquakes ( $M \approx 6$ ) on the Parkfield segment of the San Andreas fault; the vertical axis has no meaning.

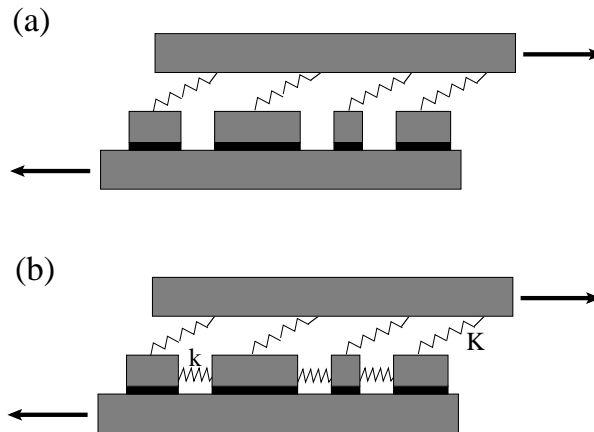


Figure 2.4: Sketch of one-dimensional spring-block model with more than one block: (a) “uncoupled” system, (b) “coupled” system.

Despite the high degree of simplicity, this model captures the main features of conceptual fault models: (1) long-term stress increase resulting from tectonic plate motion, (2) sudden stress drop when a critical material strength is reached. Earthquakes have uniform size, because the fault segment (modeled by the block) moves always as a whole. As pointed out before, this approach provides only a rough approximation to the Parkfield situation, because the occurrence time of at least two earthquakes on this fault segment deviates significantly from the 22-year period.

## 2.2 Spring-block systems and cellular automata

The most unrealistic feature of a single-block system is probably the assumption that a large fault segment performs a uniform slip during an earthquake. Taking into account the dimensions of such a segment, which are about some hundreds of square kilometers, leads to the conclusion that this approach is clearly oversimplified. Adding more blocks to the system as shown in Fig. 2.4(a) overcomes this problem to some degree, because fault segmentation and earthquakes with variable size can be modeled. However, earthquake sequences are obtained by a simple superposition of the sequences from the corresponding single-block systems. Especially the largest earthquakes, generated by slip events of the largest block, occur still periodically in time.

A more physical approach is given in Fig. 2.4(b), which shows a sketch of a coupled block system. Apart from the coupling with the driver plate, the blocks are coupled with the nearest neighbors by additional springs. If a block begins to slip, stress is redistributed along the chain and a slip event in a second block may be triggered. In general, an earthquake can be described by an avalanche of slipping blocks. The size of the earthquake can be defined by the total slip of all blocks during the earthquake, starting from the first block slip and ending when all blocks stick again on the surface. Even if all blocks have uniform size, earthquakes with different size and a complex temporal behavior can occur.

This modification leads straightforward to the model of BURRIDGE AND KNOPOFF [1967], which consists of a two-dimensional coupled network of blocks of uniform size simulating

a two-dimensional planar fault. Assuming an  $N \times N$  network of blocks with positions  $x_{ij}$  ( $i, j = 1, \dots, N$ ), nearest neighbor interaction between the blocks and a velocity-dependent frictional force  $f(\dot{x}_{ij})$ , the model equations are obtained by generalizing Eq. (2.1) to an  $N \times N$  system of ordinary differential equations,

$$m\ddot{x}_{ij} = k \cdot (x_{i+1j} + x_{i-1j} + x_{ij+1} + x_{ij-1} - 4x_{ij}) - K \cdot (vt - x_{ij}) - f(\dot{x}_{ij}), \quad (2.2)$$

where  $v$  is the velocity of the driver plate,  $K$  is the spring constant between each block and the driver plate, and  $k$  is the spring constant of the springs between the blocks, as indicated in Fig. 2.4 for the one-dimensional model. Due to the discontinuous and thus nonlinear character of the frictional force  $f(\dot{x}_{ij})$ , many dynamical regimes are observed. In a two-block system, HUANG AND TURCOTTE [1990a; 1990b] found deterministic chaos including bifurcations and period doubling. In a three-block realization, GABRIELOV *et al.* [1994] showed that, depending on the position in parameter space, the model can produce either deterministic and periodic behavior.

The presence of many blocks is associated with a high complexity of the motion and leads also to a considerable computational effort. It is, therefore, convenient to assume instantaneously occurring slip events, which are separated by long-term tectonic loading periods. In natural seismicity, the intra-event time scale has a duration of seconds, while the waiting time between earthquakes in the same region lasts from days to many decades depending on the magnitude. This approximation corresponds to the neglect of inertia effects. In sum, the dynamic model characterized by Newton's equations, reduces to a kinematic model, which is described by maps and includes two basic mechanisms, occurring in series:

1. linear increase of stress  $\tau(x_i, t)$  in each block (position denoted as  $y_i$ ) until a material strength  $\tau_s(x_i)$  is reached (“tectonic loading”)
2. slip of a block and redistribution of stress to the nearest neighbors triggering eventually slip events of other blocks (“earthquake”).

The first process, which is also phrased as “interseismic”, has a finite duration and is continuous, while the second process, denoted as “coseismic” occurs instantaneously. Because of the mixture of continuous and discrete processes, this type of model is also called a continuous cellular automaton model.

Cellular automaton versions of spring-block models have the advantage that they can be modified easily, e.g. with respect to spatial heterogeneities or interaction between fault segments. Quenched spatial heterogeneities can be defined by space-dependent brittle parameters, e.g. using different values of the material strength (see Fig. 2.2). The nearest-neighbor interaction in the spring-block system can be replaced by the long-range interaction kernel of an elastic half-space, which decays like  $1/r^3$  as a function of the distance  $r$  between two blocks. Furthermore, complex rheologies including viscoelastic terms [HAINZL *et al.*, 1999] can be implemented. Therefore this model class provides a useful and flexible framework for more complex and physically motivated fault models.

## Chapter 3

# Modeling seismicity in real fault regions

In the previous chapter, we introduced spring-block models and continuous cellular automata. In this context, it is important that these models are so-called “inherently discrete” models; that is, they are not obtained by discretizing the differential equations from a continuous model – the discreteness is an inherent feature of the imposed physics. In this section, we focus on the question, how the framework of conceptual models can be adjusted in order to simulate seismicity of a real fault region, e.g. the Parkfield segment of the San Andreas fault in California.

### 3.1 Fault geometry and model framework

A first constraint for a specific model is to include the geometry of the fault segment. As shown in Fig. 3.3, the region of Parkfield is characterized by a distribution of fault segments, which have in good approximation the same orientation. It is therefore reasonable to map these segments in the model on a straight line from SE to NW. Using a similar procedure in depth leads to a rectangular fault plane. The dimensions of the fault segment are chosen to be  $70km$  in length and  $17.5km$  in depth. As discussed in [BEN-ZION AND RICE, 1993], this geometry corresponds approximately to the San Andreas fault near Parkfield. It is emphasized that the plate boundary is assumed to have infinite length, but the brittle processes are calculated on the above defined segment of finite length. The discretization of the plane is imposed by a computational grid with  $128 \times 32$  computational cells of uniform size, where stress and slip are calculated. The size of the computational cells is not determined by observational findings, rather it depends on the magnitude range under consideration and the computational effort; a single cell would correspond to a single magnitude as in Fig. 2.2. A higher resolution of the grid increases the magnitude range, because the magnitude is calculated from the slip of all cells during an earthquake. The degree of complexity as a function of the model geometry is determined by the resolution of the computational grid. A change of the physical dimensions leads only to a rescaling of time and magnitude axis. Following [BEN-ZION AND RICE, 1993], the material surrounding the fault is assumed to be a homogeneous elastic half space of infinite size, which is

characterized by two quantities:

1. The elastic properties are expressed by the Lamé constants  $\lambda$  and  $\mu$ , which connect stress and strain in Hook's law. For many rocks, these constants are almost equal; therefore we use  $\lambda = \mu$ , denoting  $\mu$  as the rigidity. An elastic solid with this property is called a *Poisson solid*. Because the strain is dimensionless,  $\mu$  has the same dimension as the stress. In the present study, we use  $\mu = 30\text{GPa}$ .
2. The (static) Green's function  $G(\mathbf{y}_1, \mathbf{y}_2)$  defines the static response of the half space at a position  $\mathbf{y}_1$  on a displacement at  $\mathbf{y}_2$ , which may arise from (coseismic) slip or (aseismic) creep motion. Due to the discretization of the fault plane into computational cells, we use the Green's function for static dislocations on rectangular fault patches of width  $dx$  and height  $dz$ , which is given in [CHINNERY, 1963] and [OKADA, 1992]. For a model including a single vertical fault, the Green's function is calculated only on a plane:  $G(x_1, z_1; x_2, z_2)$ , where  $x$  and  $z$  denote the coordinates along strike and in depth (for a sketch see Fig. 3.1). Further reduction of the computational effort is given by the symmetry along strike  $G(x_1, z_1; x_2, z_2) = G(|x_1 - x_2|, z_1, z_2)$ . Therefore,  $x_2 = 0$  can be used without loss of generality and the Green's function has the following form:

$$G(x_1, z_1; 0, z_2) = \frac{\mu}{2\pi} \cdot \sum_{i=1}^4 \sigma_i \cdot \left[ \frac{2}{3}(\varepsilon_A^i + \varepsilon_B^i) + \frac{1}{2}\varepsilon_C^i \right]. \quad (3.1)$$

The sign  $\sigma_i$  is defined by

$$\begin{aligned} \sigma_1 &= 1 & \sigma_2 &= -1 \\ \sigma_3 &= -1 & \sigma_4 &= 1. \end{aligned} \quad (3.2)$$

With the notation

$$\begin{aligned} t_1 &= dx/2 - x_1 & t_2 &= dx/2 - x_1 \\ t_3 &= -dx/2 - x_1 & t_4 &= -dx/2 - x_1 \end{aligned} \quad (3.3)$$

$$\begin{aligned} q_1 &= z_2 + dz/2 - z_1 & q_2 &= z_2 - dz/2 - z_1 \\ q_3 &= z_2 + dz/2 - z_1 & q_4 &= z_2 - dz/2 - z_1 \end{aligned} \quad (3.4)$$

$$\begin{aligned} p_1 &= z_2 + dz/2 + z_1 & p_2 &= z_2 - dz/2 + z_1 \\ p_3 &= z_2 + dz/2 + z_1 & p_4 &= z_2 - dz/2 + z_1, \end{aligned} \quad (3.5)$$

the three parts in Eq. (3.1) can be written as follows:

$$\begin{aligned} \varepsilon_A^i &= t_i \cdot \left( \frac{1}{\sqrt{t_i^2 - q_i^2} \cdot (q_i + \sqrt{t_i^2 - q_i^2})} + \frac{1}{\sqrt{t_i^2 - p_i^2} \cdot (p_i + \sqrt{t_i^2 - p_i^2})} \right), \\ \varepsilon_B^i &= t_i \cdot \left( \frac{\frac{1}{4}\sqrt{t_i^2 - p_i^2} + q_i}{\sqrt{t_i^2 - p_i^2} \cdot (p_i + \sqrt{t_i^2 - p_i^2})^2} - \frac{(p_i^2 - q_i^2) \cdot (2\sqrt{t_i^2 - p_i^2} + p_i)}{2(t_i^2 - p_i^2)^{3/2} (p_i + \sqrt{t_i^2 - p_i^2})^2} \right), \\ \varepsilon_C^i &= \frac{q_i}{\sqrt{t_i^2 - q_i^2} \cdot (\sqrt{t_i^2 - q_i^2} + t_i)} + \frac{p_i}{\sqrt{t_i^2 - p_i^2} \cdot (\sqrt{t_i^2 - p_i^2} + t_i)}. \end{aligned} \quad (3.6)$$

The main difference of this Green's function to the nearest-neighbor interaction of spring-block models is the infinite-range interaction following a decay according to  $1/r^3$ , where  $r$  is the distance between source cell and receiver point.

A sketch of the fault model framework is given in Fig. 3.2.

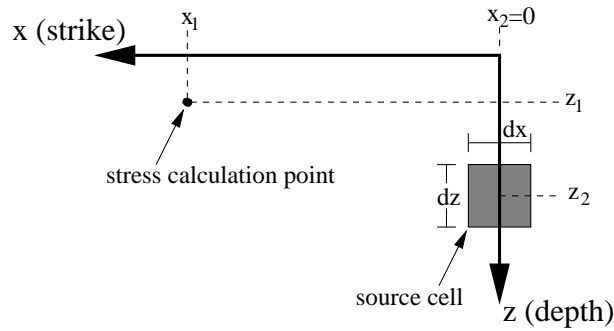


Figure 3.1: Sketch to illustrate the terms in Eq. (3.1)-(3.6).

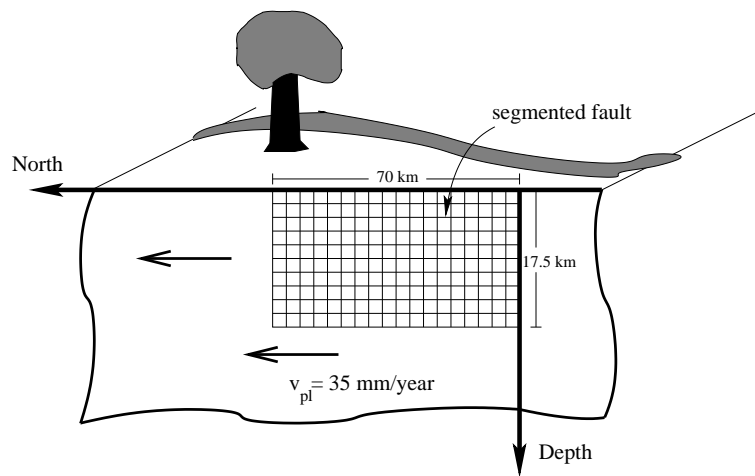


Figure 3.2: Sketch of the fault model framework.

## 3.2 Plate motion

The motion of the tectonic plates, indicated in Fig. 3.3, is responsible for the build-up of stress in the fault zone. Satellite-based measurements of surface displacements allow to

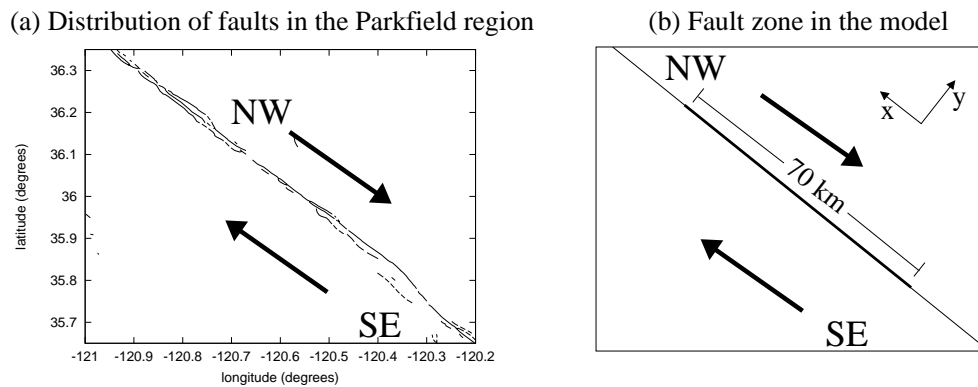


Figure 3.3: (a) Distribution of faults in the Parkfield (California) region; (b) fault region in the model.



estimate the velocity of the plates. For the San Andreas fault, a value of  $v_{pl} = 35\text{mm/year}$  as a long-term average is widely accepted and is therefore adopted for the model [SAVAGE *et al.*, 1999]. The displacement  $\Delta u(i, j)$  of a cell with coordinate  $i$  along strike and  $j$  in depth during a time period  $\Delta t$  is simply  $\Delta u(i, j) = v_{pl} \cdot \Delta t$ . While the average slip rate  $\dot{u}$  is independent of the location of the cell, the stress rate  $\dot{\tau}$  depends on the space. The assumption that the fault zone is embedded in a medium which performs constant creep, suggests that cells at the boundaries of the grid are in general higher loaded than cells in the center of the grid. The properties of the elastic medium are determined by the Green's function  $G(i, j; k, l)$ , which defines the interaction of points  $(i, j)$  and  $(k, l)$  in the medium. In particular, the stress response at a position  $(i, j)$  on a static change of the displacement field  $\Delta u(k, l)$  is given by

$$\Delta \tau(i, j) = - \sum_{(k, l) \in \text{halfspace}} G(i, j; k, l) \cdot \Delta u(k, l), \quad (3.7)$$

where the minus sign stems from the fact that forward (right-lateral) slip of regions around a locked fault segment is equivalent to back (left-lateral) slip of the locked fault segment. Taking into account that

$$\sum_{(k, l) \in \text{halfspace}} G(i, j; k, l) = 0, \quad (3.8)$$

Eq. (3.7) can be written as

$$\tau(i, j; t) = - \sum_{(k, l) \in \text{halfspace}} G(i, j; k, l) \cdot [u(k, l; t) - v_{pl}t], \quad (3.9)$$

where  $u(k, l; t)$  is the total displacement at position  $(k, l)$  and time  $t$  since the begin of the simulation. Because the surrounding medium performs stable sliding,  $u(k, l; t) = v_{pl}t$  for  $(k, l) \notin \text{grid}$ , the slip deficit outside the fault region vanishes and it is sufficient to perform the summation on the computational grid:

$$\tau(i, j; t) = \sum_{(k, l) \in \text{grid}} G(i, j; k, l) \cdot [v_{pl}t - u(k, l; t)]. \quad (3.10)$$

Equation (3.10) can be decomposed in a part for the tectonic loading and a residual part for other processes, especially coseismic slip. The tectonic loading follows the formula

$$\tau_{load}(i, j; t) = \gamma(i, j) \cdot t \quad (3.11)$$

with the space-dependent, but time-independent loading rate

$$\gamma(i, j) = v_{pl} \cdot \sum_{(k, l) \in \text{grid}} G(i, j; k, l). \quad (3.12)$$

### 3.3 Friction and coseismic stress transfer; quasidynamic approach

It is widely accepted that most earthquakes are due to frictional processes on pre-existing faults. The friction is therefore an important empirical ingredient of a fault model [SCHOLZ,

1998]. Numerous laboratory experiments have been carried out to characterize frictional behavior of different materials (see e.g. [BYERLEE, 1978]). An important finding is that the friction defined as the ratio of shear stress  $\tau_{shear}$  and normal stress  $\tau_{normal}$ ,  $\mu_f = \tau_{shear}/\tau_{normal}$  at the initiation of slip, is approximately constant for many materials; the value of  $\mu_f$  lies between 0.6 and 0.85. This observation, known as *Byerlee's law*, is related to the Coulomb failure criterion [BRACE, 1960] for the Coulomb stress  $CS$ ,

$$CS = \tau_{shear} - \mu_f \tau_{normal}. \quad (3.13)$$

The Coulomb stress depends on a plane, where shear stress and normal stress are calculated. The Coulomb criterion for brittle failure is

$$CS \geq 0, \quad (3.14)$$

which is for  $CS = 0$  Byerlee's law.

The North-American plate and the Pacific plate move in opposite direction along the fault plane performing strike-slip motion. The absence of normal and thrust faulting reduces the problem to a one-dimensional motion: all parts of the fault move along the fault direction. The stress state of the fault is fully determined by the shear stress  $\tau_{xy}$  in the coordinates given in Fig. 3.3(b). Slip is initiated, if  $\tau_{xy}$  exceeds  $\mu_f \tau_{yy}$ . This quantity, which is called the material strength or static strength  $\tau_s$ , is constant in time, if  $\mu_f$  is assumed to be constant. Note that the normal stress on a strike-slip fault does not change [AKI AND RICHARDS, 2002]. The shear stress  $\tau_{xy}$  will be denoted simply by  $\tau$ . In this notation, the failure criterion Eq. (3.14) reduces to

$$\tau \geq \tau_s \quad (3.15)$$

in agreement with the conceptual models discussed in Chapter 2 (see, e.g., Fig 2.2(b)).

When a cell  $(k, l)$  fails, the stress drops in this cell to the arrest stress  $\tau_a$ :

$$\tau(k, l) \rightarrow \tau_a, \quad (3.16)$$

with a constant value  $\tau_a$ , which may become space-dependent later. In terms of slip, this corresponds to a displacement

$$\Delta u(k, l) = \frac{\tau(k, l) - \tau_a}{G(k, l; k, l)} \quad (3.17)$$

with the self-stiffness  $G(k, l; k, l)$  of cell  $(k, l)$ .

The observational effect of dynamic weakening includes also a strength drop from the static strength to a lower dynamic strength:

$$\tau_s \rightarrow \tau_d. \quad (3.18)$$

In particular, slipping material becomes weaker during rupture and recovers to the static level at the end of the rupture. This behavior of the strength corresponds to the static-kinetic friction law.

The values  $\tau_s$ ,  $\tau_d$ , and  $\tau_a$  are connected by the dynamic overshoot coefficient  $D$ :

$$D = \frac{\tau_s - \tau_a}{\tau_s - \tau_d}. \quad (3.19)$$

MADARIAGA [1976] proposed  $D = 1.25$  motivated by elastodynamic model simulations, which is used to constrain the choice of these values in our model.

The redistribution of the stress release  $\Delta\tau(k, l) = \tau(k, l) - \tau_a$  from cell  $(k, l)$  to a point  $(i, j)$  at time  $t$  is

$$\tau(i, j; t) = G(i, j; k, l) \cdot \delta\left(t - \frac{r(i, j; k, l)}{v_s}\right) \cdot \frac{\tau(k, l) - \tau_a}{G(k, l; k, l)}, \quad (3.20)$$

where  $\delta(x, y)$  denotes the  $\delta$ -function, which is 1 for  $x = y$  and 0 else;  $v_s$  is the constant shear-wave velocity, and  $r(i, j; k, l)$  is the distance between source cell  $(k, l)$  and receiver position  $(i, j)$ . That is, cells far from the slipping cell receive their stress portion later than cells close to the slipping cell. The value of  $v_s$  is assumed to be constant. Each “stress transfer event” denotes an instantaneous transfer of a stress  $\Delta\tau$  from a source cell  $(k, l)$  to a receiver cell  $(i, j)$  at time  $t$ . This time-dependent stress transfer is called the *quasidynamic* approach in contrast to the *quasistatic* approach used in most of the similar models.

The evolution of stress and strength in a cell, where an earthquake is initiated (hypocenter cell), is shown in a sketch in Fig. 3.4. When the earthquake is initiated, the stress and the strength drop. Due to coseismic stress transfer during the event, the cell may slip several times, before the earthquake is terminated and instantaneous healing takes place in all cells. The piecewise constant failure envelope (dashed line) indicates static-kinetic friction. In a first step towards more realistic healing properties the instantaneous healing at the end of the event can be replaced by  $\log(t)$  healing starting immediately after the strength drop (see also Section 3.6). This is shown in Fig. 1 of Appendix K.

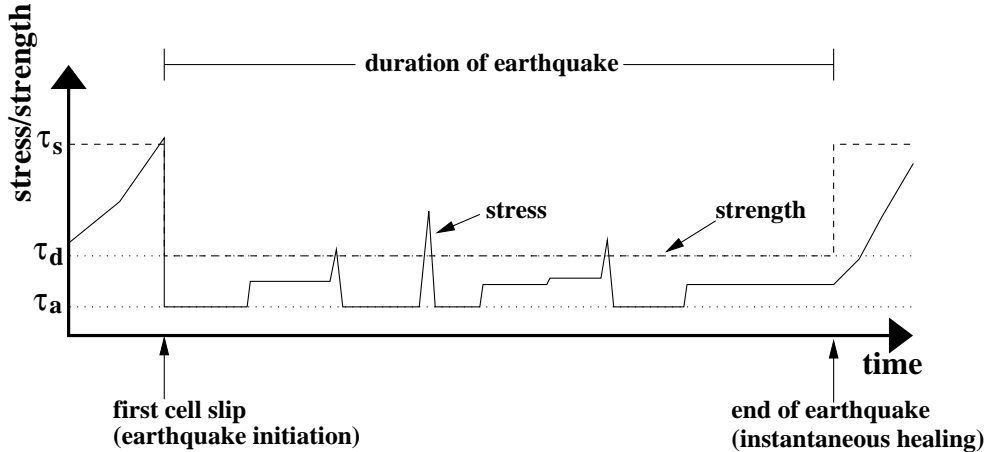


Figure 3.4: Pictorial evolution of stress (solid line) and strength (dashed line) of a hypocenter cell in the quasidynamic approach.

We note that the Green’s function leads to an infinite interaction range. Using open boundary conditions with respect to the computational grid, the stress release from a slipping cell is not conserved on the grid, but on the (infinite) fault plane.

### 3.4 Model algorithm

Equation (3.17) shows the correspondence of stress and slip in our model. The model can be formulated either by maintaining stress or by maintaining slip. The algorithm is given for both formulations.

#### Stress formulation:

1. Load the fault according to Eq. (3.11), until the first cell is *critical*; that is, the cell fulfills the failure criterion Eq. (3.15). Initiate earthquake.
2. Reduce stress in critical cell to  $\tau_a$  and strength to  $\tau_d$ . Schedule stress transfer events according to Eq. (3.20) on the intra-event timescale.
3. Perform stress transfer event with the smallest time. Check whether receiver cell is critical.
  - (a) If no, remove current stress transfer event from the scheduler: (i) if last stress transfer event, terminate earthquake and go to point 4; (ii) else go back to the beginning of point 3.
  - (b) If yes, go to point 2.
4. Set strength to  $\tau_s$  for all cells (instantaneous healing).

#### Slip formulation:

1. Load the fault according to Eq. (3.11), until the first cell is *critical*; that is, the cell fulfills the failure criterion Eq. (3.15). Initiate earthquake.
2. Reduce stress in critical cell to  $\tau_a$  and strength to  $\tau_d$ ; update coseismic slip  $u \rightarrow u + \Delta u$  in this cell with  $\Delta u$  from Eq. (3.17). Schedule stress transfer events according to Eq. (3.20) on the intra-event timescale.
3. Perform stress transfer event with the smallest time. Check whether receiver cell is critical.
  - (a) If no, remove current stress transfer event from the scheduler: (i) if last stress transfer event, terminate earthquake and go to point 4; (ii) else go back to the beginning of point 3.
  - (b) If yes, go to point 2.
4. Set strength to  $\tau_s$  for all cells (instantaneous healing).
5. Calculate stresses  $\tau(i, j)$  of all cells after the earthquake from the initial stresses  $\tau(i, j; 0)$  and the new positions  $u(k, l; t)$ :

$$\tau(i, j; t) = \tau(i, j; 0) + \sum_{(k, l) \in \text{grid}} G(i, j; k, l) \cdot [v_{pl}t - u(k, l; t)]. \quad (3.21)$$

### 3.5 Limits and parameters of the model

The model framework described in the previous sections includes the basic properties of seismicity, namely tectonic loading and coseismic stress transfer. Although these mechanisms are also part of simple slider-block and cellular automaton models, the implementation described above provides a more physical approach, because it is derived from dislocation theory and uses the same Green's function for both processes. The coseismic propagation of stress and slip overcomes the unrealistic assumption of an instantaneous occurring earthquake and is therefore more physical than the quasistatic approach. The quasidynamic model is, however, still too simple in order to govern the full complexity of dynamic rupture simulations. Despite the pulse-like shape (arising from the  $\delta$  function in Eq. (3.20)) of the stress transfer events and the step-like slip functions, the computational effort may become very large and result in a memory exhaustion due to the large number of single slips. Therefore, it is useful to constrain single events to occur at discrete times. The resolution of the discretization can be tuned between a single time value corresponding to the quasistatic model and a large number of time bins close to the continuous case. This number determines also the required memory for a simulation.

An advantage of the model is the limited number of parameters. Keeping physically chosen values fixed, e.g. the plate velocity  $v_{pl}$ , the rigidity  $\mu$ , and the dynamic overshoot coefficient  $D$ , the brittle parameters  $\tau_s$ ,  $\tau_d$ , and  $\tau_a$  have to be determined. To produce a certain degree of complex dynamics, the values should be chosen disordered depending on space, reflecting quenched spatial heterogeneity.

### 3.6 Model extensions

The features described in Section 3.1 to 3.4 provide a basic framework of a simulation tool for the Parkfield region and other real fault zones. In order to make the computer code as flexible as possible, the ingredients have been implemented in a modular C++ class library. This includes mainly three hierarchy levels: the system, the fault, and the computational cells. The system controls the global time and checks for criticality of the faults (in the present state: only one fault), each fault checks for criticality of its cells. A cell maintains stress, strength, and displacement. The mechanisms include a loading model for the interseismic processes and an intra-event scheduler, which organizes the coseismic stress and displacement changes. Both parts depend on the Green's function, which is a separate class. The modular design allows to reproduce other models, for instance, cellular automaton models similar to [OLAMI *et al.*, 1992], in a straightforward manner: the Green's function is replaced by a nearest-neighbor interaction kernel and the matrix elements of loading rates in Eq. (3.12) become constant. On the other hand, additional mechanisms can be included as additional classes without modifying the whole code. In the following, we give a brief list of additional mechanisms, which have been implemented or will be implemented in the future.

1. Boundary conditions: For the Parkfield segment, the boundary conditions are known. While the northern end is bounded by a creeping section, the fault zone south from the Parkfield segment is locked and ruptured only during the M8 Fort Tejon earthquake in 1857. This event can be implemented by adding a slip portion instantaneously.

neously on the fault in 1857. The fact that the segment is locked during the rest of the time, reduces the stress increase on the computational grid between earthquakes accordingly.

2. Aseismic creep and brittle-ductile transition: The presence of stable creep in fault zones is known from satellite-based observations, e.g. [LYONS AND SANDWELL, 2003] and from laboratory experiments [MARONE *et al.*, 1991]. Especially the increase of temperature and pressure with depth leads to ductile behavior; that is, the stress from the tectonic plate motion will predominantly be compensated by stable creep instead of coseismic slip. In the present work, creep is implemented according to the system of coupled differential equations for the creep velocities [BEN-ZION AND RICE, 1993]:

$$v_{creep}(i, j; t) = c(i, j) \cdot \tau^3(i, j; t), \quad (3.22)$$

with  $\tau(i, j; t)$  from Eq. (3.10) and time-independent creep rates  $c(i, j)$ , which are assumed to increase with depth. The slip rate in the interseismic periods becomes time-dependent now:

3. Normal faulting and dip-slip behavior, buried faults: The generalization

$$\dot{u}(i, j; t) = v_{pl} - v_{creep}(i, j; t). \quad (3.23)$$

to other fault mechanisms is straightforward; the equations for the Green's function are listed in [OKADA, 1992]. These equations are also valid for buried faults.

4. Fault systems consisting of more than one fault: Using again the equations from [OKADA, 1992] for the response of an arbitrary point in the 3D elastic half space on a static dislocation of a source cell, this extension is also straightforward, but leads to a high computational effort, e.g. in the case of two interacting faults consisting of  $N_1$ , respectively  $N_2$  cells, the Green's function will be given by  $N_1^2 \cdot N_2^2$  values.
5. Continuous healing: So far, the material strength is a piecewise constant function with the unrealistic assumption of instantaneous healing when the earthquake stops. However, laboratory experiments point to a more continuous healing, where the strength increases according to  $\log(t)$  on a time scale of months to years [RUINA, 1983; SCHOLZ, 1998]. This process results in a coupling of interevent and the intra-event time scale.
6. Other friction laws: The static-kinetic friction is a simplification of the more general rate and state dependent friction law [DIETERICH, 1994], which is an empirical constitutive law that has been fit to observations. This law includes both, a dependence on the velocity  $V$  (slip rate) and on the time-dependent state represented by a state variable  $\theta$ . The friction  $f$  as a function of  $V$  and  $\theta$  is given by

$$f(V, \theta) = f^0 + a \ln \left( \frac{V}{V_0} \right) + b \ln \left( \frac{V_0 \theta}{D_c} \right) \quad (3.24)$$

with material parameters  $a$  and  $b$  and a critical slip distance  $D_c$ . The value  $\tau_f^0$  denotes the friction at a reference velocity  $V_0$ . The state variable  $\theta$  evolves like

$$\dot{\theta} = 1 - \frac{V\theta}{D_c}. \quad (3.25)$$

In the static case  $\theta = D_c/V$ , this law reduces to

$$f_{stat}(V) = f^0 + (a - b) \ln\left(\frac{V}{V_0}\right) \quad (3.26)$$

The terms in Eq. (3.26) are illustrated in Fig. 3.5. The fast process corresponds to the dynamic weakening in the static-kinetic friction law, the recovery of the friction after the step-like decrease is the healing process mentioned in the previous point.

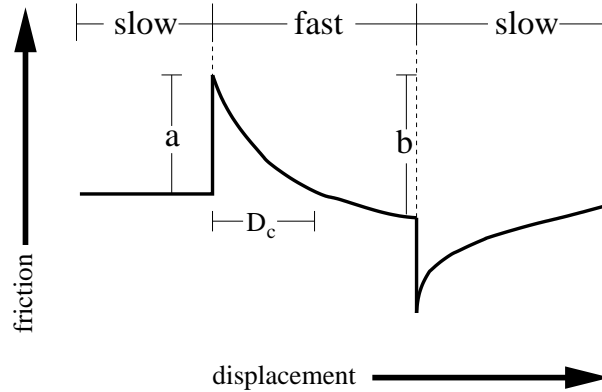


Figure 3.5: Schematic description of the frictional response on a velocity step in the presence of rate and state dependent friction.

Depending on the sign of  $a - b$  in Eq. (3.26), the frictional response may be velocity strengthening ( $a - b \geq 0$ ) or velocity weakening ( $a - b < 0$ ). The latter case is a necessary condition for unstable behavior, while the first case terminates slip and thus leads to a stabilization of the system. The bifurcation diagram including regions of stability and unstable behavior is given in [SCHOLZ, 2002]. Here we only mention that static loading of a stick-slip system with rate and state dependent friction may lead to an instability (earthquake) that is preceded by a period of accelerated sliding. This nucleation period is of particular interest for earthquake prediction.

The full calculation of rate and state dependent friction in the model would be complicated, because Eq. (3.24) is a differential equation which affects both time scales, the *inter*-event time scale and the *intra*-event time scale [HILLERS *et al.*, 2005]. So far, these time scales are separated.

7. Damage: In the present state of model development, earthquakes are assumed to occur on pre-existing faults which do not change in time. However, experimental and theoretical studies [LOCKNER *et al.*, 1991; LYAKHOVSKY *et al.*, 1997] indicate the presence of damage in terms of an evolution of fault geometry and elastic properties. Taking a physical damage rheology into account, would increase the complexity of the model significantly. Therefore, an effective approach with a single damage state variable as in [LYAKHOVSKY *et al.*, 2005], provides a feasible way to include evolving damage.

At the present state of model development, the mechanisms described in points 1-3 have been included. Continuous healing on the intra-event time scale has also been taken into account. Details and results are given in the appendices. The remaining mechanisms are

related with a significant increase of the computational effort and are therefore left for future studies.

### 3.7 Data types

The model produces two types of data, earthquake catalogs and histories of stress and displacement. As demonstrated below, all parameters of the model have physical dimensions and can therefore be compared directly with real data. This is in contrast to most of the slider-block and cellular automaton models.

1. Earthquake catalogs include time, coordinates of the hypocenter, and the earthquake size. The time of an earthquake is the time of the first slip; the hypocenter is determined by the position of the corresponding cell along strike and depth. The size of an event can be described by different measures: The rupture area  $A$  is the total area, which slipped during an earthquake. The potency

$$P = \int_{grid} \Delta u(x, z) dx dz \quad (3.27)$$

measures the total slip during the event and is related to the seismic moment  $m_0$  by the rigidity:  $m_0 = \mu P$ . The (moment) magnitude  $M$  can be calculated from the potency using

$$M = (2/3) \log_{10}(P) + 3.6, \quad (3.28)$$

where  $P$  is given in  $cm \cdot km^2$  [BEN-ZION, 1996].

2. Stress  $\tau(x, z; t)$  and displacement  $u(x, z; t)$  as a function of space and time can be monitored during the whole simulation. In particular, the spatiotemporal evolution of stress and slip during an earthquake is accessible in the model. In contrast to earthquake catalogs, these data are only available for real fault systems in limited cases, where slip distributions have been inverted.



# Chapter 4

## Results

Numerous simulations of the model described in the previous chapter have been performed. The first catalogs [ZÖLLER *et al.*, 2004] produced by simulations have been studied with respect to the influence of the quasidynamic approach and the discretization of the intra-event time scale in comparison with the quasistatic model of BEN-ZION AND RICE [1993]. Then, a large fraction of the parameter space has been analyzed to find relationships between input parameters and observed seismicity features. Finally, new mechanisms have been adopted (see Section 3.6) in order to overcome unrealistic behavior and to adjust the model towards real faults. All results are presented and discussed in detail in the publications given in Appendix A to N. In this chapter, the key results are highlighted and discussed in the light of critical states of seismicity.

### 4.1 Frequency-size distributions

The frequency-size (FS) distribution is one of the most important characteristics of observed seismicity. For worldwide seismicity as well as for large faults systems, this distribution is given by the Gutenberg-Richter law (Eq. (1.1)). Figure 4.1 shows the FS distribution of California from 1970 to 2004. Here we use the non-cumulative version of Eq. (1.1), where  $N$  is the number of earthquakes with magnitude between  $M$  and  $M + dM$  with a time bin  $dM$ . For individual faults or small fault systems, the FS distribution can deviate from Eq. (1.1), especially for high magnitudes. An example is given in Fig. 4.2, which shows the FS distribution of the Parkfield segment (Fig. 4.2(a)) and for the San Jacinto fault (Fig. 4.2(b)) in California calculated for a time span of 45 years. The distribution of the Parkfield segment consists of two parts: A scaling regime for  $2.2 \leq M \leq 4.5$  and a significant “bump” for  $4.5 < M \leq 6.0$ . For the San Jacinto fault, the scaling range is observed for almost all events ( $2.2 \leq M \leq 5.0$ ). The slight decrease for  $M \approx 2$  in both plots is due to lacking catalog completeness.

A FS distribution as shown in Fig. 4.2(a) is called a characteristic earthquake distribution, because of the increased probability for the occurrence of a large (“characteristic”) event. In contrast, distributions with a broad scaling regime following power-law behavior according to the Gutenberg-Richter law, are denoted as “scale-free”, because a power law distribution indicates the absence of a characteristic scale of the earthquake size [TUR-

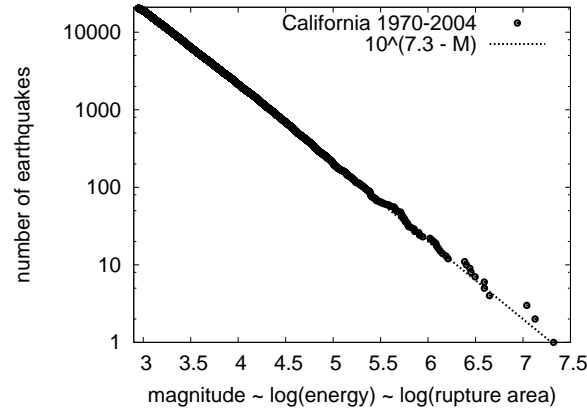


Figure 4.1: Frequency-size distribution for California from 1970 to 2004; the dashed line denotes a power-law fit to the data.

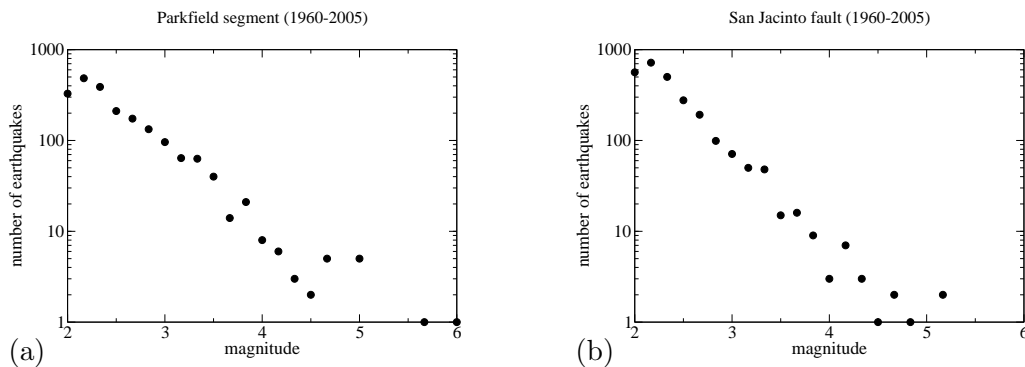


Figure 4.2: Frequency-size distribution for two faults in California: (a) the Parkfield segment, and (b) the San Jacinto fault calculated over 45 years.

COTTE, 1997]. In terms of critical point processes, the absence of a characteristic length scale indicates that the system is close to the critical point. In this state, earthquakes of all magnitudes can occur, or each small rupture can grow into a large one. Therefore, the frequency-size distribution can serve as a proxy for the current state of a system in relation to a critical point.

In a model, the easiest way to tune the FS distribution is a variation of the mean stress  $\langle \tau \rangle$  on the fault, where  $\langle \rangle$  denotes the spatial average of all cells. This can be achieved, for instance, by varying brittle properties, e.g. in terms of the dynamic overshoot coefficient  $D$  (Eq. (3.19)), or by introducing dissipation [HAINZL AND ZÖLLER, 2001; ZÖLLER *et al.*, 2004]. Figure 4.3 shows FS distributions for two different values of  $D$ , first  $D = 1.25$  (Fig. 4.3(a)) from MADARIAGA [1976], and second a higher value  $D = 1.67$  (Fig. 4.3(b)). While Fig. 4.3(a) follows a characteristic earthquake behavior similar to the Parkfield case (Fig. 4.2(a)), Fig. 4.3(b) resembles the shape of the FS distribution of the San Jacinto fault (Fig. 4.2(b)).

As an outcome, three cases can be distinguished by means of a critical mean stress  $\tau_{crit}$ :

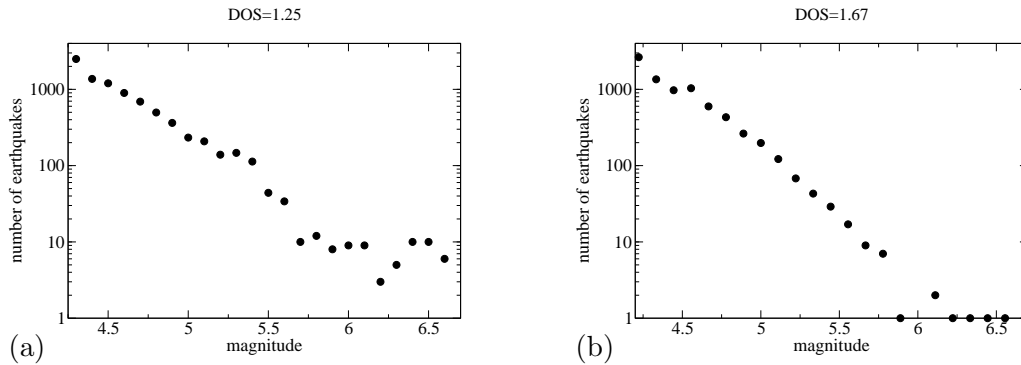


Figure 4.3: Frequency-size distribution for model realizations with different dynamic overshoot coefficients (Eq. (3.19)): panel (a)  $D = 1.25$ , panel (b)  $D = 1.67$ .

1. subcritical fault ( $\langle \tau \rangle < \tau_{crit}$ ): the mean stress on the fault is too small to produce large events. The system is always far from the critical point. The FS distribution is a truncated Gutenberg-Richter law.
2. supercritical fault ( $\langle \tau \rangle > \tau_{crit}$ ): the mean stress is high and produces frequently large events. After a large earthquake (critical point), the stress level is low (system is far from the critical point) and recovers slowly (approaches the critical point). The FS distribution is a characteristic earthquake distribution.
3. critical fault ( $\langle \tau \rangle \approx \tau_{crit}$ ): the system is always close to the critical point with scale-free characteristics. The FS distribution is a Gutenberg-Richter law with a scaling range over all magnitudes.

This result demonstrates that, for isolated faults, the Gutenberg-Richter law is not the rule, but the exception. If the FS distribution is plotted as a function of the parameters controlling  $\langle \tau \rangle$ , this result can be visualized by a phase diagram [DAHMEN *et al.*, 1999; HAINZL AND ZÖLLER, 2001; ZÖLLER *et al.*, 2004; 2005c].

While it is obvious that the mean stress drop  $\langle \Delta \tau \rangle \approx \langle \tau_s - \tau_a \rangle$  controls the mean stress  $\langle \tau \rangle$  on the fault, it has also been found that the spatial distribution of the stress drop has significant influence on the FS distribution. This is apparent in the case of a cellular automaton with a tectonic loading rate  $\gamma$  (see Eq. (3.12)), which is not only time-independent, but also space-independent. In this case, the cells will synchronize, and from the time of synchronization the dynamics will be periodic culminating in a large event. Thus, the FS distribution will follow a characteristic earthquake law. This trivial case can be overcome by introducing quenched (time-independent) spatial disorder. If, for instance, a barrier with a high static strength is included in a homogeneous fault, a system-wide event will be terminated at the barrier with some probability.

Quenched spatial heterogeneity is introduced in the model from Chapter 3 by means of a variable arrest stress  $\tau_a$ ; the static strength  $\tau_s$  remains homogeneous and the dynamic strength  $\tau_d$  is constraint by the dynamic overshoot coefficient  $D$  (Eq. (3.19)). The results indicate that the degree of heterogeneity measured by the range of spatial size scales acts as a tuning parameter for the FS distribution [ZÖLLER *et al.*, 2005c]. This behavior is clearly

visible for discontinuous distributions of stress drops, e.g. high stress drop barriers in a low stress drop environment. The range of size scales can be quantified by the standard deviation of the distribution of circular areas which are placed between the barriers. These circles give rough estimates for patches where a rupture can evolve unperturbed. In models of real faults, such barriers provide a simplified way to simulate fault segmentation like step-over regions and offsets.

## 4.2 Temporal occurrence of large earthquakes

The finding that quenched spatial heterogeneities have influence on the rupture propagation suggests that also temporal clustering properties will be affected. While the end member case of a smooth fault produces regular occurrence of events, it can be assumed that a strongly disordered fault will show irregular earthquake occurrence. In Fig. 4.4, we focus on the regularity of the largest earthquakes in a simulation, e.g. earthquakes with  $M \geq 5.7$ , for two different degrees of spatial disorder. Each plot is based on an earthquake sequence covering 1000 years. Figure 4.4(a) corresponds to a smooth fault and Fig. 4.4(b) to a rough (disordered) fault; the ordinate has no meaning. Although no strictly periodic mainshock occurrence is observed, the sequence for the smooth fault (Fig. 4.4(a)) is characterized by relatively regular mainshock sequences. In contrast, the sequence for the highly disordered fault Fig. 4.4(b) shows a more disordered and clustered behavior. It is interesting to note that sequences similar to the Parkfield sequence can be found in Fig. 4.4(a), e.g. between  $t \approx 600\text{years}$  and  $t \approx 720\text{years}$ , where an almost periodic mainshock sequence is followed by a gap before the next large event occurs. This resembles the most recent Parkfield event on September 28, 2004, which occurred 16 years after it was predicted based on the approximate period of 22 years for  $M6$  events on this fault segment.

A more quantitative measure for temporal clustering properties of earthquake sequences is the coefficient of variation

$$CV = \sigma_{\Delta t} / \langle \Delta t \rangle \quad (4.1)$$

calculated for the interevent-time distribution, where  $\sigma_{\Delta t}$  is the standard deviation and  $\langle \Delta t \rangle$  the mean value of the interevent-time distribution. High values of  $CV$  denote clustered activity, while low values represent quasiperiodic occurrence of events. The limit case  $CV = 1$  corresponds to a random Poisson process [DALEY AND VERE-JONES, 1988]. Table 1 in Appendix L shows the systematic dependence of  $CV$  as a function of the degree of spatial disorder, and Fig. 4.5 demonstrates (for a smooth fault) that quasiperiodic earthquake occurrence is found for the largest events, while intermediate and small events occur irregular.

## 4.3 The stress field for different degrees of disorder

The observation that smooth faults show a more regular earthquake occurrence than rough faults, can be explained by the ability of the stress field to synchronize on certain fault patches. On a disordered fault, this type of synchronization is unlikely. Figure 4.6(a) shows the stress field at the beginning of a large earthquake on a smooth fault. The most

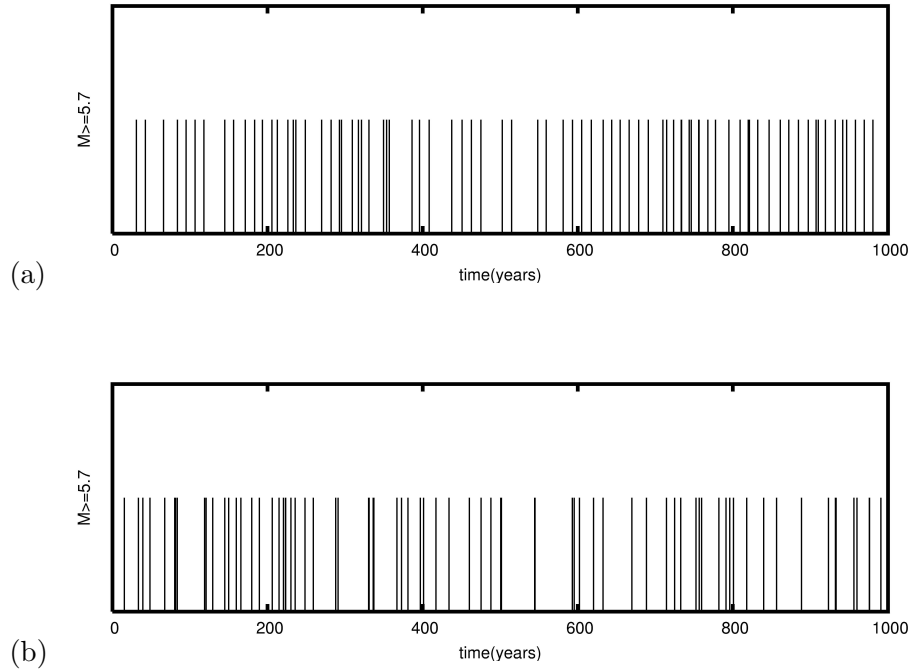


Figure 4.4: Mainshock sequence from model simulations of a smooth fault (panel (a)) and a rough fault (panel (b)). The plots show earthquakes with  $M \geq 5.7$ ; the ordinate has no meaning.

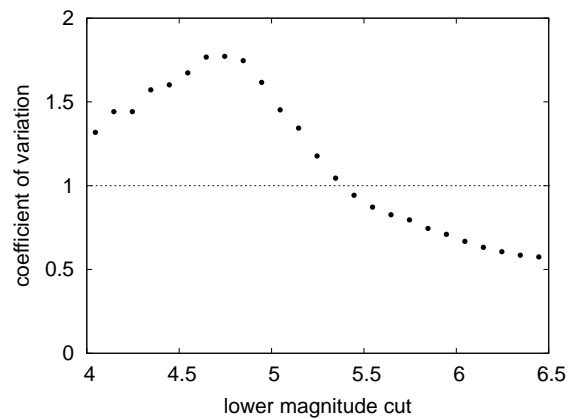


Figure 4.5: Temporal earthquake occurrence quantified by the coefficient of variation (Eq. (4.1)) as a function of the lower magnitude cutoff.

striking feature is the emergence of clearly defined patches with highly loaded boundaries. During rupture evolution, these patches rupture almost in series until the fault is nearly unloaded (see Fig. 10(f) in Appendix L). A different situation is shown in Fig. 4.6(b) corresponding to a rough fault with a brittle-ductile transition zone resulting from creep

rates which increase with depth [BEN-ZION, 1996]. Here, the stress field in the brittle regime is irregular without obvious pattern formation. Similar behavior is found in the case, where dynamic weakening is switched off ( $\tau_d = \tau_s$  or  $D \rightarrow \infty$ ); in other words, the material heals instantaneously. Figure 4.6(c) shows the stress field in this case. As discussed by FISHER *et al.* [1997] and DAHMEN *et al.* [1999], this corresponds exactly to a critical point in the phase diagram for the FS distribution spanned by stress dissipation and dynamic weakening.

Although the stress field shows a complex evolution during a simulation, the presence or absence of characteristic length scales indicating the relation to a critical point is easily detected. However, from an observational point of view, the stress field is not accessible, but the FS distribution can serve to some extent as a proxy for the degree of disorder of the stress field.

If the model is in the transition regime between Gutenberg-Richter statistics and characteristic earthquake behavior (see Fig. 4 in Appendix K), the ability of the stress field to synchronize on parts of the fault, can have additional impact on the dynamics of seismicity: for a model with small cells and high stress fluctuations along the cell boundaries arising from a high degree of spatial disorder, the system can undergo a spontaneous transition from an ordered state and a characteristic earthquake law to a disordered state following Gutenberg-Richter statistics (see Fig. 4.7). Due to the high fluctuations in the stress field, there is some probability that a certain number of cells synchronize by chance, leading to an ordered behavior for some seismic cycles, until the order is destroyed, again resulting from stress fluctuations. This mode-switching has been observed earlier in a mean-field model by DAHMEN *et al.* [1999]. In this more unrealistic model where the stress redistribution is governed by a constant (space-independent) Green's function, analytical expressions for persistence times have been calculated [FISHER *et al.*, 1997]. Although BEN-ZION *et al.* [1999] claim some evidence for mode-switching behavior in a seismic record based on sediment and paleoseismic data from the Dead Sea region, the relevance of mode-switching from an observational point of view cannot finally be evaluated due to a lack of very long records.

## 4.4 Aftershocks and foreshocks

The most pronounced pattern in observed seismicity is the emergence of strongly clustered aftershock activity following a large earthquake. Apart from the Omori law (Eq. (1.2)), it is widely accepted that aftershocks are characterized by the following properties:

1. The aftershock rate scales with the mainshock size [REASENBERG, 1985].
2. Aftershocks occur predominantly at the edges of the ruptured fault segments [UTSU, 2002].
3. Båth's law [BÅTH, 1965]: The magnitude of the largest aftershock is  $M_m - D_1$ , where  $M_m$  is the mainshock magnitude and  $D_1 \approx 1.2$ .

Deviations from the Omori law, especially for rough faults, are discussed in [NARTEAU *et al.*, 2003]. While aftershocks are observed after almost all large earthquakes, foreshocks

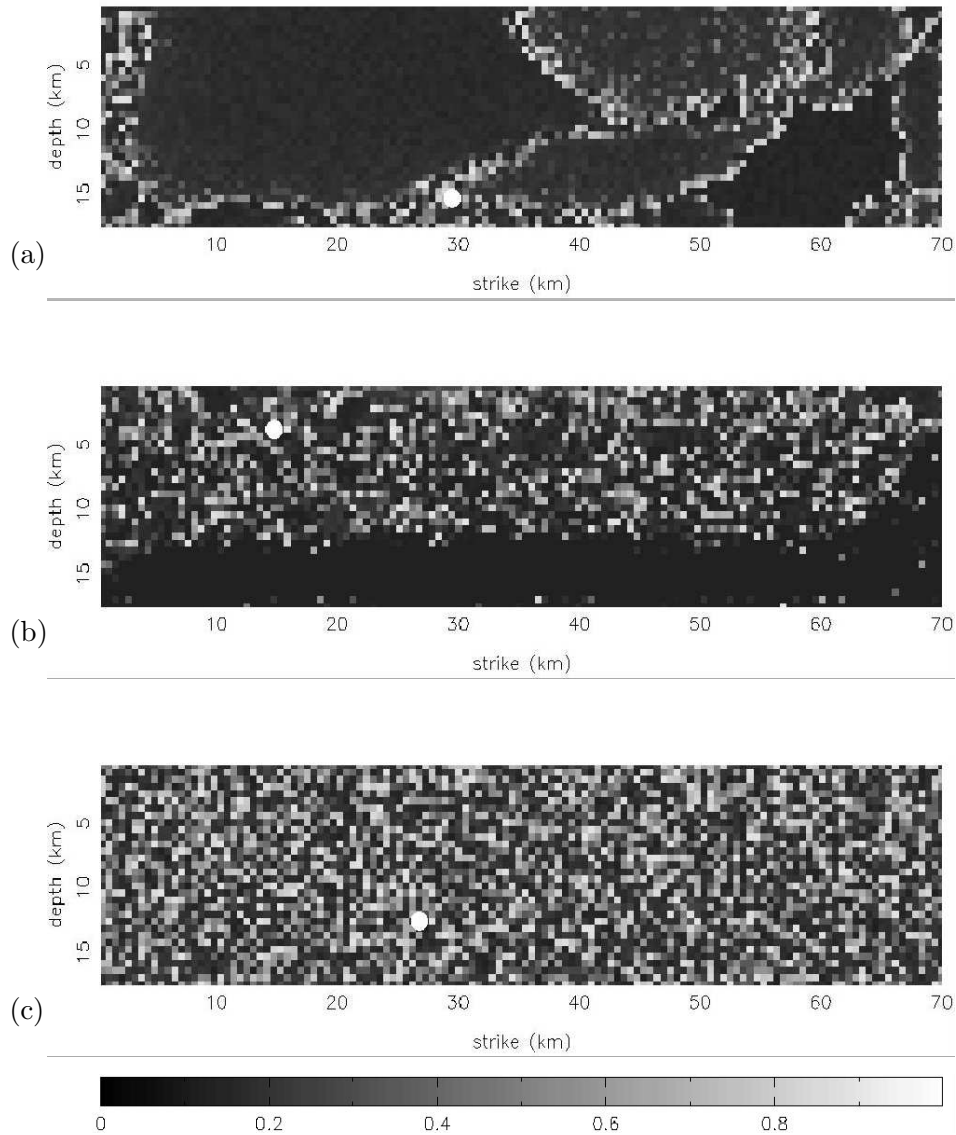


Figure 4.6: Snapshot of the stress field (normalized between 0 and 1) before a large earthquake for three model realizations: (a) a smooth fault without aseismic creep; (b) a rough fault with aseismic creep and depth-dependent creep rates leading to a brittle-ductile transition at a depth of about  $12.5\text{km}$ ; (c) a fault without dynamic weakening ( $\tau_d = \tau_s$ ) corresponding to a dynamic overshoot coefficient  $D \rightarrow \infty$  (Eq. (3.19)).

occur less frequent [WYSS, 1997]. As a consequence, much less is known about the properties of these events. KAGAN AND KNOPOFF [1978] and JONES AND MOLNAR [1979] propose a power law increase of activity according to an “inverse” Omori law.

Figure 4.8(a) shows an example for the aftershock sequence following the  $M7$  Landers earthquake in California on June 28, 1992. An earthquake of similar size generated by the model is given in Fig. 4.8(b). The absence of aftershocks in the simulation is clearly

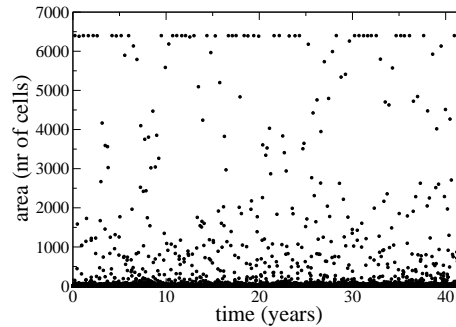


Figure 4.7: Earthquake area as a function of time for a simulation of a heterogeneous fault with  $128 \times 50$  cells. Note that the higher number of cells results effectively in a smaller cell size.

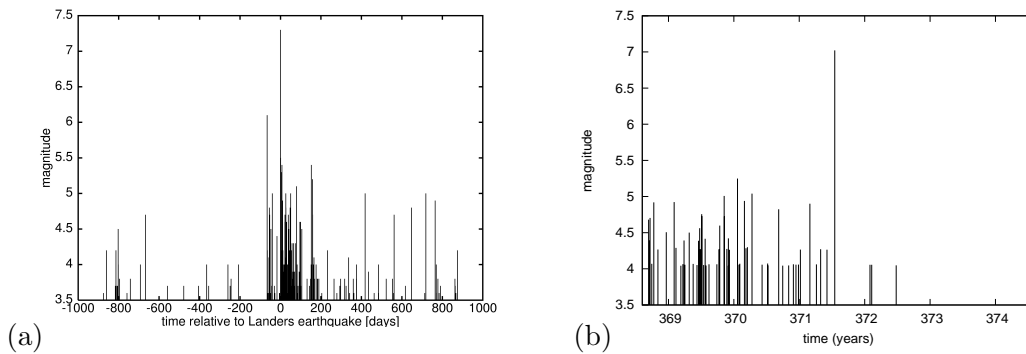


Figure 4.8: Earthquakes before and after a mainshock: (a) the  $M7$  Landers (California) earthquake; (b)  $M7$  earthquake in the basic version of the model.

visible. The reason for the lack of aftershocks is the unloading of the fault due to the mainshock, which is demonstrated in Fig. 10(f) in Appendix L. When a large fraction of the fault has ruptured, the stress in this region will be close to the arrest stress after the event. Consequently, the seismic rate will be almost zero until the stress field has recovered to a moderate level.

It is not surprising that a model which imposes only tectonic loading and coseismic stress redistribution, produces no aftershocks, because it is likely that aftershocks are due to additional mechanisms triggered by the mainshock. A discussion on candidates for such mechanisms is given in [ZÖLLER *et al.*, 2005b]. A common feature is the presence of post-seismic stress which generates aftershock activity. In [HAINZL *et al.*, 1999], for instance, postseismic stress has been attributed to a viscoelastic relaxation process following the mainshock. In the present work, creep motion following the constitutive law in Eq. (3.22) is assumed. Additionally, the computational grid is divided by aseismic barriers from the free surface to depth into a couple of seismically active fault segments (see Fig. 3 in Appendix M). As discussed in [ZÖLLER *et al.*, 2005b], this modification results in a concentration of stress in the aseismic regions during rupture and, subsequently in a



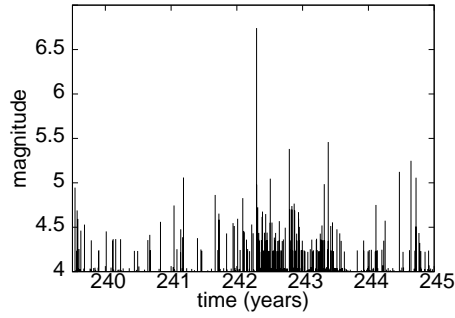


Figure 4.9: Earthquakes before and after a mainshock with  $M = 6.8$  in the modified model.

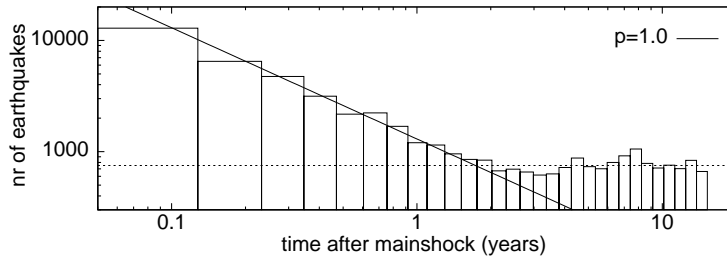


Figure 4.10: Earthquake rate as a function of time for the model with seismic and aseismic regions. The calculation is based on a simulation with 20,000 earthquakes covering about 500 years; the earthquake rates are averaged over about 30 mainshocks. A fit of the Omori law (Eq. (1.2)) with  $p = 1$  is denoted as a solid line. The dashed line gives the estimated background level of seismicity.

release of stress after the event according to the coupled process from Eq. (3.22). This stress release triggers aftershock sequences obeying the Omori law (Eq. (1.2)). A typical aftershock sequence after a  $M6.8$  event is shown in Fig. 4.9. According to Båth's law, the strongest aftershock has the magnitude  $M = 5.5$ . The sequence shows also the effect of secondary aftershocks, namely aftershocks of aftershocks [SORNETTE AND SORNETTE, 1999]. The evolution of stress in the seismic and in the aseismic parts of the fault and the corresponding earthquake occurrence is shown explicitly in Figure 4 of Appendix M: during a large event, stress is stored in the creeping zones, and afterwards the stress is released to the entire fault triggering an aftershock sequence.

In Appendix M, the earthquake rate, stacked for a large number of mainshocks, is analyzed as a function of the distribution of the creep coefficients  $c(i, j)$  in Eq. (3.22). A realistic exponent of  $p = 1$  is found if the barriers are characterized by creep coefficients, which are by factor of  $10^5$  higher than the creep coefficients in the seismic patches. The stacked earthquake rate as a function of the time after the mainshock is given in Fig. 4.10. In [ZÖLLER *et al.*, 2005a; 2005b], it is demonstrated that the simulated aftershock sequences show a high correspondence with natural aftershock activity, and that they are qualitatively compatible with satellite-based observation of afterslip along fault zones (see e.g. [BÜRGMANN *et al.*, 2002]).

Aftershock sequences like in in Fig. 4.9 emerge after all large events in the extended model. In contrast, there is no clear foreshock signal visible in single sequences. However, stacking many sequences together, unveils a slight increase of the earthquake rate prior to a main-

shock supporting the observation of rarely occurring foreshock activity. An explanation of these events can be given in the following way: Between two mainshocks, the stress field organizes itself towards a critical state, where the next large earthquake can occur. This critical state is characterized by a disordered stress field and the absence of a typical length scale, where earthquakes of all sizes can occur. The mainshock may occur immediately or after some small to moderate events. The latter case can be considered as a single earthquake, which is interrupted in the beginning. This phenomenon of delayed rupture propagation has already provided a successful explanation of foreshocks and aftershocks in a cellular automaton model [HAINZL *et al.*, 2000a; 2003].

The hypothesis that foreshocks occur in the critical point and belong, in principle, to the mainshock, can be verified by means of the findings from Section 4.1. In particular, the frequency-size distribution in the critical point (or close to the critical point) is expected to show scale-free statistics. If an overall smooth model fault following characteristic earthquake statistics is studied over a long time period, the approach of the critical point can be calculated precisely in terms of a change of the frequency-size distribution towards Gutenberg-Richter behavior. This change of frequency-size statistics is observed in the model (Fig. 4.11) and supports thus the validity of the critical point concept.

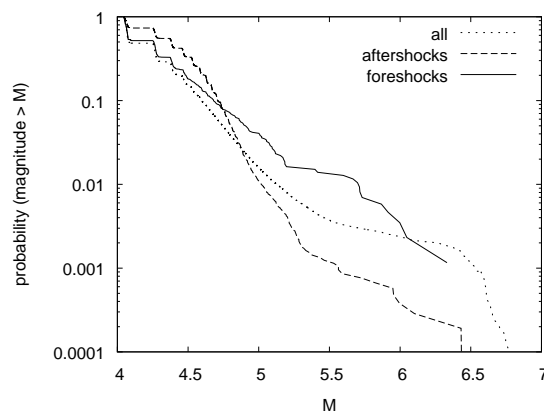


Figure 4.11: Frequency-magnitude distribution of all earthquakes, foreshocks and aftershocks, respectively. Foreshocks and aftershocks are defined as earthquakes occurring within one month before and after an earthquake with  $M \geq 6$ .

## 4.5 Accelerating moment release

In the previous Section, it has been argued that large earthquakes are associated with a critical point and the preparation process is characterized by increasing disorder of the stress field and increasing tendency to scale-free characteristics in the frequency-size distribution. Further support for critical point dynamics has been provided by the observational finding of BUFE AND VARNES [1993] that the cumulative Benioff strain  $\Sigma\Omega(t)$  follows a power law time-to-failure relation prior to the  $M7$  Loma Prieta earthquake on October

17, 1989:

$$\Sigma\Omega(t) = \sum_{i=1}^{N(t)} \sqrt{E_i} = A + B(t_f - t)^m \quad (4.2)$$

Here,  $E_i$  is the energy release of earthquake  $i$ , and  $N(t)$  is the number of earthquakes before time  $t$ ;  $t_f$  is the failure time and  $A, B$  and  $m > 0$  are constants. The systematic study of BOWMAN *et al.* [1998] verifies this behavior also for other large earthquakes in California. Similar studies for numerous seismically active regions followed (see [ZÖLLER *et al.*, 2001]) and references therein).

The time-to-failure relation Eq. (4.2) has been proposed by SORNETTE AND SAMMIS [1995] and SALEUR *et al.* [1996] from the viewpoint of renormalization theory. Moreover, they demonstrated that a complex exponent  $m = \alpha + i\beta$  results in an additional term of log-periodic oscillations decorating the power-law increase of  $\Sigma\Omega(t)$ . This law has been fit by SORNETTE AND SAMMIS [1995] to the data of BUFE AND VARNES [1993]. Although the fit shows good agreement with the data, there is no evidence that this concept is feasible for the prediction of earthquakes so far. In particular, the fit operates with a large number of free parameters including amplitude and phase of the fluctuations and a cutoff time. Therefore, Eq. (4.2) with real  $m$  will be used to describe accelerating moment release in this study.

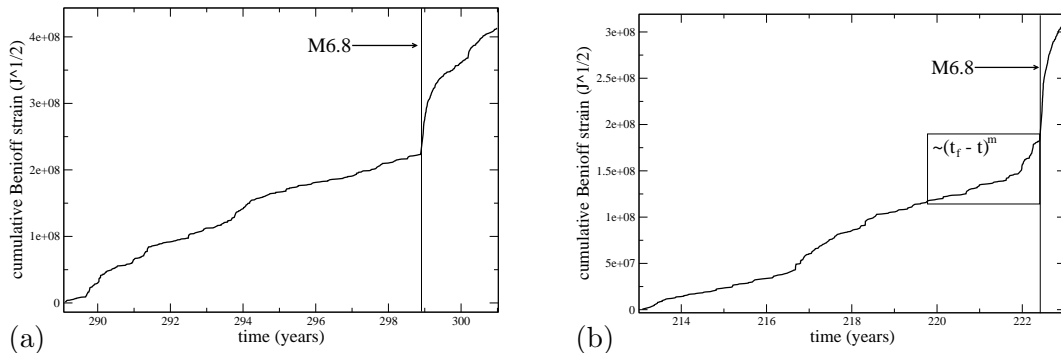


Figure 4.12: Cumulative Benioff strain (Eq. (4.2)) before and after two  $M6.8$  earthquakes in the model.

Figure 4.12 shows the cumulative Benioff strain before and after two earthquakes with  $M = 6.8$ . The increase of the curves immediately after the mainshock is due to the energy release of the mainshock itself and the subsequent aftershocks. In Fig. 4.12(a), no power-law behavior according to Eq. (4.2) can be observed. In contrast, Fig. 4.12(b) includes a period (marked by a box), where such a power-law can be fit to the data. Similar to the findings about foreshocks, this pattern is not universal. Therefore, a stacking procedure is adopted in order to obtain more robust results on the validity of Eq. (4.2) in the model. This is not straightforward, since the interval of accelerating moment release is not known a priori and the duration of a whole seismic cycle, as an upper limit, is not constant. To normalize the time interval for the stacking, the potency release (Eq. (3.27)) is computed as a function of the (normalized) stress level (Fig. 4.13). Taking into account that the stress level increases almost linearly during a large fraction of the seismic cycle, as shown in Fig. 7 of Appendix N, the stress level axis in Fig. 4.13 can effectively be replaced by the

time axis leading to a power-law dependence of the potency release on time. The best fit is provided with an exponent  $s = -1.5$ . Transforming the potency release to the cumulative Benioff strain (Eq. (4.2)), results in an exponent  $m = 0.25$  in Eq. (4.2). This finding is based on a simulation over about 5000 years; the exponent is in good agreement with the theoretical work of RUNDLE *et al.* [2000], who derive also  $m = 0.25$  from a spinodal model, and the analytical result of  $m = 0.3$  in the damage mechanics model of BEN-ZION AND LYAKHOVSKY [2002]. The observational study of BOWMAN *et al.* [1998] finds  $m$  between 0.1 and 0.55.

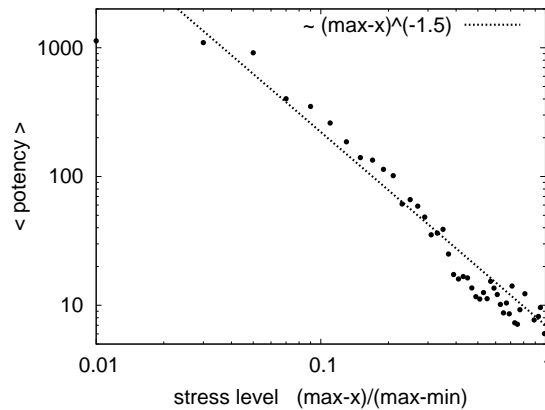


Figure 4.13: Mean potency release (Eq. (3.27)) as a function of the stress level. The stress level is normalized to the maximum ( $\max$ ) and minimum ( $\min$ ) observed stress.

## 4.6 Critical point analysis of seismicity in California

The detection of critical point dynamics in synthetic seismicity is relatively easy, because earthquake catalogs with arbitrary length and homogeneous reporting down to the minimum magnitude can be generated. This allows to calculate frequency-size distributions accurately. Furthermore, the significance of seismicity patterns can be analyzed by means of a stacking procedure with reasonable statistics. The detection of foreshocks and accelerating moment release in the previous sections, for instance, is based on a simulation with 200.000 events covering a period of about 5.000 years. The minimum magnitude, which is identical with the magnitude of completeness in the model, is  $M_c = 4$ . The stacking procedure includes 225 mainshocks with  $M \geq 6$ . In natural data, the number of mainshocks which are accomplished by a reporting of intermediate and small events with similar quality, is in general smaller than ten. Additionally, the data are full of artificial and man-made effects like

- varying magnitude of completeness in space and time due to network changes
- man-made seismicity (explosions, quarry blasts)
- relocation errors, especially for the hypocenter depth
- duplicate events (multiple solutions to the same earthquake)

Numerous methods have been developed to deal with these problems. Some methods are based solely on a catalog study, e.g. the day- to nighttime analysis to detect quarry blasts [WIEMER AND BAER, 2000a] or the deviation of the frequency-size distribution from a power-law for small events indicating the magnitude of completeness [WIEMER AND BAER, 2000b]. However, these methods are often based on ad-hoc assumptions and allow to correct a catalog only on average. The decision whether a single event is a quarry blast, requires more knowledge, e.g. about the source mechanism.

The ANSS (Advanced National Seismic System) catalog for California seismicity which grew out of the CNSS (Council of the National Seismic System) catalog, is one of the best available data sets for the analysis of seismicity patterns, because it deals with most of the above mentioned problems, especially the detection of man-made seismicity and duplicate events. The catalog was already adopted by BOWMAN *et al.* [1998] to study the critical earthquake concept in terms of accelerating moment release and critical regions where this pattern emerges. They find a scaling relation  $\log R \sim 0.44M$  between the critical region  $R$  and the magnitude of the upcoming mainshock  $M$ . It is interesting to note that  $R$  varies between  $73km$  for the Northridge earthquake on Jan. 17, 1994 ( $M = 6.7$ ) and  $325km$  for the  $M = 7.5$  Kern County earthquake on July 21, 1952. An analysis of the  $M8.6$  Assam (India) earthquake on Aug. 15, 1950 results even in  $R = 900km$ . These findings demonstrate that critical point dynamics takes place in large spatial regions which include many faults. Therefore, the following study will be carried out in a region of about  $1000km \times 1000km$  shown in Fig. 4.14.

As discussed before, the most conspicuous feature of a spatially extended critical point system is the growth of the spatial correlation length  $\xi(t)$  when the critical point is approached. This growth is assumed to follow a power law [BRUCE AND WALLACE, 1989]

$$\xi(t) \sim (t_f - t)^{-k} \quad (4.3)$$

with  $k > 0$ . It is emphasized that  $\xi(t)$  is not a cumulative quantity like  $\Sigma\Omega(t)$  (Eq. (4.2)). The main question is: How can the correlation length be calculated, or measured, from an earthquake catalog? It is reasonable to relate  $\xi$  with the clustering properties of epicenters. In the Ising model for ferromagnetic material, above a critical temperature  $T_c$  the emergence of clusters with the same spin value is found. The size of the largest cluster is referred to as the spatial correlation length. Accordingly, the correlation length of a spatially clustered set of earthquakes, like an aftershock sequence or a swarm,  $\xi$  will be small, whereas for widespread events,  $\xi$  will be large. It has been found that an algorithm based on single-link cluster analysis [FROHLICH AND DAVIS, 1990] provides a simple, but powerful and robust technique to measure the clustering properties and thus the spatial correlation length. A detailed description of the algorithm is given in [ZÖLLER *et al.*, 2001]. Using this method allows to compute time series of  $\xi(t)$  and to fit Eq. (4.3) to the data. The quality of the fit is obtained from a curvature parameter [BOWMAN *et al.*, 1998] which is the ratio of root-mean-square errors of the power law fit and the fit of a constant function to the data (Appendix C, Eq. (4)).

When the statistical testing is designed, the problem of limited amount of data has to be addressed. For the synthetic data, robust results have been found by averaging over a large number of mainshocks. In the ANSS catalog, the lower magnitude cutoff has been set to  $M_{cut} = 4.0$  and nine mainshocks with  $M \geq 6.5$  are studied. Here, we compare the results of the nine cases with a large number of realizations of a stochastic earthquake

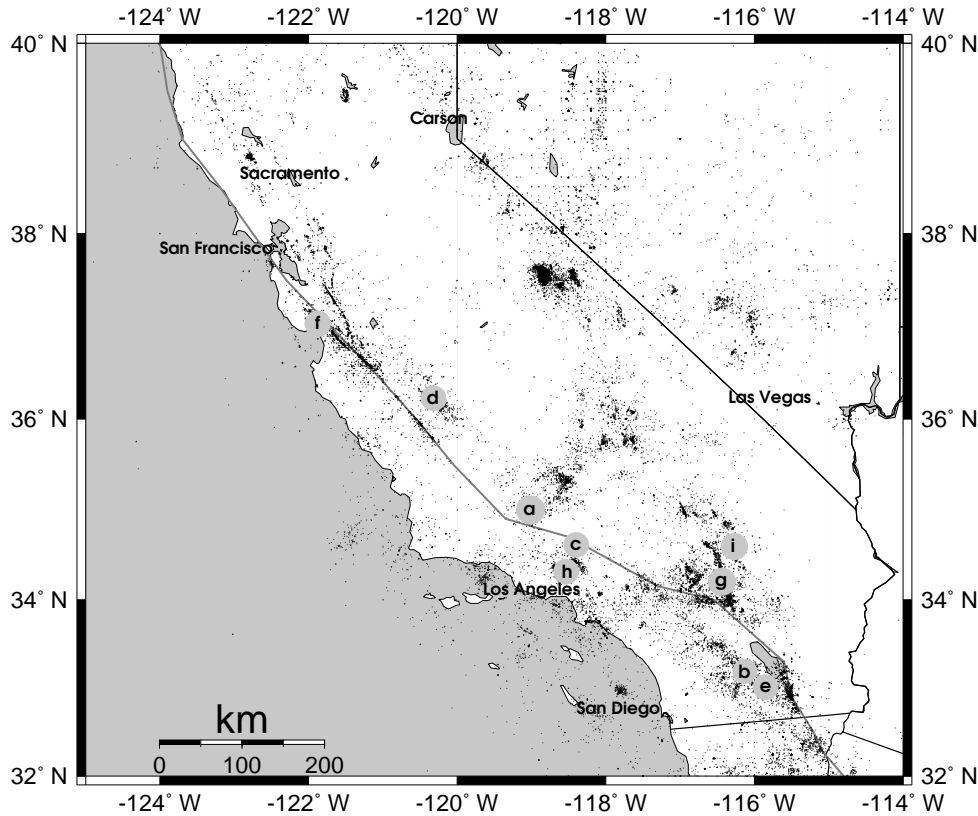


Figure 4.14: Earthquakes with  $M \geq 3$  in California since 1910. The filled circles denote the events with  $M \geq 6.5$  since 1952: (a) 1952  $M = 7.5$  Kern County, (b) 1968  $M = 6.5$  Borrego Mountain, (c) 1971  $M = 6.6$  San Fernando, (d) 1983  $M = 6.7$  Coalinga, (e) 1987  $M = 6.6$  Superstition Hills, (f) 1989  $M = 7.0$  Loma Prieta, (g) 1992  $M = 7.3$  Landers, (h) 1994  $M = 6.6$  Northridge, (i) 1999  $M = 7.1$  Hector Mine.

model producing similar catalogs as the original one, except for the time evolution, which follows a random Poisson process [DALEY AND VERE-JONES, 1988]. In particular, the random (surrogate) catalogs conserve (1) the frequency-size distribution ( $a$  and  $b$  value in Eq. (1.1)), (2) the epicenter distribution, and (3) the presence of aftershocks following the Omori law Eq. (1.2). The model corresponds to the stochastic model of EPSTEIN AND LOMNITZ [1966] with additional aftershock activity. Imposing this model as a null hypothesis for the analysis, the probability that an observed pattern is not random, can be calculated. The free parameters, e.g. the spatial region around the epicenter of the upcoming earthquake and time interval before occurrence time  $t_c$ , are optimized with respect to the parameters space in order to provide the best power-law fit. Here it is important that the whole algorithm is applied exactly in the same way to the real data and the surrogate data. Figure 4.15 shows an example for the  $M7$  Loma Prieta earthquake

in 1989 with the curvature parameter  $\mathcal{C} = 0.34$ , the exponent  $k = 0.41$  (Eq. (4.3)), and the critical region  $R = 270km$ , which is significantly larger than the source volume of the mainshock.

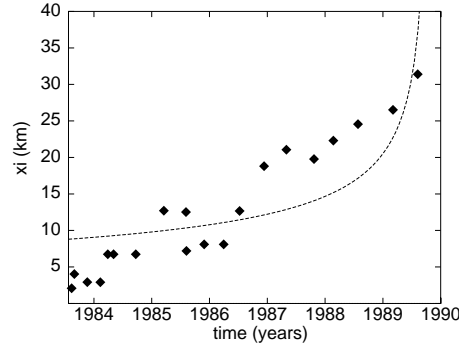


Figure 4.15: Correlation length before the  $M7$  Loma Prieta earthquake on October 18, 1989 and best power-law fit (Eq. (4.3)).

The best power-law fits for the other mainshocks are shown in Fig. 3 of Appendix C. The probabilities that a pattern of similar or better quality (with respect to the curvature parameter) is observed in the surrogate data, vary between 2.9% and 48% around the mean value  $\bar{p} = 26.4\%$  (see Tab. 1 in Appendix C). However, the probability that the mean value of nine random numbers drawn from a Gaussian distribution is equal to or smaller than 26.4%, is 0.7%. We conclude that our results are non-random with a significance level up to 99.3%. The observation that both, the critical region  $R$  and the mean correlation length  $\langle \xi \rangle$  scale with the mainshock magnitude according to  $\log R \sim s_1 M$ , respectively  $\log \langle \xi \rangle \sim s_2 M$  (see Fig. 6 in Appendix C), and that the slopes  $s_1$  and  $s_2$  are similar to studies based on acceleration moment release, e.g. [JAUMÉ AND SYKES, 1999], indicates that growing correlation length and accelerating moment release stem from the same underlying mechanism, namely a critical point [ZÖLLER *et al.*, 2001].

The question whether the detection of the growth of the spatial correlation length provides a feasible algorithm for predicting earthquakes is addressed in [ZÖLLER AND HAINZL, 2001; 2002], and [ZALIAPIN *et al.*, 2002]. So far, the epicenter and the time of the mainshock have been used to detect the pattern. The method can be generalized by introducing a grid search technique for the entire space-time volume of the catalog. This allows to map curvature parameters in space and time [ZÖLLER AND HAINZL, 2001] (see Fig. 2 in Appendix E). Applying again a statistical testing based on the stochastic model introduced above, probabilities for non-randomness can be mapped. These results are given in Fig. 4.16 for the time steps before the largest events. A quantitative assessment indicates significant correlations between the largest earthquakes ( $M \geq 6.5$ ) and the anomalies (see Fig. 1 in Appendix G). Although a correlation between space-time regions with high tendency towards growing spatial correlation length and subsequent large earthquakes is visible, the anomalies cover a large fraction of the entire space-time volume and fail to give an accurate prediction of the upcoming event.

If accelerating moment release (Eq. (4.2)) instead of growing spatial correlation length (Eq. (4.3)) is detected, the results are qualitatively similar (see Tab.1 and Fig. 3 in Appendix G). The growth of the spatial correlation length gives, however, an overall better performance of observed seismicity [ZÖLLER AND HAINZL, 2002]. We note that the two approaches reflect different aspects of the same underlying process, namely the critical point process. Accelerating moment release deals with the energy release and growing spatial correlation length with epicenter clustering. The fact that both techniques provide similar results, supports the presence of the critical point dynamics and is therefore encouraging for further developments in this respect.



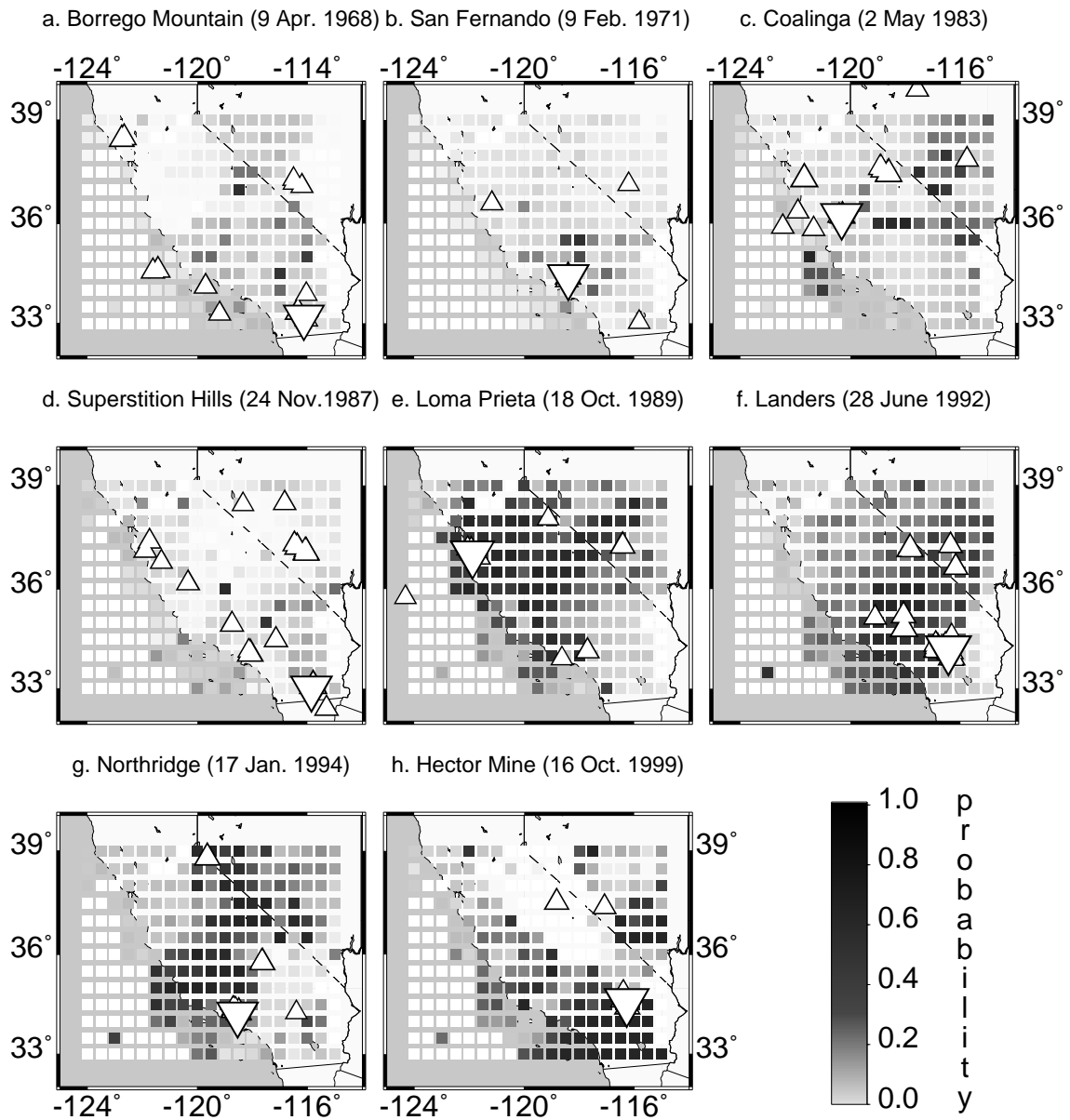


Figure 4.16: Probability indicating the significance for the growth of the spatial correlation length prior to eight large earthquakes in California. The large triangle denotes the mainshock epicenter, whereas the smaller triangles refer to the earthquakes with  $M \geq 5$  which occurred up to one year after the mainshock.

## Chapter 5

# Summary and conclusions

The present work deals with the analysis, the understanding and the interpretation of seismicity patterns with a special focus on the critical point concept for large earthquakes. Both, physical modeling and data analysis are employed. This study aims at practical applications to model data and earthquake catalogs from real fault systems. A point of particular interest is the detection of phenomena prior to large earthquakes and their relevance for a possible prediction of these events. While aftershocks are an almost universal phenomenon, there is no precursor obeying a similar degree of universality. It is, therefore, interesting to study the less frequent precursory phenomena with respect to two questions:

1. Is the phenomenon physically reliable? That is, can it be explained by a physical mechanism?
2. Is the phenomenon statistically significant, or is it due to random fluctuation in a noisy data set?

To address these questions, we use two important tools: 1. A numerical model which is on the one hand to some degree physical, and on the other hand simple enough that it allows to perform long simulations; 2. A sophisticated statistical testing procedure based on stochastic earthquake models to discriminate between “real” patterns and statistical fluctuations up to a certain significance level in a given data set.

The basic version of the model consists of a segmented two-dimensional strike-slip fault in a three-dimensional elastic half space and is inherently discrete, because it does not arise from discretizing a continuous model. The model dynamics is governed by realistic boundary conditions consisting of constant velocity motion of the regions around the fault, static/kinetic friction, and stress transfer based on static dislocation theory. The dynamic rupture is approximated on a finite intra-event time scale using a constant stress propagation velocity (“quasidynamic model”) instead of instantaneous stress transfer.

The results of the simulations indicate an overall good agreement of the synthetic seismicity with real earthquake catalogs, with respect to frequency-size distributions and various features of earthquake sequences. A major role for the characteristics of a simulated catalog seems to play the degree of spatial heterogeneity on the fault, which is implemented by means of space-dependent brittle parameters. Smooth faults are governed by characteristic earthquake statistics, regular occurrence of mainshocks and overall smooth stress

fields. On the other hand, rough faults obey scale-free Gutenberg-Richter statistics, irregular mainshock occurrence, and overall rough stress fields. A closer look at the disorder of the stress field shows, however, that even on a smooth fault a gradual roughening takes place when the next large earthquake is approached. This is reflected in the frequency-size distribution which evolves towards the Gutenberg-Richter law. Such a state is denoted as a critical state of seismic dynamics. This finding allows to establish a relation between the closeness to the underlying critical point, the (unobservable) stress field, and the (observable) frequency-size distribution. Moreover, the concepts of “self-organized criticality” and the “critical earthquake concept” can be interpreted as special cases of a generalized concept, which is further supported by the observation of accelerating moment release in the model as well as in observations, and by the detection of growing spatial correlation length in the epicenter distribution of California seismicity. A rigorous statistical testing unveils correlations between the pattern of growing correlation length and subsequent large earthquakes. The space and time windows, where these precursors are found, are, however, too large for an accurate prediction of the upcoming event. However, in combination with other parameters, e.g. accelerating seismic moment release, this pattern may provide a significant contribution to an improved time-dependent seismic hazard assessment.

## Chapter 6

# Outlook

The main result of the present work is the clear evidence of the presence of a critical point in the dynamics of seismicity. When the trajectory of the system gets close to the critical point, or close to the next mainshock, a critical state is entered, which is characterized by clear anomalies in various seismicity functions. Further refinements, especially of the data analysis, regarding a more precise characterization of the critical state may lead to progress in a possible prediction of large events or an improved time-dependent hazard assessment. This work should be accomplished by extensions of the model towards a more realistic resemblance of real fault zones. So far, the model has been compared with real faults using parameters from the frequency-size distribution or spatiotemporal clustering properties. The way, how the input parameters have to be chosen in order to simulate seismicity on real faults, has been shown. An important goal, however, is the development of a detailed phase diagram including several parameters, and the assignment of a real fault to a position in this phase diagram. It is furthermore interesting to study, whether the position in the phase diagram can also be characterized by means of observable parameters, e.g. the surface deformation field, which is accessible in the model by using the equations of OKADA [1992] with stress calculation points (see Fig. 3.1) on the free surface. Since corresponding geodetic data are ubiquitous, the analysis of the surface deformation field in relation to seismicity and the underlying physics will be an important subject of future studies.

Further work will focus on slip histories of single earthquakes calculated with the quasi-dynamic approach. Tuning the friction law in a way that slip histories become similar to those of real earthquakes, the simulated slip histories can serve as input for concepts based on numerical Green's functions [WANG AND IGEL, 2004] in order to calculate ground motion, and finally seismic hazard maps.

# Bibliography

- [AKI AND RICHARDS, 2002] AKI, K., AND RICHARDS, P. G., *Quantitative seismology*, University Science Books., 2002
- [BAK, 1996] BAK, P., *How Nature Works. The Science of Self-Organised Criticality*, Oxford University Press, 1996
- [BAK AND TANG, 1996] BAK, P., AND TANG, C., *Earthquakes as a phenomenon of self-organised criticality*, J. Geophys. Res., *94*, 15,635–15,6637 (1989).
- [BÅTH, 1965] BÅTH, M., *Lateral inhomogeneities in the upper mantle*, Tectonophysics, *2*, 483–514 (1965).
- [BEN-ZION, 1996] BEN-ZION, Y., *Stress, slip, and earthquakes in models of complex single-fault systems incorporating brittle and creep deformations*, J. Geophys. Res., *101*, 5677–5706 (1996).
- [BEN-ZION *et al.*, 1999] BEN-ZION, Y., DAHMEN, K., LYAKHOVSKY, V., ERTAS, D., AND AGNON, A., *Self-driven mode switching of earthquake activity on a fault system*, Earth and Plan. Sci. Lett., *172*, 11–21 (1999).
- [BEN-ZION AND LYAKHOVSKY, 2002] BEN-ZION, Y., AND LYAKHOVSKY, V., *Accelerated Seismic Release and Related Aspects of Seismicity Patterns on Earthquake Faults*, Pure Appl. Geophys., *159*, 2385–2412 (2002).
- [BEN-ZION AND LYAKHOVSKY, 2003] BEN-ZION, Y., AND LYAKHOVSKY, V., *A generalized law for aftershock rates in a damage rheology model*, Eos Trans. AGU, *84(46)*, Fall Meet. Suppl., Abstract NG12C-02 (2003).
- [BEN-ZION AND RICE, 1993] BEN-ZION, Y., AND RICE, J. R., *Earthquake failure sequences along a cellular fault zone in a three-dimensional elastic solid containing asperity and nonasperity regions*, J. Geophys. Res., *98*, 14,109–14,131 (1993).
- [BINNEY *et al.*, 1993] BINNEY, J. J., DOWRICK, N. J., FISHER, A. J., AND NEWMAN, M. E. J., *The theory of critical phenomena*, Oxford University Press., 1993
- [BLASIUS *et al.*, 1999] BLASIUS, B., HUPPERT, A., AND STONE, L., *Complex dynamics and phase synchronization in spatially extended ecological systems*, Nature, *399*, 354–359 (1999).

- [BOWMAN *et al.*, 1998] BOWMAN, D. D., OULLION, G., SAMMIS, C. G., SORNETTE, A., AND SORNETTE, D., *An observational test of the critical earthquake concept*, J. Geophys. Res., *103*, 24,359–24,372 (1998).
- [BRACE, 1960] BRACE, W. F., *An extension of the Griffith theory of fracture to rocks*, J. Geophys. Res., *65*, 3477–3480 (1960).
- [BRUCE AND WALLACE, 1989] BRUCE, A., AND WALLACE, D. *Critical point phenomena: Universal physics at large length scales*, in *The New Physics*, edited by P. Davis, pp. 236–267, Cambridge Univ. Press, New York, 1989.
- [BUFE AND VARNES, 1993] BUFE, C. G., AND VARNES, D. J., *Predictive modeling of the seismic cycle of the greater San Francisco Bay region*, J. Geophys. Res., *98*, 9871–9883 (1993).
- [BÜRGMANN *et al.*, 2002] BÜRGMANN, R., ERGINTAV, S., SEGALL, P., HEARN, E. H., MCCLUSKY, S., REILINGER, R. E., WOITH, H., AND ZSCHAU, J., *Time-dependent distributed afterslip on and deep below the Izmit earthquake rupture*, Bull. Seism. Soc. Am., *92*, 126–137 (2002).
- [BURRIDGE AND KNOPOFF, 1967] BURRIDGE, R., AND KNOPOFF, L., *Model and theoretical seismicity*, Bull. Seim. Soc. Am., *57*, 341–371 (1967).
- [BYERLEE, 1978] BYERLEE, J. D., *Friction of rocks*, Pure Appl. Geophys., *116*, 615–616 (1978).
- [CHINNERY, 1963] CHINNERY, M., *The stress changes that accompany strike-slip faulting*, Bull. Seim. Soc. Am., *53*, 921–932 (1963).
- [DAHMEN *et al.*, 1999] DAHMEN, K., ERTAS, D., AND BEN-ZION, Y., *Gutenberg-Richter and characteristic earthquake behavior in simple mean-field models of heterogeneous faults*, Phys. Rev. E, *58*, 1494–1501 (1998).
- [DALEY AND VERE-JONES, 1988] DALEY, D. J., AND VERE-JONES, D., *An Introduction to the Theory of Point Processes*, Springer, New York, 1988.
- [DIETERICH, 1994] DIETERICH, J. H., *A constitutive law for earthquake production and its application to earthquake clustering*, J. Geophys. Res., *99*, 2601–2618 (1994).
- [EPSTEIN AND LOMNITZ, 1966] EPSTEIN, B., AND LOMNITZ, C., *A model for the occurrence of large earthquakes*, Nature, *211*, 954–956 (1966).
- [FISHER *et al.*, 1997] FISHER, D. S., DAHMEN, K., RAMANATHAN, S., AND BEN-ZION, Y., *Statistics of earthquakes in simple models of heterogeneous faults*, Phys. Rev. Lett., *78*, 4885–4888 (1997).
- [FROHLICH AND DAVIS, 1990] FROHLICH, C., AND DAVIS, S. D., *Single-link cluster analysis as a method to evaluate spatial and temporal properties of earthquake catalogues*, Geophys. J. Int. *100*, 19–32 (1990).
- [GABRIELOV *et al.*, 1994] GABRIELOV, A., NEWMAN, W. I., AND KNOPOFF, L., *Lattice models of failure: Sensitivity to the local dynamics*, Phys. Rev. E, *50*, 188–197 (1994).

- [GUTENBERG AND RICHTER, 1956] GUTENBERG, B., AND RICHTER, C. F., *Earthquake magnitude, intensity, energy and acceleration*, Bull. Seismol. Soc. Am., *46*, 105–145 (1956).
- [HAINZL AND ZÖLLER, 2001] HAINZL, S., AND ZÖLLER, G., *The role of disorder and stress concentration in nonconservative fault systems*, Physica A, *294*, 67–84 (2001) → **Appendix D**.
- [HAINZL *et al.*, 1999] HAINZL, S., ZÖLLER, G., AND KURTHS, J., *Similar power laws for fore- and aftershock sequences in a spring-block model for earthquakes*, J. Geophys. Res., *104*, 7243–7253 (1999).
- [HAINZL *et al.*, 2000a] HAINZL, S., ZÖLLER, G., AND KURTHS, J., *Self-organization of spatio-temporal earthquake clusters*, Nonlin. Proc. Geophys., *7*, 21–29 (2000) → **Appendix A**.
- [HAINZL *et al.*, 2000b] HAINZL, S., ZÖLLER, G., KURTHS, J., AND ZSCHAU, J., *Seismic quiescence as an indicator for large earthquakes in a system of self-organized criticality*, Geophys. Res. Lett., *27*, 597–600 (2000) → **Appendix B**.
- [HAINZL *et al.*, 2003] HAINZL, S., ZÖLLER, G., AND SCHERBAUM, F., *Earthquake clusters resulting from delayed rupture propagation in finite fault segments*, J. Geophys. Res., *108*, 2013, doi 10.1029/2001JB000610 (2003) → **Appendix I**.
- [HILLERS *et al.*, 2005] HILLERS, G., BEN-ZION, Y., AND MAI, P. M., *Seismicity on a fault controlled by rate- and state dependent friction with spatial variations of the critical slip distance*, J. Geophys. Res., *submitted*. (2005)
- [HUANG AND TURCOTTE, 1990a] HUANG, J., AND TURCOTTE, D. L., *Are earthquakes an example of deterministic chaos?*, Geophys. Res. Lett., *17*, 223–226 (1990).
- [HUANG AND TURCOTTE, 1990b] HUANG, J., AND TURCOTTE, D. L., *Evidence for chaotic fault interactions in the seismicity of the San Andreas fault and the Nankai trough*, Nature, *348*, 234–236 (1990).
- [ITO AND MATSUZAKI, 1990] ITO, K., AND MATSUZAKI, M., *Earthquakes as self-organized critical phenomena*, J. Geophys. Res., *95*, 6853–6860 (1990).
- [JAUMÉ AND SYKES, 1999] JAUMÉ, S. C., AND SYKES, L. R., *Evolving towards a critical point: A review of accelerating seismic moment/energy release prior to large and great earthquakes*, Pure Appl. Geophys., *155*, 279–306 (1999).
- [JONES AND MOLNAR, 1979] JONES, L. M., AND MOLNAR, P., *Some characteristics of foreshocks and their possible relation to earthquake prediction and premonitory slip on faults*, J. Geophys. Res., *84*, 3596–3608 (1979).
- [KAGAN AND KNOPOFF, 1978] KAGAN, Y. Y., AND KNOPOFF, L., *Statistical study of the occurrence of shallow earthquakes*, Geophys. J. R. Astron. Soc., *55*, 67–86 (1978).
- [LANGBEIN, *et al.*, 2005] LANGBEIN, J., BORCHERDT, R., DREGER, D., FLETCHER, J., HARDEBECK, J. L., HELLWEG, M., JI, C., JOHNSTON, M., MURRAY, J. R., NADEAU, R., RYMER, M. J., AND TREIMAN, J. A., *Preliminary Report on the 28 September 2004, M 6.0 Parkfield, California Earthquake*, Seismol. Res. Lett., *76*, 1–17 (2005).

- [LOCKNER *et al.*, 1991] LOCKNER, D. A., BYERLEE, J. D., KUKSENKO, V., PONOMAREV, A., AND SIDORIN, A., *Quasi-static fault growth and shear fracture energy in granite*, *Nature*, *350*, 39–42 (1991).
- [LOMNITZ-ADLER, 1999] LOMNITZ-ADLER, J., *Automaton models of seismic fracture: constraints imposed by the magnitude-frequency relation*, *J. Geophys. Res.*, *98*, 17,745–17,756 (1999).
- [LORENZ, 1963] LORENZ, E. N., *Deterministic nonperiodic flow*, *J. Atmos. Sci.*, *20*, 130–141 (1963).
- [LYAKHOVSKY *et al.*, 1997] LYAKHOVSKY, V., BEN-ZION, Y., AND AGNON, A., *Distributed damage, faulting and friction*, *J. Geophys. Res.*, *102*, 27,635–27,649 (1997).
- [LYAKHOVSKY *et al.*, 2005] LYAKHOVSKY, V., BEN-ZION, Y., AND AGNON, A., *A viscoelastic damage rheology and rate- and state-dependent friction*, *Geophys. J. Int.*, *161*, 179–190, doi 10.1111/j.1365-246X.2005.02583.x. (2005).
- [LYONS AND SANDWELL, 2003] LYONS, S., AND SANDWELL, D., *Fault creep along the southern San Andreas from interferometric synthetic aperture radar, permanent scatterers, and stacking*, *J. Geophys. Res.*, *108*, 2047, doi 10.1029/2002JB001831 (2003).
- [MADARIAGA, 1976] MADARIAGA, R., *Dynamics of an expanding circular fault*, *Bull. Seim. Soc. Am.*, *66*, 639–666 (1976).
- [MAIN *et al.*, 2004] MAIN, I. G., O'BRIAN, G., AND HENDERSON, J. R., *Statistical physics of earthquakes: Comparison of distribution exponents for source area and potential energy and the dynamic emergence of log-periodic quanta*, *J. Geophys. Res.*, *105*, 6105–6126 (2000).
- [MARONE *et al.*, 1991] MARONE, C. J., SCHOLZ, C. H., AND BILHAM R., *On the mechanisms of earthquake afterslip*, *J. Geophys. Res.*, *96*, 8441–8452 (1991).
- [NARTEAU *et al.*, 2003] NARTEAU, C., SHEBALIN, P., HAINZL, S., ZÖLLER, G., AND HOLSCHNEIDER, M., *Emergence of a band-limited power law in the aftershock decay rate of a slider-block model*, *Geophys. Res. Lett.*, *30*, art. no. 1568, doi 10.1029/2003GL017110 (2003) → **Appendix J**.
- [NUR AND BOOKER, 1972] NUR, A., AND BOOKER, J. R., *Aftershocks caused by pore fluid flow?*, *Science*, *175*, 885–887 (1972).
- [OKADA, 1992] OKADA, Y., *Internal deformation due to shear and tensile faults in a half space*, *Bull. Seism. Soc. Am.*, *82*, 1018–1040 (1992).
- [OLAMI *et al.*, 1992] OLAMI, Z., FEDER, H. S., AND CHRISTENSEN, K., *Self-organized criticality in a continuous, nonconservative cellular automaton modeling earthquakes*, *Phys. Rev. Lett.*, *68*, 1244–1247 (1992).
- [OMORI, 1894] OMORI, F., *On the aftershocks of earthquakes*, *J. Coll. Sci. Imp. Univ. Tokyo*, *7*, 111–200 (1894).



- [RAHMSTORF, 2001] RAHMSTORF, S., *A simple model of seasonal open ocean convection. Part I: Theory*, *Ocean Dyn.* 52, 26–35 (2001).
- [REASENBERG, 1985] REASENBERG, P., *Second-order moment of central California seismicity*, *J. Geophys. Res.* 90, 5479–5495 (1985).
- [REID, 1910] REID, H. F., *The Mechanics of the Earthquake, The California Earthquake of April 18, 1906, Report of the State Investigation Commission, Vol. 2*, Carnegie Institution of Washington, Washington, D.C., 1910.
- [RUINA, 1983] Ruina, A. L., *Slip instability and state variable friction laws*, *J. Geophys. Res.*, 88, 10,359–10,370 (1983).
- [RUNDLE *et al.*, 2000] RUNDLE, J. B., KLEIN, W., TURCOTTE D. L., AND MALAMUD, B. D., *Precursory seismic activation and critical point phenomena*, *Pure Appl. Geophys.* 157, 2165–2182 (2000).
- [SALEUR *et al.*, 1996] SALEUR, H., SAMMIS, C. G., AND SORNETTE, D., *Discrete scale invariance, complex fractal dimensions, and log-periodic fluctuations in seismicity*, *J. Geophys. Res.*, 101, 17,661–17,677 (1996).
- [SAVAGE *et al.*, 1999] SAVAGE, J. C., SVARC, J. L., AND PRESCOTT, W. H., *Geodetic estimates of fault slip rates in the San Francisco Bay area*, *J. Geophys. Res.*, 104, 4995–5002 (1999).
- [SCHOLZ, 1998] Scholz, C. H., *Earthquakes and friction laws*, *Nature*, 391, 37–42 (1998).
- [SCHOLZ, 2002] Scholz, C. H., *The mechanics of earthquakes and faulting*, Cambridge University Press, 2002.
- [SHCHERBAKOV AND TURCOTTE, 2004] SHCHERBAKOV, R., AND TURCOTTE, D. L., *A damage mechanics model for aftershocks*, *Pure and Applied Geophys.* 161, 2379, doi 10.1007/s00024-004-2570-x (2004).
- [SORNETTE, 2004] SORNETTE, D., *Critical Phenomena in Natural Sciences. Chaos, Fractals, Self-organization and Disorder: Concepts & Tools*, Springer Series in Synergetics, Heidelberg, 2004.
- [SORNETTE AND SAMMIS, 1995] SORNETTE, D., AND SAMMIS, C. G., *Complex critical exponents from renormalization group theory of earthquakes: Implication for earthquake predictions*, *J. Phys.* 1, 5, 607–619 (1995).
- [SORNETTE AND SORNETTE, 1999] SORNETTE, D., AND SORNETTE, A., *Renormalization of earthquake aftershocks*, *Geophys. Res. Lett.*, 6, 1981–1984 (1999).
- [SPARROW, 1982] SPARROW, C., *The Lorenz Equations: Bifurcations, Chaos, and Strange Attractors*, Springer, New York, 269pp., 1982.
- [STOMMEL, 1961] STOMMEL, H., *Thermohaline convection with two stable regimes of flow*, *Tellus*, 13, 224–230 (1961).
- [TURCOTTE, 1997] TURCOTTE, D. L., *Fractals and chaos in geology and geophysics*, Cambridge University Press, New York, 1997.

- [UTSU, 2002] UTSU, T., *Statistical features of seismicity*, International handbook of earthquake and engineering seismology, Vol. 81A, edited by the Int'l Assoc. Seismol & Phys. Earth's Interior, pp. 719–732, Academic Press, 2002.
- [UTSU *et al.*, 1995] UTSU, T., OGATA, Y., AND MATSU'URA, R. S., *The centenary of the Omori formula for a decay law of aftershock activity*, J. Phys. Earth, *43*, 1–33 (1995).
- [WANG AND IGEL, 2004] WANG, H., AND IGEL, H., *Some primary observations from earthquake scenario simulations using numerical Green's functions*, Eos Trans. AGU, *85(47)*, Fall Meet. Suppl., Abstract S31A-1031 (2004).
- [WIEMER AND BAER, 2000a] WIEMER, S., AND BAER, M., *Mapping and removing quarry blast events from seismicity catalogs: Examples from Alaska, the Western United States, and Japan*, Bull. Seism. Soc. Am., *90*, 525–530 (2000).
- [WIEMER AND WYSS, 2000b] WIEMER, S., AND WYSS, M., *Minimum magnitude and complete reporting in earthquake catalogs: Examples from Alaska, the Western United States, and Japan*, Bull. Seism. Soc. Am., *90*, 859–869 (2000).
- [WYSS, 1997] WYSS, M., *Cannot earthquakes be predicted?*, Science, *278*, 487 (1997).
- [WYSS AND HABERMANN, 1988] WYSS, M., AND HABERMANN, R. E., *Precursory seismic quiescence*, Pure Appl. Geophys, *126*, 319–332 (1988).
- [ZALIAPIN *et al.*, 2002] ZALIAPIN, I., LIU, Z., ZÖLLER, G., KEILIS-BOROK, V., AND TURCOTTE, D., *On increase of earthquake correlation length prior to large earthquakes in California*, Computational Seismology, *33*, 141–161 (2002) → **Appendix H**.
- [ZÖLLER AND HAINZL, 2001] ZÖLLER, G., AND HAINZL, S., *Detecting premonitory seismicity patterns based on critical point dynamics*, Natural Hazards and Earth System Sciences, *1*, 93–98 (2001) → **Appendix E**.
- [ZÖLLER AND HAINZL, 2002] ZÖLLER, G., AND HAINZL, S., *A systematic spatiotemporal test of the critical point hypothesis for large earthquakes*, Geophys. Res. Lett., *29*, doi 10.1029/2002GL014856 (2002) → **Appendix G**.
- [ZÖLLER *et al.*, 2001] ZÖLLER, G., HAINZL, S., AND KURTHS, J., *Observation of growing correlation length as an indicator for critical point behavior prior to large earthquakes*, J. Geophys. Res., *106*, 2167–2175 (2001) → **Appendix C**.
- [ZÖLLER *et al.*, 2005a] ZÖLLER, G., HAINZL, S., BEN-ZION, Y., AND HOLSCHNEIDER, M., *Earthquake activity related to seismic cycles in a model for a heterogeneous strike-slip fault*, Tectonophysics, *submitted* (2005) → **Appendix N**.
- [ZÖLLER *et al.*, 2005b] ZÖLLER, G., HAINZL, S., HOLSCHNEIDER, M., AND BEN-ZION, Y., *Aftershocks resulting from creeping sections in a heterogeneous fault*, Geophys. Res. Lett., *32*, L03308, doi 10.1029/2004GL021871 (2005) → **Appendix M**.
- [ZÖLLER *et al.*, 2002] ZÖLLER, G., HAINZL, S., KURTHS, J., AND ZSCHAU, J., *A systematic test on precursory seismic quiescence in Armenia*, Natural Hazards, *26*, 245–263 (2002) → **Appendix F**.

- [ZÖLLER *et al.*, 2004] ZÖLLER, G., HOLSCHNEIDER, M., AND BEN-ZION, Y., *Quasi-static and quasi-dynamic modeling of earthquake failure at intermediate scales*, Pure Appl. Geophys, *161*, 2103–2118 (2004) → **Appendix K**.
- [ZÖLLER *et al.*, 2005c] ZÖLLER, G., HOLSCHNEIDER, M., AND BEN-ZION, Y., *The role of heterogeneities as a tuning parameter of earthquake dynamics*, Pure Appl. Geophys, *162*, doi 10.1007/s00024-004-2660-9 (2005) → **Appendix L**.

# Acknowledgments

I would like to thank my colleagues Sebastian Hainzl, Yehuda Ben-Zion, Matthias Holschneider, Jürgen Kurths, Ilya Zaliapin, and Clément Narteau for interesting and fruitful cooperations, continuous support, and stimulating discussions. I am also indebted to Heiner Igel, Paul Martin Mai, Jörn Davidsen, and Christian Goltz for inviting me to their departments, for their hospitality, and for interesting discussions and suggestions. Comments from Sebastian Hainzl and Douglas Maraun helped me to improve the manuscript.

The ANSS catalog has been provided by the Northern California Earthquake Data Center (NCEDC) and the organizations that contributed data to the NCEDC. I acknowledge financial support from the collaborative research center “Complex Nonlinear Processes” (SFB555) of the German Research Society (DFG) and the state Brandenburg (HSPIII 1.6).

# Appendix A

## Self-organization of spatio-temporal earthquake clusters

Autors:	S. Hainzl, G. Zöller, and J. Kurths
Journal:	<i>Nonlinear Processes in Geophysics,</i>
Volume (Nr.):	<b>7(1-2)</b>
Pages:	21-29
Year:	2000

# Self-organization of spatio-temporal earthquake clusters

S. Hainzl, G. Zöller and J. Kurths

Institute of Physics, University of Potsdam, D-14469 Potsdam, Germany

Received: 20 January 1998 – Accepted: 17 March 2000

**Abstract.** Cellular automaton versions of the Burridge-Knopoff model have been shown to reproduce the power law distribution of event sizes; that is, the Gutenberg-Richter law. However, they have failed to reproduce the occurrence of foreshock and aftershock sequences correlated with large earthquakes. We show that in the case of partial stress recovery due to transient creep occurring subsequently to earthquakes in the crust, such spring-block systems self-organize into a statistically stationary state characterized by a power law distribution of fracture sizes as well as by foreshocks and aftershocks accompanying large events. In particular, the increase of foreshock and the decrease of aftershock activity can be described by, aside from a prefactor, the same Omori law. The exponent of the Omori law depends on the relaxation time and on the spatial scale of transient creep. Further investigations concerning the number of aftershocks, the temporal variation of aftershock magnitudes, and the waiting time distribution support the conclusion that this model, even “more realistic” physics is missed, captures in some ways the origin of the size distribution as well as spatio-temporal clustering of earthquakes.

where  $N$  is the number of earthquakes with magnitude greater than or equal to  $M$ . Considering the relation between the magnitude  $M$  and its source size  $S$ , i.e.  $M \sim \log S$  (Kanamori and Anderson, 1975; Purcaru and Berckhemer, 1978), the Gutenberg-Richter law describes a power law for the number of observed earthquakes with sizes greater than  $S$ ,

$$N \sim S^{-B}. \quad (2)$$

The exponent  $B$  varies over a wide range of values for different faults, namely, between 0.80 and 1.05 (Ekström and Dziewonski, 1988; Pacheco et al., 1992).

The first generation of SOC earthquake models, derived from the sandpile model (Bak et al., 1987), implying a conservation law with regard to the internal coupling rules (Bak and Tang, 1989; Ito and Matsuzaki, 1990). They reproduce the power law size distribution, but the observed  $B$  value was found to be universal and too small.

On the other hand, a geophysically motivated fault model, which was proposed earlier by Burridge and Knopoff (1967) (hereinafter referred to as BK), has also been shown to reproduce the Gutenberg-Richter law. In this case, a fault is modeled as a spring-block system lying between two moving rigid tectonic plates. Several modifications of this model have been analyzed by different authors (e.g., Carlson and Langer, 1989a, b). In the quasi-static limit; that is, if instantaneous block slips are assumed (Nakanishi, 1990; Brown et al., 1991; Olami et al., 1992; Rundle and Klein, 1995), this spring-block model is very similar to the first generation of SOC models, differs only in a deterministic instead of a stochastic forcing and in its nonconservative characteristics which comes from a coupling by springs between the blocks within the fault plane and the tectonic plate. Olami et al. (1992) (hereinafter referred to as OFC) have shown that the proper  $B$  value and its empirically observed variability can be reproduced, if the level of conservation decreases in these cellular automaton versions of the BK

## 1 Introduction

The dynamics of earthquakes has attracted much attention as a real-world example for a self-organized critical phenomenon, introduced by Bak et al. (1987). The hallmarks of systems exhibiting self-organized criticality (SOC) are spatial and temporal correlation functions with power law behavior.

In fact, earthquakes show several types of power law behavior. In particular, their frequency-size distribution is well defined by the Gutenberg-Richter law (Gutenberg and Richter, 1954)

$$\log_{10} N = a - b \cdot M, \quad (1)$$

Correspondence to: S. Hainzl

model. According to the OFC model, the exponent  $B$  is close to 0 in the case of high levels of conservation and increases to values above 2 for low levels of conservation.

However, all of these models fail to reproduce the spatio-temporal clustering of smaller events accompanying large earthquakes in real fault systems, namely the occurrence of foreshocks and aftershocks. On average, both the decay of aftershock sequences and the time distribution of foreshocks follow power laws. The aftershocks are described by the modified Omori law (Omori, 1894; Utsu et al., 1995)

$$R_a \sim (c_a + t - t_M)^{-p} \quad (3)$$

and the foreshocks by a similar power law, an inverse Omori law (Kagan and Knopoff, 1978; Jones and Molnar, 1979)

$$R_f \sim (c_f + t_M - t)^{-q}, \quad (4)$$

where  $t_M$  indicates the occurrence time of the mainshock;  $R_a$  and  $R_f$  denote the occurrence rate of aftershocks and foreshocks, respectively; and  $c_a$ ,  $c_f$  are small constants scattering from 0.01 days to over 1 day with a median of about 0.3 days (Utsu et al., 1995). Both exponents  $p$  and  $q$  are found to be almost identical for empirical earthquake catalogs, whereas their value can vary between 0.9 and 1.5 (Papazachos, 1975; Utsu et al., 1995).

An aseismic phenomenon, which is correlated with large earthquakes in real fault systems, is postseismic creep. This transient process is observed to occur subsequently to earthquakes in the vicinity of the fault over days to years (Peltzer et al., 1996; Heki et al., 1997; Savage and Svarc, 1997). We have shown in previous investigations (Hainzl et al., 1999) that the introduction of postseismic transient creep characteristics in cellular automaton versions of the BK model leads to a reproduction of the empirically observed spatio-temporal earthquake clusters, especially to foreshock and aftershock sequences obeying the Omori law. In our previous work, the effect of stress recovery due to the transient creep was restricted only to the slipped block or to its four nearest neighbors neglecting more realistic long-range effects. Thus it is important to analyze the model results with regard to long-range interactions. This is the first aim of this paper. Furthermore, we give some more insights in the properties of the simulated spatio-temporal event clustering, especially concerning the aftershock sequences and the distribution of waiting times, and compare these results with empirical observations.

## 2 Model

Our aim is to characterize the qualitative behavior due to a time-dependent stress modulation subsequently to earthquakes. However, we do not want to model earthquake nucleation and rupture processes in detail. By

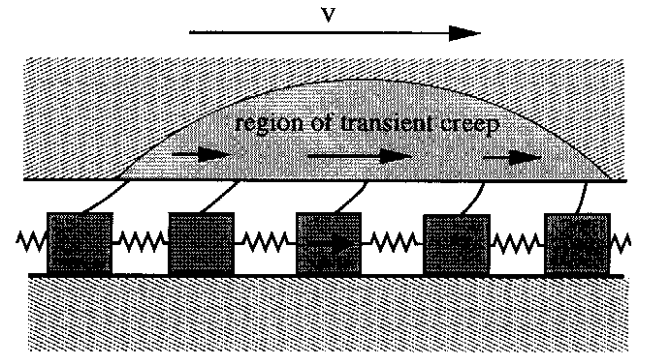


**Fig. 1.** One-dimensional sketch of the investigated two-dimensional spring-block model. The bottom blocks, which perform stick-slip motion, are connected to its neighbors by springs. Furthermore, each block is coupled by a loader spring to the upper tectonic plate moving with a velocity  $V$  and frictionally to the lower plate. The sliding of a block during an earthquake triggers subsequently transient creep within the tectonic plate, which leads locally to an increased loading after the earthquake.

analogy with the BK model, the fault is represented by a network of interconnected blocks lying between two tectonic plates. The blocks are driven by the slow relative movement of these two plates. Once the stress on a block exceeds the static friction, sliding is initiated and the frictional resistance of the block is assumed to drop instantaneously to the dynamic friction. The slip of the block redefines the stress of the blocks in the neighborhood. This can result in further slips and a chain reaction, i.e. an avalanche, can evolve, which is identified with an earthquake.

In contrast to the BK model and its cellular automaton version (OFC model), we do not assume total rigidity of the tectonic plates, because material creep, plasticity, fluid flow, and other processes are important in real fault systems. For example, afterslip or transient creep are known to induce a stress release in the order of the coseismic release (Heki et al., 1997; DeMets, 1997). Therefore we study, as an extension of the BK model, postseismic transient creep in the vicinity of the stuck fault layer blocks. A one-dimensional sketch of the investigated two-dimensional block system is shown in Figure 1. In general, a local failure changes the stress within the crust over a zone with a characteristic length set by the screening of the elastic Green function. Transient creep is expected to occur in this region. In previous investigations (Hainzl et al., 1999), we have restricted our analysis in a first-order approximation to transient creep that affects only the slipped block and its nearest neighbors. In this paper, we study alternatively long-range interactions. Thereby, the relaxation process of the crust is modeled by standard linear solids, which exhibit elastic properties in addition to transient creep characteristics. The response of a standard linear solid to an instantaneous stress change is described by a partial stress relaxation according to an exponential

function (see, e.g., Dieterich, 1972).

In real fault systems, the duration of large earthquakes is of the order of minutes, whereas the duration of aftershock sequences is of the order of weeks or months, and the recurrence times of large earthquakes are of the order of hundreds years. Consequently, the dynamics of a single earthquake are much faster than the assumed crust relaxation and tectonic loading. Therefore we assume that the crust relaxation and the tectonic loading have no effect on the dynamics of an individual event. Thus the evolution of a single earthquake depends only on the elastic properties of the block system and can be described by analogy with the OFC model. In the inter-occurrence time intervals between successive earthquakes, the stresses increase according to the tectonic loading and, additionally, in contrast to the OFC model, according to the transient creep in the crust.

We implement our model in the form of a continuous cellular automaton by defining an  $L \times L$  array of blocks  $(i, j)$ , where  $i, j$  are integers,  $1 \leq i, j \leq L$ . The total force (or stress if unit area is assumed) on each block is given by  $\sigma(i, j)$ . The model algorithm consists of two steps, (1) the evolution of a single earthquake and (2) the stress changes in the inter-occurrence time between successive events.

1. The evolution of a single event is described in the following way: The friction law adopts the Mohr-Coulomb law with a spatially constant static failure threshold  $\sigma_F$  and residual stress  $\sigma_R$ . If the stress on a block  $(k, l)$  exceeds the static failure threshold,  $\sigma(k, l) \geq \sigma_F$ , sliding is initiated at this block. The moving block slips to the position with the residual stress  $\sigma_R$ , and the stress  $\Delta\sigma \equiv \sigma(k, l) - \sigma_R$  is distributed to the adjacent blocks and to the crust. The stresses of the four nearest neighbors  $(k_{\pm}, l_{\pm})$  are set according to the rule

$$\sigma(k_{\pm}, l_{\pm}) \rightarrow \sigma(k_{\pm}, l_{\pm}) + \alpha \Delta\sigma \quad (5)$$

and the stress of the sliding site is reset to

$$\sigma(k, l) \rightarrow \sigma_R. \quad (6)$$

The elastic coupling constant  $\alpha$  depends on the spring constants and can vary in the range of  $0 \leq \alpha \leq 0.25$ , where  $\alpha = 0.25$  refers to the conservative case (Olami et al., 1992; Hainzl et al., 1999). The block sliding leads to a reduced expansion of the loader spring, which connects the block with the tectonic plate; that is, to a reduced resistance force of the fault layer in this region  $(1 - 4\alpha)\Delta\sigma$ . This stress change is assumed to cause the relaxation process within the crust following subsequently to the earthquake (step 2). We introduce the stress levels  $\sigma_{cr}^N(i, j)$  indicating these stress changes. The values of  $\sigma_{cr}^N(i, j)$  are set to 0 at the beginning of the earthquake (with index  $N$ ) occurring at time  $t_N$ .

(a) Nearest neighbor interactions (NN model):<sup>1</sup>

The stresses in the crust are assumed to increase in the positions of the four adjacent blocks:

$$\sigma_{cr}^N(k_{\pm}, l_{\pm}) \rightarrow \sigma_{cr}^N(k_{\pm}, l_{\pm}) + (0.25 - \alpha) \Delta\sigma \quad (7)$$

(b) Long-range interactions (LR model):

In this case, the stresses in the crust are assumed to increase spatially according to a Gaussian distribution:

$$\sigma_{cr}^N(i, j) \rightarrow \sigma_{cr}^N(i, j) + \frac{1-4\alpha}{\pi Q^2} e^{-\frac{(i-k)^2+(j-l)^2}{Q^2}} \Delta\sigma \quad (8)$$

Instead of the Gaussian function, we could use alternatively the appropriate form to a perfectly elastic solid  $1/r^3$  or an exponential screening function. However, the Gaussian function has the numerical advantage that it can be normalized and that it is spatially localized. Hence, finite size effects are less important and huge grid-sizes with high computational efforts can be avoided.

According to Eq. (5), the sliding of block  $(k, l)$  redefines the stresses  $\sigma(k_{\pm}, l_{\pm})$  acting on the adjacent blocks. This may lead to an instability, i.e.,  $\sigma(k_{\pm}, l_{\pm}) \geq \sigma_F$ , in one or more adjacent blocks. In this case, a chain reaction starts and the stresses are distributed according to Eqs. (5), (6), and (7), respectively (8), until the earthquake is terminated, i.e., until  $\sigma(i, j) < \sigma_F$  for all blocks  $(i, j)$ . The spatial size  $S$  of the event is measured; that is, the blocks, which slipped at least once in the avalanche, are counted.

2. In the inter-occurrence time interval between successive events, the dynamics are described in the following way: The evolution of a single earthquake is set to be instantaneous; that is, the crust relaxation process and the tectonic loading have no effect during the evolution of an earthquake. After an earthquake occurring at time  $t_n$ , transient creep is assumed to lead to a stress increase

$$\Delta\sigma^n(i, j, t) = \kappa \sigma_{cr}^n(i, j) (1 - e^{-\frac{t-t_n}{T}}), \quad (9)$$

where the relaxation time  $T$  as well as  $\kappa$  are parameters of the model. The parameter  $\kappa$  denotes the fraction  $0 < \kappa < 1$  of the instantaneous stress jump in the crust  $\sigma_{cr}^n$ , which is redistributed to the fault in time. A schematic plot of this temporal dependence is shown in Figure 2. The overall dynamics due to all relaxation processes, triggered by the earthquakes in the past, can be determined by superposition. Additionally to the crust relaxation process, the movement of the tectonic plates increases the stress on each block with a constant rate  $(\sigma_F - \sigma_R)/T_0$ , where  $T_0$  is the tectonic reloading time. Therefore the time evolution of the stress distribution following an earthquake at time  $t = t_N$  can be described

<sup>1</sup>This case is called nonlocal model in (Hainzl et al., 1999).



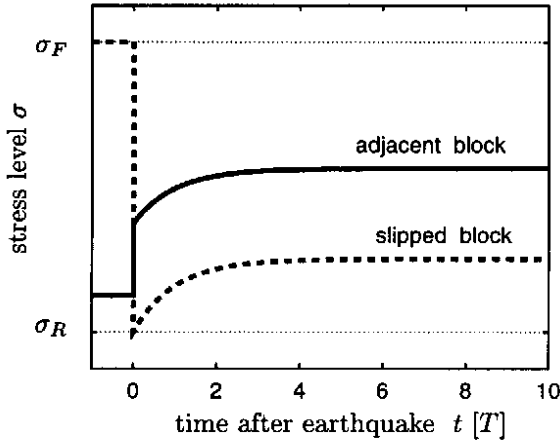


**Fig. 2.** The schematic plot illustrates the time-delayed stress changes subsequently to the instantaneous stress jumps due to an earthquake at time 0. At the occurrence time of the earthquake, the stress drops instantaneously at the slipped block and increases at adjacent blocks. As a result of the crust relaxation process with relaxation time  $T$ , the stresses increase after the earthquake on the four nearest neighbors (NN model), respectively, on the slipped block as well as on its extended neighborhood (LR model).

by

$$\begin{aligned} \sigma(i, j, t) &= \sigma(i, j, t_N) + \frac{\sigma_F - \sigma_R}{T_0} (t - t_N) \\ &\quad + \sum_{n=1}^N [\Delta\sigma^n(i, j, t) - \Delta\sigma^n(i, j, t_N)] \\ &= \sigma(i, j, t_N) + \frac{\sigma_F - \sigma_R}{T_0} (t - t_N) \\ &\quad + \kappa S_N(i, j) (1 - e^{-\frac{t-t_N}{T}}). \end{aligned} \quad (10)$$

The function  $S_N(i, j)$  can be calculated iteratively by

$$\begin{aligned} S_N(i, j) &\equiv \sum_{n=1}^N \sigma_{cr}^n(i, j) e^{-\frac{t_N - t_n}{T}} \\ &= \sigma_{cr}^N(i, j) + S_{N-1}(i, j) e^{-\frac{t_N - t_{N-1}}{T}}, \end{aligned} \quad (11)$$

where  $t_n$  is the occurrence time of the  $n$ th event. To determine the onset of the following earthquake (index  $N+1$ ), the equations  $\sigma(i, j, \tilde{t}_{ij}) = \sigma_F$  are solved with Newton's method and the block with the minimal time  $t_{\min} = \min\{\tilde{t}_{ij} | i, j \in 1, \dots, L\}$  is picked up. The next earthquake is initiated at this block and occurs at time  $t_{N+1} = t_{\min}$ . All stresses are changed to the values  $\sigma(i, j, t_{\min})$  according to (10), and step 1 is repeated for the next earthquake.

### 3 Numerical simulations

For the numerical simulations, we use open boundary conditions and start with random values of  $\sigma(i, j)$  uniformly distributed in the interval  $[\sigma_R, \sigma_F]$ . The values

of  $\sigma_R$  and  $\sigma_F$  have no influence on the dynamics. They are set arbitrarily to  $\sigma_R=0$  and  $\sigma_F=1$ . Furthermore, the tectonic reloading time  $T_0$  can be fixed arbitrarily, because it defines just the time scale. Therefore, apart from the system size  $L \times L$ , the parameters of our model are the elastic coupling constant  $\alpha$ , the relative stress relaxation time  $T/T_0$ , the feedback strength  $\kappa$ , and additionally in the case of long-range interactions, the spatial coupling length  $Q$ . The system is iterated until it reaches a statistically stationary state.

By setting  $\kappa=0$ , our model is equivalent to the OFC model. To illustrate the consequences of  $\kappa \neq 0$ ; that is, the effect of the memory term in Eq. (10), an example of the seismic activity accompanying a large event is shown in Fig. 3 for both cases. The transient creep leads obviously to a clustering of smaller events in the temporal vicinity of the mainshock, whereas clustering is absent in the case of the OFC model. In the following sections, the simulations are analyzed in more detail. At first, we study the distribution of event sizes. In the second part, we investigate the spatio-temporal patterns

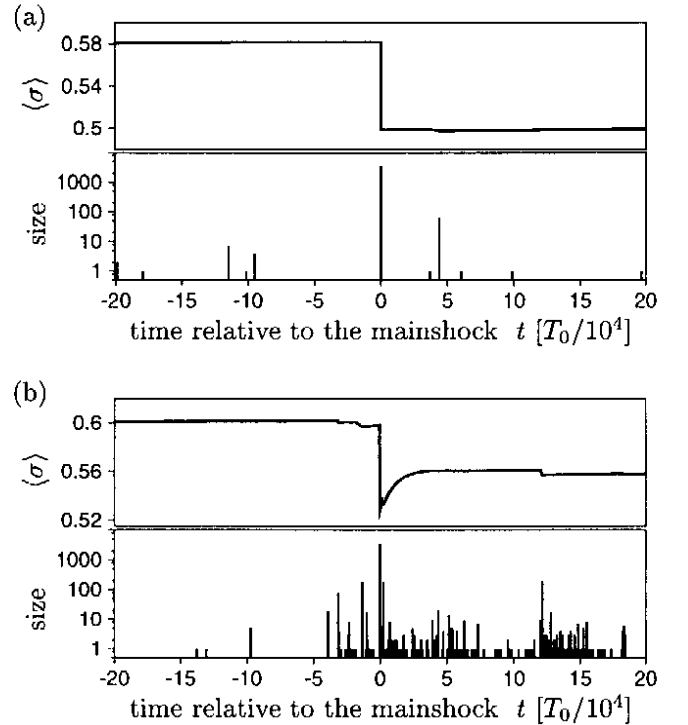


**Fig. 3.** The effect of transient creep is illustrated by means of typical examples of the seismic activity accompanying large events: (a) without the relaxation mechanism ( $\kappa=0$ ,  $\alpha=0.2$ ); that is, the OFC model; and (b) including the relaxation mechanism (NN model with  $\kappa=0.5$ ,  $\alpha=0.2$ , and  $T/T_0=10^{-4}$ ). For both  $100 \times 100$  block simulations, the mean stress level  $\langle \sigma \rangle = \sum \sigma(i, j) / L^2$  (upper curve) and the size of occurring events (bottom curve) are shown as a function of time. In the case of the extended model, the assumed transient characteristics are responsible for the partial stress recovery subsequent to earthquakes leading to a pronounced bunching of events in the vicinity of the largest earthquake. Note that transient creep occurs subsequently to all events, although the plotted curve  $\langle \sigma \rangle(t)$  reflects this for the largest events only.

of the earthquake dynamics, in particular, we analyze the characteristics of foreshock and aftershock sequences as well as the waiting time distribution.

### 3.1 Frequency-size distribution

For the NN model, previous investigations (Hainzl et al., 1999) have shown that the model dynamics evolve independent of the initial conditions in a statistically stationary state which is characterized by a power law scaling of the size distribution, limited only by the finite system size. By analogy with the OFC model (Olami et al., 1992), the observed exponent  $B$  (Eq. 2) is significantly influenced only by the elastic parameter  $\alpha$  and increases, if  $\alpha$  decreases. Realistic values,  $B \approx 1$ , can be reproduced with  $\alpha \approx 0.2$ .

In the case of the long-range interactions, these characteristics are maintained. For the coupling constant  $\alpha = 0.2$ , Fig. 4 shows the distributions for different coupling length  $Q$  in comparison to that obtained using nearest neighbor interactions. No significant deviations are found.

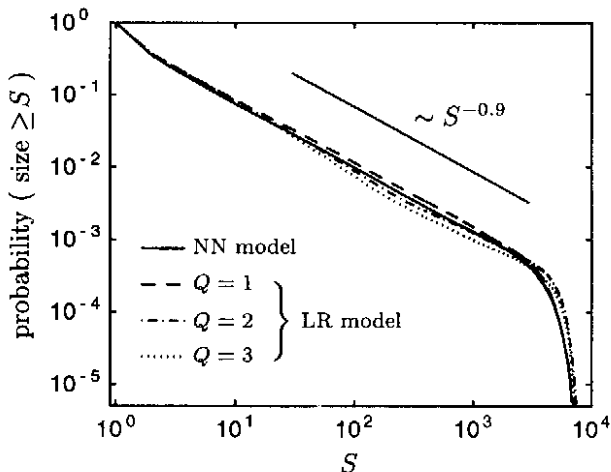


**Fig. 4.** Probability density of observing an earthquake of size greater than  $S$  as a function of  $S$  for the model with nearest neighbor, respectively long-range interactions. Each distribution results from a simulation of a  $100 \times 100$  block-system with model parameters  $T/T_0 = 10^{-4}$ ,  $\alpha = 0.2$ , and  $\kappa = 0.5$ .

In the following sections, we restrict our analysis to simulations with the parameter  $\alpha = 0.2$  yielding a realistic Richter  $B$  value.

### 3.2 Foreshock and aftershock sequences

In this section, we analyze our model simulations with regard to spatio-temporal clusters accompanying mainshocks. A mainshock is defined as an event of size  $S \geq S_{\text{cut}}$ , which is the largest event within its temporal vicinity  $\pm \Delta t_M$ . For the analyzed  $100 \times 100$  block simulations, we use the definitions  $S_{\text{cut}} = 1000$  and  $\Delta t_M = T_0/10$ .

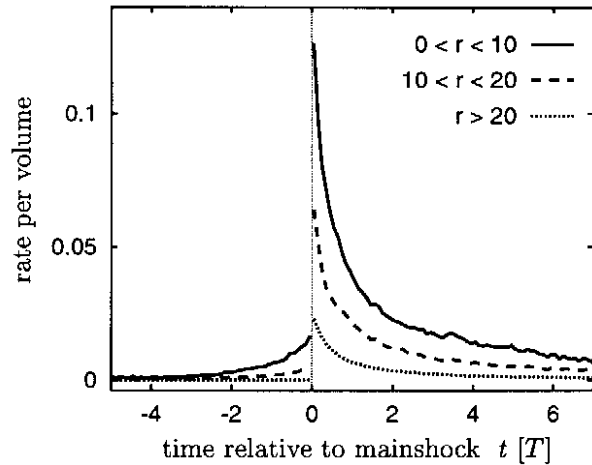


**Fig. 5.** Averaged earthquake occurrence rate per spatial volume formed by stacking the records of seismic rate relative to mainshock occurrence times. The rate depends on the distance  $r$  to the hypocenter of the mainshock. The curves show the average of the seismic rate regarding the 5000 mainshocks occurring in a  $100 \times 100$  block simulation of about  $10^7$  earthquakes (NN model with  $T/T_0 = 10^{-4}$ ,  $\alpha = 0.2$ , and  $\kappa = 0.5$ ).

#### 3.2.1 Rate of foreshocks and aftershocks

We compute the seismic activity, especially the rate of events, occurring on average relative to those mainshocks. For the NN model, Fig. 5 shows the averaged occurrence rate per spatial volume in dependence on the spatial distance  $r$  to the hypocenter (initiation point) of the mainshock. An increasing number of foreshocks is generated, on average, just before the mainshock. Aftershocks turn on instantaneously with the mainshock, followed by a decay of the aftershock rate. The rate of aftershocks exceeds the rate of foreshocks by about 1 order of magnitude. It is important to note that the number of foreshocks as well as the number of aftershocks decreases with increasing distance  $r$  from the hypocenter of the mainshock; that is, the clusters are localized around the hypocenter of the mainshock. These characteristics are not restricted to the case of nearest neighbor coupling, rather it is also observed in the case of spatially extended regions of transient creep (LR model).

In Fig. 6 the occurrence rates of events are shown in log-log plots for the NN model as well as for the LR model with  $Q=1, 2$ , and  $3$ . The relative relaxation time is set to  $T/T_0 = 10^{-4}$  in all cases. The variations in each data set, namely the increase of foreshock as well as the decrease of aftershock activity, can be fitted quite well by, aside from a factor, identical modified Omori laws (Eq. 3, respectively 4). This is in good agreement with findings for real fault systems (Papazachos, 1975; Kagan and Knopoff, 1978; Jones and Molnar, 1979; Davis and Frohlich, 1991). In previous investigations of the NN model, we have found that the relative relaxation time  $T/T_0$  determines the power law exponent (Hainzl

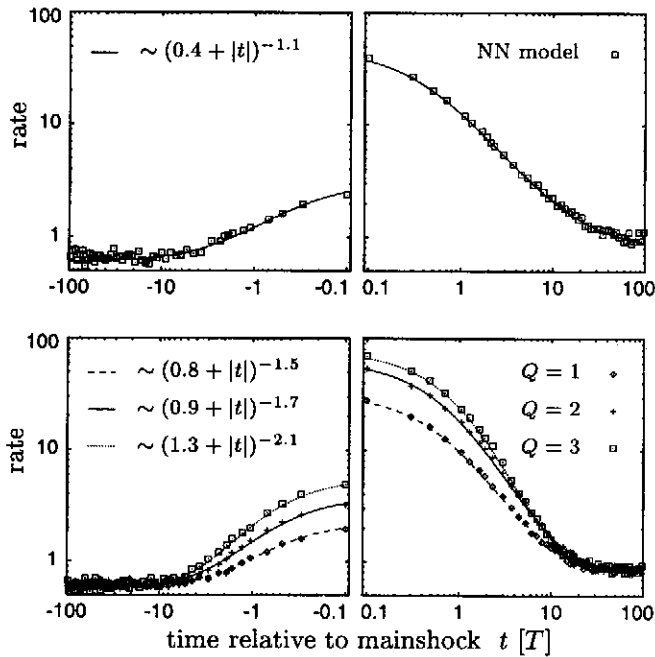


**Fig. 6.** Log-log plots of earthquake clustering formed by stacking the records of seismic activity relative to mainshock times. The plots show the average of event clustering corresponding to 5000 mainshocks of size  $S \geq 1000$  occurring in  $100 \times 100$ -grid model simulation with  $T/T_0 = 10^{-4}$ ,  $\alpha = 0.2$  and  $\kappa = 0.5$ . The results are shown for the NN model (upper plots), and the LR model with  $Q=1, 2$ , and  $3$  (bottom plots). For each data set the increase of foreshock activity (left column) as well as the decrease of aftershock activity (right column) can be fitted by similar power laws differing in a prefactor only.

et al., 1999). The exponent of the power law decreases approximately by 1.6, 1.1, and 0.6 for increasing ratio  $T/T_0 = 10^{-5}$ ,  $10^{-4}$ , and  $10^{-3}$ , respectively. Thus the empirical values  $p, q \approx 1$  can be reproduced in this case by a ratio  $T/T_0$  of the order of  $10^{-4}$ .

Here, we find that also the spatial extension of transient creep changes significantly the exponent: The larger  $Q$  the larger is the exponent. An explanation is that mainshocks occur when the block-system is critical loaded. The stress redistribution due to the mainshock unloads the system only partly remaining other parts of the block-system critical loaded. The subsequent stress increase owing to transient creep triggers aftershocks which trigger further aftershocks and so on, until the whole system is subcritical. In the case of long-range interactions, each event can trigger more subsequent events, thus the process decays faster.

Therefore in addition to different relaxation times, a variable spatial scale of transient creep can be responsible for the variation of empirically observed  $p$  values scattering between 0.9 and 1.5 (Utsu et al., 1995).

In summary, the main characteristics, in particular the power law distribution of event sizes and the occurrence of foreshock and aftershock sequences obeying the Omori law, are reproduced independently of the spa-

tial range of creep. Only in the unrealistic case that transient creep is restricted to the slipped blocks, the empirical observations cannot be reproduced (Hainzl et al., 1999). For the further investigations we use nearest neighbor instead of the long-range interactions, because of less computational efforts. The model parameters are set to  $T/T_0 = 10^{-4}$  and  $\alpha = 0.2$  leading to the empirically observed power law exponents  $B, p$ , and  $q$ .

### 3.2.2 Temporal variations of aftershock sizes

Up to now, we have analyzed only the temporal variations of the aftershock rate. Now, we want to characterize the aftershock size in dependence on the aftershock occurrence time relative to the mainshock. The sizes of aftershocks occurring subsequently to 1000 mainshocks are measured in time bins of  $\Delta t = T$ . Fig. 7 shows the temporal variation of the mean as well as of the maximum size of aftershocks occurring in these time bins, on average, after a mainshock. The mean aftershock size is almost independent of time, whereas the maximum size decreases with time from approximately 100 immediately after the mainshocks down to approximately 14. Therefore the maximum aftershock size is on average at least one order of magnitude less than the mainshock size. This is in good agreement with empirical findings (Scholz, 1994). The decrease of the maximum size is due to the fact that the rate of aftershocks decreases with time (see Fig. 6); thus the probability to observe larger aftershocks is higher in the vicinity of the mainshock, although the probability distribution for event sizes is almost stable.

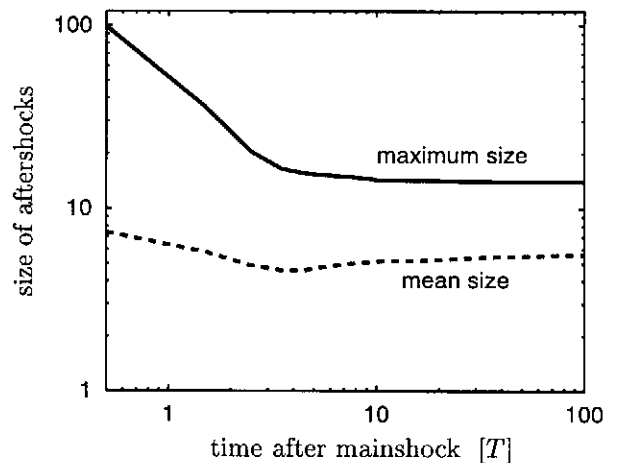


**Fig. 7.** The size of aftershocks in dependence on their occurrence times after the mainshock. The mean and the maximum aftershock size are computed by averaging over the 1000 mainshocks with size greater than 1000 which have occurred in a  $100 \times 100$ -lattice simulation of about  $2 \times 10^6$  events (NN model with  $T/T_0 = 10^{-4}$ ,  $\alpha = 0.2$ , and  $\kappa = 0.5$ ).

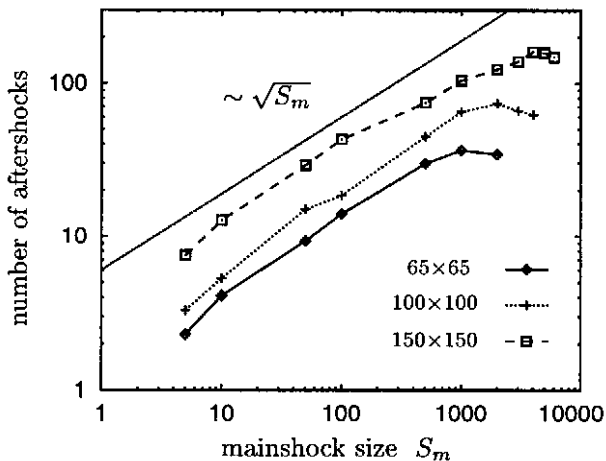


**Fig. 8.** The cumulative number of aftershocks occurring on average within  $10 \times T$  after mainshocks of size  $S_m$ . The three curves, corresponding to different system sizes  $L \times L$ , are compared with the power law  $\sim \sqrt{S_m}$ . The analyzed simulations (NN model with  $T/T_0 = 10^{-4}$ ,  $\alpha = 0.2$ , and  $\kappa = 0.5$ ) consist in the case of  $L = 65$ , respectively 100, of  $10^7$  events and in the case of  $L = 150$  of  $2 \times 10^6$  events.

### 3.2.3 Cumulative number of aftershocks

The number of aftershocks depends on the size of the triggering mainshock. This is shown in Fig. 8. For that plot, we have counted all events occurring within the time window of  $10 \times T$  subsequently to mainshocks of size  $S_m$ . Here, we have used a slightly different definition for a mainshock of size  $S_m$ , namely, it is defined as an event of size  $S \in [S_m - S_m/10, S_m + S_m/10]$ , which is the largest event within a time interval  $\pm 10 \times T$ .

The characteristics of all three curves, corresponding to different lattice sizes, are the same: The number of aftershocks increases almost according to a power law  $\sim S_m^{0.5}$ , limited only by the finite system size. The finite size effect manifests itself in the deviation from power law behavior observed for the largest mainshocks. However, the larger the lattice size, the later occurs this deviation. In agreement with our results, a power law increase can also be fitted to the cumulative number of real aftershocks, although approximations of the exponent vary largely, mainly between 0.3 and 1 (Reasenber, 1985; Guo and Ogata, 1997). The exponent of nearly 0.5, which is found in our model simulations, indicates that aftershocks are triggered mostly on the edge of the fracture area of the mainshock. In the case of a circular fracture area  $S_m$ , the edge is proportional to the radius, i.e. proportional to  $\sqrt{S_m}$ .

### 3.3 Distribution of waiting times

To study the overall characteristics of temporal clustering in our model simulation, we analyze the distribution of waiting times  $t_w$ ; that is, the inter-occurrence time intervals between successive events. This distribution is

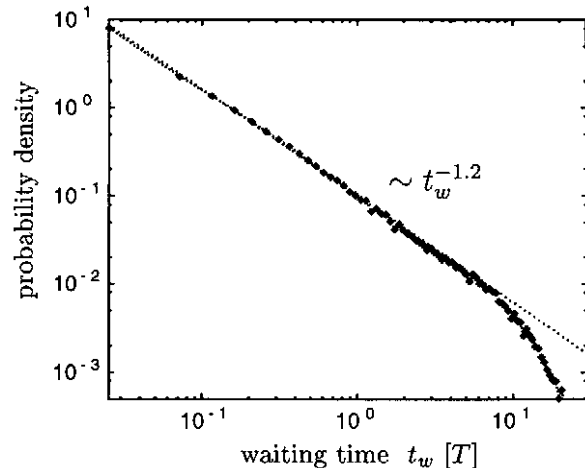


**Fig. 9.** The probability density of observing a waiting time  $t_w$  between two successive events. The plot results from a simulation of  $10^6$  events (NN model with  $T/T_0 = 10^{-4}$ ,  $\alpha = 0.2$ ,  $\kappa = 0.5$ , and  $L = 100$ ). The dotted line indicates the power law  $t_w^{-1.2}$ .

shown in Fig. 9 for a simulation of the NN model with a relative relaxation time  $T/T_0 = 10^{-4}$ . The distribution can be fitted over almost three orders of magnitude by a power law with exponent -1.2. This power law behavior is in good agreement with empirical observations (Ito, 1995; Utsu et al., 1995). However, this is not surprising owing to the power law behavior of aftershock sequences. Senshu (1959) showed that if the aftershocks are represented by a non-stationary Poisson process whose intensity is proportional to  $t^{-p}$ , a power law distribution  $t_w^{-p_w}$  of waiting times is derived directly and the relation between  $p$  and  $p_w$  should be

$$p_w = 2 - p^{-1}. \quad (12)$$

In our model, simulations with  $T/T_0 = 10^{-4}$  lead to an exponent  $p \approx 1.1$  of the modified Omori law (Eq. 3). Thus Eq. (12) is nearly fulfilled for our deterministic model, although the exponent of the waiting time distribution  $p_w$  is obtained in this case for the whole sequence including all events belonging to the background activity.

In the following part, we want to characterize the waiting time distribution, if events greater than a minimal size  $S_{cut}$  are considered only. A suitable measure to characterize the waiting time distribution is the coefficient of variation  $C_V$ , which is defined as the standard deviation normalized by the mean waiting time  $\langle t_w \rangle$  (Kagan and Jackson, 1991)

$$C_V = \frac{\sqrt{\langle (t_w)^2 \rangle - \langle t_w \rangle^2}}{\langle t_w \rangle}. \quad (13)$$

For a simple periodic signal  $C_V$  vanishes, whereas for a Poisson process the distribution function of the waiting times is an exponential function yielding  $C_V = 1$ . A clustering of events is indicated by  $C_V > 1$ .

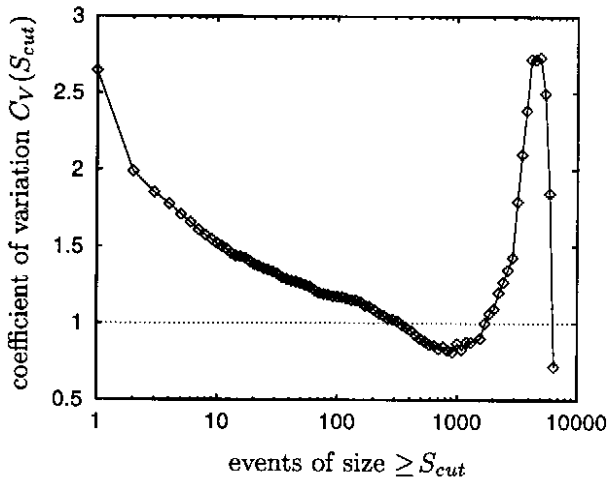


**Fig. 10.** The coefficient of variation  $C_V$  (Eq. 13), calculated for all events greater than  $S_{cut}$ , as a function of the lower cut. The result is shown for the same simulation analyzed in Fig. 9. Small and large earthquakes are characterized by a coefficient greater than 1, implying earthquake bunching.

We compute the coefficient of variation for the simulation analyzed in Fig. 9. Now, we consider only earthquakes with a size greater than  $S_{cut}$ . Figure 10 shows the value of  $C_V$  in dependence on this lower cut. The coefficient  $C_V$  is greater than 1 for small and large values of  $S_{cut}$ , implying earthquake clustering. The decrease for very large earthquakes is a finite size effect and thus related to the cutoff in the frequency-size distribution (Fig. 4). For intermediate values of  $S_{cut}$ , the earthquake occurrence seem to be uncorrelated.

Clustering for small values of  $S_{cut}$  can be explained by foreshock and aftershock sequences triggered by transient creep. These clusters consist mainly of smaller events (see Fig. 7). Thus increasing of  $S_{cut}$  leads to partial deletion of these sequences and consequently to a decrease of  $C_V$ .

In contrast, large events are correlated in time because they are correlated in space. This correlation emerges because of dissipation ( $\alpha < 0.25$  and  $\kappa < 1$ ). This is already known for the nonconservative, cellular automaton versions of the BK model; that is, for our model with  $\kappa = 0$ . In this case, Rundle and Klein (1995) found strong correlations between the spatial fracture areas of subsequent large earthquakes and Christensen and Olami (1992) observed, in analogy to our results with  $\kappa \neq 0$ , temporal clustering of large events. For the case of  $\kappa = 0.5$ , Fig. 11 shows an example of large events occurring subsequently in a simulation of the NN model. They are obviously bunched, which is in good agreement with observations of the occurrence of large earthquakes in nature (Kagan and Jackson, 1991). These clustering characteristics are found to be independent of the assumed spatial extension of transient creep, namely they are observed also in the LR model.

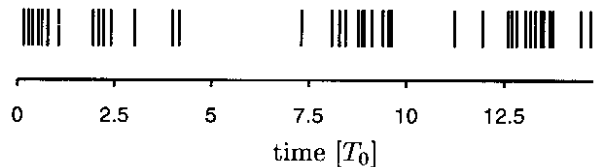


**Fig. 11.** An example of temporal occurrence of successive large events ( $S > 3000$ ) in the NN model.

#### 4 Summary and conclusion

It was known before that nonconservative, cellular automaton versions of the BK model can reproduce the empirically observed power law behavior of the frequency-size distribution of earthquakes. However, they have failed to reproduce the most conspicuous characteristics of spatio-temporal clustering observed in real fault systems, namely the occurrence of foreshock and aftershock sequences accompanying large earthquakes as well as the occurrence of swarms of small events. We have shown that this inability can be redressed by considering transient creep, which is observed to occur subsequently to earthquakes in real fault systems. In a first order approximation we have modeled the characteristics of transient creep by an exponential function decay in time and nearest neighbor as well as long-range effects in space. The model reproduces independently of the parameters and the spatial range of transient creep (as long as the effect of transient creep is not restricted to the slipped blocks) the most obvious characteristics manifested in real earthquake catalogs: (a) the distribution of earthquake sizes fulfills a power law (Gutenberg-Richter law), (b) the temporal increase of foreshock as well as the decrease of aftershock activity is characterized by similar power laws (modified Omori law), (c) foreshocks and aftershocks are spatially localized in the vicinity of the mainshock, (d) much more aftershocks than foreshocks occur, (e) the size of the largest aftershock is on average at least one order of magnitude less than the mainshock size, (f) the number of aftershocks increasing with the mainshock size according to a power law, and (g) small as well as large events are more likely to occur clustered than random. In further agreement with observations, we have shown in a previous work (Hainzl et al., 1999) that (h) the simulated foreshocks are characterized by a significant smaller Richter  $B$  value in comparison to aftershocks, or other events, and that (i) swarm events occur.

While the choice of model parameters does not change these characteristics in principle, the exponents of the frequency-size distribution  $B$  as well as of the Omori law  $p$  is found to dependent on this choice: The  $B$  value is determined mainly by the coupling constant  $\alpha$ , whereas the relative relaxation time  $T/T_0$  as well as the spatial scale  $Q$  of transient creep change the  $p$  value. On the other hand the parameter characterizing the strength of

transient creep  $\kappa$  and the spatial size of the system  $L$  do not influence any of the power law exponents significantly. However, the number of foreshocks and aftershocks occurring in the simulations are positively correlated with  $\kappa$  and  $L$  (Hainzl et al., 1999).

In summary, we have shown that block systems, involving nothing else than elastic interactions with an exponentially decaying memory in addition, self-organize into a statistically stationary state with striking similarities to empirical observations. In spite of the fact that the actual dynamical processes involved in earthquake faults are much more complicated, we believe that our conceptual model bears a strong resemblance to the mechanisms most important for the underlying dynamics of earthquakes.

*Acknowledgements.* The authors are grateful to R. Engbert, F. Scherbaum, and J. Zschau for stimulating discussions. This work was supported by the Sonderforschungsbereich 555 "Komplexe Nichtlineare Prozesse" and the state Brandenburg (Hochschulsonderprogramm III 1.6).

## References

- Bak, P., and Tang, C., Earthquakes as a self-organized critical phenomenon, *J. Geophys. Res.*, *94*, 15635–15637, 1989.
- Bak, P., Tang, C., and Wiesenfeld K., Self-organized criticality: An explanation of  $1/f$  noise, *Phys. Rev. Lett.*, *59*, 381–384, 1987.
- Brown, S. R., Scholz, C. H., and Rundle, J. B., A simplified spring-block model of earthquakes, *Geophys. Res. Lett.*, *18*, 215–218, 1991.
- Burridge, R., and Knopoff, L., Model and theoretical seismicity, *Bull. Seis. Soc. Am.*, *57*, 341–371, 1967.
- Carlson, J. M., and Langer, J. S., Properties of earthquakes generated by fault dynamics, *Phys. Rev. Lett.*, *62*, 2632–2635, 1989a.
- Carlson, J. M., and Langer, J. S., A mechanical model of an earthquake fault, *Phys. Rev. A*, *40*, 6470–6484, 1989b.
- Christensen, K., and Olami, Z., Variation of the Gutenberg-Richter  $b$ -values and nontrivial temporal correlations in a spring-block model for earthquakes, *J. Geophys. Res.*, *97*, 8729–8735, 1992.
- Davis, S. D., and Frohlich, C., Single-link cluster analysis of earthquake aftershocks: Decay laws and regional variations, *J. Geophys. Res.*, *96*, 6335–6350, 1991.
- DeMets, C., Afterslip no longer an afterthought, *Nature*, *386*, 549, 1997.
- Dieterich, J. H., Time-dependent friction as a possible mechanism for aftershocks, *J. Geophys. Res.*, *77*, 3771–3781, 1972.
- Ekström, G., and Dziewonski, A. M., Evidence of bias in estimations of earthquake size, *Nature*, *332*, 319–323, 1988.
- Guo, Z., and Ogata, Y., Statistical relations between the parameters of aftershocks in time, space, and magnitude, *J. Geophys. Res.*, *102*, 2857–2873, 1997.
- Gutenberg, B., and Richter, C. F., Earthquake magnitude, intensity, energy and acceleration, *Bull. Seismol. Soc. Am.*, *46*, 105–145, 1954.
- Hainzl, S., Zöller, G., and Kurths, J., Similar power laws for foreshock and aftershock sequences in a spring block model for earthquakes, *J. Geophys. Res.*, *104*, 7243–7253, 1999.
- Heki, K., Miyazaki, S., and Tsuji, H., Silent fault slip following an interplate thrust earthquake at the Japan Trench, *Nature*, *386*, 595–598, 1997.
- Ito, K., Punctuated-equilibrium model of biological evolution is also a self-organized-criticality model of earthquakes, *Phys. Rev. E*, *52*, 3232–3233, 1995.
- Ito, K., and Matsuzaki, M., Earthquakes as self-organized critical phenomena, *J. Geophys. Res.*, *95*, 6853–6860, 1990.
- Jones, L. M., and Molnar, P., Some characteristics of foreshocks and their possible relationship to earthquake prediction and premonitory slip on faults, *J. Geophys. Res.*, *84*, 3596–3608, 1979.
- Kagan, Y. Y., and Jackson, D. D., Long-term earthquake clustering, *Geophys. J. Int.*, *104*, 117–133, 1991.
- Kagan, Y. Y., and Knopoff, L., Statistical study of the occurrence of shallow earthquakes, *Geophys. J. R. Astron. Soc.*, *55*, 67–86, 1978.
- Kanamori, H., and Anderson, D. L., Theoretical basis of some empirical relations in seismology, *Bull. Seis. Soc. Am.*, *65*, 1073–1095, 1975.
- Nakanishi, H., Cellular-automaton model of earthquakes with deterministic dynamics, *Phys. Rev. A*, *41*, 7086–7089, 1990.
- Olami, Z., Feder, H. S., and Christensen, K., Self-organized criticality in a continuous, nonconservative cellular automaton modeling earthquakes, *Phys. Rev. Lett.*, *68*, 1244–1247, 1992.
- Omori, F., On the aftershocks of earthquakes, *J. Coll. Sci. Imp. Univ. Tokyo*, *7*, 111–200, 1894.
- Pacheco, J. F., Scholz, C. H., and Sykes, L. R., Changes from frequency-size relationship from small to large earthquakes, *Nature*, *355*, 71–73, 1992.
- Papazachos, B. C., Foreshocks and earthquake prediction, *Tectonophysics*, *28*, 213–226, 1975.
- Peltzer, G., Rosen, P., Rogez, F., and Hudnut, K., Postseismic rebound in fault step-overs caused by pore fluid flow, *Science*, *273*, 1202–1204, 1996.
- Purcaru, G., and Berckhemer, H., A magnitude scale for very large earthquakes, *Tectonophysics*, *49*, 189–198, 1978.
- Reasenberg, P., Second-order moment of Central California seismicity, 1969–1982, *J. Geophys. Res.*, *90*, 5479–5495, 1985.
- Rundle, J. B., and Klein, W., Dynamical segmentation and rupture patterns in a toy slider-block model for earthquakes, *Nonlin. Proc. Geophys.*, *2*, 61–79, 1995.
- Savage, J. C., and Svarc, J. L., Postseismic deformation associated with the 1992  $M_w=7.3$  Landers earthquake, southern California, *J. Geophys. Res.*, *102*, 7565–7577, 1997.
- Scholz, C. H., *The Mechanics of Earthquakes and Faulting*, Cambridge University Press, 1994.
- Senshu, T., On the time interval distribution of aftershocks, *Zisin, Ser. 2*, *12*, 149–161, 1959 (in Japanese).
- Utsu, T., Ogata, Y., and Matsu'ura, R. S., The centenary of the Omori formula for a decay law of aftershock activity, *J. Phys. Earth*, *43*, 1–33, 1995.

# Appendix B

**Seismic quiescence as an indicator for large earthquakes in a system of self-organized criticality**

Autors:	S. Hainzl, G. Zöller, J. Kurths, and J. Zschau
Journal:	<i>Geophysical Research Letters</i> ,
Volume (Nr.):	<b>27(5)</b>
Pages:	597-600
Year:	2000

# Seismic quiescence as an indicator for large earthquakes in a system of self-organized criticality

Sebastian Hainzl, Gert Zöller, and Jürgen Kurths

Institute of Physics, University of Potsdam, Potsdam, Germany

Jochen Zschau

GeoForschungsZentrum, Potsdam, Germany

**Abstract.** Seismically active fault systems may be in a state of self-organized criticality (SOC). Investigations of simple SOC models have suggested that earthquakes might be inherently unpredictable. In this paper, we analyze the question of predictability in a more complex and realistic SOC model, which consists of a spring-block system with transient creep characteristics. Additionally to the power law distribution of earthquake sizes, this model reproduces also foreshock and aftershock sequences. Aside from a short-term increase of seismicity immediately prior to large model earthquakes, these events are preceded on average by an intermediate-term period of reduced seismicity. The stronger and the longer the duration of this period, the larger on average is the subsequent mainshock. We find that the detection of seismic quiescence can improve the time-independent hazard assessment. The improvement is most significant for the largest target events.

## Introduction

For the last several years, a continuing debate has taken place on whether or not earthquakes are inherently unpredictable [Geller *et al.*, 1997; Wyss, 1997; *Nature debate*, 1999]. The statement of an inherent unpredictability is founded on the assumption that “the Earth is in a state of self-organized criticality, where any small earthquake has some probability of cascading into a large event” [Geller *et al.*, 1997]. In the concept of self-organized criticality (SOC), which was first introduced by Bak *et al.* [1987], a driven dissipative system with many degrees of freedom evolves spontaneously into a statistically stationary state characterized by power-law behavior of spatial and temporal correlation functions. Thus, a self-organized critical state of fault systems can explain the frequency-size distribution of earthquakes, that is, the Gutenberg–Richter law. Examples for earthquake models showing SOC, and therefore reproducing the Gutenberg–Richter law, are the models proposed by Bak and Tang, [1989], and by Olami *et al.*, [1992]. On the other hand, these models fail to reproduce some important properties of the spatiotemporal clustering of earthquakes observed in real fault systems. In particular, they do not show foreshock and aftershock sequences correlated to large earthquakes as well as earthquake swarms. It is questionable,

to what extent simple SOC models, which exclude these fundamental features, can be used to draw reliable conclusions concerning the predictability of earthquakes.

The counterclaim to an inherent unpredictability is based on the observation of precursory phenomena. They are assumed to indicate a change of the system state [Wyss, 1997]. Foreshocks are the most obvious premonitory phenomenon preceding large earthquakes. In advance, however, foreshocks can be identified as such only with a low probability [Ogata *et al.*, 1996]. Aside from foreshocks, other precursory phenomena have been observed, e.g. ground water changes or electromagnetic emissions [Wyss and Dmowska, 1997]. In contrast to foreshocks, the statistical evidence for these observations is brought into question [Geller *et al.*, 1997]. This is valid also for the phenomenon of precursory seismic quiescence. A period of reduced earthquake activity is observed to last between months or years prior to many mainshocks. The duration is found to be the longer the larger the subsequent mainshock is [Wyss and Habermann, 1988]. Therefore, precursory seismic quiescence could be a promising candidate for intermediate-term predictions. However, its statistical significance is difficult to prove using seismicity catalogs, because the latter represent only a brief record of the system relative to the time scale of the seismic cycle.

In this paper, we try to bridge both the hypothesis of an underlying self-organized critical system state and the occurrence of precursory phenomena. Pre-existing hierarchical fault systems showing precursory phenomena have been already investigated with regard to the predictability of large events [Huang *et al.*, 1998]. Here, we analyze a recently proposed SOC model [Hainzl *et al.*, 1999] representing the class of homogeneous spring-block systems. This earthquake model reproduces in addition to the Gutenberg–Richter law several observed spatiotemporal characteristics of earthquakes, including foreshocks and precursory seismic quiescence. Although the synthetic earthquake catalogs contain much more information, in particular the spatial distribution of hypocenters as well as magnitudes, we restrict our analysis to the temporal variations of the seismic rate. The underlying question is to what extent fluctuations in the high-dimensional system state are reflected in such an easily observable quantity. In contrast to real earthquake catalogs, the predictability of large earthquakes can be checked in the numerically generated data with statistical significance.

## Model

The model used here has been described elsewhere [Hainzl *et al.*, 1999]. Its basis is a cellular automaton version [Olami

Copyright 2000 by the American Geophysical Union.

Paper number 1999GL011000.  
0094-8276/00/1999GL011000\$05.00



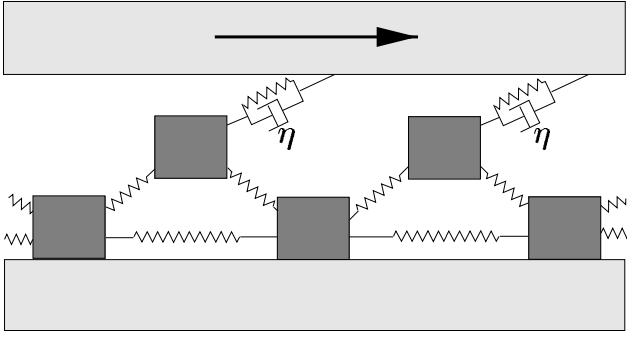


**Figure 1.** One-dimensional sketch of the investigated two-dimensional spring-block model. The bottom blocks, which perform stick-slip motion, are interconnected by springs. Additionally, they are coupled by further springs and dashpots (with viscous coefficient  $\eta$ ) to the moving tectonic plate and frictionally to the lower plate. In the case of  $\eta=0$ , the model is equivalent to the model proposed by *Olami et al.* [1992].

*et al.*, 1992] of the two-dimensional spring-block model originally proposed by *Burridge and Knopoff* [1967]. In extension to previous models, *Hainzl et al.* [1999] take into account in a first-order approximation transient creep characteristics observed in real fault systems [*Savage and Svarc*, 1997]. A one-dimensional sketch of the investigated two-dimensional block model is shown in Figure 1. The model parameters are (i) the elastic coupling constant between two adjacent blocks  $\alpha$ , which can vary in the range of  $0 \leq \alpha \leq 0.25$ , (ii) the stress relaxation time  $T$ , which is proportional to the assumed viscous coefficient  $\eta$  of the material, (iii) the tectonic reloading time  $T_0$ , and (iv) the fraction of postseismically distributed stress  $\kappa(1-4\alpha)$ , where  $\kappa$  can vary between 0 and 1. However, block systems of this type evolve independently of the initial conditions into a statistically stationary state, which depends mainly on only two parameters, namely on  $\alpha$  and  $T/T_0$ .

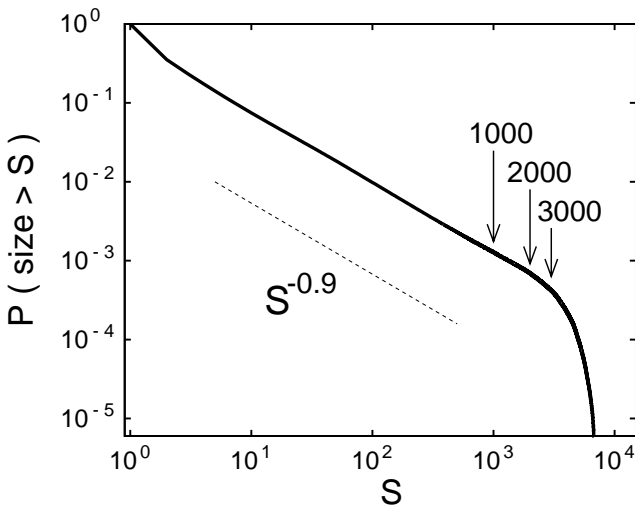


**Figure 2.** The probability density of observing an event of source size greater than  $S$  blocks as a function of  $S$  in the case of the analyzed model sequences. The dotted line corresponds to a  $B$  value of 0.9, whereas the arrows indicate the lower cutoffs for the mainshock definitions used in our investigations.

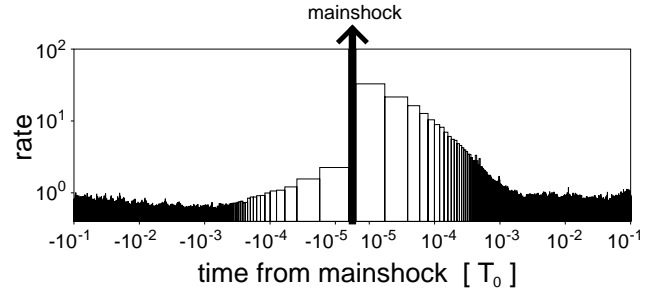


**Figure 3.** Log-log plot of the earthquake occurrence rate relative to the mainshock occurrence time. The curve shows the average of the seismic rate regarding 5000 mainshocks with size greater than 1000 blocks occurring in the analyzed model sequences.

In correspondence with the fully elastic model [*Olami et al.*, 1992], the model shows SOC. The self-organized state is characterized by a power law distribution of event sizes, limited only by the finite size of the block-system. The value of the power law exponent  $B$  increases, if  $\alpha$  decreases. Figure 2 illustrates the size distribution for  $100 \times 100$ -block simulations with  $\alpha = 0.2$ . In this case the  $B$  value is within the range of empirically observed values, scattering around 1 [*Turcotte*, 1997].

In contrast to the fully elastic model, the visco-elastic model reproduces several observed spatiotemporal patterns of earthquakes: Large events are followed by aftershock sequences obeying the modified Omori law; and are preceded by localized foreshocks, which are initiated after a time period of seismic quiescence (see Figure 3). While a considerable variability of precursory seismicity is observed, the averaged earthquake activity, which is formed by stacking the records of seismic activity relative to the mainshock occurrence times, increases immediately prior to the mainshocks according to a power law. The exponent of the power law increase is identical to the Omori exponent  $p$  characterizing the power law decay of aftershocks. This is also known from empirical observations [*Jones and Molnar*, 1979]. The value of  $p$  depends on the normalized relaxation time  $T/T_0$ . Additionally, it is found in further agreement with real observations [*Suyehiro et al.*, 1964] that, compared with aftershocks, the distribution of foreshock sizes is characterized by a significantly smaller  $B$  value.

The analyzed synthetic catalogs (simulated with parameters  $\alpha=0.2$ ,  $\kappa=0.25$  and  $T/T_0=10^{-4}$ ) reproduce the empirically observed event size distribution ( $B \approx 1$ ), the temporal clustering relative to mainshocks ( $p \approx 1$ ), and additionally, swarm events, namely sequences of strongly clustered smaller events not associated with a mainshock. Large events themselves occur highly clustered, rather than periodic in time.

## Predictability

In these synthetic catalogs, a short-term power law increase of seismic activity occurs immediately prior to the mainshocks on average. However, the precursory seismic patterns are found to vary largely for different mainshocks. Only in approximately half of the mainshocks, can correlated foreshocks be identified in retrospect. Furthermore, in the case of their occurrence, no obvious correlation be-

tween the size of foreshocks and the size of the mainshocks exists. This observation is in agreement with empirical findings [Jones and Molnar, 1979]. Thus it is not straightforward, maybe impossible, to identify foreshocks in advance; especially, a discrimination by means of the different size distribution of foreshocks, i.e. the smaller  $B$  value, is not feasible because of the small number of foreshocks.

However, in these simulations mainshocks are preceded on average by a further phenomenon, namely by a time interval of reduced seismic activity, which occurs prior to the foreshock activity. To illustrate this, we count the number of events preceding mainshocks in the time interval  $T_0/10$ . Here, a mainshock is defined as the largest event within its temporal vicinity  $\pm T_0/10$ . We find that the larger the mainshock is, the less events occur in this time interval (Figure 4a). Furthermore, one observes a transition in the seismic activity from a higher to a lower level. The onset of this relative seismic quiescence depends on the size of the following mainshock, namely the longer the duration of the seismic quiescence is, the larger is on average the subsequent mainshock (Figure 4b). This is in agreement with empirical observations [Wyss and Habermann, 1988]. The model mechanism for this dependence is simple. Due to the tec-

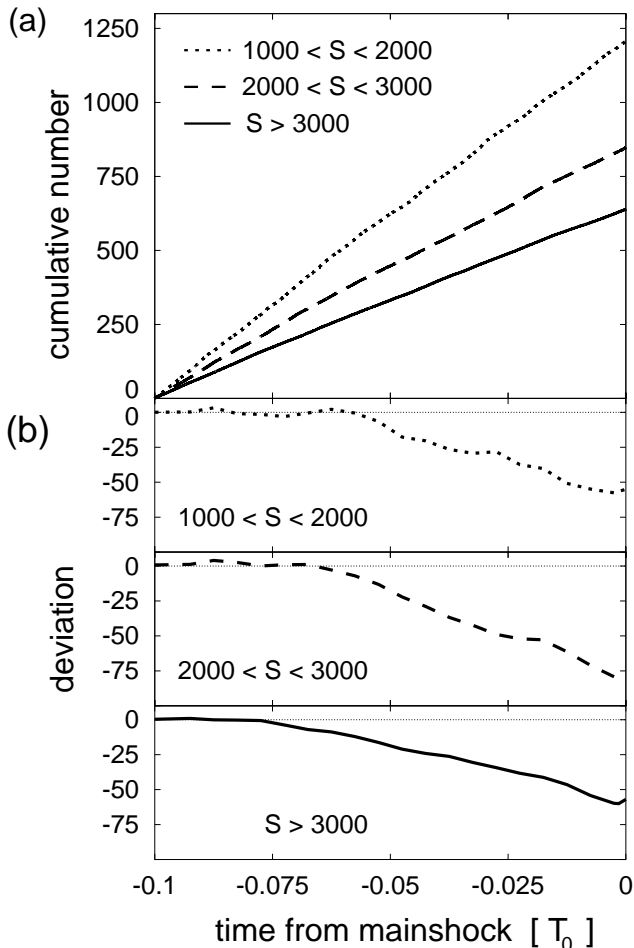


**Figure 4.** The time-dependence of the averaged seismic activity preceding mainshocks of different sizes: (a) the cumulative number of events prior to the mainshocks, and (b) the deviations from a linear increase. Each curve represents the average of the seismic rate regarding 1000 mainshocks of the noted size  $S$ .

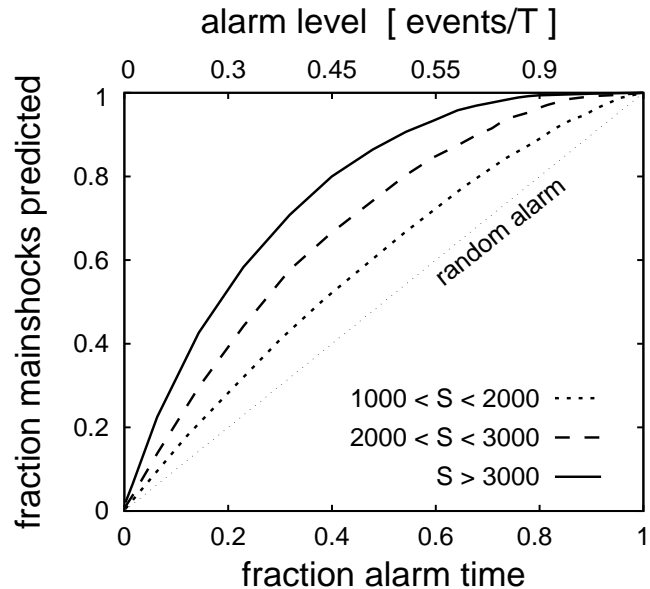


**Figure 5.** The success curve for predictions based on reduced seismic activity. An alarm is claimed or extended, if the seismic rate is below the alarm level.

tonic movement, the accumulated energy increases with the duration of seismic quiescence; that is, the probability for a large event also increases.

In comparison to the duration of foreshock sequences, which is of the order of  $10^{-4}T_0$ , the duration of the seismic quiescence is much longer, namely of the order of  $5 \times 10^{-2}T_0$ . Thus, to identify such periods of quiescence, the seismic activity can be averaged over longer time intervals in order to smooth short-term fluctuations. To analyze the predictability of large events on the basis of seismic quiescence, we calculate the seismic rates in moving time windows of length  $T_0/100$ . Other window sizes do not change the results qualitatively. Alarm conditions are implemented in the way that alarm is announced or extended for the following time interval  $T_0/100$ , if the measured rate is below a certain threshold. The fraction of the total alarm time depends on the value of this threshold. We determine the fraction of large events predicted by alarms as a function of the threshold value, respectively the fraction of alarm time. This analysis is performed for simulations, which consist of several thousands of mainshocks, leading to statistically significant results. In Figure 5 the results are shown for mainshocks belonging to three different magnitude bands. We find that in all cases the number of predicted mainshocks exceeds the successful predictions for the case of randomly distributed alarms. Furthermore, the degree of predictability increases with increasing size of the target events. For example in the case of the largest events, approximately 50% of the targets are predicted when the alarm is on for 15% of the total time. Thus our investigations show that the time-independent hazard assessment can be improved by time-dependent estimations; that is, that large synthetic earthquakes are to a certain degree predictable.

## Conclusions

Simple SOC models have been used as basis for the hypothesis of an inherent unpredictability of earthquakes,

although these models fail to reproduce realistic spatiotemporal earthquake patterns. However, more complex models can reproduce some of these spatiotemporal characteristics [e.g. Cowie *et al.*, 1993; Lyakhovskiy *et al.*, 1997]. With regard to predictability, we have analyzed a recently proposed SOC model [Hainzl *et al.*, 1999] showing in a realistic way clustering of earthquakes. In particular, two precursory signals known from real earthquake data are preceding large events in this model on average: an intermediate-term seismic quiescence and, immediately prior to the mainshocks, a short-term increase of seismic activity. The observed characteristics of both precursory phenomena, concerning the spatiotemporal patterns as well as the variation of the  $B$  value, are in good agreement with empirical findings. Thus, in comparison to previous investigations of SOC spring-block systems which lack realistic spatiotemporal dynamics [Pepke and Carlson, 1994], the analysis of this model seems to be more appropriate to judge the stated unpredictability of earthquakes.

It is difficult to identify the model foreshocks in advance. However we have found that the detection of epochs of reduced seismic activity can improve the hazard assessment for large earthquakes. In particular, the estimations are the better the larger the target events are. However, because of highly variable seismic activity prior to large earthquakes, the success ratio - that is, the factor of improvement in comparison to a time-independent estimation - is only of the order of three. On the other hand, it is behind the scope of our paper to optimize the prediction algorithms. Our investigations show that the self-organized state of a more realistic SOC earthquake model performs fluctuations correlated to the largest events. These variations are reflected to a certain degree in measurable quantities, even in simple measures such as event rates. In general, the degree of predictability seems to be determined by the amplitudes of these fluctuations, which are caused mainly by the energy dissipation due to earthquakes.

We have shown in accordance with results for hierarchical fault systems [Huang *et al.*, 1998; Sornette, 1999] that even for homogeneous fault systems the hypothesis of an underlying self-organized critical state does not lead automatically to an inherent unpredictability of earthquakes.

## References

- Bak, P., and C. Tang, Earthquakes as a self-organized critical phenomenon, *J. Geophys. Res.*, *94*, 15,635–15,637, 1989.
- Bak, P., C. Tang, and K. Wiesenfeld, Self-organized criticality: An explanation of  $1/f$  noise, *Phys. Rev. Lett.*, *59*, 381–384, 1987.
- Burridge, R., and L. Knopoff, Model and theoretical seismicity, *Bull. Seismol. Soc. Am.*, *57*, 341–371, 1967.
- Cowie, P. A., C. Vanneste, and D. Sornette, Statistical physics model for the spatiotemporal evolution of faults, *J. Geophys. Res.*, *98*, 21,809–21,821, 1993.
- Geller, R. J., D. D. Jackson, Y. Y. Kagan, and F. Mulargia, Earthquake cannot be predicted, *Science*, *275*, 1616–1617, 1997.
- Hainzl, S., G. Zöller, and J. Kurths, Similar power laws for foreshock and aftershock sequences in a spring-block model for earthquakes, *J. Geophys. Res.*, *104*, 7243–7254, 1999.
- Huang, Y., H. Saleur, C. Sammis, and D. Sornette, Precursors, aftershocks, criticality and self-organized criticality, *Europhys. Lett.*, *41*, 43–48, 1998.
- Jones, L. M., and P. Molnar, Some characteristics of foreshocks and their possible relationship to earthquake prediction and premonitory slip on faults, *J. Geophys. Res.*, *84*, 3596–3608, 1979.
- Lyakhovskiy, V., Y. Ben-Zion, and A. Agnon, Distributed damage, faulting, and friction, *J. Geophys. Res.*, *102*, 27,635–27,649, 1997.
- Nature debate, Is the reliable prediction of individual earthquakes a realistic scientific goal?, <http://helix.nature.com/debates/earthquake/>, April 1999.
- Ogata, Y., T. Utsu, and K. Katsura, Statistical discrimination of foreshocks from other earthquakes, *Geophys. J. Int.*, *127*, 17–30, 1996.
- Olami, Z., H. S. Feder, and K. Christensen, Self-organized criticality in a continuous, nonconservative cellular automaton modeling earthquakes, *Phys. Rev. Lett.*, *68*, 1244–1247, 1992.
- Pepke, S. L., and J. M. Carlson, Predictability of self-organizing systems, *Phys. Rev. E*, *50*, 236–242, 1994.
- Savage, J. C., and J. L. Svarc, Postseismic deformation associated with the 1992  $M_w=7.3$  Landers earthquake, southern California, *J. Geophys. Res.*, *102*, 7565–7577, 1997.
- Sornette, D., Towards a truly multidisciplinary approach to earthquake prediction, in [Nature debate, 1999].
- Suyehiro, S., T. Asada, and M. Ohtake, Foreshocks and aftershocks accompanying a perceptible earthquake in central Japan - On a peculiar nature of foreshocks, *Pap. Meteorol. Geophys.*, *15*, 71–88, 1964.
- Turcotte, D. L., *Fractals and Chaos in Geology and Geophysics*, Cambridge University Press, 1997.
- Wyss, M., Cannot earthquakes be predicted?, *Science*, *278*, 487–488, 1997.
- Wyss, M., and R. Dmowska (Eds.), *Earthquake prediction - state of the art*, Pageoph Topical Volumes, Birkhäuser, Basel, 1997.
- Wyss, M., and R. E. Habermann, Precursory seismic quiescence, *Pure Appl. Geophys.*, *126*, 319–332, 1988.

S. Hainzl, J. Kurths, and G. Zöller, Institute of Physics, University of Potsdam, POB 601553, 14415 Potsdam, Germany. (hainzl@agnld.uni-potsdam.de)

J. Zschau, GeoForschungsZentrum, Telegrafenberg, 14473 Potsdam, Germany. (zschau@gfz-potsdam.de)

(Received August 12, 1999; revised September 23, 1999; accepted December 22, 1999.)

# Appendix C

Observation of growing correlation length as an indicator for critical point behavior prior to large earthquakes

Autors:	G. Zöller, S. Hainzl, and J. Kurths
Journal:	<i>Journal of Geophysical Research,</i>
Volume (Nr.):	<b>106(B2)</b>
Pages:	2167-2176
Year:	2001

# Observation of growing correlation length as an indicator for critical point behavior prior to large earthquakes

Gert Zöller, Sebastian Hainzl, and Jürgen Kurths

Institute of Physics, University of Potsdam, Potsdam, Germany

**Abstract.** We test the critical point concept for earthquakes in terms of the spatial correlation length. A system near a critical point is associated with a diverging correlation length following a power law time-to-failure relation. We estimate the correlation length directly from an earthquake catalog using single-link cluster analysis. Therefore we assume that the distribution of moderate earthquakes reflects the state of the regional stress field. The parameters of the analysis are determined by an optimization procedure, and the results are tested against a Poisson process with realistic distributions of epicenters, magnitudes, and aftershocks. A systematic analysis of all earthquakes with  $M \geq 6.5$  in California since 1952 is conducted. In fact, we observe growing correlation lengths in most cases. The null hypothesis that this behavior can be found in random data is rejected with a confidence level of more than 99%. Furthermore, we find a scaling relation  $\log R \sim 0.7M$  ( $\log \langle \xi_{\max} \rangle \sim 0.5M$ ), between the mainshock magnitude  $M$  and the critical region  $R$  (the correlation length  $\langle \xi_{\max} \rangle$  before the mainshock), which is in good agreement with theoretical values.

## 1. Introduction

In the recent past, time-to-failure methods have become important for the quantitative description of seismicity prior to large earthquakes [Varnes, 1989; Sykes and Jaumé, 1990; Bufe and Varnes, 1993; Saleur *et al.*, 1996; Jaumé and Sykes, 1999; Main, 1999]. The main assumption in this approach is that an underlying critical point resulting from many-body interactions in the Earth's crust is responsible for the emergence of long-range interactions characterized by power laws. Using equations from crack propagation [Das and Scholz, 1981] and damage mechanics [Leckie and Hayhurst, 1977], Bufe and Varnes [1993] derived a formula for the cumulative seismic release  $\Sigma\Omega$ :

$$(\Sigma\Omega)(t) = A + B(t_f - t)^m. \quad (1)$$

Here,  $t_f$  is the failure time, the constant  $A$  is positive, the constant  $B$  is negative and the critical exponent  $m$  is constrained between 0 and 1.  $\Omega$  is a measure of the earthquake size that is related to the magnitude  $M$  by

$$\log \Omega = cM + d \quad (2)$$

with constants  $c$  and  $d$ . In other words, the region that

is preparing for a large earthquake is characterized by accelerated seismic release [Sykes and Jaumé, 1990].

As a measure of earthquake size, many seismologists use the cumulative Benioff strain, which is defined as the square root of the energy  $(\Sigma\Omega)(t) = \sum_{i=1}^{N(t)} \sqrt{E_i}$ . In a retrospective analysis, Bufe and Varnes [1993] showed that (1) provides good estimates for the time and the magnitude of the 1989 Loma Prieta earthquake in California. Bowman *et al.* [1998] presented a systematic analysis for California seismicity. They found that eight earthquakes with  $M \geq 6.5$  in their data set were preceded by accelerated seismicity with a confidence level of 99.6% and that the size of the critical region scales with the magnitude of the oncoming event according to  $\log R \sim 0.44M$ . Brehm and Braile [1998, 1999] used a refined time-to-failure analysis to predict mainshocks in the New Madrid Seismic Zone and in southern California. A review is given by Jaumé and Sykes [1999].

In terms of critical point behavior the acceleration of seismic release is the consequence of the growth of the spatial correlation length. In this view, a small rupture can only grow into a large earthquake if a critical value of the spatial correlation length is reached. In the preparatory process of a mainshock, long-range correlations are established by the redistribution of stress from smaller to larger scales. Thus, in a highly correlated stress field a small rupture can jump barriers and grow into a large earthquake, while the rupture process is halted earlier in a less correlated stress field. When

Copyright 2001 by the American Geophysical Union.

Paper number 2000JB900379.

0148-0227/01/2000JB900379\$09.00

criticality is reached, the system may remain near this state. Such behavior is known as self-organized criticality [Bak and Tang, 1989; Geller et al., 1997; Hainzl et al., 1999, 2000]. At the critical point the correlation length is only limited by the size of the physical system [Sammis and Smith, 1999]. The increase of the correlation length can be modeled using the renormalization group theory [Saleur et al., 1996], which also reproduces (1). Sornette and Sammis [1995] presented a model for a discrete hierarchical ordered fault network, which reproduces a power law increase of Benioff strain according to (1) with an additional term of (second-order) log-periodic fluctuations. Such log periodicity has been observed and documented in several cases [Sornette and Sammis, 1995; Varnes and Bufe, 1996].

This paper attempts to test directly for growing spatial correlation lengths prior to large earthquakes. This is an independent approach to detect critical point behavior in observed seismicity. In contrast to the Benioff strain, which can be easily calculated from an earthquake catalog, it is not straightforward to calculate the correlation length. Therefore we assume that the distribution of moderate earthquakes reflects the actual state of the regional stress field. This view is justified by the fact that in a stress field, which is correlated over a large region, earthquake triggering over long distances is likely to occur. In particular, earthquakes are initiated preferably at the ends of a crack. If the stress changes at one end and friction is negligible, the stress is directly transferred to the other end. Far from a critical point, small cracks are distributed randomly, and thus the distribution of epicenters is approximately random. Near the critical point, the emergence of longer cracks makes longer stress transfers possible. Hence it is reasonable to assume that the epicenter distribution changes when the critical point is approached. In this view, the correlation length can be considered as a characteristic distance, or cluster size, of events in a certain time interval. A powerful method to extract “natural” distances from earthquake catalogs, is single-link cluster analysis (hereinafter referred to as SLC) introduced by Frohlich and Davis [1990].

For the calculation of the correlation length as a function of the time a space window has to be specified. Zöller et al. [1998] showed that the dynamics of spatially extended complex systems is most clearly observable on intermediate spatial scales between the noisy microscales and the large scales that include uncorrelated regions. Thus we optimize the space window in order to provide the best observation of growing correlation length. Using synthetic catalogs, the probability that the results come from spurious patterns generated by the procedure itself can be estimated. With regard to the optimization procedure mentioned above, it is clear that these synthetic data play an important role. The use of catalogs with uniformly distributed epicenters and random occurrence times, for instance, is not appropriate for this purpose because the inhomoge-

nously distributed epicenters as well as the aftershock activity in the original catalog may result in an erroneous rejection of the null hypothesis. In our study, we construct a significance test based on a Poisson process model for seismicity that accounts for the distributions of epicenters, magnitudes, and aftershocks in the genuine data.

This paper is organized in the following way: In section 2 the data and the method to test the hypothesis of growing correlation length are described in detail. The results of the data analysis are presented in section 3 and discussed in section 4. Finally, the conclusions are given in section 5.

## 2. Data and Method

In this work, we analyze the seismicity in California between 32° N and 40° N latitude. The data are taken from the Council of the National Seismic System (CNSS) Worldwide Earthquake Catalog (available via the Internet (<http://quake.geo.berkeley.edu/cnss>)). The catalog covers the time span from 1910 to the present. The distribution of earthquakes is shown in Figure 1. To account for completeness of the data, we restrict the analysis to nine mainshocks with  $M \geq 6.5$  since 1952 (see Figure 1).

The test on growing correlation lengths can be decomposed in three parts, which are described in sections 2.1–2.3.

### 2.1. Correlation Length

If a system approaches a critical point, the correlation length  $\xi$  is expected to grow according to a power law [Bruce and Wallace, 1989]:

$$\xi(t) \sim (t_f - t)^{-k}, \quad (3)$$

where  $k$  is positive. Assuming a scaling relation  $E \sim \xi^n$ , (3) leads also to (1) for the cumulative Benioff strain.

The correlation length  $\xi$  is estimated using a specified version of SLC analysis, which is described in detail by Frohlich and Davis [1990]. For that, we consider a distribution of  $N$  earthquakes. Each individual event is linked with its nearest neighbor event in space to form a set of small clusters. In the next step, each cluster is linked with its nearest neighbor cluster. This process is repeated, recursively, until the  $N$  events are connected with  $N - 1$  links. The probability density function  $\rho(s)$  gives the probability that a link length is smaller than or equal to  $s$ . We define the correlation length  $\xi$  by the condition  $\rho(\xi) = 0.5$ .

The time evolution of the spatial correlation length is calculated in the following way (see Figure 2): The space window is a circular region around the mainshock epicenter (Figure 2a); the time interval, which begins with the first event in the catalog (1910) and ends with the mainshock occurrence time  $t_f$ , is divided into overlapping time bins  $[t_{i-1}; t_i]$ . Therefore we use a sliding

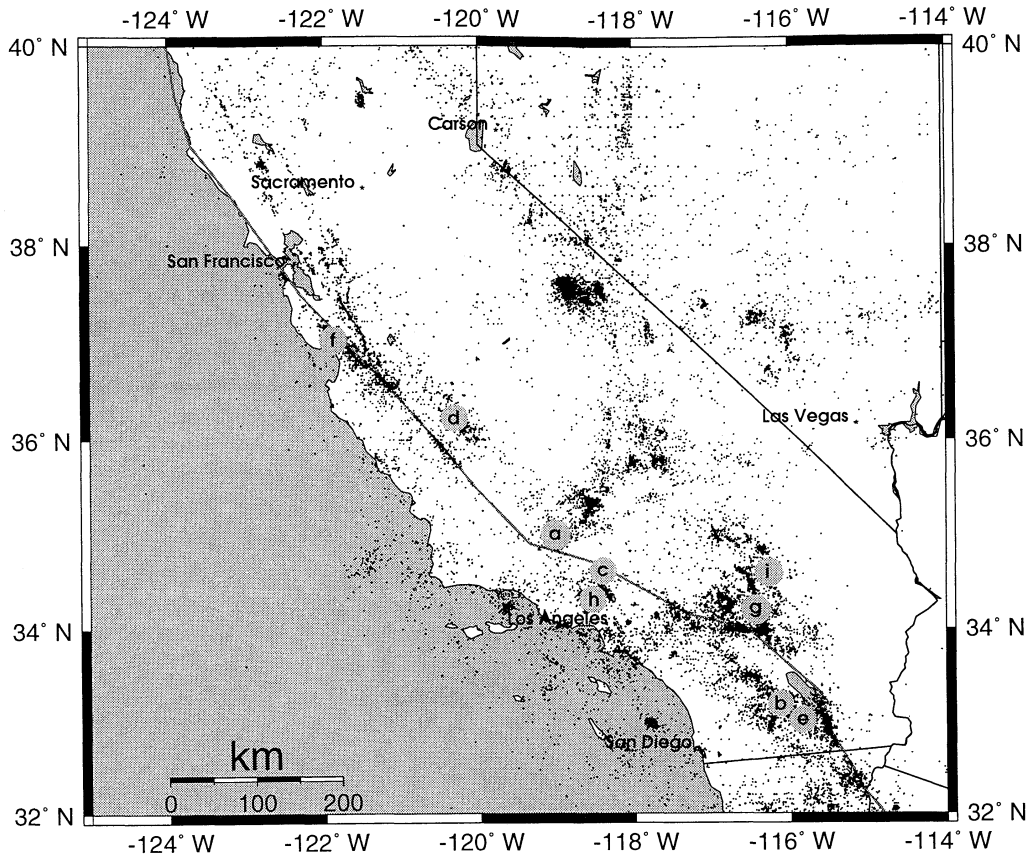


**Figure 1.** Earthquakes with  $M \geq 3.0$  in California since 1910. Solid circles denote the events with  $M \geq 6.5$  since 1952: circle a, 1952  $M = 7.5$  Kern County; circle b, 1968  $M = 6.5$  Borrego Mountain; circle c, 1971  $M = 6.6$  San Fernando; circle d, 1983  $M = 6.7$  Coalinga; circle e, 1987  $M = 6.6$  Superstition Hills; circle f, 1989  $M = 7.0$  Loma Prieta; circle g, 1992  $M = 7.3$  Landers; circle h, 1994  $M = 6.6$  Northridge; and circle i, 1999  $M = 7.1$  Hector Mine.

window which moves with a step  $\Delta t$ , corresponding to four events. Because of statistical reasons, we do not fix the length of the time bins, rather we use bins that contain the same number of events. In this study, each value  $\xi(t_i)$  is based on 20 events (Figure 2b). However, we find that the results are relatively robust if this number is changed.

## 2.2. Power Law Fit

From the procedure described in section 2.1, the correlation length  $\xi(t)$  is obtained for a fixed value of  $R$ . In order to test the critical point concept we fit relation (3) to this function in the time interval  $[t_0; t_f]$ , where  $t_0$  is a free parameter (see Figure 2c). The underlying assumption is that the growth of the correlation length is only observable in the last time interval, where the signal exceeds the noisy background.

Altogether, we have to fix three parameters: The radius  $R$ , which defines the space window for the calculation of  $\xi(t)$  (see section 2.1), and the time  $t_0$  and the critical exponent  $k$ , which determine the power law fit. Following *Bowman et al.* [1998], we use an optimization

technique, where a curvature parameter  $\mathcal{C}$  measures the degree of acceleration:

$$\mathcal{C} = \frac{\text{power law fit root-mean-square error}}{\text{constant fit root-mean-square error}}. \quad (4)$$

When the correlation length  $\xi(t)$  can be fit by a power law,  $\mathcal{C}$  will be small. Conversely, if no acceleration takes place, the values of  $\xi(t)$  will scatter around a constant and consequently  $\mathcal{C}$  is close to 1. For each mainshock we determine those values of  $t_0$ ,  $k$ , and  $R$ , which provide the smallest curvature parameter  $\mathcal{C}$ . The critical exponent  $k$  is constrained between 0.01 and 1.

## 2.3. Significance Test

We have to test the significance of our results because the growth of the correlation length according to the power law (3) might occur by chance in a random data set. Such a random pattern would be detected by the optimization procedure described above. In this context, it is also important to note that the correlation length  $\xi$  is more sensitive to fluctuations in the data than a cumulative quantity, e.g., the cumulative Be-

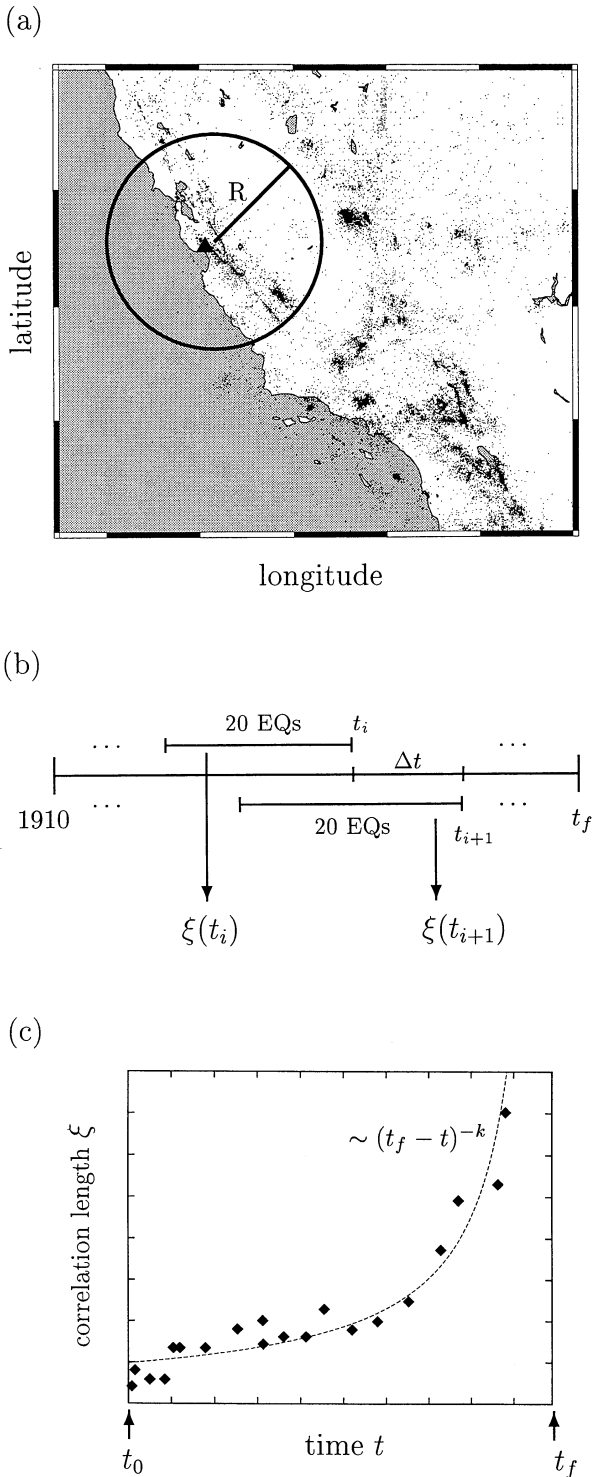


**Figure 2.** Sketch of data analysis: (a) The space window for calculation of  $\xi$ . It is a circular region with radius  $R$  around the mainshock epicenter (solid triangle). (b) Definition of time bins. A sliding window that contains 20 earthquakes moves with a step  $\Delta t$ , corresponding to four earthquakes. In each time bin, single-link cluster analysis is applied to calculate the spatial correlation length  $\xi(t_i)$ . (c) Power law fit. The function  $\xi(t_i)$  (denoted as solid diamonds) is fit by a power law  $(t_f - t)^{-k}$  in a time interval  $[t_0; t_f]$ . The free parameters  $R$ ,  $k$ , and  $t_0$  are optimized in order to provide the best power law fit.

nioff strain, where fluctuations are smoothed out. An example for such a fluctuation is the occurrence of aftershock sequences from a previous mainshock. The petering out of an aftershock sequence leads also to an increase of the correlation length and can thus be interpreted erroneously as a critical point phenomenon.

We want to emphasize that we cannot decide whether an observed increase of the correlation length in a special case comes from an underlying critical point process or is due to a random fluctuation or a pattern coming from a different process, e.g., an aftershock sequence. Rather we can say with what probability the latter possibility can be ruled out if we apply the entire procedure to synthetic data that can also produce such patterns.

To calculate appropriate synthetic catalogs, we proceed in the following way:

1. The CNSS catalog is declustered using the algorithm of *Reasenber* [1985].
2. Random epicenters are calculated so that the epicenter distribution of the declustered CNSS catalog is fit.
3. The earthquake occurrence times are drawn from a Poisson process.
4. The earthquake magnitudes are taken randomly from a probability distribution fulfilling the *Gutenberg and Richter* [1956] law.
5. Aftershocks according to the *Omori* [1894] law are added using the algorithm of *Reasenber* [1985] in inverse direction.

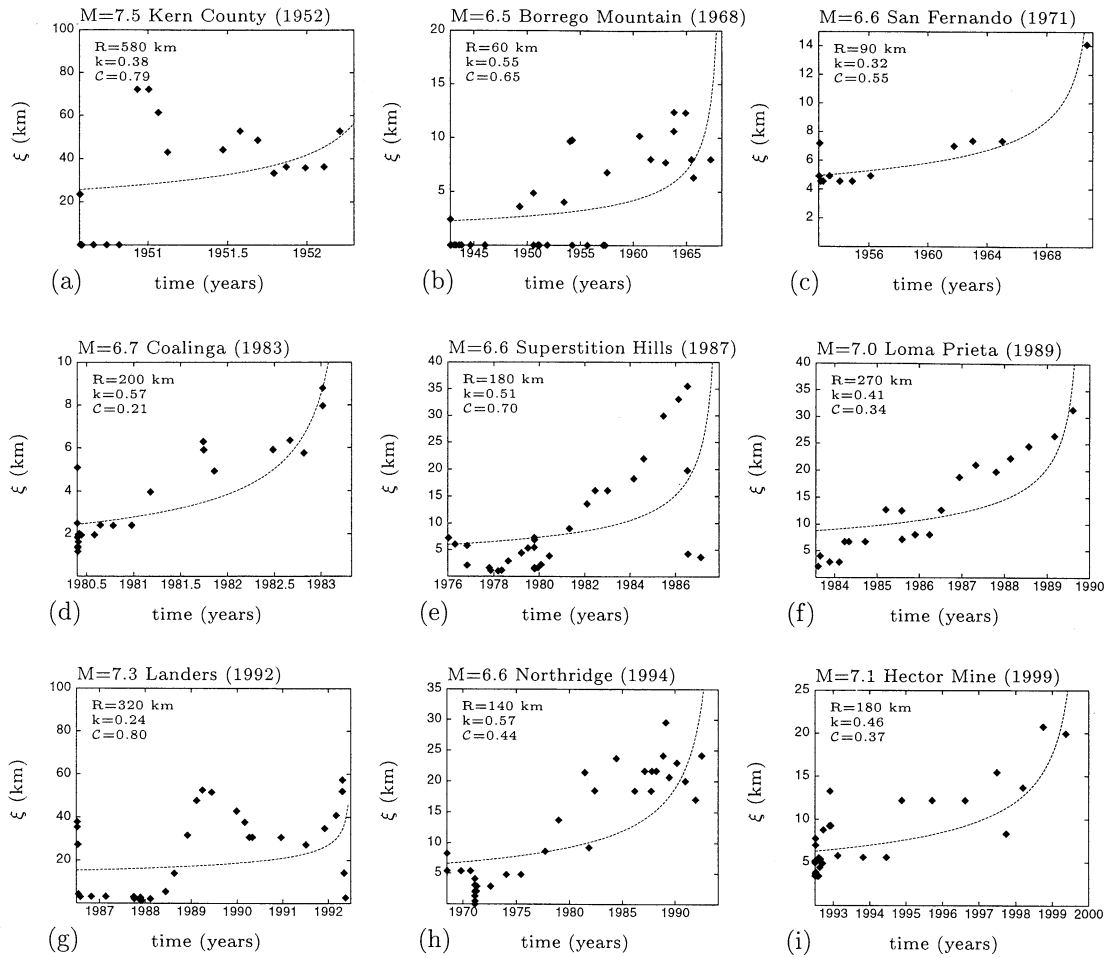
Items 3 and 4 define the well-known stochastic earthquake model proposed by *Epstein and Lomnitz* [1966]. The resulting synthetic earthquake catalog corresponds to a Poisson process in time with additional aftershock activity. The distributions of epicenters and magnitudes are similar to those of the genuine catalog.

To estimate the statistical significance of a curvature parameter  $C$ , calculated for a mainshock with magnitude  $M$  in the CNSS catalog, we first generate 1000 synthetic catalogs. In each catalog we pick up an event with magnitude  $M$  and apply the optimization procedure. From the resulting 1000 values of  $C$  we finally compute the probability that a curvature parameter smaller than or equal to a certain value of  $C$  can be found in a synthetic catalog.

### 3. Data Analysis

The technique presented in section 2 is now applied to the California earthquake catalog. To account for artificial seismicity variations, we have to introduce a lower magnitude cutoff. In previous studies the acceleration process has been found to be most obvious for earthquakes with magnitudes within about two units of the mainshock magnitude [*Jaumé and Sykes*, 1999; *Knopoff et al.*, 1996]. However, because the data analysis requires a minimum number of earthquakes, we use the lower value  $M_{\text{cut}} = 4.0$ . To evaluate the stability of the results with respect to  $M_{\text{cut}}$ , we have repeated the calculations with  $M_{\text{cut}} = 3.5$  and found no qualitative difference in the results.





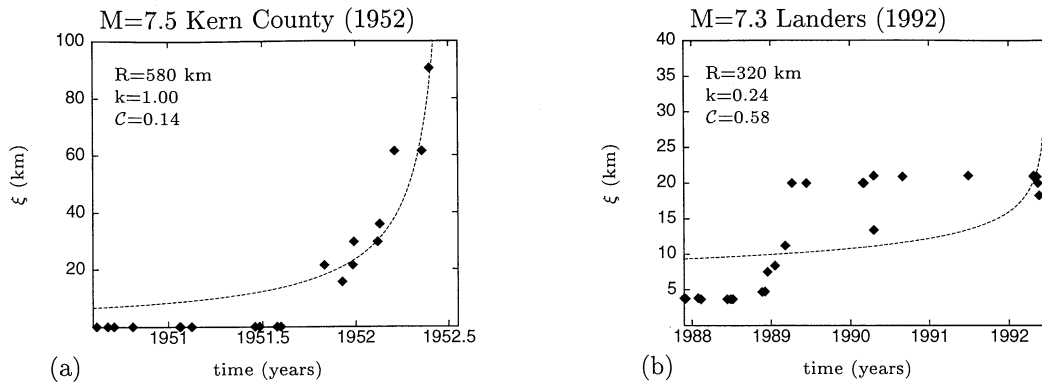
**Figure 3.** Correlation length  $\xi$  (solid diamonds) as a function of the time  $t$  for the nine mainshocks in Figure 1 and corresponding power law fits (see section 2.2). The time range is given by the interval  $[t_0; t_f]$  (see Figure 2).

Figure 3 shows the correlation length  $\xi(t)$  for the nine earthquakes with  $M \geq 6.5$  since 1952, calculated with the optimized parameters, and the power law fit corresponding to (3). Note that for all fits,  $t_f$  is fixed by the occurrence time of the mainshock.

In general, the correlation length grows when the system approaches the mainshock occurrence time. An exception is the 1952 Kern County earthquake. The 1983 Coalinga earthquake shows the best example for a power law increase, spanning the last three years before the event occurs. In two cases (Figures 3e and 3g) a sudden decrease of  $\xi$  is observed before the mainshock occurs. This is due to aftershock sequences of other mainshocks in the space window, for example, in the Landers case (Figures 3g) the signal of increasing  $\xi$  is disturbed by the aftershocks of the  $M = 6.1$  Joshua Tree earthquake on April 23, 1992, which occurred close to the epicenter of the Landers earthquake. Furthermore, it is striking that the two strongest earthquakes, the Kern County earthquake and the Landers earthquake, do not show critical point behavior in terms of a

low curvature value. A possible explanation for this is the influence of the smaller earthquakes ( $4 \leq M \leq 5$ ). This can be tested by increasing the magnitude cutoff toward  $M_{\text{cut}} = 4.5$  instead of  $M_{\text{cut}} = 4.0$ . Because the number of data points decreases with  $M_{\text{cut}} = 4.5$ , we use now a time step  $\Delta t$  for the sliding window corresponding to one event. The result is shown in Figure 4 for the same parameters as in Figure 3. Now, the points for the Kern County earthquake can be fit very well by a power law, and the quality of the fit for the Landers event is clearly improved.

Next, we calculate the probability that the curvature parameter  $C$ , which is observed for a mainshock with magnitude  $M$  in the original catalog, can be found in a random catalog (see section 2.3). Figure 5 shows the cumulative probability distribution  $p(C)$  for 1000 earthquakes with  $M = 7.0$ , each drawn from a random catalog. The resulting probability for the 1989 Loma Prieta earthquake (see Figure 3f) from the CNSS catalog is  $p = 8.2\%$ . For this example the null hypothesis that the power law increase of the correlation length occurs



**Figure 4.** The value of  $\xi(t)$  calculated with the magnitude cutoff  $M_{\text{cut}} = 4.5$  for (a) the Kern County earthquake and (b) the Landers earthquake.

by chance can be rejected with 91.8% confidence level. The results for all mainshocks are summarized in Table 1. The nine values of  $p$  scatter around the mean value  $\bar{p} = 0.264$ . The significance of this result can be evaluated by a comparison with the distribution of the mean value of nine random numbers in the unit interval. It can easily be shown that this mean value is Gaussian distributed around 0.5 with the standard deviation  $\sigma = 1/\sqrt{9 \times 12}$ . The probability for nine random numbers in the interval  $[0; 1]$  to have a mean value smaller than or equal to  $\bar{p} = 0.264$  is  $P = 0.7\%$ . Thus the null hypothesis that the observed patterns can occur in a random catalog can be rejected with 99.3% confidence level.

#### 4. Discussion

In our data analysis we have determined three parameters using an optimization technique. We want to discuss now to what extent these parameter values can be understood in terms of seismology.

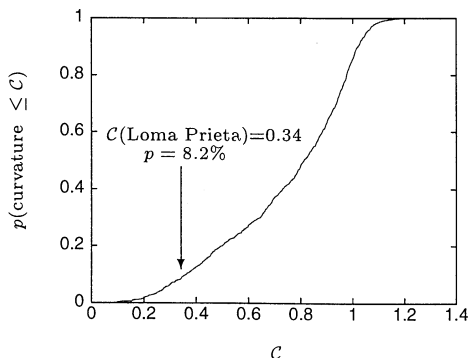


**Figure 5.** Probability distribution to find a curvature parameter smaller than or equal to  $C$  in a random earthquake catalog based on 1000 events with  $M = 7.0$ , each drawn from such a synthetic catalog. The value calculated for the  $M = 7.0$  Loma Prieta earthquake corresponds to a probability of  $p = 8.2\%$ .

#### 4.1. Critical Region $R$ and Correlation Length Before the Mainshock $\langle \xi_{\text{max}} \rangle$

One of the most important quantities is the radius of the critical region  $R$ . In our study, we observe a critical region versus magnitude relation, which is shown in Figure 6a. The results can be fit pretty good using the relation  $\log R \sim (0.70 \pm 0.15)M$ , which is denoted as a straight line in the plot. Following the arguments of *Bowman et al.* [1998], we conclude that this scaling relation is consistent with

$$E \sim R^{2.1 \pm 0.45}, \quad (5)$$

if  $\log E \sim 1.5M$  [*Kanamori and Anderson, 1975*] is assumed. Note that  $E \sim R^2$ , which translates to  $\log R \sim 0.75M$ , is expected for large earthquakes ( $M \geq 6$ ) because the crust ruptures over its entire thickness and energy is released predominantly in two directions. In contrast, a small earthquake corresponds to a three-dimensional rupture ( $E \sim R^3$  or  $\log R \sim 0.5M$ ). Although our result for this relation is based only on a small magnitude band, it agrees fairly well with theoretical findings.

Next, we study the correlation length  $\xi$  before the mainshock. Because  $\xi(t)$  diverges at the time of the mainshock  $t = t_f$  in (3), we define a quantity  $\langle \xi_{\text{max}} \rangle$  as the mean value of  $\xi$  over 2 years before the mainshock occurs. This quantity is plotted versus the mainshock magnitude in Figure 6b. The data points can be fit by the relation  $\log \langle \xi_{\text{max}} \rangle \sim (0.50 \pm 0.20)M$ , which is also close to the above mentioned theoretical value.

Our findings are also comparable with the empirical relations  $\log R \sim 0.43M$  used by *Keilis-Borok and Kossobokov* [1990] for their pattern recognition technique and  $\log L \sim 0.7M$  between the magnitude and the length of the surface rupture [*Lowrie, 1997*].

#### 4.2. Exponent $k$ and Time $t_0$

The critical exponent  $k$  is found to scatter between the extreme values  $k_{\text{min}} = 0.24$  and  $k_{\text{max}} = 0.57$  (see

**Table 1.** Earthquakes With  $M \geq 6.5$  in California Since 1952 and Results of the Critical Point Analysis<sup>a</sup>

Earthquake	Date	$M$	$R$ , km	$k$	$\mathcal{C}$	$p$	
a	Kern County	July 21, 1952	7.5	580	0.38(1.00)	0.79(0.14)	0.472(0.009)
b	Borrego Mountain	April 9, 1968	6.5	60	0.55	0.65	0.349
c	San Fernando	Feb. 9, 1971	6.6	90	0.32	0.55	0.283
d	Coalinga	May 2, 1983	6.7	200	0.57	0.21	0.029
e	Superstition Hills	Nov. 24, 1987	6.6	180	0.51	0.70	0.395
f	Loma Prieta	Oct. 18, 1989	7.0	270	0.41	0.34	0.082
g	Landers	June 28, 1992	7.3	320	0.24(0.24)	0.80(0.58)	0.480(0.248)
h	Northridge	Jan. 17, 1994	6.6	140	0.57	0.44	0.185
i	Hector Mine	Oct. 16, 1999	7.1	180	0.46	0.37	0.105

<sup>a</sup> $R$  is the space window and  $k$  is the critical exponent (3) (see Figure 2);  $\mathcal{C}$  is the curvature parameter in (4), and  $p$  is the probability that a curvature smaller than or equal to  $\mathcal{C}$  can be found in a random catalog (see section 2.3). The values in the parentheses refer to the calculation with  $M_{\text{cut}} = 4.5$  (see Figure 4).

Table 1) with the average  $\bar{k} = 0.45$ . From a theoretical point of view, *Rundle et al.* [1996] have suggested a scaling exponent of  $k = 0.25$  for the correlation length, which is observed in three cases, approximately. However, because of the sparse data, predictions of the scaling exponent  $k$  from our procedure are rather speculative.

We find no reasonable correlation between the fitting parameter  $t_0$ , which defines the duration of the precursory process, and the mainshock magnitude. Physically, one would expect a longer duration of accelerated seismicity for larger mainshocks because large earthquakes require more energy. Nevertheless, the results in Figure 3 suggest that there might be a correlation of  $t_0$  with the occurrence times of aftershock sequences from a previous mainshock. This can be identified by small values for the correlation length and a large number of earthquakes in this time.

Although it is likely that the parameter  $t_0$  is influenced by aftershocks, the significance test described in section 2.3 suggests with a high confidence level (see last column in Table 1) that the observed patterns itself are not a consequence of previous aftershocks. This is also

supported by the observation that the duration of the detected acceleration is much longer than typical durations of aftershock sequences. Such problems typically arise when noisy functions are analyzed: The signal (increasing correlation length) is perturbed (aftershocks), and the end of the perturbation is considered as the onset of the signal. Therefore the optimization technique should be improved in the future.

#### 4.3. Comparison With Accelerated Moment Release Models

Is there a relation between the present results and the results of methods based on accelerated moment release? Both approaches are different viewpoints of the same assumption, namely, that large earthquakes are related to a critical point process in the Earth's crust. We have studied variations in the epicenter distribution, while the accelerated moment release models consider variation with respect to the energy release. Consequently, these models emphasize the largest earthquakes, whereas in our analysis the intermediate earthquakes with  $4 \leq M \leq 5$  are more important because they occur more frequently. Therefore it is not

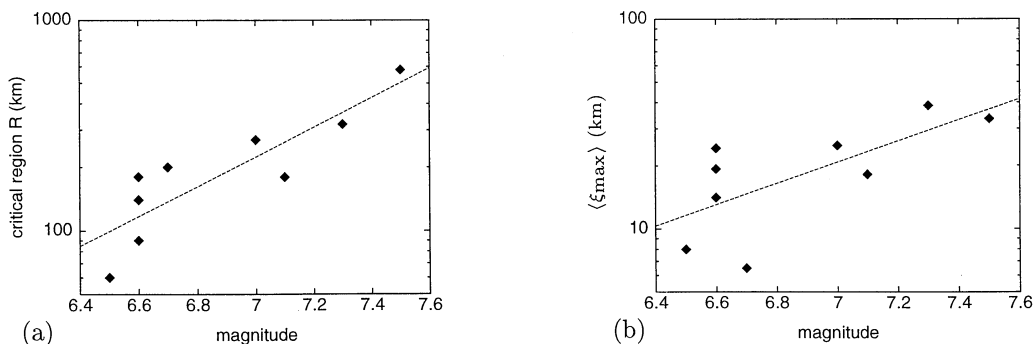


**Figure 6.** (a) Radius  $R$  of the critical region as a function of the mainshock magnitude for the earthquakes in Table 1. (b) Correlation length  $\langle \xi_{\text{max}} \rangle$  averaged over 2 years before the mainshock. The straight line is a fit to the data with the slope 0.70 in Figure 6a and 0.50 in Figure 6b.

surprising that in both cases the detected patterns are observed for different parameter values. As an example, the space windows in the present study are on average larger than those in the analysis of *Bowman et al.* [1998]. Consequently, we mostly cannot observe both features simultaneously in the same space window.

However, we can compare the scaling relations reported in section 4.1 with the findings from accelerated moment release models. *Bowman et al.* [1998] find that the radius  $R$  is related to the mainshock magnitude  $M$  according to  $\log R \sim 0.44M$ , while *Brehm and Braile* [1998] suggest that  $\log R \sim 0.75M$ , which is close to our result for  $R$ . Plotting the results of *Bowman et al.* [1998] and *Brehm and Braile* [1998] together, *Jaumé and Sykes* [1999] find  $\log R \sim 0.36M$ . On average, our results are very close to those of the accelerated moment release models, although they are based on a completely different technique.

In summary, it is an important result that two different features of the same process are observable with high statistical significance. Both results together support the hypothesis of an underlying critical point.

## 5. Conclusions

In our study, we have tested the critical point concept for earthquakes in terms of growing spatial correlation length. The data analysis was designed in order to conduct a systematic investigation of an earthquake catalog. In principle, the same procedure can be applied to any other catalog that is homogeneous over several years. A main ingredient of the method is the determination of free parameters, using an optimization technique. This leads apparently to large uncertainties, especially when three parameters are optimized simultaneously. Thus we have combined this procedure with an appropriate significance test using synthetic data of high quality.

Our main finding is the observation of growing correlation length before several large earthquakes, which strongly supports the hypothesis that earthquakes are a critical point phenomenon. It is important that this precursory phenomenon cannot be reproduced using random catalogs with realistic distributions of epicenters, magnitudes, and aftershocks. The confidence level that the observed patterns are not a consequence of random fluctuations is found to be above 99%. Furthermore, both the critical region and the correlation length before the mainshock show a reasonable scaling with respect to the mainshock magnitude.

In a future work, the predictive power of growing correlation length should be tested. Therefore  $t_f$  will become a new fitting parameter, and the question whether  $t_0$  and  $k$  can be fixed by empirical values has to be addressed. A grid search technique can be applied to extract regions of growing correlation length systematically from a data set. The occurrence time of the expected mainshock is then related to the new fitting

parameter  $t_f$ , and the estimates for the epicenter and the magnitude are obtained from the critical region and the correlation length before the mainshock. For a further reduction of uncertainties in a predictive approach it also appears promising to combine the concepts of growing correlation length and accelerated moment release.

**Acknowledgments.** We are grateful to Frank Scherbaum for stimulating discussions on synthetic earthquake catalogs. The comments of Yaolin Shi, an anonymous reviewer, and an anonymous Associate Editor helped to improve the quality of the manuscript significantly. The earthquake data used in this study have been provided by the Northern California Earthquake Data Center (NCEDC) and include contributions of the member networks of the Council of the National Seismic System (CNSS). To produce Figures 1 and 2, we used the GMT system [*Wessel and Smith*, 1991]. This work was supported by the Deutsche Forschungsgemeinschaft (Sonderforschungsbereich 555 "Komplexe Nicht-lineare Prozesse") and the state Brandenburg (Hochschulsonderprogramm III 1.6).

## References

- Bak, P., and C. Tang, Earthquakes as a self-organized critical phenomenon, *J. Geophys. Res.*, *94*, 15,635–15,637, 1989.
- Bowman, D. D., G. Oullion, C. G. Sammis, A. Sornette, and D. Sornette, An observational test of the critical earthquake concept, *J. Geophys. Res.*, *103*, 24,359–24,372, 1998.
- Brehm, D. J., and L. W. Braile, Intermediate-term earthquake prediction using precursory events in the New Madrid Seismic Zone, *Bull. Seismol. Soc. Am.*, *88*, 564–580, 1998.
- Brehm, D. J., and L. W. Braile, Intermediate-term earthquake prediction using the modified time-to-failure method in southern California, *Bull. Seismol. Soc. Am.*, *89*, 275–293, 1999.
- Bruce, A., and D. Wallace, Critical point phenomena: Universal physics at large length scales, in *The New Physics*, edited by P. Davis, pp. 236–267, Cambridge Univ. Press, New York, 1989.
- Bufe, C. G., and D. J. Varnes, Predictive modeling of the seismic cycle of the greater San Francisco Bay region, *J. Geophys. Res.*, *98*, 9871–9883, 1993.
- Das, S., and C. H. Scholz, Theory of time-dependent rupture in the Earth, *J. Geophys. Res.*, *86*, 6039–6051, 1981.
- Epstein, B., and C. Lomnitz, A model for the occurrence of large earthquakes, *Nature*, *211*, 954–956, 1966.
- Frohlich, C., and S. D. Davis, Single-link cluster analysis as a method to evaluate spatial and temporal properties of earthquake catalogues, *Geophys. J. Int.*, *100*, 19–32, 1990.
- Geller, R. J., D. D. Jackson, Y. Y. Kagan, and F. Mulargia, Earthquakes cannot be predicted, *Science*, *275*, 1616–1617, 1997.
- Gutenberg, B., and C. F. Richter, Earthquake magnitude, intensity, energy and acceleration, *Bull. Seismol. Soc. Am.*, *46*, 105–145, 1956.
- Hainzl, S., G. Zöller, and J. Kurths, Similar power laws for foreshock and aftershock sequences in a spring-block model for earthquakes, *J. Geophys. Res.*, *104*, 7243–7253, 1999.
- Hainzl, S., G. Zöller, and J. Kurths, Seismic quiescence as an indicator for large earthquakes in a system of self-organized criticality, *Geophys. Res. Lett.*, *27*, 597–600, 2000.

- Jaumé, S. C., and L. R. Sykes, Evolving towards a critical point: A review of accelerating seismic moment/energy release prior to large and great earthquakes, *Pure Appl. Geophys.*, *155*, 279–306, 1999.
- Kanamori, H., and D. L. Anderson, Theoretical basis of some empirical relations in seismology, *Bull. Seismol. Soc. Am.*, *65*, 1073–1095, 1975.
- Keilis-Borok, V. I., and V. G. Kossobokov, Premonitory activation of earthquake flow: algorithm M8, *Phys. Earth Planet. Inter.*, *61*, 73–83, 1990.
- Knopoff, L., T. Levshina, V. I. Keilis-Borok, and C. Mattoni, Increased long-range intermediate-magnitude earthquake activity prior to strong earthquakes in California, *J. Geophys. Res.*, *101*, 5779–5796, 1996.
- Leckie, F. A., and D. R. Hayhurst, Constitutive equations for creep rupture, *Acta Metall.*, *25*, 1059–1070, 1977.
- Lowrie, W., *Fundamentals of Geophysics*, 122 pp., Cambridge Univ. Press, New York, 1997.
- Main, I. G., Applicability of time-to-failure analysis to accelerated strain before earthquakes and volcanic eruptions, *Geophys. J. Int.*, *139*, F1–F6, 1999.
- Omori, F., On the aftershocks of earthquakes, *J. Coll. Sci. Imp. Univ. Tokyo*, *7*, 111–200, 1894.
- Reasenber, P. A., Second-order moment of central California seismicity, *J. Geophys. Res.*, *90*, 5479–5495, 1985.
- Rundle, J. B., W. Klein, and S. Gross, Dynamics of a traveling density wave model for earthquakes, *Phys. Rev. Lett.*, *76*, 4285–4288, 1996.
- Saleur, H., C. G. Sammis, and D. Sornette, Discrete scale invariance, complex fractal dimensions, and log-periodic fluctuations in seismicity, *J. Geophys. Res.*, *101*, 17,661–17,677, 1996.
- Sammis, C. G., and S. W. Smith, Seismic cycles and evolution of stress correlation in cellular automaton models of finite fault networks, *Pure Appl. Geophys.*, *155*, 307–334, 1999.
- Sornette, D., and C. G. Sammis, Complex critical exponents from renormalization theory group of earthquakes: implications for earthquake predictions, *J. Phys. I*, *5*, 607–619, 1995.
- Sykes, L. R., and S. C. Jaumé, Seismic activity on neighboring faults as a long-term precursor to large earthquakes in the San Francisco Bay area, *Nature*, *348*, 595–599, 1990.
- Varnes, D. J., Predicting earthquakes by analyzing accelerating precursory seismic activity, *Pure Appl. Geophys.*, *130*, 661–686, 1989.
- Varnes, D. J., and C. G. Bufe, The cyclic and fractal seismic series preceding an  $M_b = 4.8$  earthquake on 1980 February 14 near the Virgin Islands, *Geophys. J. Int.*, *124*, 149–158, 1996.
- Wessel, P., and W. H. F. Smith, Free software helps map and display data, *Eos Trans. AGU*, *72*, 441, 445–446, 1991.
- Zöller, G., R. Engbert, S. Hainzl, and J. Kurths, Testing for unstable periodic orbits to characterize spatiotemporal dynamics, *Chaos Solitons Fractals*, *9*, 1429–1438, 1998.

---

S. Hainzl, J. Kurths, and G. Zöller, Institute of Physics, University of Potsdam, Am Neuen Palais, D-14469 Potsdam, Germany. (gert@agnld.uni-potsdam.de)

(Received February 25, 2000; revised July 5, 2000; accepted October 4, 2000.)

# Appendix D

The role of disorder and stress concentration in nonconservative fault systems

Autors:	S. Hainzl, and G. Zöller
Journal:	<i>Physica A</i> ,
Volume (Nr.):	<b>294(1-2)</b>
Pages:	67-84
Year:	2001



ELSEVIER

Physica A 294 (2001) 67–84

PHYSICA A

www.elsevier.com/locate/physa

# The role of disorder and stress concentration in nonconservative fault systems

S. Hainzl<sup>a,b,\*</sup>, G. Zöller<sup>b</sup>

<sup>a</sup> *Institute of Earth Sciences, University of Potsdam, Germany*

<sup>b</sup> *Institute of Physics, University of Potsdam, POB 601553, 14415 Potsdam, Germany*

Received 20 September 2000

---

## Abstract

The aim of this paper is to understand the origin of the deviations from the Gutenberg–Richter law observed for individual earthquake faults. The Gutenberg–Richter law can be reproduced by slider-block fault models showing in its quasi-static limit self-organized criticality. However, in this model limit the earthquake ruptures are described by propagating narrow slip pulses leading to unrealistic low stress concentrations at the rupture front. To overcome such unrealistic rupture behavior, we introduce a new state-dependent stress distribution rule accounting for broader slip pulses up to crack-like behavior. Our systematic analysis of the generalized model shows that the earthquake characteristics can be described in terms of critical point behavior, resulting in subcritical, critical, and supercritical system states. We can explain the realized state of self-organized systems by the effect of individual ruptures on the stress field. This effect depends strongly on the fault roughness. For spatially smooth systems, more realistic rupture characteristics lead to supercritical behavior, equivalent to characteristic earthquake distributions empirically observed for several individual faults. For rough faults, earthquakes cannot rupture the whole system and seismic energy is released by small events only. The transition between both regimes occurs at an intermediate degree of heterogeneity, where the earthquake activity is reminiscent of self-organized criticality. Thus, our results predict that for individual faults one should in general observe systematic deviations from the Gutenberg–Richter law for large earthquake sizes. © 2001 Elsevier Science B.V. All rights reserved.

*PACS:* 64.60.L; 61.43.–j; 91.30.–f

*Keywords:* Rupture characteristics; Surface roughness; Earthquake modeling

---

\* Corresponding author. Tel.: +49-331-977-1175; fax: +49-331-977-1142.  
*E-mail address:* hainzl@agnld.uni-potsdam.de (S. Hainzl).

## 1. Introduction

The dynamics of earthquakes has attracted much attention as a real-world example for a self-organized critical phenomenon. The hallmarks of systems exhibiting self-organized criticality (SOC) are spatial and temporal correlation functions with power law behavior [1,2]. In fact, the most conspicuous statistical feature of earthquakes is the Gutenberg–Richter law [3], which is equivalent to a power-law for the number of observed earthquakes with rupture areas greater than  $S$  [4]

$$N \sim S^{-b}. \quad (1.1)$$

The recorded exponents  $b$  vary between 0.8 and 1.2 for different fault systems [5]. In detailed studies of several individual faults [6,7], however, deviations from this power law behavior have been observed supporting a weak characteristic earthquake model in which the number of large events is greater than would be predicted by extrapolating from the power-law distribution of small and intermediate earthquakes. Further investigations of the geometrical complexity lead to the suggestion that smoother faults are more likely to have such characteristic earthquake distributions [7].

Burridge and Knopoff [8] (BK) proposed a model useful in understanding the scaling of the frequency-size distribution. The BK model consists of a system of blocks sliding on a frictional surface, where each block is coupled by springs to the adjacent blocks and to a moving tectonic plate. In the quasi-static limit, i.e., if instantaneous block slips are assumed, this model is equivalent to a class of non-conservative cellular automaton models with nearest-neighbor interactions [9–13]. Because these cellular automata require relative little computation time, simulations of large system sizes and long earthquake catalogs can be used to study a variety of seismic phenomena, including scaling relations, correlations, and prediction. These model systems show SOC; that is, they evolve independently of initial conditions into a statistically stationary state which is characterized by the Gutenberg–Richter law, where the exponent  $b$  in Eq. (1.1) depends on the degree of conservation [11–13]. Assuming some degree of dissipation, the empirical observed  $b$ -values can be reproduced. Furthermore, if retarded stress transfers modeling empirically observed transient creep are additionally introduced, these models are able to reproduce also the spatio-temporal clustering of earthquakes, especially foreshocks and aftershocks according to the Omori law as well as earthquake swarms and periods of precursory seismic quiescence [14–17]. Thus models of this type seem to bear a strong resemblance to the actual dynamical process involved in earthquake faults.

However, in these models representing the BK-model in its quasi-static limit instantaneous slip and healing of material strength is assumed. Therefore earthquake ruptures are described by propagating slip pulses with a width of one block only (hereinafter referred to as  $\delta$ -type slip pulses). Although there is some observational evidence that active slip was restricted to a narrow propagating band for several earthquakes [18],  $\delta$ -type slip pulses are obviously an oversimplification. The contrary end-member model is a crack-like rupture propagation assuming that no healing of the frictional resistance



takes place during the evolution of the rupture. In this case the slip duration within the rupture area is longer than the rupture rise time. Analyzing ruptures in a continuum model with a rate and state friction law, Nielsen et al. [19] observe a smooth crossover from narrow, self-healing slip pulses to crack-like solutions in dependence on the parameters of the friction law. However, because the frictional behavior of earthquakes is almost unknown so far, it is a priori not clear which rupture characteristics are relevant for earthquakes. The most important difference resulting from different slip characteristics consists in the amount of dynamic stress concentration ahead of the rupture front. Whereas for crack-like behavior the whole dynamic stress released during the rupture accumulates ahead of the rupture front, narrow slip pulses stress concentration is less pronounced due to partial reloading behind the slip pulse. Although continuum models would be more appropriate than inherently discrete models to simulate realistic rupture dynamics, the numerical effort allows only for the latter model class a statistical analysis of synthetic earthquake catalogs. Thus we introduce in non-conservative cellular automaton models a state-dependent stress distribution rule with tunable stress transfers to blocks in front of the rupture to account for more realistic rupture characteristics. By means of a new parameter, the dynamical behavior can change gradually between the two end-member models,  $\delta$ -like slip pulses (previous models [9–13]), and crack-like propagation.

We show that the type of rupture has a significant influence on the stress field variation due to an earthquake. Crack-like ruptures lead to smooth stress fields within the rupture zone whereas narrow slip pulses preserve or enlarge stress field heterogeneities. We can characterize these behavior by a quantitative measure allowing to understand the overall characteristics of earthquake sequences in self-organized stress fields. In this way, we can explain the previous observations that criticality is lost in the cellular automaton versions of the BK-model ( $\delta$ -type slip pulses) in the presence of external heterogeneities [20,21]. Such heterogeneities will always be present in real fault systems due to varying frictional parameters as well as geological structures. Thus we study in this paper the role of external heterogeneities in the case of more realistic rupture characteristics. Our systematic analysis shows that the degree of dynamically produced stress field heterogeneities is strongly connected with the frequency-size distribution of the simulated earthquakes. For given rupture characteristics, the fault roughness determines which of the observed distributions in nature, seismic creep, Gutenberg–Richter, or characteristic earthquake distribution, is relevant and whether or not nucleation phases during rupture growth will occur.

The remainder of this paper is organized as follows. In Section 2 we describe the model. The characteristics of model ruptures in static stress fields are analyzed in Section 3. These investigations lead to some ingredients for understanding the behavior of the self-organized systems, which are analyzed in Section 4. In Section 5 we summarize the main ideas and discuss the conclusions.

## 2. Model algorithm

The basis of the analyzed model is the spring-block model proposed by Burridge and Knopoff [8], which represents a fault zone by a network of interconnected blocks lying between two tectonic plates. Each block is coupled to the adjacent blocks and to the upper tectonic plate by springs and is connected frictionally with the bottom tectonic plate. It is assumed that the blocks perform stick-slip motion. All blocks are driven simultaneously by the slow relative movement of the two plates.

In the quasi-static limit, i.e., if instantaneous block slips are assumed, Olami et al. [11–13] show that the model can be described by continuous nonconservative cellular automata (hereinafter referred to as OFC-model). Our model is an extension of the OFC-model. We analyze  $L \times L$  arrays of blocks  $(i, j)$ , where  $i, j$  are integers,  $1 \leq i, j \leq L$ . The total force (or stress if unit area is assumed) on each block is given by  $\sigma(i, j)$ . By analogy with the OFC-model, the evolution of a single earthquake is described in the following way: The friction law adopts the Mohr–Coulomb law with a static failure threshold  $\sigma_F(i, j)$ . If the stress on a block  $(k, l)$  exceeds the static failure threshold,  $\sigma(k, l) \geq \sigma_F(k, l)$ , sliding is initiated at this block. The moving block slips to the zero-force position and the stress  $\Delta\sigma \equiv \sigma(k, l)$  is partially distributed to the four nearest neighbors  $(k_{\pm}, l_{\pm})$ . The stresses of the  $N_u$  nearest neighbors, which are unbroken during the rupture so far, are set according to the rule

$$\sigma(k_{\pm}, l_{\pm}) \rightarrow \sigma(k_{\pm}, l_{\pm}) + \frac{\gamma g}{\gamma N_u + N_b} \Delta\sigma, \quad (2.1)$$

and the  $N_b$  nearest neighbors, which have been already failed, are set according to

$$\sigma(k_{\pm}, l_{\pm}) \rightarrow \sigma(k_{\pm}, l_{\pm}) + \frac{g}{\gamma N_u + N_b} \Delta\sigma. \quad (2.2)$$

The stress of the sliding site is reset to

$$\sigma(k, l) \rightarrow 0. \quad (2.3)$$

The elastic coupling constant  $g$  depends on the spring constants and can vary in the range of  $0 \leq g \leq 1$ . The value of  $g$  defines additionally the degree of conservation, where  $g = 1$  refers to the case of conservation which is rather unrealistic due to seismic radiation, heat, and permanent deformation. As an extension of the OFC-model, the stress distribution is now state-dependent to account for more realistic stress enhancement ahead of the rupture front. Generalizing the state-dependent rule of Steacy and McCloskey [22], we introduce the new parameter  $\gamma$  determining the stress concentration of the rupture front. In the case of  $\gamma = 1$ , our model is equivalent to the OFC-model assuming instantaneous healing within the rupture area, whereas larger values of  $\gamma$  accounts for slower healing processes approximated by an effective weakening of the coupling strength to already broken blocks. In the case of  $\gamma \rightarrow \infty$ , no healing occurs and broken blocks remain sliding during the further evolution of the earthquake (crack-like behavior).

The redefined stress on the adjacent blocks  $\sigma(k_{\pm}, l_{\pm})$  may lead to an instability, i.e.,  $\sigma(k_{\pm}, l_{\pm}) \geq \sigma_F(k_{\pm}, l_{\pm})$ , in one or more blocks. In this case, a chain reaction starts

(at time step  $t = 1$ ) and the stresses at all instable blocks are distributed in parallel at time step  $t = 2$  according to Eqs. (2.1)–(2.3) leading maybe to further instabilities at time  $t = 3$ , and so on, until the earthquake is terminated, i.e., until  $\sigma(i, j) < \sigma_F(i, j)$  for all blocks  $(i, j)$ .

### 3. Static stress field

At first, we want to characterize the rupture kinematics for known initial stress fields. Therefore, we consider  $100 \times 100$  block-systems with stresses randomly distributed in the interval  $[c\sigma_F(i, j), \sigma_F(i, j)]$  with  $0 \leq c \leq 1$ . This leads to a mean stress level of  $(c + 1)\langle\sigma_F(i, j)\rangle/2$ , where  $\langle\sigma_F(i, j)\rangle$  denotes the mean value of the static failure thresholds. Quenched disorder is introduced in the way that the values of  $\sigma_F(i, j)$  are randomly distributed in the interval  $[2/(1 + V), 2V/(1 + V)]$  with  $V \geq 1$ . Thus the mean threshold value is 1, and  $V$  defines the ratio between upper and lower bound, that is,  $V$  characterizes the spatial variability of stress transfers due to block slidings. Furthermore, we use open boundary conditions, which implies that the blocks in the boundary layer are coupled to rigid boundary blocks. For each initial condition, all stresses are increased simultaneously until the first chain reaction starts, that is, the stress at one block reaches  $\sigma_F$ . The time evolution and the total size of this chain reaction is measured. The total size is defined by the sum of blocks which slipped at least once during the rupture. This procedure is repeated for many realizations of random stress distributions with the same mean value.

#### 3.1. Critical point behavior

We find that the model systems can be characterized by critical point behavior; that is, for given model parameters a critical stress level exists where the spatial correlation length diverges and the frequency-size distribution can be described by a power law. This behavior is universal in the sense that the same exponents of the power laws are found independently of the parameters. Only the value of the critical load depends on the model parameters, especially on the coupling constant  $g$ .

The divergence of the spatial correlation length is manifested by the growth of the mean rupture size according to a power law  $\langle S \rangle \sim \Delta\sigma^{1.2}$ , when the mean stress level of the system approaches the critical stress level. This is illustrated in Fig. 1(a).

The critical point can be characterized by the condition that ruptures are self-sustained, i.e., the stress concentration at the rupture front remains constant on average. Then ruptures of all sizes can occur where the maximum size is limited only by the finite system size. In the critical point ( $\langle\sigma\rangle = \sigma_{crit}$ ), the frequency-size distribution can be described in our model very well by a power law with exponent  $-1.2$ . By contrast, in the subcritical regime ( $\langle\sigma\rangle < \sigma_{crit}$ ) the ruptures die out due to the heterogeneities within the stress field. The cutoff in the frequency-size distribution becomes independent of the system size and shifts to smaller event sizes for decreasing stress levels. In the supercritical

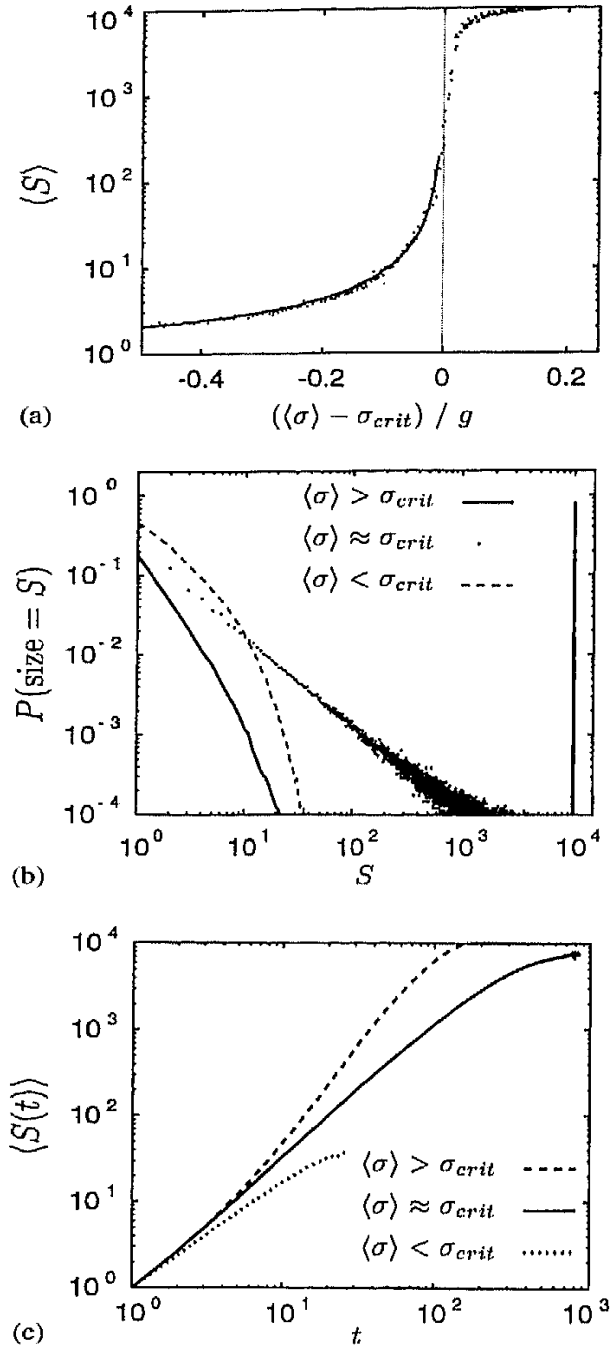


Fig. 1. Critical point behavior for static stress fields: (a) Approaching the critical stress level, the mean rupture area  $\langle S \rangle$  (points:  $\gamma = 1$ ,  $g = 0.2, 0.6, 1$ ) diverges approximately according to a power law  $1 + 0.45(\Delta\sigma/g)^{-1.2}$  (solid line). For critical stress loads, (b) the frequency-size distribution and (c) the temporal growth of ruptures are characterized independently of the model parameters by the power laws,  $P(S) \sim S^{-1.2}$  and  $S(t) \sim t^{1.58}$ , respectively. The results for critical loads are compared with examples for the subcritical and supercritical regime (parameters:  $\gamma = 1$ ,  $g = 0.8$ ). In (c) each data point is determined by averaging over the sizes  $S(t)$  of all events having grown longer than time  $t$ .

regime ( $\langle \sigma \rangle > \sigma_{crit}$ ) the stress concentration at the rupture front increases continuously leading to runaway events which are terminated only due to finite size effects. In this regime, the frequency-size distribution is characterized by system-wide events and, in addition, by small events distributed approximately according to a power law. However, the distribution of these micro events becomes steeper, i.e., the exponent becomes larger, if the stress level is increased further. At very high stress levels, all triggered events rupture the whole system. In Fig. 1(b) the frequency-size distribution is shown for critical stress loads and for examples of subcritical and supercritical stress loads.

Furthermore, we find that the temporal growth of ruptures varies systematically for the three regimes. Although individual events differing very much in their energy-release histories, averaging over many events lead to distinguishable characteristics (see Fig. 1c): We find that in the critical state the growth can be fit by a power law increase  $t^{1.58}$  independently of the model parameters. An almost identical exponent has been found for two-dimensional sandpile models connecting the size of an avalanche with its duration [23]. This exponent indicates an anisotropic growth of the rupture, because a circular propagating rupture front with constant radial velocity would lead to the larger exponent 2. We have proven this interpretation by studying several ruptures individually. In the subcritical regime, the rupture growths is almost one-dimensional leading to an exponent close to 1. By contrast, in the supercritical regime, the ruptures grow after an initial time interval or nucleation phase according to a power law with exponent 2 indicating that a block sliding leads to an instability at the next time step on all unbroken adjacent blocks. Note that the nucleation phase does not result from the averaging procedure, it is also present for the system-wide events only. The occurrence of this phase, where the growth is almost critical, is due to the time needed to accumulate enough stress at the rupture front before becoming a runaway event. Therefore, the occurrence of power law like distributed event sizes of the micro earthquakes in the supercritical regime is strongly related to the existence and duration of this nucleation phase. The duration of the nucleation phase depends on the stress level and becomes shorter for higher stress loads. For very high loads, all initiated events are runaway events and no nucleation phase occurs.

### 3.2. Stress field variations due to earthquakes

In the last subsection, we have shown that the different rupture kinematics in static stress fields can be characterized by the same underlying critical point behavior. Although the value of the critical stress load depends on the level of conservation  $g$ , the stress intensity factor  $\gamma$ , and the degree of quenched disorder  $V$ , the critical exponents for the divergence of the mean rupture sizes, the frequency-size distribution, and the critical rupture growth are independent of the model parameters and external heterogeneities.

However, our aim is to understand the behavior of self-organized systems, where the actual stress field is the result of the stress changes due to previous events as well as due to external forcing in the form of tectonic plate movement (see Section 4).

Thus we analyze now the effect of earthquake ruptures with regard to the stress field. In particular, we are interested in the dependence of the stress field variations on model parameters and the degree of external heterogeneities. For that, we compute the standard deviation of the stress lacks  $\sigma_F(i, j) - \sigma(i, j)$  on the rupture area before and after an event occurs in the case of critical stress loads. The ratio  $Q$  of both standard deviations is a measure for the dynamically produced increase or decrease of the stress field heterogeneity due to an earthquake rupture. Note that due to our stress field preparation, we investigate the effect of ruptures in spatially uncorrelated stress field with almost uniformly distributed stress values. However, the resulting stress distribution within the rupture will not be uniform, because the stress distribution rules prefer the stress values  $ng/4$  with  $n=1, \dots, 4$  [24]. We account for this effect in the way that we normalize the observed  $Q$ -values by the value resulting for the conservative model with  $\gamma = 1$ . This is due to the fact that for the conservative model with  $\gamma = 1$ , the mean stress level remains almost constant after the rupture, resulting in a  $Q$ -value which only measures this effect of redistribution into a non-uniform distribution.

We find that in the case of homogeneous block systems  $V = 1$  and isotropic stress distribution rules  $\gamma = 1$ , the ratio  $Q$  between both standard deviations is almost independent of the degree of conservation. Thus for smooth fault systems,  $\delta$ -like slip pulses do not change the degree of stress field heterogeneity. In the case of quenched disorder  $V > 1$ , this relation holds only for the conservative case  $g = 1$ , whereas in the case of  $g < 1$  ruptures enhance dynamically the stress field heterogeneity leading to an effective turning back from the critical state. In particular, the disordering effect of ruptures, or equivalent the repelling force increases, with decreasing  $g$  and increasing levels of disorder  $V$ . This is shown in Fig. 2(a) and (b).

However, if we consider enhanced stress concentration factors  $\gamma > 1$ , the results change. On the one hand,  $\gamma > 1$  leads to a smoother stress field behind the rupture front. In the case of crack-like behavior ( $\gamma \rightarrow \infty$ ), the stress levels of broken cells are all equal to 0 and disorder within the rupture area is only due to external disorder of the failure strength. On the other hand, system-wide ruptures can occur for  $\gamma > 1$  in more uncorrelated stress fields; that is, for larger degrees of heterogeneity. Both effects lead to a smaller disordering effects, respectively larger smoothing effects of earthquakes, or equivalently to an increase of the ratio  $Q$ , for increasing  $\gamma$ . This is shown in Fig. 2(c). The increase depends on the level of conservation  $g$  and on the degree of quenched disorder  $V$ . The two-dimensional parameter space spanned by  $g$  and  $V$ , is divided in two parts separated by a border line  $V_b(g)$ , which increases from  $V_b(0) = 1$  up to  $V_b(1) = \infty$ . In the lower part,  $V < V_b(g)$ , the function  $Q(\gamma)$  crosses the value 1; that is, crack-like ruptures smooth the stress field. In the case of larger disorder  $V > V_b(g)$ , all rupture types lead to an effective increase of the heterogeneity ( $Q(\gamma) < 1$ ).

In the next section, we will see that the dynamically produced change of the stress field heterogeneity quantified by  $Q$ , can explain the varying behavior of the self-organized systems for different model parameters and different degrees of external disorder. The preservation of the degree of heterogeneity by earthquake ruptures  $Q(\gamma) \approx 1$

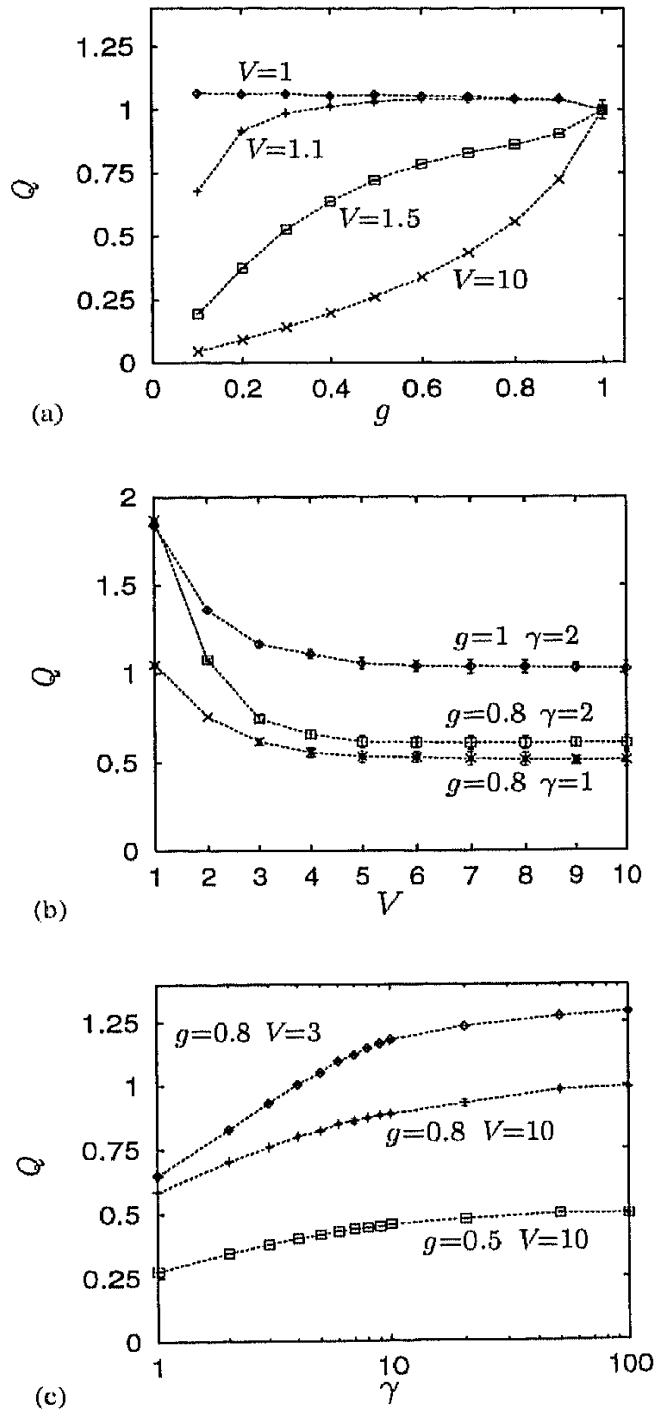


Fig. 2. The measure  $Q$  (defined in the text) for the stress field variation due to ruptures.  $Q > 1$  indicates smoothening effects, whereas  $Q < 1$  corresponds to an increase of heterogeneity. (a) Shows the dependence of  $Q$  on the level of conservation  $g$  for smooth systems ( $V = 1$ ) and heterogeneous systems ( $V > 1$ ) in the case of  $\gamma = 1$ . The dependence of  $Q$  on the degree of quenched disorder and the stress concentration factor  $\gamma$ , is shown in (b) and (c), respectively, for different parameter combinations.

seems to be the condition for forced systems to show self-organized criticality, whereas  $Q(\gamma) < 1$ , respectively  $Q(\gamma) > 1$  leads to subcritical, respectively supercritical behavior.

#### 4. Self-organized systems

Now, we want to analyze the self-organization of such systems in the presence of external, tectonic forcing. We investigate simulations of  $100 \times 100$  block-systems with open boundary conditions, where the initial stress levels  $\sigma(i, j)$  are randomly chosen from the interval  $[0, \sigma_F(i, j)]$ . All blocks are simultaneously increased with a constant rate until the stress level on one block reaches the static failure threshold  $\sigma_F$ . Then, the avalanche kinematics are calculated according to Eqs. (2.1)–(2.3). When the rupture stops, all stresses are increased again with the constant rate owing to the tectonic loading. We assume total healing of the frictional resistance in the interoccurrence time interval between successive events; that is, all blocks are referred to be unbroken again. The system is iterated until it reaches a statistically stationary state.

##### 4.1. Homogeneous systems

At first, we analyze simulations with a stress concentration factor  $\gamma = 1$ , but different degrees of conservation  $g$ . It is already known from previous investigations [11–13,25] that such systems show SOC in the sense that the frequency-size distributions can be described by power laws. The exponent of the power law  $P(S) \sim S^{-b}$ , however, depends on the coupling constant (level of conservation)  $g$ . This is shown in Fig. 3(a). The exponent  $b$  is found to increase with decreasing  $g$ . This dependence is in contrast to our results found for ruptures in static stress fields (Section 3), where the distributions are obeying the power law  $S^{-1.2}$  independently of the parameter  $g$ . In self-organized systems, a power law with this exponent is only observed in the conservative case  $g = 1$ .

Here, we examine additionally the temporal growth of the rupture areas. We find that the temporal growing rates of the ruptures occurring in these simulations depend only slightly on  $g$ . In Fig. 3(b) it is shown that the increase can be characterized quite well by the power law  $t^{1.58}$ , which was already observed for rupture growths in critically loaded, static stress fields (Section 3). However, the frequency-size distributions reflect the fact that the probability for a rupture to last for longer times is significantly decreased for lower levels of conservation  $g$ .

The results can be understood in the way that most events occur within two-dimensional spatially extended, critical loaded patches. Within each of these patches an event of size  $S$  will occur with a probability of  $\sim S^{-1.2}$ , limited only by the finite patch size, as we already know from the investigation of the static model. This explains that the temporal growth of ruptures can be described almost by the same power law behavior as in the static systems for  $\langle \sigma \rangle \approx \sigma_{crit}$ , although the results for the forced systems are



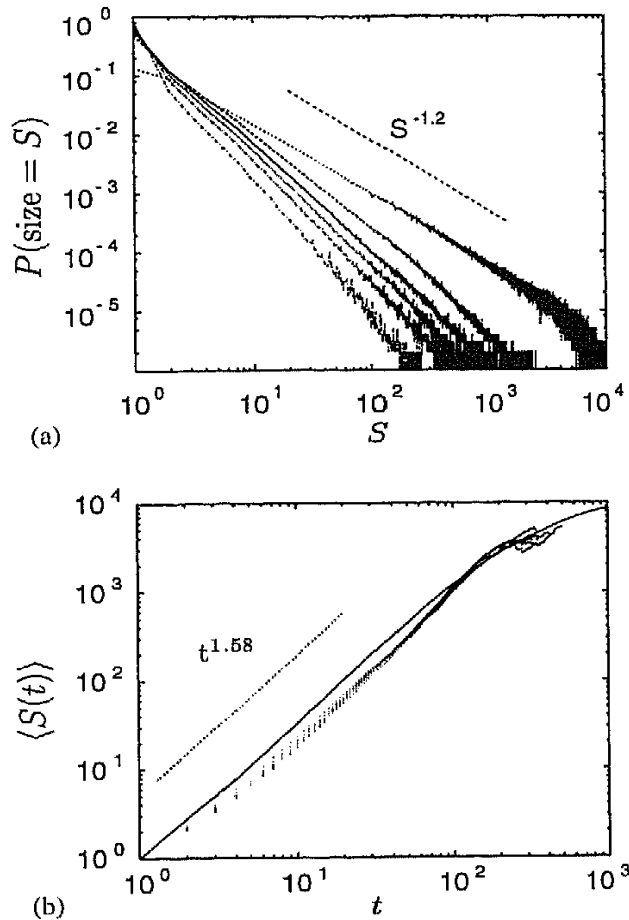


Fig. 3. Self-organized, smooth systems with  $\gamma=1$  for the different coupling constants  $g=0.5, 0.6, 0.7, 0.8, 0.9$ , and 1: (a) The probability to observe events of size  $S$  as a function of  $S$ , where the curves correspond from bottom to top to  $g=0.5, 0.6, 0.7, 0.8, 0.9$ , and 1. For the same simulations, (b) shows the temporal growth of the rupture areas, where each data point is determined by averaging over all ruptures having grown longer than time  $t$ . The solid line indicates the result for  $g=1$ , whereas results for  $g < 1$  are marked by dots.

superpositions of ruptures occurring at different global loading states  $\langle \sigma \rangle$ . The slightly lower growing rates for small rupture sizes (see Fig. 3(b)) are likely to be the result of very small patch sizes, where boundary effects are important. The overall observed frequency-size distribution is built up by the superposition of  $S^{-1.2}$ -distributions with cutoffs corresponding to the patch sizes occurring in the system. The dependence of the frequency-size distribution on  $g$  emerges from differences in the patch size distribution. Smaller patch sizes occur more frequently for smaller values of  $g$ . To understand this, consider an event occurring within a larger critical loaded region. Due to the dissipation, the event leads to a stress reduction at blocks within the rupture area which is in the order of  $\Delta\sigma = (1-g)\sigma_{crit}$ . Thus, the smaller the coupling constant  $g$  is, the larger is the stress gap afterwards. Because of this relation, the tendency of the system to separate into smaller, almost uncoupled spatial patches, is strengthened for smaller  $g$ . Because for  $g=1$  no separation will occur, the overall frequency-size distribution can be described by  $P(S) \sim S^{-1.2}$ . For  $g < 1$  it is already known that in the case of

periodic boundary conditions, the ongoing separation leads to a periodic state with almost only small event sizes [24,26,27]. In the case of open boundaries, the inhomogeneities at the boundaries prevent such a periodic state [28]. Due to the complex interplay between synchronization and desynchronization effects in the case of  $g < 1$ , at most times only small patches will occur, whereas with a low but finite probability a system-wide critical loaded patch can build up sometimes.

#### 4.2. Heterogeneous systems

It is already known from previous studies [20,21] that even low degrees of quenched disorder destroy the SOC-behavior in the case of non-conservation  $g < 1$ , whereas for  $g=1$  the system remains critical. Summing up our investigations in Section 3.2, we can understand this behavior in terms of the disordering effects of ruptures (quantified by  $Q < 1$ ) for non-conservative systems in the presence of external heterogeneities. For conservative systems  $g=1$ , it is expected from our previous analysis (Fig. 2a) that the system with  $\gamma=1$  stays critical even for very high degrees of external disorder  $V$ . To prove this, we have analyzed the frequency-size distribution for  $V = 1, 1.5, 3, 10$ , and 1000, finding no significant changes.

Now, we analyze the effect of enhanced stress concentrations ahead of the rupture fronts in heterogeneous systems; that is, we study self-organized systems with quenched disorder for the case  $\gamma > 1$ . We find that in the case of  $g < 1$  and moderate degrees of quenched disorder, a transition occurs from subcritical behavior for small values of  $\gamma$  to supercritical behavior for large  $\gamma$ -values. The subcritical regime is dominated by small events and the largest ruptures do not cross the entire system. The supercritical regime is characterized by frequently occurring events which rupture almost the whole system. At the transition  $\gamma_{crit}$  between these two regimes, the system shows self-organized criticality; that is, the frequency-size distribution is characterized by a power law. Thus the behavior is very similar to those characteristics observed for subcritical, critical, or supercritical loaded static stress fields in Section 3. However, the power law exponent of the frequency-size distribution for the critical value  $\gamma_{crit}$  is for self-organized systems no longer universal, rather it depends on the level of conservation  $g$ . These characteristics are illustrated in Fig. 4(a) for a system with quenched disorder  $V = 1.5$  and a level of conservation  $g=0.8$ . The results for three different values of  $\gamma$  represent the subcritical, critical, and supercritical behavior. In the critical regime, the frequency-size distribution can be fit very well by a power law  $\sim S^{-1.9}$ , which also fits the distribution for  $g=0.8$  with the different parameters  $V = \gamma = 1$ ; that is, the distribution which is observed in spatially uniform systems with state-independent coupling.

For the same examples, the averaged temporal evolution of the ruptures is shown in Fig. 4(b). In agreement with the static system (see Fig. 1c), the critical system state is defined by a power law growth  $t^{1.58}$  of the rupture area, whereas the subcritical case is characterized by a slower and the supercritical state by a faster growth after a nucleation phase. In contrast to the static system, the observed characteristics resulting from a superposition of events occurring at different mean stress levels. However, the

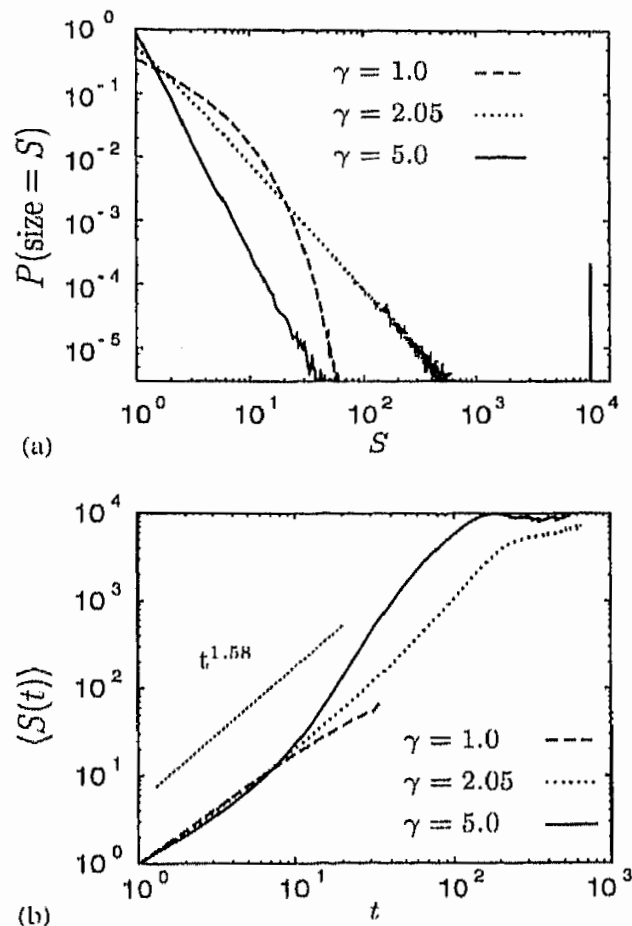


Fig. 4. Results for self-organized systems with  $g = 0.8$  and quenched disorder  $V = 1.5$  in the case of three different stress concentration factors  $\gamma$ : (a) shows the frequency-size distribution, and (b) the temporal growth of ruptures. Each data point in (b) is determined by averaging over all avalanches having grown longer than  $t$ .

consideration of the largest ruptures only leads to almost unchanged characteristics. This result supports our interpretation that in the case of SOC most of the ruptures occurring within two-dimensional spatially extended, critically loaded patches (see Section 4.1). On the other hand, supercritical behavior can be understood by the smoothing effects of small and intermediate events with regard to the stress field leading after reloading to supercritical stress loads.

However, there are limitations for finding critical or supercritical behavior in systems with quenched disorder. The limitations are similar to those found for the static system (Section 3.2). We find that for a given level of dissipation  $g$  the degree of quenched disorder has to be smaller than a certain value  $V_b(g)$  to reach the supercritical regime for large stress concentration factors  $\gamma \rightarrow \infty$ . The limiting value varies between  $V_b(0) = 1$  and  $V_b(1) = \infty$ . In Fig. 5 the frequency-size distribution is shown for systems with quenched disorder  $V = 10$  and a large stress concentration factor  $\gamma = 100$  in the case of three different levels of conservation. In the conservative case, the system shows supercritical behavior, whereas the system with  $g = 0.5$  remains still in the subcritical

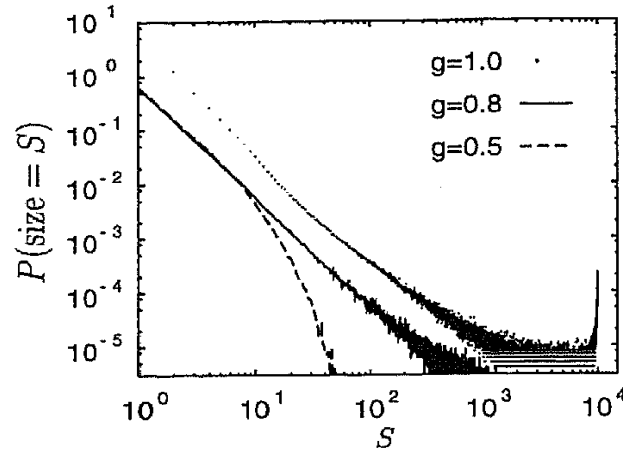


Fig. 5. Frequency-size distributions observed in systems with heterogeneities ( $V = 10$ ) and a high stress concentration factor ( $\gamma = 100$ ) for three different levels of conservation ( $g = 0.5, 0.8$ , and  $1$ ). The results for  $g = 1$  are multiplied by 10.

regime. For  $g = 0.8$ , the system shows SOC-like behavior. In Section 3.2 (Fig. 2c), we have found that for this parameter set ( $g = 0.8$ ,  $\gamma = 100$ ,  $V = 10$ ) the events approximately preserve the degree of the stress field heterogeneity ( $Q \approx 1$ ), whereas for  $g = 0.5$  ( $\gamma = 100$ ,  $V = 10$ ) ruptures enhance the heterogeneities ( $Q < 1$ ). Further investigations of other parameter combinations have supported our result that  $Q \approx 1$  is a criterion for criticality.

#### 4.3. Boundary effects

Although the simulations shown in the previous sections have been performed with open boundary conditions, the results are not restricted to this special choice in the presence of quenched disorder. This is in contrast to results previously found for homogeneous fault models, where periodic boundary conditions lead to periodic solutions with mainly small events [24,26–28]. In smooth systems, inhomogeneities emerging from the boundaries are necessary to counteract this tendency.

In systems with quenched disorder  $V > 1$ , the boundaries remain important for the termination of runaway events, whereas they do not play any more a crucial role with respect to the critical state. Now inhomogeneities exist everywhere, preventing periodic solutions. Instead of the boundaries, the inhomogeneities within the block-system are mainly responsible for the desynchronization effect which is necessary for the emergence of SOC in dissipative systems. This is also reflected in much shorter transients. We have checked this, by analyzing different dissipative heterogeneous systems with periodic boundary conditions, where  $\gamma$  has been fixed by the value leading to critical behavior in the system with open boundary conditions.

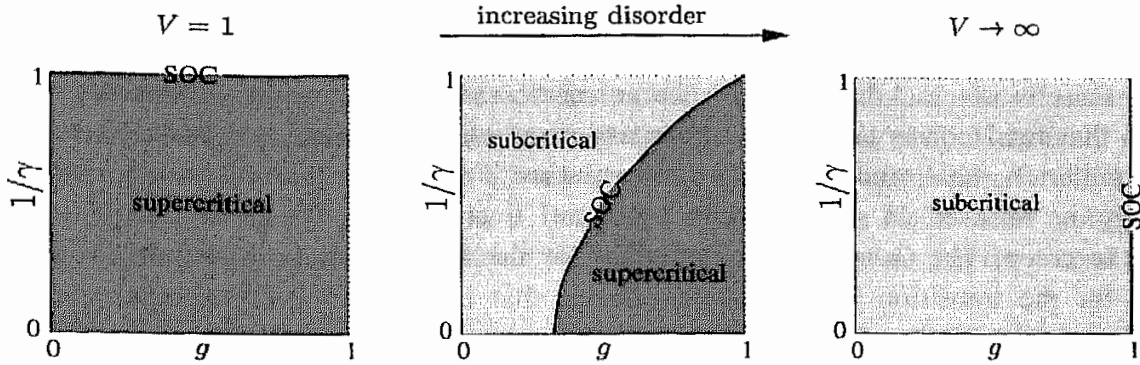


Fig. 6. Schematic phase diagram of the system in dependence on the degree of quenched disorder.

## 5. Summary and discussion

The Gutenberg–Richter law for earthquakes has been claimed to be the result of an underlying self-organized critical state of the fault zones. This hypothesis has been supported by the Burridge–Knopoff (BK) model, in particular its cellular automaton versions which show SOC, i.e., reproduce the Gutenberg–Richter law. However, although the Gutenberg–Richter law is a good approximation for regional seismicity, empirical observations suggest that individual faults are more likely to show characteristic earthquake distributions or seismic creep. Our aim is to understand the origin of such deviations from the Gutenberg–Richter law. The investigation of scaling laws requires long earthquake catalogs produced on large system sizes. Therefore, cellular automata are suitable because they need relative little computation time.

We have investigated cellular automaton versions of the BK-model with a new state-dependent stress distribution rule to account for more realistic stress concentration ahead of the propagating rupture front. The frictional characteristics of ruptures are defined by the level of conservation  $g$  and the stress intensity factor  $\gamma$ . Because real rupture dynamics at tectonic scales are almost unknown so far, we have studied different rupture types gradually varying between the end-member models, crack-like propagation and  $\delta$ -type slip pulses, respectively.

Our main finding is the strong relation between the roughness of faults and the frequency-size distribution, respectively the temporal growth of the earthquakes. Thereby the earthquake characteristics can be described in terms of critical point behavior, resulting in subcritical, critical, and supercritical states. The realized state of self-organized systems can be explained by means of the effect of individual ruptures on the stress field. Fig. 6 illustrates our results for the case of a smooth, moderate rough, and very rough fault. These results predict that characteristic earthquake distributions (supercritical behavior), observed empirically for several individual fault systems [6,7], can be expected for smooth fault systems. In massive simulations of smooth faults, characteristic earthquake distributions occur naturally [29,30], because in these models broader

slip pulses occur due to inertia which correspond to  $\gamma > 1$  in the cellular automaton versions of the same model type. For rough faults, supercritical behavior can be expected only for almost crack-like rupture characteristics and high degrees of conservation  $g$ . Note that total conservation ( $g = 1$ ) is an unrealistic assumption, at least due to seismic radiation, heat, and permanent deformation. For other rupture characteristics, the energy is released in rough faults by small events only, which is reminiscent of seismic creep. The Gutenberg–Richter law for the frequency-size distribution is found only for the transition between both phases; that is, only for very special parameter combinations. Similar to the SOC characteristics for  $\delta$ -type slip pulses in smooth systems, the exponent of the Gutenberg–Richter law depends on the degree of conservation.

Additionally to the frequency-size distribution, the different model states are reflected in different characteristics of the temporal evolution of earthquakes. In the case of SOC, the growth of the ruptures is not isotropical and can be expressed on average by a power law increase  $t^{1.58}$ , whereas in the supercritical regime ruptures grow isotropically ( $\sim t^2$ ) after a nucleation phase with the critical, slower growing rate.

Thus our model investigations show that characteristic earthquake distributions are strongly related to the occurrence of nucleation phases which have been recorded for several real earthquakes [31–33]. Furthermore, our findings are in agreement with empirical observations suggesting that smoother faults are more likely to have characteristic earthquake distributions [7].

These results seem to be independent of the special kind of inhomogeneities. Our investigations of Gaussian instead of uniform distributed failure thresholds as well as previous investigations of the frequency-size distributions in the case of a conservative model with spatially fractal distributed failure thresholds [22] support this view. Furthermore, the overall behavior seems not to be restricted to nearest-neighbor interactions, because similar results have been found for mean-field models, where enhanced stress concentrations emerge from material weakening effects [34,35].

In this paper, we have shown that characteristic earthquake distributions can result naturally from more realistic stress concentrations at the rupture front than assumed in previously studied models showing SOC. An alternative explanation has been proposed by Rundle and Klein [36] who found that higher plate velocities lead, in the presence of time delays between an instability and the earthquake initiation, to characteristic earthquake distributions. However, the time scale of tectonic loading is orders of magnitudes larger compared to the typical interoccurrence times between successive small and intermediate events [37]. Thus it is questionable, if tectonic driving rates can play such a crucial role.

In conclusion, our model investigations of individual faults predict that the Gutenberg–Richter law is an exception rather than the usual case. This might have important implications for the predictability of earthquakes, because characteristic earthquake distributions are equivalent to more pronounced seismic cycles leading to an increased predictability. On the other hand, our results seem to be in contrast to the observation that the Gutenberg–Richter law is a good approximation for regional

seismicity, i.e., for fault populations. The apparent inconsistency can be cleared up by the fact that the Gutenberg–Richter law can result from the superposition of the characteristic earthquake distributions occurring on different faults, if one considers the fact that the fault lengths are approximately fractal distributed [38]. However, interactions between different faults have been neglected in this explanation. It will be an interesting question for future work, if networks of interacting faults with non-fractal fault length distribution can also lead to the Gutenberg–Richter law for the overall size distribution.

In sum, the consideration of heterogeneities and more realistic rupture characteristics in non-conservative cellular automaton models enables to understand the emergence of the whole scenario of frequency-size distributions observed for individual faults in nature.

### Acknowledgements

This work was supported by the Deutsche Forschungsgemeinschaft (SCH280/13-1 and SFB 555) and the state Brandenburg (HSP III 1.6).

### References

- [1] P. Bak, C. Tang, K. Wiesenfeld, *Phys. Rev. Lett.* 59 (1987) 381.
- [2] P. Bak, C. Tang, K. Wiesenfeld, *Phys. Rev. A* 38 (1988) 364.
- [3] B. Gutenberg, C.F. Richter, *Ann. Geofis.* 9 (1956) 1.
- [4] H. Kanamori, D.L. Anderson, *Bull. Seismol. Soc. Am.* 65 (1975) 1073.
- [5] C. Frohlich, S.D. Davis, *J. Geophys. Res.* 98 (1993) 631.
- [6] S.G. Wesnousky, *Bull. Seismol. Soc. Am.* 84 (1994) 1940.
- [7] M.W. Stirling, S.G. Wesnousky, K. Shimazaki, *Geophys. J. Int.* 123 (1996) 833.
- [8] R. Burridge, L. Knopoff, *Seis. Soc. Am. Bull.* 57 (1967) 341.
- [9] J.B. Rundle, D.D. Jackson, *Bull. Seism. Soc. Am.* 67 (1977) 1363.
- [10] H. Nakanashi, *Phys. Rev. A* 43 (1991) 6613.
- [11] Z. Olami, H.S. Feder, K. Christensen, *Phys. Rev. Lett.* 68 (1992) 1244.
- [12] K. Christensen, Z. Olami, *Phys. Rev. A* 46 (1992) 1829.
- [13] K. Christensen, Z. Olami, *J. Geophys. Res.* 97 (1992) 8729.
- [14] S. Hainzl, G. Zöller, J. Kurths, *J. Geophys. Res.* 104 (1999) 7243.
- [15] S. Hainzl, G. Zöller, J. Kurths, *Int. J. Bif. Chaos* 9 (1999) 2249.
- [16] S. Hainzl, G. Zöller, J. Kurths, *Nonl. Proc. Geophys.* 7 (2000) 21.
- [17] S. Hainzl, G. Zöller, J. Kurths, J. Zschau, *Geophys. Res. Lett.* 27 (2000) 597.
- [18] T.H. Heaton, *Phys. Earth & Planetary Int.* 64 (1990) 1.
- [19] S.B. Nielsen, J.M. Carlson, K.B. Olsen, *J. Geophys. Res.* 105 (2000) 6069.
- [20] I.M. Janosi, J. Kertesz, *Physica A* 200 (1993) 179.
- [21] H. Ceva, *Phys. Rev. E* 52 (1995) 154.
- [22] S.J. Steacy, J. McCloskey, *Geophys. Res. Lett.* 26 (1999) 899.
- [23] C. Tang, P. Bak, *Phys. Rev. Lett.* 60 (1988) 2347.
- [24] P. Grassberger, *Phys. Rev. E* 49 (1994) 2436.
- [25] I.G. Main, G. O'Brien, R. Henderson, *J. Geophys. Res.* 105 (2000) 6105.
- [26] J.E.S. Socolar, G. Grinstein, C. Jayaprakash, *Phys. Rev. E* 47 (1993) 2366.
- [27] S. Lise, A.L. Stella, *Phys. Rev. E* 57 (1998) 3633.
- [28] A.A. Middleton, C. Tang, *Phys. Rev. Lett.* 74 (1995) 742.

- [29] J.M. Carlson, J.S. Langer, *Phys. Rev. Lett.* 62 (1989) 2632.
- [30] J.M. Carlson, J.S. Langer, *Phys. Rev. A* 40 (1989) 6470.
- [31] Y. Iio, *Geophys. Res. Lett.* 19 (1992) 477.
- [32] R. Abercombie, J. Mori, *Bull. Seism. Soc. Am.* 84 (1994) 725.
- [33] W.L. Ellsworth, G.C. Beroza, *Science* 268 (1995) 851.
- [34] D.S. Fisher, K. Dahmen, S. Ramanathan, Y. Ben-Zion, *Phys. Rev. Lett.* 78 (1997) 4885.
- [35] K. Dahmen, D. Ertas, Y. Ben-Zion, *Phys. Rev. E* 58 (1998) 1494.
- [36] J.B. Rundle, W. Klein, *J. Stat. Phys.* 72 (1993) 405.
- [37] C.H. Scholz, *The Mechanics of Earthquakes and Faulting*, Cambridge University Press, New York, 1994.
- [38] C.H. Scholz, *Bull. Seis. Soc. Am.* 87 (1997) 1074.



# Appendix E

Detecting premonitory seismicity patterns based on critical point dynamics

Autors:	G. Zöller, and S. Hainzl
Journal:	<i>Natural Hazards and Earth System Sciences,</i>
Volume (Nr.):	<b>1(1-2)</b>
Pages:	93-98
Year:	2001

# Detecting premonitory seismicity patterns based on critical point dynamics

G. Zöller<sup>1</sup> and S. Hainzl<sup>1,2</sup>

<sup>1</sup>Institute of Physics, University of Potsdam, Germany

<sup>2</sup>Institute of Earth Sciences, University of Potsdam, Germany

Received: 8 May 2001 – Accepted: 16 July 2001

**Abstract.** We test the hypothesis that critical point dynamics precedes strong earthquakes in a region surrounding the future hypocenter. Therefore, we search systematically for regions obeying critical point dynamics in terms of a growing spatial correlation length (GCL). The question of whether or not these spatial patterns are correlated with future seismicity is crucial for the problem of predictability. The analysis is conducted for earthquakes with  $M \geq 6.5$  in California. As a result, we observe that GCL patterns are correlated with the distribution of future seismicity. In particular, there are clear correlations in some cases, e.g. the 1989 Loma Prieta earthquake and the 1999 Hector Mine earthquake. We claim that the critical point concept can improve the seismic hazard assessment.

## 1 Introduction

Different critical point concepts have been discussed extensively with respect to the predictability of earthquakes (Bufe and Varnes, 1993; Jaumé and Sykes, 1999; Hainzl et al., 1999, 2000; Hainzl and Zöller, 2001). Motivated by damage mechanics and laboratory experiments (Leckie and Hayhurst, 1977; Das and Scholz, 1981), the time-to-failure approaches assume that the preparatory process of a large earthquake is characterized by a highly correlated stress field with a growing correlation length (GCL) and an accelerating energy/moment (AMR) release. In practice, these concepts have been tested by fitting time-to-failure relations to seismicity data. For the AMR model, this relation is

$$(\Sigma\sqrt{E})(t) = A - B(t_f - t)^m, \quad (1)$$

with positive constants  $A$ ,  $B$ ,  $m$ , the time-to-failure  $t_f$ , and the cumulative Benioff strain  $(\Sigma\sqrt{E})(t)$ , where  $E$  is the energy release of an earthquake. In the GCL model, the corre-

lation length  $\xi$  is expected to diverge for  $t \rightarrow t_f$  according to

$$\xi(t) = C(t_f - t)^{-k} \quad (2)$$

with positive constants  $C$  and  $k$ . Both approaches describe the same underlying mechanism, namely, the critical point dynamics. An important problem is the determination of free parameters, which are in addition to  $A$ ,  $B$ ,  $t_f$ , and  $m$  in Eq. (1), respectively,  $C$ ,  $t_f$ , and  $k$  in Eq. (2), which represent windows for space, time, and magnitude.

The accelerating moment release in terms of cumulative Benioff strain has been documented in several cases, e.g. for California seismicity (Bufe and Varnes, 1993; Bowman et al., 1998; Brehm and Braile, 1998, 1999). The growth of the spatial correlation length has been concluded from variations in the epicenter distribution (Zöller et al., 2001). However, these studies have not been conducted systematically in space and time, i.e. the analysis was restricted to the occurrence time and the epicenter of the largest events. Thus, possible false alarms (critical point behaviour without a subsequent strong earthquake) have not been examined. Therefore, it is an open question whether or not the observed phenomena are unique, i.e. the occurrence of patterns prior to large earthquakes is only meaningful if there is a systematic correlation between these patterns and subsequent earthquakes.

In the present work, we compare patterns based on critical point dynamics in terms of GCL before strong earthquakes with the epicenters of these events, and subsequent intermediate to large earthquakes. By performing a systematic spatial search algorithm, we address the question of spatial correlations. To estimate the significance of the results, the method is also applied to catalogues from an appropriate Poisson process model.

## 2 Data and method

In this section, we present the data and the method to detect spatial correlations between GCL patterns and subsequent

Correspondence to: G. Zöller (gert@agnld.uni-potsdam.de)

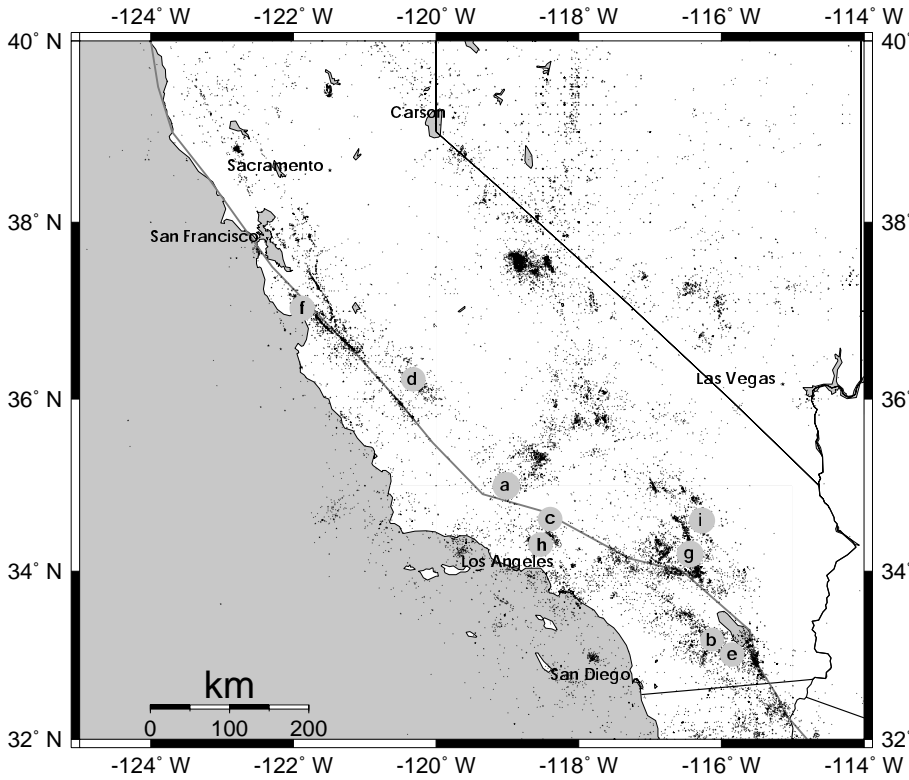


**Fig. 1.** Earthquakes with  $M \geq 3.0$  in California since 1910. Solid circles denote the events with  $M \geq 6.5$  since 1952: circle (a), 1952  $M = 7.5$  Kern County; circle (b), 1968  $M = 6.5$  Borrego Mountain; circle (c), 1971  $M = 6.6$  San Fernando; circle (d), 1983  $M = 6.7$  Coalinga; circle (e), 1987  $M = 6.6$  Superstition Hills; circle (f), 1989  $M = 7.0$  Loma Prieta; circle (g), 1992  $M = 7.3$  Landers; circle (h), 1994  $M = 6.6$  Northridge; and circle (i), 1999  $M = 7.1$  Hector Mine.

seismicity.

We analyze the seismicity in California between the  $32^\circ$  N and  $40^\circ$  N latitude and the  $-125^\circ$  W and  $-114^\circ$  W longitude. The data are taken from the Council of the National Seismic System (CNSS) Worldwide Earthquake Catalogue. The catalogue covers the time span from 1910 to 2000. The distribution of earthquakes is shown in Fig. 1. To account for the completeness of the data, we restrict the analysis to the nine strongest earthquakes with  $M \geq 6.5$  since 1952. Note that completeness of the CNSS catalogue was not achieved until 1940.

For a detailed description of the GCL model, we refer to Zöller et al. (2001). The method is based on a fit of Eq. (2) to the data in a circular space window with radius  $R$  and in a time interval  $(t_0; t_f)$  for earthquakes with magnitudes  $M \geq M_{\text{cut}} = 4.0$ . The exponent  $k$  is set to  $k = 0.4$  according to the result of Zöller et al. (2001). The power law fit is then compared with the fit of a constant and the quality of the power law fit is measured by the curvature value introduced by Bowman et al. (1998),

$$C = \frac{\text{power law fit root-mean-square error}}{\text{constant fit root-mean-square error}}. \quad (3)$$

Around each epicenter of a strong earthquake, the curvature parameter has been calculated for different values of  $R$  and  $t_0$ . The set of parameters for which  $C$  is minimal is used for further calculations; i.e. the space window ( $R$ ) and the length of the time interval ( $t_0$ ) are adjusted in order to optimize  $C$ . The approach of looking at different spatial scales is

based on the observation of Zöller et al. (1998), that the dynamics of a spatially extended system is most clearly visible on intermediate spatial scales between the noisy microscales and the large scales, where the dynamics are hidden due to the averaging. The  $C$  values are determined on a spatial grid with a resolution of  $0.5^\circ$  in longitude and latitude at nine different times  $t_f^i$ , corresponding to the occurrence times of the nine earthquakes with  $M \geq 6.5$ , denoted with index  $i$ . The result is a function  $C^i(\mathbf{x})$  for the GCL model, which is compared with the epicenter distribution of the earthquakes with  $M \geq 5.0$  in the time interval  $(t_f^i; t_f^i + 1 \text{ year})$ . This set of epicenters is called the pattern  $Q^i(\mathbf{x})$  for the  $i$ th strongest earthquake. The (arbitrary) magnitude threshold  $M = 5.0$  defining the pattern  $Q^i(\mathbf{x})$  has been introduced, since the premonitory patterns are assumed to be correlated not only with the strongest earthquake, but also with some subsequent main shock activity.

In the next step, the curvature parameter  $C_{\text{APC}}^i(\mathbf{x})$  is calculated for 100 adjusted Poisson catalogues (APC) in order to derive a measure for the statistical significance of the results. These catalogues are calculated according to the algorithm of Zöller et al. (2001):

1. The CNSS catalogue is declustered using the algorithm of Reasenber (1985);
2. Random epicenters according to the epicenter distribution of the declustered CNSS catalogue are calculated;
3. The earthquake occurrence times are drawn from a Poisson process;

4. The earthquake magnitudes are taken randomly from a probability distribution fulfilling the Gutenberg-Richter law (Gutenberg and Richter, 1956);
5. Aftershocks according to the law of Omori (1894) are added using the algorithm of Reasenber (1985) in the inverse direction.

The resulting earthquake catalogue corresponds to a Poisson process in time with additional aftershock activity. The distributions of the epicenters and the magnitudes are similar to those of the genuine catalogue. Note that only the spatiotemporal correlations of the seismicity are randomized and all other features are preserved. Therefore, the APCs allow one to test for systematic spatiotemporal behaviour.

The likelihood ratio test has been proposed by Gross and Rundle (1998) in order to compare two models with respect to their suitability to describe an observed data set. In this work, the observed data are given by the set  $Q^i(\mathbf{x})$  of epicenters with  $M \geq 5.0$  after the  $i$ th strongest earthquake. Model 1 is defined by the GCL pattern of the original catalogue before the  $i$ th strongest earthquake, i.e. the distribution of curvature parameters  $C^i(\mathbf{x})$  in space. Model 2 is the corresponding pattern  $C_{\text{APC}}^i(\mathbf{x})$  for an APC. For both models, the likelihood function  $L$  is computed with respect to the  $N$  earthquakes, forming the pattern  $Q^i(\mathbf{x})$ :

$$L = \prod_{k=1}^N P(\mathbf{x}_k, C_k). \quad (4)$$

$P(\mathbf{x}_k, C_k)$  is the normalized probability density for an event occurring at the epicenter  $\mathbf{x}_k$  with a premonitory GCL pattern characterized by the curvature parameter  $C_k$ . To apply the likelihood ratio test, we assume Gaussian probability density functions  $P(\mathbf{x}, C) = p_1(\mathbf{x}) \times p_2(C)$  consisting of a two-dimensional Gaussian function  $p_1$  around the spatial grid node  $\mathbf{x}$  with standard deviation  $\sigma_1$  and a (right wing) Gaussian function  $p_2$  depending on the curvature parameter  $C$  with standard deviation  $\sigma_2$ . The value of  $\sigma_1$  is the distance between two adjacent grid nodes and  $\sigma_2 = 0.35$  is an empirical value (Zöller et al., 2001). It should be noted that Eq. (4) must be applied cautiously, since this equation only holds if the  $N$  earthquakes are statistically independent.

The likelihood function is also measured for each of the APCs (model 2). The likelihood ratio  $LR^i = L/L_{\text{APC}}$  of the normalized likelihood functions for model 1 and model 2 is equal to the probability ratio  $p/p_{\text{APC}}$ , where  $p$  denotes the probability that  $Q^i(\mathbf{x})$  arises from the original data (model 1) and  $p_{\text{APC}}$  is the corresponding probability for the APCs (model 2). In the case of  $LR^i > 1$ , the detected GCL patterns in the original catalogue are more correlated with the subsequent occurring intermediate to large earthquakes. In contrast,  $LR^i < 1$  means that the patterns from the random catalogue are correlated with the future seismicity. Due to a rather skewed distribution of  $LR^i$ , the mean value  $\langle LR^i \rangle$  is not an appropriate measure for the spatial correlations. Instead, we use the number  $N_s^i$  of APCs that is a better fit than the original model ( $LR^i < 1$ ) and represents a more robust

**Table 1.** Results of Likelihood Ratio Test.  $N_s$  is the number of adjusted Poisson catalogues, where the GCL patterns are more correlated with main shock activity than for the CNSS catalogue.  $P_{\text{conf}}$  is the probability that nine random numbers (corresponding to the nine strong earthquakes) have a mean value smaller than or equal to  $\langle N_s \rangle$ . The values in the parentheses are the results for  $\langle N_s \rangle$  and  $P_{\text{conf}}$  without the Kern County earthquake

	Earthquake	date	$M$	$N_s$
a.	Kern County	21 Jul 1952	7.5	85
b.	Landers	28 Jun 1992	7.3	34
c.	Hector Mine	16 Oct 1999	7.1	23
d.	Loma Prieta	18 Oct 1989	7.0	16
e.	Coalinga	2 May 1983	6.7	26
f.	Northridge	17 Jan 1994	6.6	62
g.	San Fernando	9 Feb 1971	6.6	16
h.	Superstition Hills	24 Nov 1987	6.6	28
i.	Borrego Mountain	9 Apr 1968	6.5	51
	$\langle N_s \rangle$			38 (32)
	$P_{\text{conf}}$			89% (97%)

measure. The value of  $N_s^i$  varies between 0 (no APCs fit better than the original model) and 100 (all APCs fit better).

### 3 Results and discussion

Results for the correlation length from Eq. (2) are shown in Fig. 2. The triangles are the earthquakes with  $M \geq 5.0$  occurring during one year after the strong shock with  $M \geq 6.5$  (largest triangle), i.e. the pattern  $Q^i(\mathbf{x})$ . The grey shaded boxes denote the GCL pattern  $C^i(\mathbf{x})$ . Analogously, Fig. 3 is the same for a catalogue from the Poisson process model. Curvature parameters above 0.7 are not shown, since power laws and constant functions are no longer distinguishable.

The likelihood ratio test introduced in Sect. 2 is now applied to compare the patterns  $C^i(\mathbf{x})$  and  $C_{\text{APC}}^i(\mathbf{x})$  with the pattern  $Q^i(\mathbf{x})$ . The quantity  $N_s^i$  ( $0 \leq N_s^i \leq 100$ ), which is the number of APCs that fit better to  $Q^i(\mathbf{x})$  than the original data, is used as a measure for the predictive power of the GCL pattern in the original catalogue before a certain strong earthquake. Note that we do not introduce alarm conditions using threshold values. The results for  $N_s^i$  are given in Table 1. The confidence level  $p_{\text{conf}}$  in the last row is the probability that nine random numbers (corresponding to the nine strongest earthquakes) have a mean value smaller than or equal to  $\langle N_s \rangle = (1/9) \sum_i N_s^i$ .

The spatial correlations of the GCL patterns with the future seismicity are clearly visible in some cases, e.g. the Hector Mine, the Loma Prieta, the Coalinga, and the San Fernando earthquakes. The most conspicuous anomaly can be observed prior to the Loma Prieta earthquake in Fig. 2d.

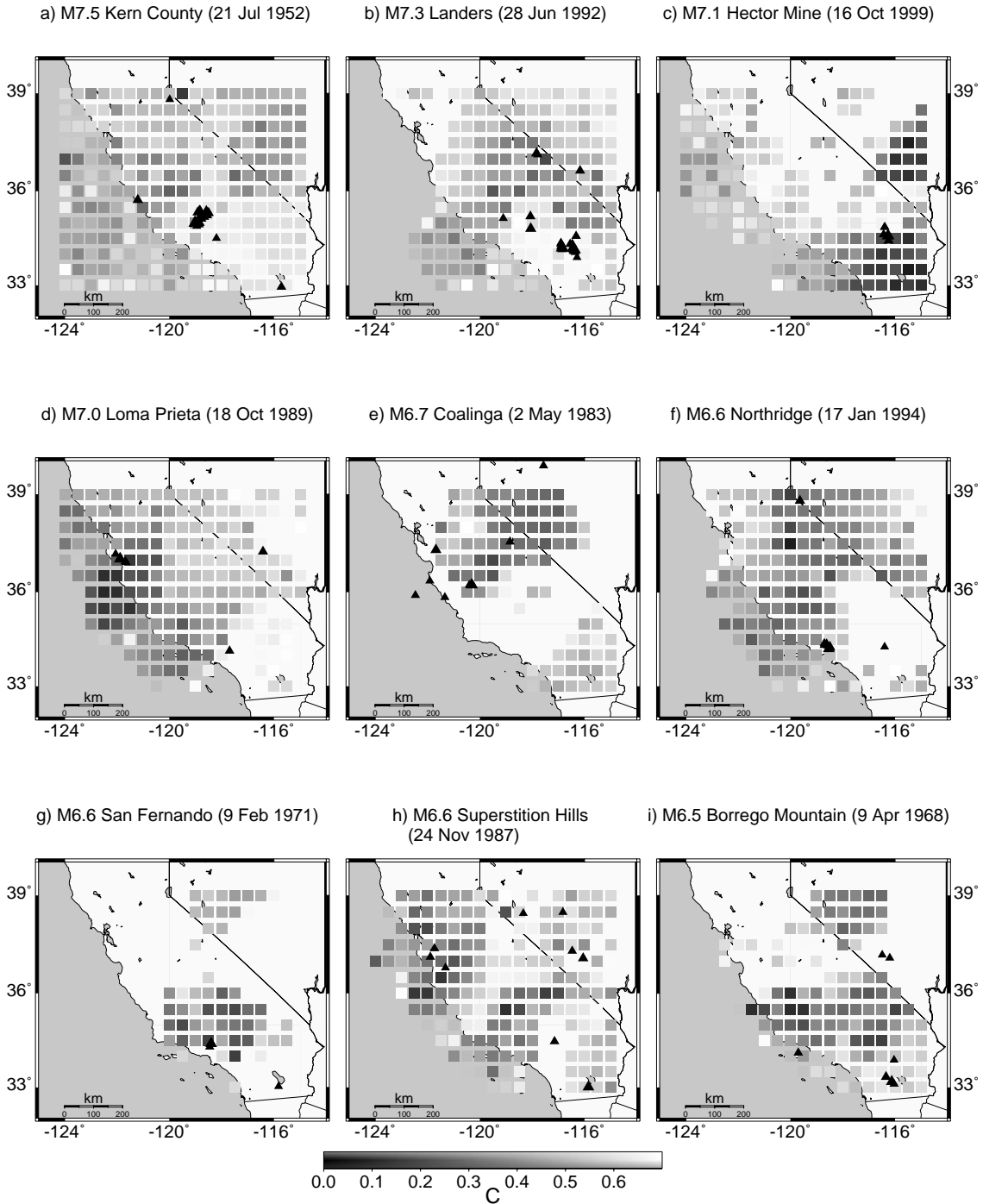


**Fig. 2.** Curvature parameter  $\mathcal{C}$  (grey shaded boxes) based on the GCL pattern. The filled triangles are the strong earthquakes (largest triangle) and the earthquakes with  $M \geq 5.0$  until one year after these events.

This is probably due to the fact that there had been no other strong earthquake in the Loma Prieta region since 1910 and consequently, the GCL pattern of this event is not disturbed by the overlapping patterns from the other events. In contrast, the result for the Kern County earthquake is close to a random response. A possible explanation is that the quality and the length of the data may not be sufficient prior to 1952.

As we have checked, the result for the Kern County event can be slightly improved with a magnitude cutoff of  $M_{\text{cut}} = 4.5$  instead of  $M_{\text{cut}} = 4.0$ . The confidence level  $p_{\text{conf}} = 89\%$  for the nine strongest earthquakes is below the typical confidence levels for statistical hypothesis tests, e.g.  $p = 95\%$ . However, if the Kern County earthquake is excluded from the analysis due to a lack of data quality, we obtain  $\langle N_s \rangle = 32$

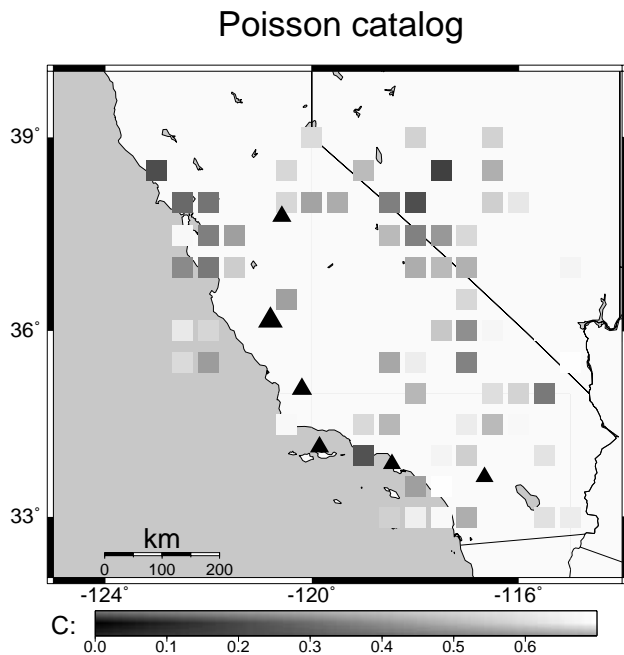


**Fig. 3.** Curvature parameter  $\mathcal{C}$  (grey shaded boxes) with respect to a strong earthquake ( $M = 7.0$ ) for an adjusted Poisson catalogue (APC). The filled triangles are the earthquakes with  $M \geq 5.0$  until one year after these events.

and a resulting probability of  $p_{\text{conf}} = 97\%$ . In this case, the null hypothesis where the results can be reproduced using a realistic Poisson process model without spatiotemporal correlations is rejected with a reasonable high confidence level.

We want to point out that all parameters in our analysis are fixed empirically or determined by the optimization techniques described in the previous section. This is a first order approach which may ignore important information in the data, leading to small significances. Therefore, it is important to determine parameters by physical conditions, e.g. scaling relations such as  $\log R = c_1 + c_2 M$  with constants  $c_1$  and  $c_2$  for the space window  $R$  (Bowman et al., 1998; Zöller et al., 2001) and  $\log T = c_3 + c_4 M$  with constants  $c_3$  and  $c_4$  for the time window  $T$  (Hainzl et al., 2000), as well as search magnitudes should be introduced in order to increase the significances. This would also be a step towards a prediction algorithm, where a spatiotemporal search for anomalies can be conducted. By introducing threshold values in terms of alarm conditions, an analysis by means of error diagrams (Molchan, 1997) could then be carried out. These refinements and extensions are left for future studies.

#### 4 Summary and conclusions

We have tested the hypothesis that spatial anomalies according to the critical point concept for earthquakes occur before strong earthquakes. Therefore, we have used the growing spatial correlation length as an indicator for critical point behaviour. To reduce the number of free parameters, we have

fixed the magnitude cutoff and the critical exponent by values known from the literature. The remaining parameters, namely, space and time windows have been determined systematically by an optimization technique. From a likelihood ratio test in combination with a sophisticated Poisson process model, we have extracted a statistical confidence level.

By applying a search algorithm in space, we find a rough agreement of the predicted regions with future seismicity. Although false alarms and false negatives are present, the original data provide significantly better results than the Poisson process model. The confidence level of 89% is enhanced by excluding the Kern County (1952) earthquake due to a lack of data quality. Further improvements in both the GCL model itself and the statistical test are possible. In particular, it is desirable to map directly probabilities instead of curvature values. This would allow one to compare the present analysis with similar approaches, especially with models based on accelerating energy/moment release.

In conclusion, we have shown that the critical point concept makes a contribution to the improvement of the seismic hazard assessment. Further studies and applications of the methods are promising to increase the significance of the results.

*Acknowledgements.* This work was supported by the Deutsche Forschungsgemeinschaft (SFB 555 and SCH280/13–1). The earthquake data used in this study have been provided by the Northern California Earthquake Data Center (NCEDC) and include contributions of the member networks of the Council of the National Seismic System (CNSS). To produce the figures, we used the GMT system (Wessel and Smith, 1991).

#### References

- Bowman, D. D., Oullion, G., Sammis, C. G., Sornette, A., and Sornette, D.: An observational test of the critical earthquake concept, *J. Geophys. Res.*, 103, 24 359–24 372, 1998.
- Brehm, D. J. and Braile, L. W.: Intermediate-term earthquake prediction using precursory events in the New Madrid Seismic Zone, *Bull. Seismol. Soc. Am.*, 88, 564–580, 1998.
- Brehm, D. J. and Braile, L. W.: Intermediate-term earthquake prediction using the modified time-to-failure method in southern California, *Bull. Seismol. Soc. Am.*, 89, 275–293, 1999.
- Bufe, C. G. and Varnes, D. J.: Predictive modeling of the seismic cycle of the greater San Francisco Bay region, *J. Geophys. Res.*, 98, 9871–9883, 1993.
- Das, S. and Scholz, C. H.: Theory of time-dependent rupture in the Earth, *J. Geophys. Res.*, 86, 6039–6051, 1981.
- Gross, S. and Rundle, J.: A systematic test of time-to-failure analysis, *Geophys. J. Int.*, 133, 57–64, 1998.
- Gutenberg, B. and Richter, C. F.: Earthquake magnitude, intensity, energy and acceleration, *Bull. Seismol. Soc. Am.*, 46, 105–145, 1956.
- Hainzl, S. and Zöller, G.: The role of disorder and stress concentration in nonconservative fault systems, *Physica A*, 294, 67–84, 2001.
- Hainzl, S., Zöller, G., and Kurths, J.: Similar power laws for foreshock and aftershock sequences in a spring-block model for earthquakes, *J. Geophys. Res.*, 104, 7243–7253, 1999.

- Hainzl, S., Zöller, G., Kurths, J., and Zschau, J.: Seismic quiescence as an indicator for large earthquakes in a system of self-organized criticality, *Geophys. Res. Lett.*, 27, 597–600, 2000.
- Jaumé, S. C. and Sykes, L. R.: Evolving towards a critical point: A review of accelerating seismic moment/energy release prior to large and great earthquakes, *Pageoph*, 155, 279–306, 1999.
- Leckie, F. A. and Hayhurst, D. R.: Constitutive equations for creep rupture, *Acta Metall.*, 25, 1059–1070, 1977.
- Molchan, G. M.: Earthquake prediction as a decision-making problem, *Pageoph*, 149, 233–247, 1997.
- Omori, F.: On the aftershocks of earthquakes, *J. Coll. Sci. Imp. Univ. Tokyo*, 7, 111–200, 1894.
- Reasenberg, P.: Second-order moment of central California seismicity, *J. Geophys. Res.*, 90, 5479–5495, 1985.
- Wessel, P. and Smith, W. H. F.: Free software helps map and display data, *Eos Trans., AGU*, 72, 441, 445–446, 1991.
- Zöller, G., Engbert, R., Hainzl, S., and Kurths, J.: Testing for unstable periodic orbits to characterize spatiotemporal dynamics, *Chaos, Solitons and Fractals*, 9, 1429–1438, 1998.
- Zöller, G., Hainzl, S., and Kurths, J.: Observation of growing correlation length as an indicator for critical point behaviour prior to large earthquakes, *J. Geophys. Res.*, 106, 2167–2176, 2001.

# Appendix F

A systematic test on precursory seismic quiescence in Armenia

Autors:	G. Zöller, S. Hainzl, J. Kurths, and J. Zschau
Journal:	<i>Natural Hazards,</i>
Volume (Nr.):	<b>26(3)</b>
Pages:	245-263
Year:	2002





## A Systematic Test on Precursory Seismic Quiescence in Armenia

G. ZÖLLER, S. HAINZL and J. KURTHS

*Institute of Physics, University of Potsdam, POB 60 15 53, 14415 Potsdam, Germany, E-mail: gert@agnld.uni-potsdam.de*

J. ZSCHAU

*Division for Solid Earth's Physics and Disaster Research, GeoForschungsZentrum Potsdam, Telegrafenberg, 14473 Potsdam, Germany*

(Received: 6 November 2000; accepted: 18 July 2001)

**Abstract.** A systematic test on seismic quiescence occurring before large earthquakes is conducted. For a fixed geographical location, the degree of clustering in space and time is analysed and the results are tested against randomized earthquake catalogs. A gridding technique allows to investigate the entire spatial volume covered by a certain earthquake catalog. The result is a significance  $K(\vec{x}, t)$  for seismic quiescence as a function of space and time. A point  $(\vec{x}, t)$  is considered as quiet, if  $K(\vec{x}, t)$  exceeds a threshold value  $K^{(99)}$  such that the null hypothesis is rejected with a probability of  $p \geq 99\%$ . Because earthquake clusters, like aftershocks and swarm events, generate erroneous quiescence, declustered catalogs are also investigated and the influence of the clusters is discussed. Applying this method to an earthquake catalog from Armenia, several cases of seismic quiescence before mainshocks are obtained. These quiescence periods occur in the original data as well as in the declustered data. Using alarm conditions, it is found that quiescence periods and mainshocks are correlated 'better-than-chance'. Thus, the results support the claim that seismic quiescence makes a contribution to the improvement of seismic hazard assessment.

**Key words:** seismic quiescence, statistical methods, earthquake prediction.

### 1. Introduction

In the recent past, an extensive discussion about the predictability of earthquakes and the significance of earthquake precursors has taken place (Nature debate, 1999). Many seismologists claim that some individual earthquakes should be predictable on the basis of precursory phenomena (Wyss, 1997a). Some of these observed premonitory phenomena are foreshocks (Jones and Molnar, 1979), periods of seismic quiescence (Habermann, 1988; Wyss and Habermann, 1988a), and patterns related to critical point dynamics in terms of accelerating moment release (Jaumé and Sykes, 1999) or growing spatial correlation length (Zöller *et al.*, 2001).

The counterclaim to the predictability based on precursory phenomena is the conclusion that earthquakes are inherently unpredictable (Geller *et al.*, 1997), because the earth is assumed to be in a state of self-organized criticality (SOC). In

this context, the significance of precursory phenomena is brought into question, because they are detected only in a limited number of cases using special values for free parameters. However, Hainzl *et al.* (2000) have shown that also in models obeying SOC, precursory phenomena occur. Especially, the detection of seismic quiescence can improve the hazard assessment in these models. The aim of this work is a systematic mapping of periods of seismic quiescence in a real earthquake catalogue and to test if positive correlations with the largest earthquakes exist.

The role of seismic quiescence as a promising candidate for an intermediate-term precursor to large earthquakes has been discussed in numerous publications (Wyss and Habermann, 1988a, 1988b; Ogata, 1992; Wyss, 1997a, 1997b; Hainzl *et al.*, 1999, 2000). Possible mechanisms for the occurrence of seismic quiescence are presented in Dieterich (1978), Dieterich and Okubo (1996), Kato *et al.* (1997), Rudnicki (1988), and Scholz (1988). It typically extends over the rupture zone of the subsequent mainshock and lasts for months to years. However, the detection of quiescence in earthquake catalogs is not straightforward due to the following reasons: (1) The occurrence of seismicity rate variations in earthquake data is “a complex mixture of real and man-made changes” (Habermann, 1987). The latter mostly arise from network changes and systematic changes in magnitudes. (2) The significance of an observed signal, e.g., a seismic quiescence, depends on the data quality as well as on the statistical testing procedure itself. For instance, the detection of quiescence becomes questionable, if the background seismicity is too low. (3) A proper definition of the background seismicity is required. The present work mainly deals with points (2) and (3). For the discrimination between real and ‘man-made’ changes, the reader is referred to Habermann (1987).

In this work, a weighted sum of earthquakes above a fixed magnitude is used to quantify seismic clustering. The weights decrease with increasing distance in space and time ( $C$ -value). The inverse of  $C$ , called  $Q$ -value, is a measure for quiescence. A common problem of all approaches is the choice of parameters needed for the analysis, e.g., space and time windows, and the magnitude cutoff. Since the quiescence signal depends on these parameters, the separation of precursory quiescence and random rate decreases is not clear. Therefore, randomized earthquake data are used to compute significances for seismic quiescence (Theiler *et al.*, 1992; Zöller *et al.*, 1998). This approach is based on bootstrap techniques (Efron and Tibshirani, 1993; Künsch, 1989), which are well-known in time series analysis. Because each  $Q$ -value of the original data can be compared with a mean value of a large number of random data, a higher degree of robustness is expected for the results.

In Section 2, the earthquake catalog and the data analysis technique are described in detail. The results of the analysis are presented and discussed in Section 3. Finally, the conclusions are given in Section 4.

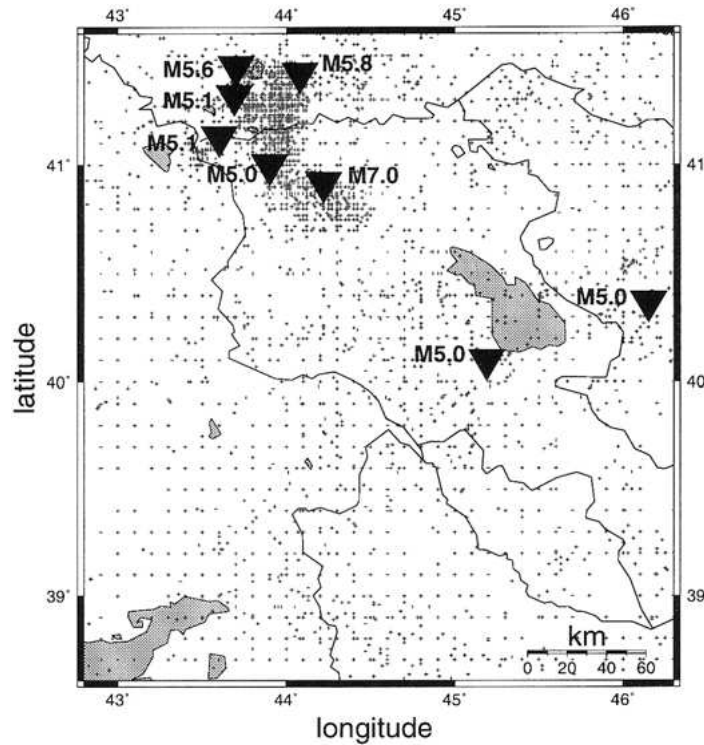


Figure 1. Map of the study area and earthquake distribution between 1962 and 1996. The crosses denote the earthquakes with  $M \geq 2.2$ ; the triangles denote the earthquakes with  $M \geq 5.0$ .

## 2. Data and Method

### 2.1. DATA AND PRE-PROCESSING

An earthquake catalog for the Armenia region ( $38.2^{\circ}$ – $42.0^{\circ}$ N/ $42.0^{\circ}$ – $47.0^{\circ}$ E) is investigated, which has been recorded by the National Survey for Seismic Protection of the Republic of Armenia between 1962 and 1996. Armenia and the adjacent regions are characterized by a diffusive distribution of earthquake epicentres, which is due to the typical mosaic-block structure formed by several differently orientated faults (Balassanian *et al.*, 1997). The study area is shown in Figure 1.

The data set contains the times, the coordinates of the epicentres, and the surface magnitudes for the total number of 11,781 events with  $M \geq 2.0$ . The depths are not taken into account, because of their large uncertainties. The epicentres are calculated to the nearest  $0.1^{\circ}$ . A change of the epicentre accuracy may introduce small volumes of erroneous seismic quiescence. Therefore, only quiescence volumes exceeding a certain size will be considered as candidates for precursory patterns (see Section 3.1).

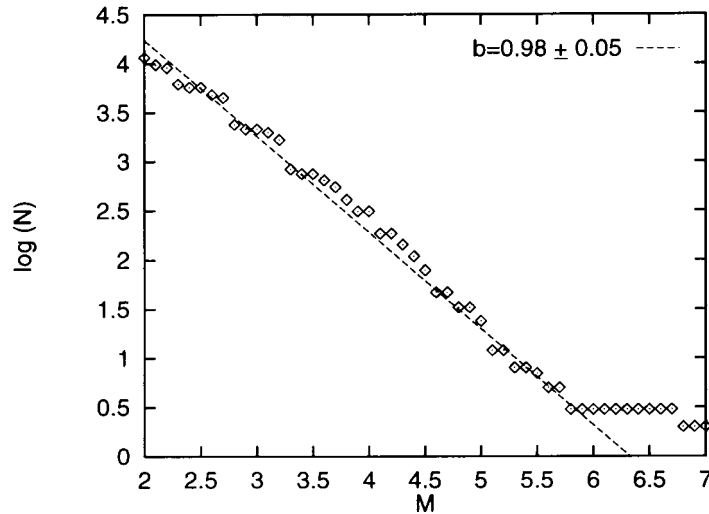


Figure 2. The frequency magnitude relation (Gutenberg–Richter law) for the Armenia data. The solid line is a fit for  $b = 0.98$  (Richter  $b$ -value).

Figure 2 shows the frequency magnitude relationship (Gutenberg and Richter, 1954) of the catalog. A straight line with the slope (Richter- $b$  value)  $b = 0.98 \pm 0.05$  is in good agreement with the distribution of magnitudes  $M \in [2.2; 5.8]$ . Thus, a lower magnitude cutoff according to  $M \geq 2.2$  is introduced. The remaining 9,314 events are the basis for the further investigations.

A detailed analysis of the catalogue homogeneity and the magnitude of completeness  $M_c$  as a function of space and time has been conducted by Wyss and Martirosyan (1998) for the same catalogue as in the present study. They found no artificial rate changes in time, but a dependence of  $M_c$  on the space. In particular,  $M_c$  increases for longitudes smaller than  $39.7^\circ$  and greater than  $41.8^\circ$  to  $M_c = 2.8$ . As Zuniga and Wiemer (1999) and Zuniga and Wyss (1995) have shown, the completeness considerations are important for the choice of the study area and should be carried out carefully to avoid misleading interpretations of observed seismicity patterns. However, the present analysis is based on the detection of relative quiescence, rather than absolute rate decreases. That is, only significant deviations from a local background seismicity are detected. Consequently, spatial changes of the magnitude of completeness can be neglected, if  $M_c$  is approximately constant in time. The quiescence analysis is thus conducted in the whole region shown in Figure 1. This study area is chosen slightly smaller than the original catalog in order to avoid boundary effects (see also Section 2.4).

Another important source of man-made changes is the occurrence of quarry blast events. Wiemer and Baer (2000) have shown that these events can be detected by comparing the daytime rate of earthquakes with the nighttime rate. For the whole study area, this analysis results in an increased activity at noon. A spatial mapping of this rate leads to the identification of two locations in the Armenian

catalogue, where a significant number of quarry blasts is probably present. These events occur with a rate that is approximately constant in time. As a consequence, the quarry explosions may introduce only artificial quiescence periods with durations of hours to days, whereas the present analysis focuses on time scales of months to years.

## 2.2. DETECTING SEISMIC QUIESCENCE

For the quantification of seismic quiescence, counting rates with additional weights corresponding to spatial and temporal overlap volumes are used (Zschau, 1998). In the following, the method is described briefly:

1. The function  $C(\vec{x}, t)$  is defined as the weighted sum of all earthquakes occurred at time  $T_i$  with epicentre  $\vec{X}_i$  in the past ( $T_i \leq t$ ):

$$C(\vec{x}, t) = \sum_{T_i < t} w^{\text{space}}(\vec{x}, \vec{X}_i) w^{\text{time}}(t, T_i), \quad (1)$$

The spatial weight  $w^{\text{space}}(\vec{x}, \vec{X}_i) = V(\vec{x}, \vec{X}_i)/(\pi R^2)$  contains the overlap volume  $V(\vec{x}, \vec{X}_i)$  of two circles with the same radius  $R$  surrounding the epicentre  $\vec{X}_i$  and the point  $\vec{x}$ , respectively:

$$V(\vec{x}, \vec{X}_i) = R^2 \cdot \begin{cases} 2 \arccos\left(\frac{r_i}{2R}\right) - \sin\left[2 \arccos\left(\frac{r_i}{2R}\right)\right], & r_i \leq 2R \\ 0, & \text{else,} \end{cases} \quad (2)$$

where  $r_i = |\vec{x} - \vec{X}_i|_S$  is the distance on the sphere.

The time weight  $w^{\text{time}}(t, T_i)$  is a piecewise linear function:

$$w^{\text{time}}(t, T_i) = \begin{cases} 1 - \frac{t-T_i}{T}, & 0 \leq t - T_i \leq T \\ 0, & \text{else.} \end{cases} \quad (3)$$

2. The inverse of  $C$  is a measure for seismic quiescence:

$$Q(\vec{x}, t) = 1/C(\vec{x}, t). \quad (4)$$

As an example, the function  $Q(\vec{x}, t)$  is calculated at the location  $\vec{x} = (40.92^\circ\text{N}, 44.22^\circ\text{E})$  of the M7 Spitak earthquake (8 December 1988) using  $2R = 60$  km and  $T = 600$  days (see Figure 3). The curve shows several peaks indicating less seismic activity. However, these signals have to be divided into real quiescence periods and statistical fluctuations. Therefore, 100 synthetic earthquake catalogs are generated by randomizing the spatiotemporal correlations in the data. In particular, the epicentres have been shuffled as a function of the time:  $(t_i, \vec{x}_i) \rightarrow (t_i, \vec{x}_{\text{rand}(i)})$ , where  $\text{rand}(\cdot)$  maps the index  $i$  on a randomly selected index  $j$ . The dashed line in Figure 3 shows the average of  $Q$  over the 100 synthetic catalogs; the errorbars indicate three standard deviations:  $\langle Q^{\text{sur}} \rangle \pm 3\sigma^{\text{sur}}$ . The comparison of both curves shows that before the Spitak earthquake,  $Q$  deviates most significantly from the background seismicity, which is assumed to be given by the synthetic earthquake data.

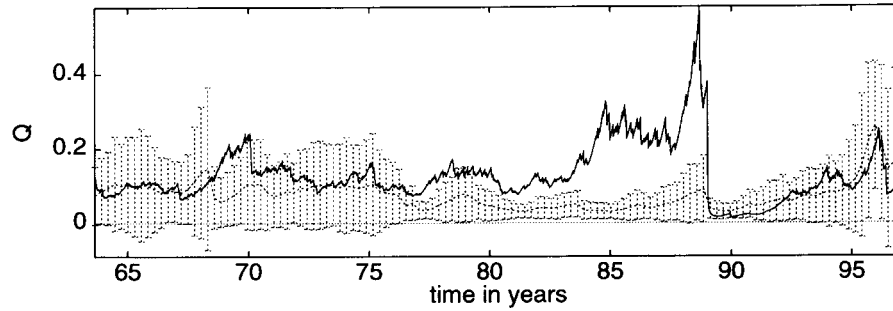


Figure 3. The function  $Q(t)$  at the location of the M7 Spitak earthquake on 7 December 1988. The solid line results from the original earthquake catalog. The dashed line is the average of 100 surrogate catalogs, each generated by scrambling the original data. The errorbars denote three standard deviations:  $\langle Q^{\text{sur}} \rangle \pm 3\sigma^{\text{sur}}$ .

### 2.3. THE NULL HYPOTHESIS

A proper definition of a null hypothesis is not straightforward (Stark, 1997; Kagan, 1997). In this paper, the null hypothesis is constructed simply by randomizing the locations of the earthquakes in the original catalog, so that the spatiotemporal correlations in the data are destroyed. This technique is convenient, because the null hypothesis is derived directly from the data set itself (Theiler *et al.*, 1992; Zöller *et al.*, 1998) such that the statistical structure of the data is preserved. In detail, the following null hypothesis for seismic quiescence is defined:

*Null Hypothesis.* The function  $Q(\vec{x}, t)$  for real earthquakes can be modelled by  $Q^{\text{sur}}(\vec{x}, t)$  obtained from surrogate earthquake data with randomized dynamics but the same statistical properties.

An important property of the surrogate data is the conservation of the event distributions, i.e., the time distribution and the spatial distribution of earthquakes. Consequently, the frequency magnitude relation shown in Figure 2 is preserved. Only the dynamics is randomized by scrambling the epicentres and thus, destroying the spatiotemporal correlations. The main advantage of this technique is that important constraints of the earthquake data remain the same.

However, the surrogate data have to be considered carefully. Therefore, note that the original data, which are the basis for the randomization, are not uniformly distributed; they contain either aftershocks and other clusters like earthquake swarms. These clusters are distributed over the entire catalog by the randomization. As a consequence, the seismic rate increases outside the cluster volume and artificial quiescence is measured almost everywhere, when original data and surrogate data are compared. There are two methods to deal with the cluster problem (Kagan and Vere-Jones, 1996): (A) declustering the earthquake catalog and (B) using a null hypothesis which explicitly includes clustering. Both techniques are related to additional parameters, because they depend on the definition of a cluster. With

respect to the latter method, a special kind of randomization, which is performed by a sequence of transpositions of two events,  $i \leftrightarrow j$ , is introduced. First, an event  $i$  is picked up randomly from the catalog. For a uniform randomization the probability that  $i$  is exchanged with  $j$ , is independent of  $i$  and  $j$ :  $p_{ij} = 1/n$ , where  $n$  is the total number of earthquakes in the catalog. In contrast to this, a Gaussian probability distribution for a modified null hypothesis is introduced:

$$p_{ij} \sim e^{-\frac{1}{2}\left(\frac{r_{ij}}{r_0}\right)^2}, \quad (5)$$

where  $r_{ij}$  is the distance of the epicentres of  $i$  and  $j$ ; the parameter  $r_0$  is set to  $r_0 = 50$  km. This technique favours a more localized randomization. Although the influence of the clusters decreases, artificial quiescence is still present. This is not surprising, because the spatial extension of most clusters is less than the typical distance  $r_0$ . On the other hand,  $r_0$  can not be chosen arbitrarily small, because the total number of events is relatively small and inhomogeneously distributed. Therefore, the method proposed by Kagan and Vere-Jones (1996) is also used. Declustered catalogs are calculated to identify quiet periods, which are artificial. Applying the decluster algorithm of Reasenberg (1985) with the parameters from Arabasz and Hill (1996), a data set of 7,892 events with  $M \geq 2.2$  remains.

Note that the declustering is an additional pre-processing of the data and thus independent of the randomization. In the next section, the test of the null hypothesis is described. The testing procedure is then applied to the original earthquake catalog including clusters, as well as to the declustered catalog.

#### 2.4. TEST OF THE NULL HYPOTHESIS

The modeling procedure can be divided into four steps and is performed for the times  $t, t + \Delta T, t + 2\Delta T, \dots$ .

- (i) For a fixed location  $\vec{x}$  and a time  $t$  the set of all events that occurred before  $t$  is considered.
- (ii) For this reduced catalog,  $N$  surrogate data sets are created by randomization.
- (iii) The statistical significance

$$K(t) = \frac{Q(t) - \langle Q^{\text{sur}} \rangle(t)}{\sigma^{\text{sur}}(t)} \quad (6)$$

is calculated, where  $\langle Q^{\text{sur}} \rangle(t)$  is the average of  $Q$  over all surrogates and  $\sigma^{\text{sur}}(t)$  the corresponding standard deviation.

- (iv) Set  $t \rightarrow t + \Delta T$  and go back to item 1.

In order to detect precursory phenomena, only events from the past ( $T_i \leq t$ ) are used to model  $Q$  at time  $t$ . Due to statistical reasons, the number of events with

$T_i \leq t$  as well as the number of events within the space–time window should not be too small. Hence, the calculations are restricted – arbitrarily – to  $t \geq 1/1980$ , so that the past contains at least 4000 earthquakes with  $M \geq 2.2$  (3500 in the declustered catalog). Furthermore, the condition is introduced that for one location  $\vec{x}$  at least three events have to satisfy for each time  $t$  the conditions  $r_i \leq 2R$  and  $0 \leq t - T_i \leq T$  from Equations (2) and (3). Else, the modelling at the location  $\vec{x}$  is not taken into account.

The steps (i) to (iv) are performed for the nodes  $\vec{x}_j$  of a  $50 \times 50$  grid in space. To avoid boundary effects, a grid that covers only the central region in space ( $38.6^\circ$ – $41.6^\circ$ N/ $42.8^\circ$ – $46.3^\circ$ E) is considered. The parameters are  $2R = 60$  km and  $T = 600$  days in order to approximate quiescence episodes with intermediate size and duration; the time bin in item 4. is set to  $\Delta T = 25$  days. For each time step a number of  $N = 100$  surrogate data files is generated.

The aforementioned procedure provides the significance  $K(\vec{x}, t)$  as a function of space and time. To transform the significance into a probability, the distribution of  $Q$ -values has to be considered. The value, below which 99% of the results fall, is extracted from each distribution and the corresponding significance  $K^{(99)}(t)$  is calculated from Equation (6). As a conservative approximation the threshold  $K^{(99)} = \max_t K^{(99)}(t)$  is chosen for the rejection of the null hypothesis. For the original catalog,  $K^{(99)} = 12$ , respectively for the declustered catalog  $K^{(99)} = 8$ , is found.

### 3. Data Analysis

#### 3.1. PERIODS OF SEISMIC QUIESCENCE IN THE ARMENIA REGION BETWEEN 1980 AND 1997

The technique introduced in the previous section is now applied to detect periods of seismic quiescence prior to mainshocks. Therefore, earthquakes with magnitude  $M \geq 5.0$  are investigated. The original catalog with clusters contains nine such events including one aftershock in the time between 1980 and 1996. These earthquakes are listed in Table I. The aftershock (event 4a in Table I) is not considered as a mainshock in the further investigations.

In order to analyse temporal correlations between quiescence and mainshocks, the fraction  $V_Q$  of quiet grid nodes, namely of grid nodes with  $K \geq K^{(99)}$  (see Equation (6)), is calculated for each time step  $t$ . Figure 4 shows the results for the earthquake catalog including clusters (Figure 4(a)) and those for the declustered catalog (Figure 4(b)). The figure shows at least four different periods of quiescence. The results obtained for the original data and the declustered data have two main differences: first, the aforementioned artificial periods of quiescence after the mainshocks, which are due to the shuffled aftershock sequences in the surrogate data, are absent in the case of declustering. Second, the results for the declustered data show a quiescence in the beginning of 1983, which is not present in the original data.



Table I. Earthquakes in the Armenia region with  $M \geq 5.0$  in the time between 1/1980 and 12/1996. Event 4a is probably an aftershock of event 4.

No.	Date	Lon. (deg.)	Lat. (deg.)	Mag.
1	June 16, 1982	43.90	41.00	5.0
2	Sep. 20, 1984	44.08	41.42	5.8
3	May 13, 1986	43.70	41.45	5.6
4	Dec. 7, 1988	44.22	40.92	7.0
4a	Dec. 7, 1988	44.22	40.85	5.7
5	Dec. 16, 1990	43.69	41.32	5.1
6	Oct. 6, 1991	43.60	41.13	5.1
7	Dec. 9, 1992	45.19	40.10	5.0
8	Sep. 24, 1994	46.15	40.37	5.0

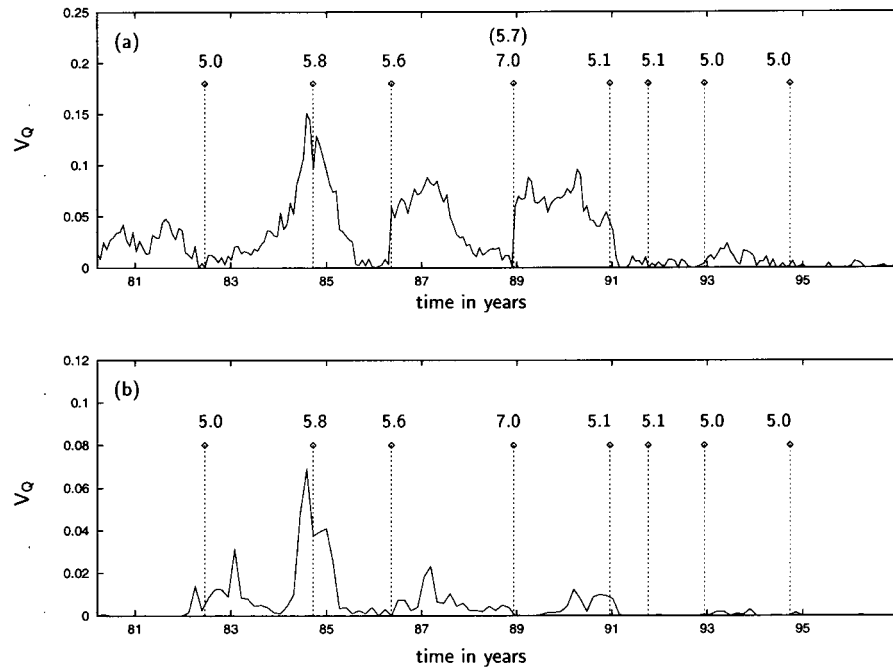


Figure 4. Fraction  $V_Q$  of the total volume covered by seismic quiescence ( $K \geq K^{(99)}$ ) for the original catalog without declustering (a) and the declustered catalog (b). The impulses apply to earthquakes with magnitude  $M \geq 5.0$ .

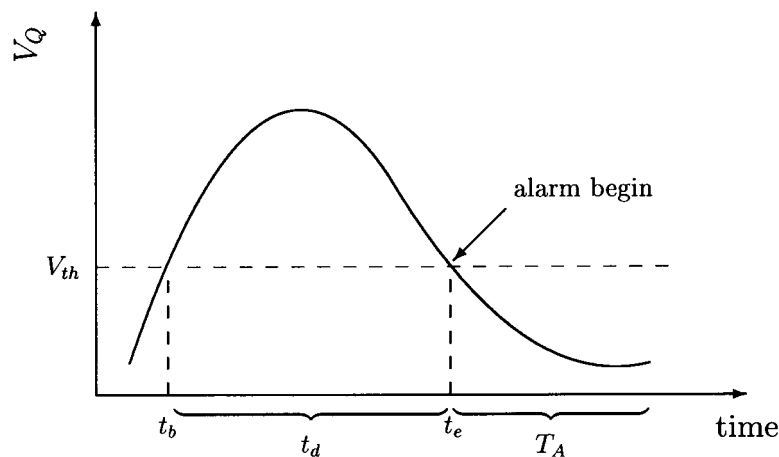


Figure 5. Pictorial definition of begin and end of a quiescence. An alarm is issued at the end of the quiescence.

Although quiescence periods before mainshocks are visible in some cases (see Figure 4), a systematic analysis is required to justify the statement that quiescence periods are correlated with large earthquakes. This problem is addressed in the next section.

### 3.2. TEMPORAL CORRELATIONS BETWEEN QUIESCENCE PERIODS AND MAINSHOCKS

For a quantitative analysis of correlations between quiescence and mainshocks, alarm conditions are defined. Afterward, the predicted events, the false alarms and the failures to predict are counted. Finally, the fraction of time covered by alarm, is computed.

The alarm conditions have the following form:

- (A1) The alarm starts, if the fraction of the quiet volume  $V_Q(t)$  falls below the threshold  $V_{th}$  (time  $t_e$ ).
- (A2) The alarm lasts for  $T_A$ .
- (A3) If condition (A1) is fulfilled during a running alarm, this alarm remains unchanged and no new alarm is issued.

A sketch of the alarm conditions is given in Figure 5.

These alarm conditions are connected with two additional parameters, the threshold volume  $V_{th}$  and the alarm duration  $T_A$ . An event is 'predicted', i.e., recognized by an alarm, if it takes place in an alarm interval  $[t_e; t_e + T_A]$ .

Figure 6 shows the positions of the alarms relative to the mainshocks for a fixed set of parameters. The alarm duration is  $T_A = 10$  months and the threshold

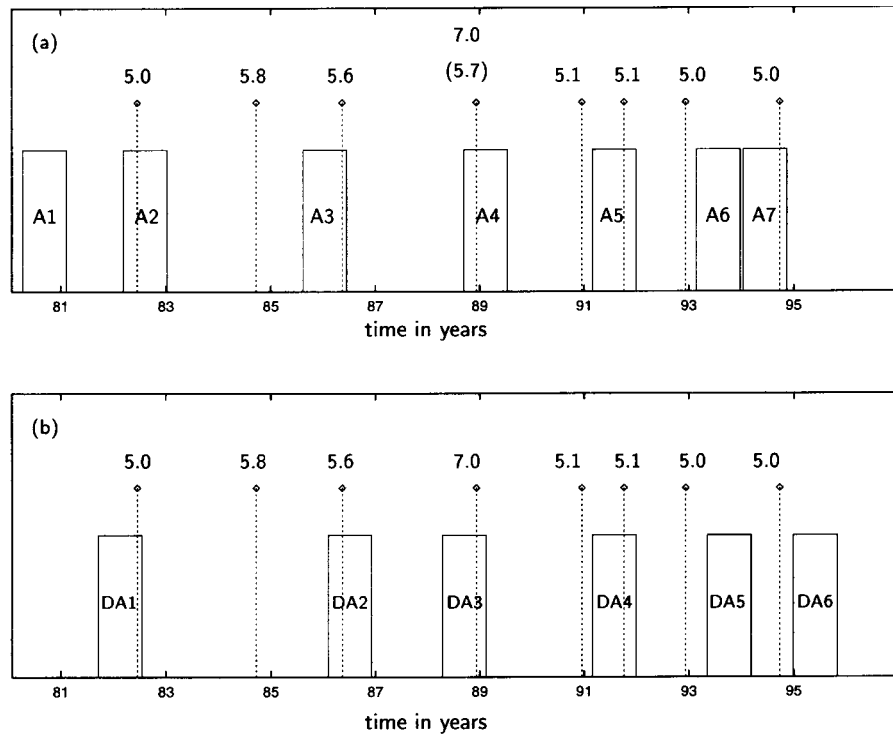


Figure 6. Temporal correlations between alarms (boxes) and earthquakes with  $M \geq 5.0$  (impulses) for the original catalog (a) and the declustered catalog (b). The threshold value for  $V_Q$  is set to  $V_{th} = 1\%$  for the original catalog and  $V_{th} = 0.5\%$  for the declustered catalog; the alarm duration  $T_A$  is 10 months, respectively.

value  $V_{th}$  is chosen to  $V_{th} = 1\%$  for the original catalog and  $V_{th} = 0.5\%$  for the declustered data. For the original catalog, 5/8 of the mainshocks are preceded by an alarm and for the declustered catalog this fraction is 4/8. Among the seven alarms, there are two false alarms and three failures to predict. In Figure 6 the fraction of the total time covered by alarm is 36% for the catalog including clusters (Figure 6(a)) and 31% for the declustered catalog (Figure 6(b)).

It is, however, not clear, if the results in Figure 6 deviate significantly from a random response. Therefore, seven alarms, each lasting for  $T_A$ , are randomly distributed over the entire time interval and the number of mainshocks covered by an alarm  $N_s$  as well as the number of false alarms is extracted. This procedure is repeated 10,000 times. A confidence level can be defined by the probability  $p_c$  to predict less than  $N_s$  mainshocks with these random alarm sets.

This calculation is performed for different values of  $T_A$  and  $V_{th}$ . The results are given in Figure 7 (catalog including clusters) and in Figure 8 (declustered catalog). Each plot corresponds to a fixed alarm duration  $T_A$  and shows the number of alarms and false alarm (lower plot) and the confidence level  $p_c$  (upper plot) as a function of  $V_{th}$ , respectively. The figures demonstrate that the distribution of alarms is, for

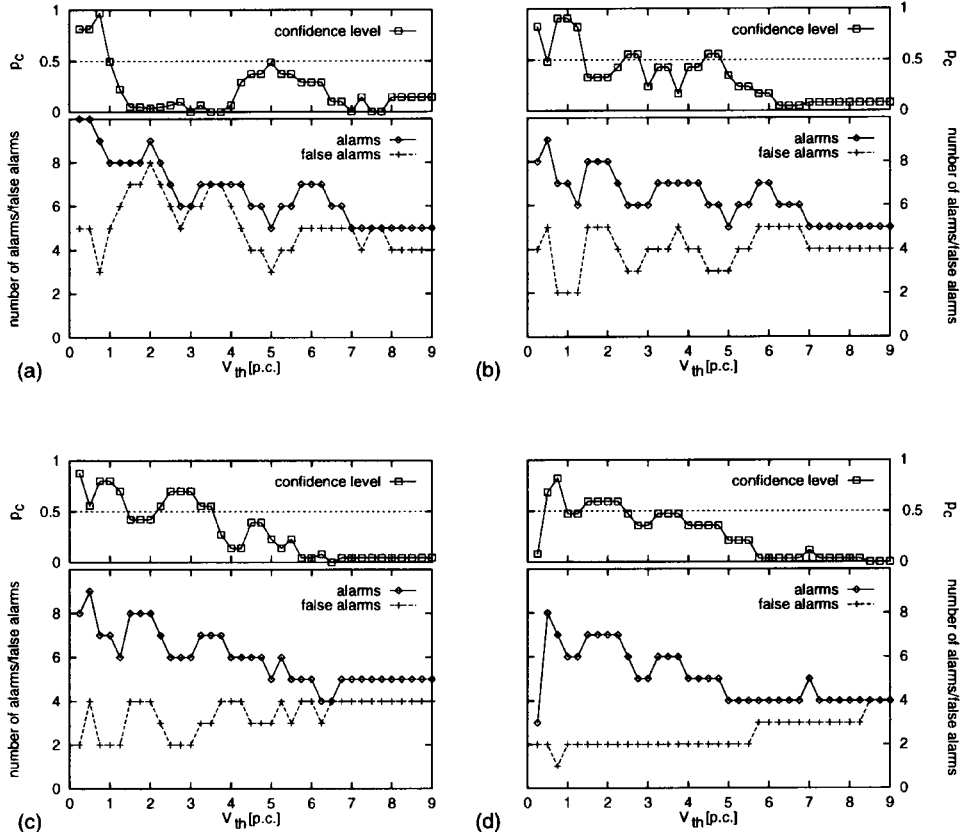


Figure 7. Catalog including clusters: number of alarms and false alarms as a function of the parameters  $T_A$  and  $V_{th}$  (bottom); confidence level  $p_c$  for the alarms not being randomly distributed (top). (a)  $T_A = 8$  months, (b)  $T_A = 10$  months, (c)  $T_A = 12$  months, (d)  $T_A = 15$  months.

certain ranges of the parameters  $V_{th}$  and  $T_A$ , far from being random. This result holds for both, the catalog including clusters and the declustered catalog. The confidence level for the example in Figure 6(a) is  $p_c = 0.91$ . For Figure 6(b) this value is  $p_c = 0.81$ .

### 3.3. LOCATIONS OF THE QUIESCENCE VOLUMES AND SPATIAL CORRELATIONS WITH THE MAINSHOCKS

In the previous section, the computed temporal correlations between episodes of seismic quiescence and subsequent mainshocks have been calculated. For certain alarm conditions, the alarms issued by the quiescence detector are far away from a random response. The alarm conditions correspond to the hypothesis that seismic quiescence prior to mainshocks exists. This hypothesis is rather general, because no further assumptions about the duration and the spatial location are taken into ac-

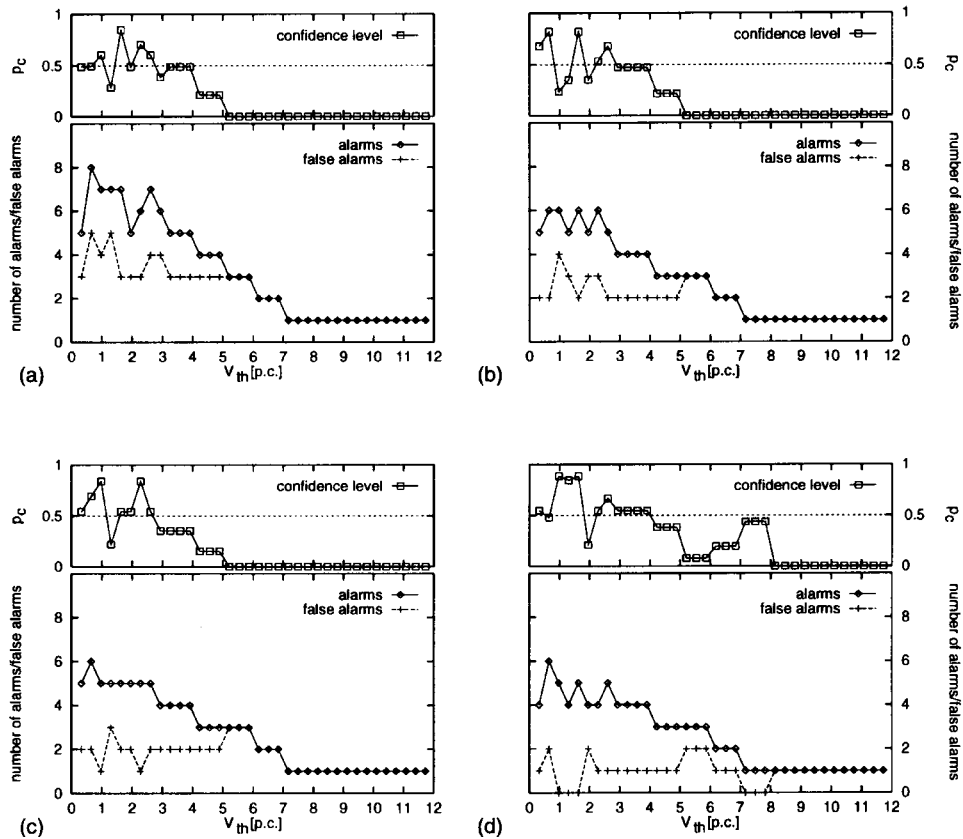


Figure 8. The same as in Figure 7 for the declustered catalogue.

count. The reason for this is that the underlying mechanisms of quiescence are not well understood and may not be applicable for all earthquakes, e.g., the earthquake mechanisms may vary with locations or depth of focus.

Figures 9 and 10 show the location of the quiescence volumes relative to the mainshock epicentre for the ‘successful’ alarms in Figure 6 for the catalog including clusters and the declustered catalog, respectively. Therefore, the quiescence volume has been defined by the set of grid points, which are quiet for at least 10% of the duration  $t_d$  in Figure 5. Short term fluctuations of the quiescence volume are thus suppressed.

Figure 9(c) and Figure 10(c) both provide a quiescence volume near the epicentre of the subsequent Spitak earthquake. In the other cases the quiescence volume is less stable with respect to the declustering procedure. Hence, the quiescence detector leads to the clearest signal for the largest mainshock, the M7 Spitak earthquake.

Finally, a criterion for the ‘prediction’ of the mainshock epicentre is introduced. That is, the mainshock must be located within the quiescence volume. For the

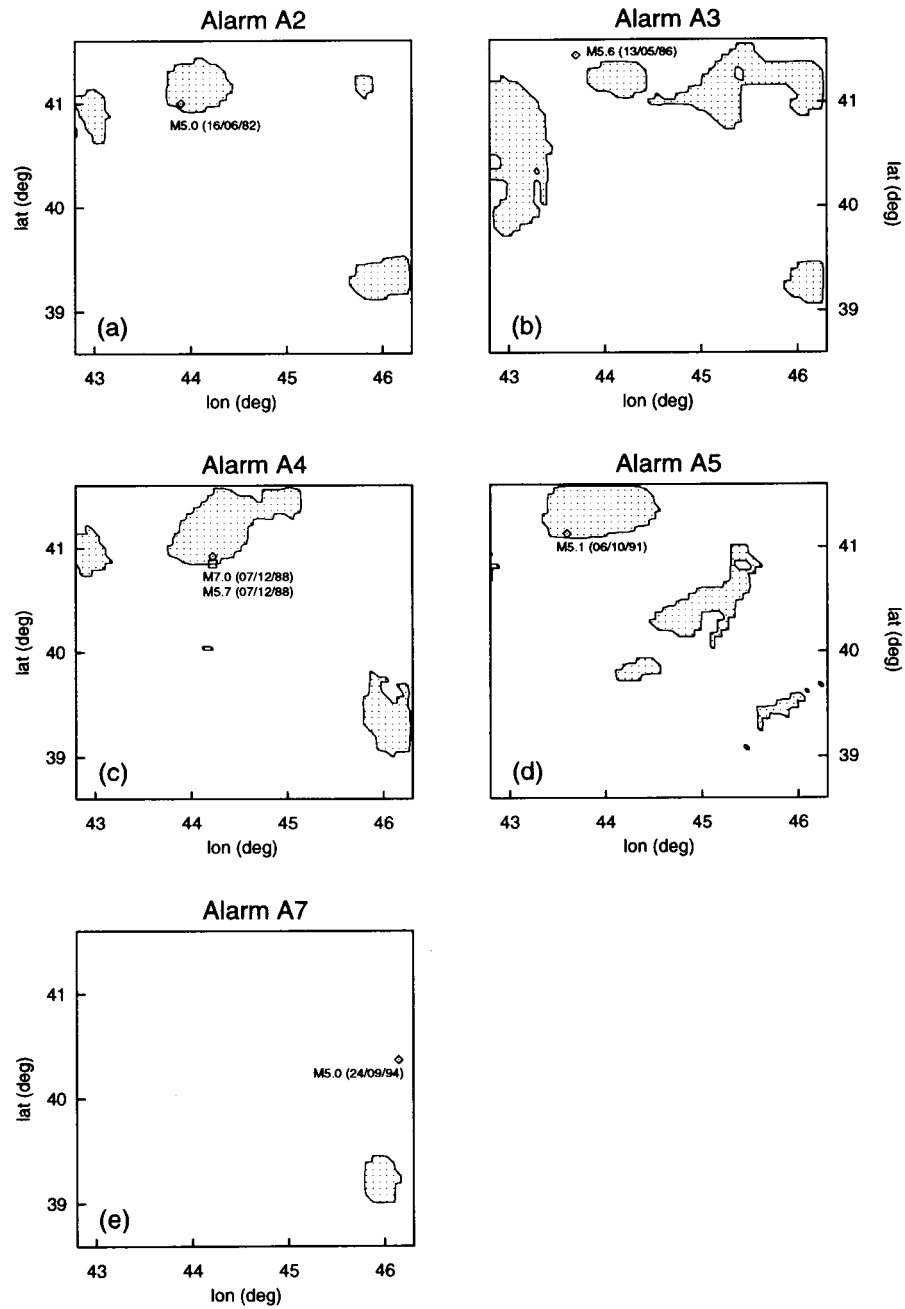


Figure 9. Catalog including clusters: location of the quiescence volume relative to the mainshock epicentre ( $V_{th} = 1\%$ ) for the matched mainshocks in Figure 6(a).

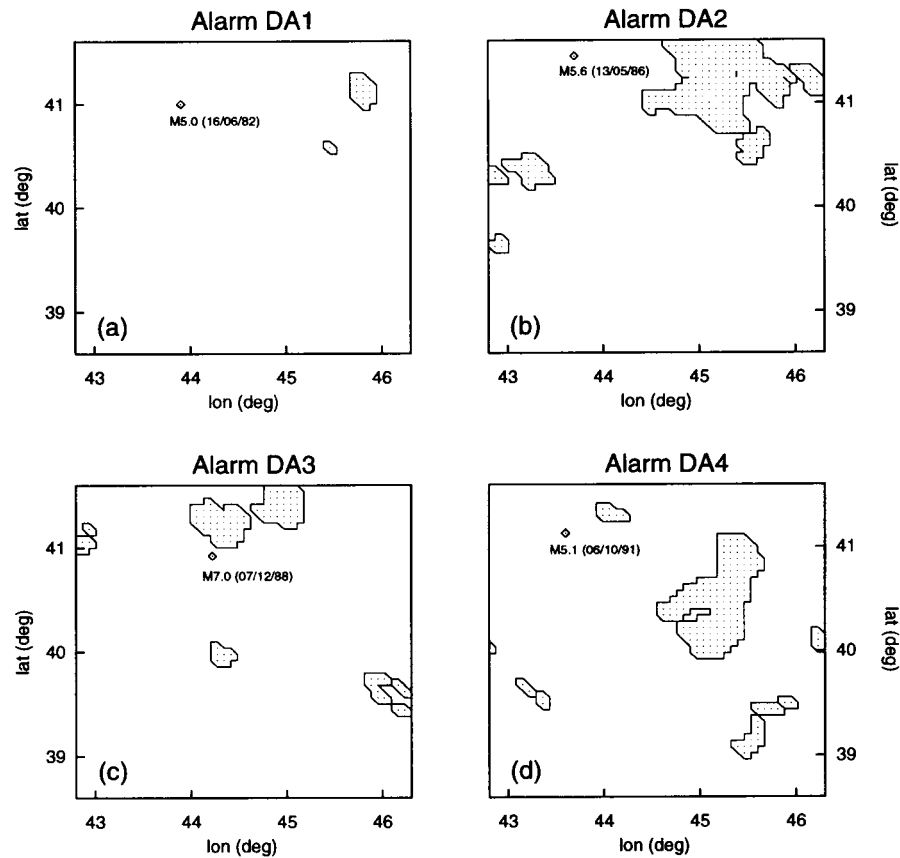


Figure 10. Declustered catalog: location of the quiescence volume relative to the mainshock epicentre ( $V_{th} = 0.5\%$ ) for the matched mainshocks in Figure 6(b).

original catalogue, this criterion results in a rate of 3/8 of predicted mainshocks in time and space. In the declustered catalogue, all mainshocks occur outside the quiescence volume. The fraction of the space-time volume covered with alarms is 3% for the original catalogue and 2% for the declustered catalogue.

### 3.4. THE M7 SPITAK EARTHQUAKE

This subsection deals with the Spitak M7 earthquake, which occurred on 7 December 1988 at 40.92°N, 44.22°E (Balassanian *et al.*, 1995; Rogozin and Philip, 1991). In a detailed study, Balassanian *et al.* (1995) claim that this earthquake was preceded by the quiescence of different durations: 5 years for the future source zone; 1.5 years along the active faults, the junction which coincides with the source zone; 1.5 months for the whole region of the Armenian uplands. This means that there is a relation between the area size and the quiescence duration. In particular, for longer quiescence durations the area is smaller and vice versa.

Wyss and Martirosyan (1998) claim that this earthquake was preceded by a quiescence of  $5 \pm 0.5$  years duration and a maximum extension of approximately 40 km. The quiescence is located north of the epicentre. This is in good agreement with the present result illustrated in Figures 9(c) and 10(c). Furthermore, the technique used in the present work, yields a maximum extension of the quiescence of approximately 80 km in February 1987. For larger values of  $V_{th}$ , the anomaly shrinks, but the location remains stable. Wyss and Martirosyan (1998) use the alarm cube method to show that the anomaly is unique with respect to the statistical significance, if the standard deviate  $z$  which determines the significance level, is increased. Taking into account the different study area, the present analysis confirms this finding, if the parameter  $V_{th}$  is increased. Note that in this approach  $V_{th}$  decides whether an alarm is issued, while this is done by the standard deviate  $z$  in the work of Wyss and Martirosyan (1998).

The main difference is found in the onset and the duration of the quiescence. Contrary to Wyss and Martirosyan (1998), the present analysis leads to a quiescence beginning in May 1986 and lasting for 2.5 years. Therefore, note that the definition of the duration and the extension is arbitrary. Wyss and Martirosyan (1998) determine these parameters by a 75% rate decrease in the crustal volume of the mainshock. This is in contrast to the quiescence detector in the this work, because the quiescence is smoothed out due to the special weights in Equation (1).

In summary, the approach in the present work is different from the those of Wyss and Martirosyan (1998) with respect to the study area, the quiescence hypothesis, the alarm conditions, and the statistical testing. These differences have been introduced in order to conduct a systematic and robust test on seismic quiescence and can also be applied to data from other regions. The fact that despite these differences the results for the Spitak earthquake are very similar, strongly supports the hypothesis that this event was preceded by a clearly pronounced seismic quiescence.

#### 4. Summary and Conclusion

This work deals with seismic quiescence as an intermediate-term precursor to large earthquakes. This phenomenon is known at least since the 1960s, and documented in several case studies. However, case studies are not suitable to assess the statistical significance of quiescence, respectively the benefit for earthquake prediction. To overcome the problem of lacking statistical significance, a systematic spatiotemporal mapping of seismic quiescence with fixed parameters has been conducted using a high quality data record from Armenia.

To quantify seismic quiescence, a simple cluster algorithm has been used. Statistical significances have been derived by means of the concept of surrogate data for spatiotemporal systems. Using a large number of surrogate data files yields results with a high degree of robustness. Applying a gridding technique provides a significance  $K(\vec{x}, t)$  for seismic quiescence as a function of space and time. With



respect to the robustness of the method, a threshold  $K^{(99)}$ , which discriminates, whether or not the actual seismicity is less than the background seismicity, has been introduced. Due to the scrambling of aftershock sequences over the entire spatial volume in the surrogate data, postseismic quiescence is observed. The application of the method to a declustered earthquake catalog shows that this postseismic quiescence is artificial.

The correlations between quiescence periods and mainshocks have been estimated by introducing alarm conditions. In the Armenian catalogue, it is found that quiescence periods and subsequent mainshocks are correlated better-than-chance for a wide range of alarm parameters. In agreement with previous studies (Balassanian *et al.*, 1995; Wyss and Martirosyan, 1998), a pronounced seismic quiescence before the M7 Spitak earthquake in 1988 is observed.

The future work will focus on refinements and improvements of the technique, e.g., a continuous spatiotemporal mapping of probabilities for the presence of quiescence. Furthermore, the restriction of fixed values  $R$  and  $T$  will be removed by searching the entire parameter space for anomalies. This will allow to rank the anomalies according to their significance and find the most significant one.

In conclusion, a correlation between quiescence patterns and large earthquakes is found, although no ‘one-to-one’ association can be established. Thus, the analysis is in good agreement with the numerical simulations of Hainzl *et al.* (2000) and their conclusion that the detection of seismic quiescence can make an important contribution to improve seismic hazard assessment. It can be expected that further studies on this phenomenon, especially on the mechanisms, allow us to obtain new interesting insights over the earthquake process.

### Acknowledgements

We are grateful to Max Wyss (University of Alaska, Fairbanks) for stimulating discussions. The comments of two anonymous reviewers helped to improve the quality of the manuscript significantly. The Armenian earthquake data have been provided by Artak H. Martirosyan (NSSP Yerevan). To produce Figure 1, we used the GMT system (Wessel and Smith, 1991). This work was supported by the Deutsche Forschungsgemeinschaft (SFB 555 and SCH280/13-1)

### References

- Arabasz, W. J. and Hill, S. J.: 1996, Applying Reasenbergs’ cluster analysis algorithm to regional earthquake catalogs outside California, *Seismol. Res. Lett.* **67**, 30.
- Balassanian, S. Y., Arakelian, A. R., Nazaretian, S. N., Avanesian, A. S., Martirosyan, A. H., Igumnov, V. A., Melkounian, M. G., Manoukian, A. V., and Tovmassian, A. K.: 1995, Retrospective analysis of the Spitak earthquake, *Annali di Geofisika* **38**, 345–372.
- Balassanian, S. Y., Nazaretian, S. N., Avanesian, A. S., Arakelian, A. R., Igumnov, V. A., Basalian, M., Martirosyan, A. H., Ambartsumian, V., and Tovmassianm, A. K.: 1997, The new seismic zonation map for the territory of Armenia, *Natural Hazards* **15**, 231–249.

- Dieterich, J. H.: 1978, Preseismic fault slip and earthquake prediction, *J. Geophys. Res.* **83**, 3940–3948.
- Dieterich, J. H. and Okubo, P. G.: 1996, An unusual pattern of seismic quiescence at Kalapana, Hawaii, *Geophys. Res. Lett.* **23**, 447–450.
- Efron, B. and Tibshirani, R. J.: 1993, *An Introduction to the Bootstrap*, Chapman & Hall, New York.
- Geller, R. J., Jackson, D. D., Kagan, Y. Y., and Mulargia, F.: 1997, Earthquakes cannot be predicted, *Science* **275**, 1616–1617.
- Gutenberg, B. and Richter, C. F.: 1954, Earthquake magnitude, intensity, energy and acceleration, *Bull. Seismol. Soc. Am.* **46**, 105–145.
- Habermann, R. E.: 1987, Man-made changes of seismicity rates, *Bull. Seism. Soc. Am.* **77**, 141–159.
- Habermann, R. E.: 1988, Precursory seismic quiescence: Past, present, and future, *Pure Appl. Geophys* **126**, 279–318.
- Hainzl, S., Zöller, G., and Kurths, J.: 1999, Similar power laws for foreshock and aftershock sequences in a spring-block model for earthquakes, *J. Geophys. Res.* **104**, 7243–7253.
- Hainzl, S., Zöller, G., and Kurths, J.: 2000, Seismic quiescence as an indicator for large earthquakes in a system of self-organized criticality, *Geophys. Res. Lett.* **27**, 597–600.
- Jaumé, S. C. and Sykes, L. R.: 1999, Evolving towards a critical point: A review of accelerating seismic moment/energy release prior to large and great earthquakes, *Pure Appl. Geophys* **155**, 279–306.
- Jones, L. M. and Molnar, P.: 1979, Some characteristics of foreshocks and their possible relationship to earthquake prediction, *J. Geophys. Res.* **84**, 3596–3608.
- Kagan, Y. Y.: 1997, Are earthquakes predictable?, *Geophys. J. Int.* **131**, 505–525.
- Kagan, Y. Y. and Vere-Jones, D.: 1996, Problems in the modeling and the statistical analysis of earthquakes. In C. C. Heyde, Y. V. Prohorov, R. Pyke and S. T. Racher (eds), *Lecture Notes in Statistics* **114**, Springer-Verlag, New York, pp. 398–425.
- Kato, N., Ohtake, M., and Hirasawa, T.: 1997, Possible mechanism of precursory seismic quiescence: Regional stress relaxation due to preseismic sliding, *Pure Appl. Geophys* **150**, 249–267.
- Künsch, H. R.: 1989, The jackknife and the bootstrap for general stationary observations, *Ann. of Stat.* **17**, 1217–1241.
- Nature Debate, 1999, Is the reliable prediction of individual earthquakes a realistic scientific goal?, <http://helix.nature.com/debates/earthquake>.
- Ogata, Y.: 1992, Detection of precursory relative quiescence before great earthquakes through a statistical model, *J. Geophys. Res.* **97**, 19845–19871.
- Reasenber, P.: 1985, Second-order moment of central California seismicity, 1969–1982, *J. Geophys. Res.* **90**, 5479–5495.
- Rogozin, E. A. and Philip, H.: 1991, Geological and tectonic study of the Spitak earthquake zone, *Izv. Akad. Nauk. SSSR, Fizika Zemli* **11**, 3–18.
- Rudnicki, J. W.: 1988, Physical models of earthquake instability and precursory processes, *Pure Appl. Geophys.* **126**, 531–554.
- Scholz, C. H.: 1988, Mechanism of seismic quiescences, *Pure Appl. Geophys.* **126**, 701–718.
- Stark, P. B.: 1997, Earthquake prediction: The null hypothesis, *Geophys. J. Int.* **131**, 495–499.
- Theiler, J., Eubank, S., Longtin, J., Galdrikian, B., and Farmer, J. D.: 1992, Testing for nonlinearity in time series: The method of surrogate data, *Physica D* **58**, 77–94.
- Wessel, P. and Smith, W. H. F.: 1991, Free software helps map and display data, *Eos Trans. AGU* **72**, 441, 445–446.
- Wiemer, S. and Baer, M.: 2000, Mapping and removing quarry blast events from seismicity catalogs: Examples from Alaska, the Western United States, and Japan, *Bull. Seism. Soc. Am.* **90**, 525–530.
- Wiemer, S. and Wyss, M.: 2000, Minimum magnitude of complete reporting in earthquake catalogs: Examples from Alaska, the Western United states, and Japan, *Bull. Seism. Soc. Am.* **90**, 859–869.
- Wyss, M.: 1997a, Cannot earthquakes be predicted, *Science* **278**, 487.

- Wyss, M.: 1997b, Nomination of precursory seismic quiescence as a significant precursor, *Pure Appl. Geophys* **149**, 79–113.
- Wyss, M. and Habermann, R. E.: 1988a, Precursory seismic quiescence, *Pure Appl. Geophys* **126**, 319–332.
- Wyss, M. and Habermann, R. E.: 1988b, Precursory quiescence before the August 1982 Stone Canyon, San Andreas Fault, earthquakes, *Pure Appl. Geophys.* **126**, 333–356.
- Wyss, M. and Martirosyan, A. H.: 1998, Seismic quiescence before the M7, 1988, Spitak earthquake, Armenia, *Geophys. J. Int.* **134**, 329–340.
- Zöller, G., Engbert, R., Hainzl, S., and Kurths, J.: 1998, Testing for unstable periodic orbits to characterize spatiotemporal dynamics, *Chaos, Solitons & Fractals* **9**, 1429–1438.
- Zöller, G., Hainzl, S., and Kurths, J.: 2001, Observation of growing correlation length as an indicator for critical point behavior prior to large earthquakes, *J. Geophys. Res.* **106**, 2167–2175.
- Zschau, J.: 1998, Quantifying seismic quiescence: An application of the SEISMOLAP-method in California seismicity, *Eos. Trans.* **79**, F585.
- Zuniga, R. F. and Wiemer, S.: 1999, Seismicity patterns: Are they always related to natural causes?, *Pure Appl. Geophys* **155**, 713–726.
- Zuniga, R. F. and Wyss, M.: 1995, Inadvertent changes in magnitude reported in earthquake catalogs: Influence of b-value estimates, *Bull. Seism. Soc. Am.* **85**, 1858–1866.

# Appendix G

**A systematic spatiotemporal test of the critical point hypothesis for large earthquakes**

Autors:	G. Zöller, and S. Hainzl
Journal:	<i>Geophysical Research Letters</i> ,
Volume (Nr.):	<b>29(11)</b>
Article/doi:	art. no. 1558, doi 10.1029/2002GL014856
Year:	2002

# A systematic spatiotemporal test of the critical point hypothesis for large earthquakes

Gert Zöller

Institute of Physics and Institute of Mathematics, University of Potsdam, Potsdam, Germany

Sebastian Hainzl

Institute of Earth Sciences and Institute of Physics, University of Potsdam, Potsdam, Germany

Received 4 February 2002; revised 12 April 2002; accepted 15 April 2002; published 15 June 2002.

[1] The critical point hypothesis for large earthquakes predicts two different precursory phenomena in space and time, an accelerating moment release and the growth of the spatial correlation length. The objective of this work is to investigate both methods with respect to their predictive power. A systematic statistical test based on appropriate random earthquake catalogs allows to quantify the correlations of a precursory pattern with the subsequent mainshock activity. The analysis of target earthquakes in California since 1960 with magnitudes  $M \geq M_{\text{cut}}$  reveals that these correlations increase systematically with growing  $M_{\text{cut}}$ , and correlations at greater than 95% confidence are observed for  $M_{\text{cut}} \geq 6.5$  in the case of the spatial correlation length. In particular, the seismicity patterns are found to be significantly correlated with each of the largest earthquakes ( $M \geq 7.0$ ), individually. The acceleration of the moment release has a similar trend, but is less significant. **INDEX TERMS:** 7260 Seismology: Theory and modeling; 7223 Seismology: Seismic hazard assessment and prediction; 7209 Seismology: Earthquake dynamics and mechanics; 3220 Mathematical Geophysics: Nonlinear dynamics

## 1. Introduction

[2] The question whether or not earthquakes are predictable is one of the “holy grails” of geophysics. The application of concepts from statistical physics and nonlinear dynamics, e.g. self-organized criticality [Bak and Tang, 1989], provided new insights into the prediction problem [Geller et al., 1997; Hainzl et al., 2000]. In the recent past, the critical point concept for large earthquakes has led to a revised understanding of the preparatory process of mainshocks. Based on the theory of crack propagation and damage mechanics [Vere-Jones, 1977; Das and Scholz, 1981], the rupture process has been reinterpreted as a critical point phenomenon in terms of statistical physics. The approach to the critical point as well as the rupture process itself is characterized by scaling rules [Allegre et al., 1982; Sornette and Sornette, 1990], e.g., for the spatial correlations of the stress field. Voight [1989] derived a second-order differential equation for material failure and showed that it can be solved for certain parameter values by the well-known time-to-failure equation. This equation has been used in recent years to quantify the acceleration of seismicity prior to large earthquakes [Bufe and Varnes, 1993; Bowman et al., 1998; Jaumé and Sykes, 1999; Bowman and King, 2001], first reported by Sykes and Jaumé [1990]. Ben-Zion and Lyakhovskiy [2001] found that accelerating moment release has predictive power, if the seismicity has a broad frequency-size statistics. Using the renormalization group formalism, Sornette and Sammis [1995] elaborated

the “critical earthquake concept” by deriving the time-to-failure equation in the framework of statistical physics. The acceleration of the moment release is a hallmark of the critical earthquake concept. However, the most important feature of spatially extended critical point systems is in general the growth of the spatial correlation length according to a power law with a singularity in the critical point [Main, 1999]. Zöller et al. [2001] investigated the scaling relation for the spatial correlations and proposed a method to measure the correlation length by means of the epicenter fluctuations.

[3] Critical point behavior prior to large earthquakes has been reported in several case studies [Jaumé and Sykes, 1999 and citations therein]. However, the analysis has only been conducted for special values of space and time. Thus, no conclusions can be drawn with respect to practical forecasting purposes. The goal of the present work is to search systematically for patterns related to critical point behavior in terms of growing spatial correlation length and accelerating moment release without tuning free parameters. The correlations of these pattern with subsequent intermediate to large earthquakes are calculated. In a recent work, Zöller and Hainzl [2001] mapped curvature parameters, which measure the quality of a power law fit to the data, in space. This method is now generalized in the way that probabilities are mapped with the advantage that different patterns can be compared in a straightforward manner. Because parameters like space or time windows are not known in advance, it is a common technique to detect the patterns related to critical point dynamics in the entire parameter space. The same procedure is then repeated for a large number of appropriate random earthquake data. The significance is measured by the deviation of the original pattern from the corresponding distribution of patterns in the random data.

## 2. Data and Method

[4] We analyze the seismicity in California between 32°N and 40°N latitude. The data are taken from the Council of the National Seismic System (CNSS) Worldwide Earthquake Catalog (available at (<http://quake.geo.berkeley.edu/cnss>)). The catalog covers the time span from 1910 to the present. To account for homogeneous reporting, we restrict the analysis to the time from 1960 to 2001.

### 2.1. Power Law Fits

[5] The method to calculate the accelerating moment release (AMR) is close to the methodology in Bowman et al. [1998]. In particular, the time-to-failure equation for the cumulative Benioff strain ( $\Sigma\Omega$ ) ( $t$ ) =  $\sum_{i=1}^{N(t)} \sqrt{E_i}$  of the earthquakes at times  $t$  with energies  $E_i$  prior to a mainshock occurring at time  $t_f$

$$(\Sigma\Omega)(t) = A + B(t_f - t)^m \quad (1)$$

is fit to the data in a circular space window with radius  $R$ , a time interval  $(t_0; t_f)$  for earthquakes with magnitudes  $M \geq 5.0$ . The

constants  $A$  and  $B$  are fit parameters. The exponent  $m$  is set to  $m = 0.3$  according to numerous AMR studies, e.g., *Bufe and Varnes* [1993]. The power law fit is compared with a linear fit  $A' - B'(t_f - t)$  and the quality of the power law fit is measured by the curvature value  $\mathcal{C}$ , which is the root mean square (rms) error of the power law fit divided by the rms error of the linear fit. The free parameters  $R$  and  $t_0$  are determined by the condition that  $\mathcal{C}$  is a minimum.

[6] The proceeding for the detection of the growth of the spatial correlation length (GSCL) is identical, except that now the equation for the spatial correlation length  $\xi$

$$\xi(t) = D(t_f - t)^{-k} \quad (2)$$

is used with the fit parameter  $D$  and  $M \geq 4.0$ . For the exponent  $k$ , we use the empirical value  $k = 0.4$  found in *Zöller et al.* [2001], although other authors suggest on theoretical grounds  $k = 0.25$  [*Rundle et al.*, 1999]. Note that equation (2) has a singularity at  $t = t_f$ , whereas  $(\Sigma\Omega)(t = t_f)$  in equation (1) remains finite. Because  $\xi$  is a non-cumulative quantity, the curvature parameter  $\mathcal{C}$  is now the rms error of the power law fit divided by the rms error of the constant fit.

[7] Both, the GSCL and the AMR patterns are detected on a spatial grid with a resolution of  $0.5^\circ$  in longitude and latitude for a fixed time  $t_f$ . To account for the temporal evolution of the pattern, a time grid for  $t_f$  is introduced. Due to the high computational effort the resolution is set to one year:  $t_i \equiv t_{f_i} = 1960.0 + i$  with  $i = 0, \dots, 41$ . The result is a function  $C(\vec{x}, t_i)$  of curvature parameters for the GSCL patterns and the AMR patterns, respectively.

## 2.2. Random Earthquake Catalogs and Significances

[8] In the next step,  $C(\vec{x}, t_i)$  is calculated for  $n_{\text{ran}} = 100$  random catalogs. The algorithm for the computation of these synthetic data is described in *Zöller et al.* [2001]. Each catalog is a realization of a random Poisson process with additional synthetic aftershock activity following Omori's law. The distributions of magnitudes and epicenters fit those of the original catalog; the latter feature is important for the GSCL patterns. The significance of an observed pattern calculated at the location  $\vec{x}$  at time  $t_i$  in the real data can be defined by the probability

$$p(\vec{x}, t_i) = n(\vec{x}, t_i) / n_{\text{ran}}, \quad (3)$$

where  $n(\vec{x}, t_i)$  is the number of random catalogs with  $C_{\text{orig}}^i(\vec{x}, t_i) \leq C_{\text{ran}}^i(\vec{x}, t_i)$ . That is, large values of  $p$  denote high significances indicating that the pattern cannot be reproduced easily by random data.

## 2.3. Likelihood Ratio Test

[9] The likelihood ratio test has been proposed *Gross and Rundle* [1998] in order to compare two models with respect to their suitability to describe an observed data set. In our case, the observed data (target events) are given by the set of  $N(t_i)$  earthquakes with  $M \geq M_{\text{cut}}$  occurring within the time interval  $[t_i; t_i + 1 \text{ year}]$ . Model 1 is defined by the GSCL, respectively AMR pattern of the original catalog, that is, the function  $p(\vec{x}, t_i)$ . Model 2 is the corresponding pattern for a random catalog. For both models, the likelihood function  $L$  is computed for the entire space-time volume and the total number  $N = \sum_i N_i(t)$  of target earthquakes:

$$L = \prod_{i=0}^{41} \prod_{k=1}^{N(t_i)} P(\vec{x}_k, t_i). \quad (4)$$

$P(\vec{x}_k, t_i)$  is the normalized probability density for an event occurring in the time interval  $[t_i; t_i + 1 \text{ year}]$  at the epicenter  $\vec{x}_k$  of a target

event with a premonitory GSCL, respectively AMR pattern. To apply the likelihood ratio test, we assume the probability density function

$$P(\vec{x}, t_i) = \kappa \cdot \int g(\vec{x}' - \vec{x}) \cdot \tilde{p}(\vec{x}' - t_i) d^2x' \quad (5)$$

consisting of a two-dimensional Gaussian function  $g$  around the spatial grid node  $\vec{x}$  with a standard deviation equal to the distance between two grid nodes. The second function is defined by  $\tilde{p}(\vec{x}) = (p(\vec{x}) - 0.5) \cdot \Theta(p(\vec{x}) - 0.5)$  with  $p(\vec{x})$  from equation (3). This definition is based on the fact that  $p(\vec{x}) = 0.5$  refers already to randomness and thus  $p(\vec{x}) \geq 0.5$  is a meaningless case which is excluded from the analysis by means of the Heavyside step function  $\Theta$ . For each catalog, the normalization factor  $\kappa$  is defined by the condition that the probability density integrates to the total number  $N$  of target earthquakes,  $\kappa = N / \int \int P(\vec{x}, t) d^2x dt$ .

[10] The likelihood function is also measured for each of the random catalogs. The likelihood ratio  $LR = L_{\text{orig}} / L_{\text{ran}}$  of the normalized likelihood functions for model 1 and model 2 is equal to the ratio  $p/p_{\text{ran}}$ , where  $p$  denotes the probability that the observed seismicity arises from the original data (model 1) and  $p_{\text{ran}}$  is the corresponding probability for the random data (model 2). In the case of  $LR(t_i) > 1$ , the detected GSCL patterns in the original catalog are more correlated with the target seismicity than the patterns from the random catalogs. By contrast,  $LR(t_i) < 1$  means that the patterns from the random catalog fit better to the target earthquakes.

## 3. Results and Discussion

[11] First, the spatiotemporal correlations are calculated according to the previous section. The number  $N_s \in [0; 100]$  of random catalogs with  $LR^i > 1$  is used as a measure to compare original data and random data in space and time. Note that due to the normalization, this quantity includes not only information about mainshocks with a precursory pattern, but also “false alarms” (patterns without a mainshock) and “false positives” (mainshocks without a pattern). Figure 3 shows  $N_s$  as a function of the lower magnitude threshold  $M_{\text{cut}}$  of the target events. For the GSCL analysis the figure shows a well defined region  $M_{\text{cut}} \geq 6.5$  where the GSCL pattern is positively correlated with the observed mainshock activity at greater than 95% confidence.

[12] Because  $N_s \approx 50$  would indicate random response, the values for  $5.0 \leq M_{\text{cut}} \leq 6.0$  reveal an anticorrelation between the observed GSCL patterns and the real seismicity. This behavior points to a small-scale clustering in space which is below the background level of the spatial correlation length. Because a minimum number of earthquakes is required to perform the power law fits, the space window cannot be reduced to such small scales and consequently, a negative correlation is found on intermediate scales. This behavior is not expected in the AMR patterns, because energy release below a certain background level still makes a small but positive contribution to  $\Sigma\Omega$  in equation (1), which is a cumulative measure. In fact, for  $M_{\text{cut}} \leq 6.4$  the results reflect almost randomness, whereas for higher values of  $M_{\text{cut}}$  the tendency is similar to those of the GSCL patterns, with lower confidence levels. These findings confirm clearly the hypothesis that patterns based on critical point dynamics are precursory phenomena to the largest earthquakes in California.

[13] Next, we consider the spatial patterns  $p(\vec{x}, t_i)$  at times  $t_i$  prior to the mainshocks ( $M \geq 6.5$ ) in California. These patterns are shown in Figure 2 for GSCL and in Figure 3 for AMR. In some cases, the spatial correlations of the GSCL pattern with the future seismicity is clearly visible, e.g., the San Fernando, Loma Prieta, and the Hector Mine earthquakes. For the AMR pattern, the San Fernando earthquake shows the best agreement. In general, the regions covered by high probabilities for critical point

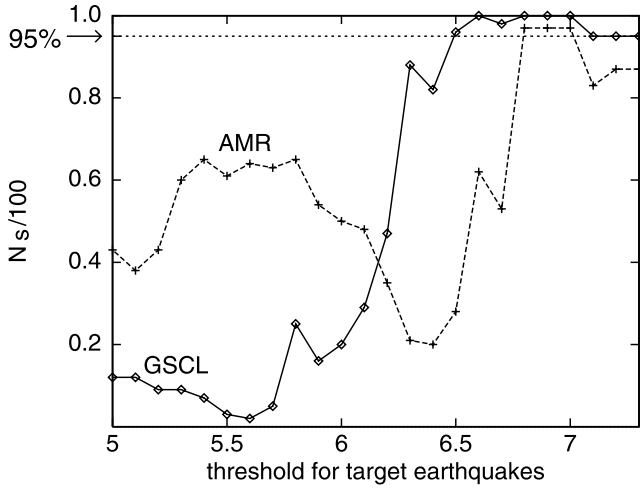


**Figure 1.** Results of the likelihood ratio test for the spatiotemporal analysis as a function of the lower threshold magnitude of the target earthquakes;  $N_s \in [1; 100]$  is the number of cases, where the results from the original catalog are more correlated with the real seismicity than the results from the random catalog.

behavior are relatively large, especially in Figure 3. This is to some degree in accordance with the earlier observations that these regions are much larger than the rupture areas of the mainshocks. However, the optimization technique may lead in some cases to an over-estimation of the space windows and to the inclusion of patterns far away from the center of the circle. As a consequence, almost the whole catalog seems to be loaded, e.g., in Figures 3f and 3g. Refinements with respect to the determination of the space window are thus expected to reduce the size of the alarm

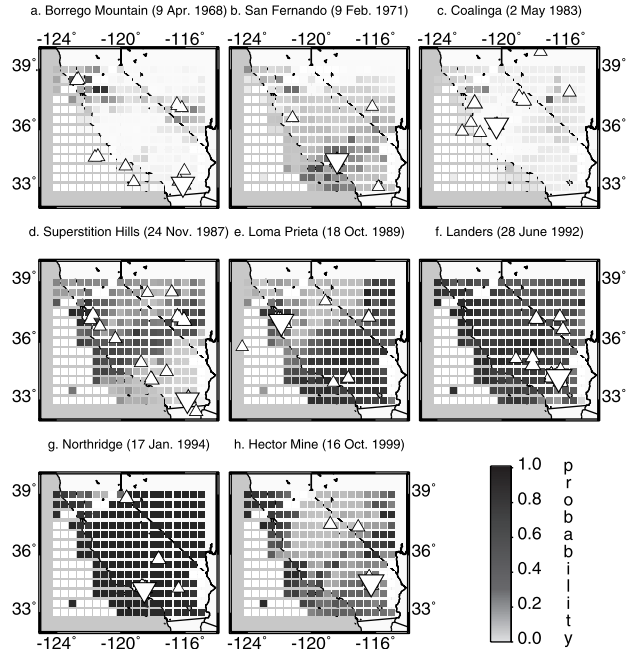


**Figure 3.** Same as Figure 1 for the AMR pattern.

area. For that, the space window could be determined for a fixed target magnitude  $M$  by an empirical scaling relation  $R \sim M$ , instead of an optimization. This work is left for future studies. Furthermore, *Bowman and King* [2001] showed that the results for accelerating moment release can be improved, if the circular critical regions, where the power law is fit, are replaced by the regions of high pre-event stress estimated from the Coulomb stress shadows after the main shock. This approach requires, however, detailed knowledge of the mainshock.

[14] However, Figure 2 and Figure 3 only show the patterns before the mainshocks. A likelihood ratio test for each time step includes more information, because the normalization provides a measure for the significance of the pattern  $p(\vec{x}, t_i)$  relative to the entire space-time distribution of  $p$ . Therefore, we compute for the eight values  $t_i$  from each figure the number of random catalogs with  $LR(t_i) > 1$ . Equation (4) reduces to a single value of  $t_i$  and the normalization factor is calculated by integrating  $P$  for  $t \leq t_i$ . The mainshock defines the target event. The results listed in Table 1 show again that GSCL patterns are most significant for the largest mainshocks, namely  $M \geq 7$ . The probability that the mean of  $\langle N_s \rangle$  is larger than or equal to the mean of eight random numbers

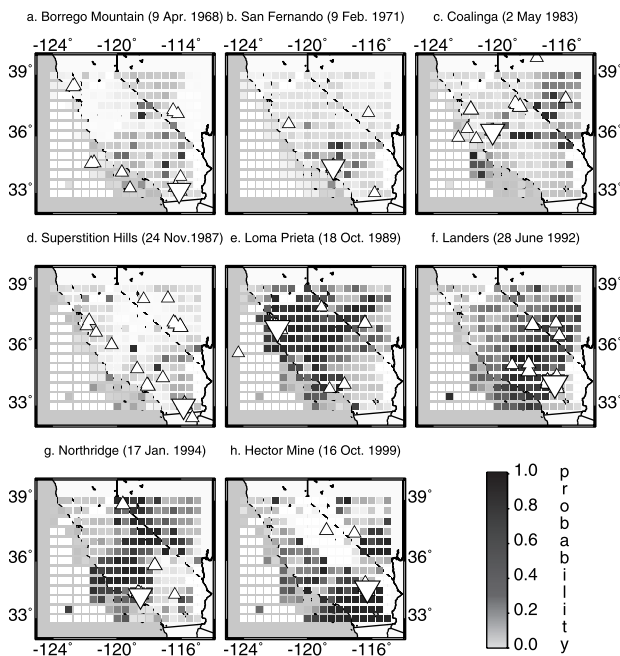


**Figure 2.** GSCL pattern  $p(\vec{x}, t_i)$  (equation (3)) prior to the eight mainshocks ( $M \geq 6.5$ ) in California between 1960 and 2001. The time step  $t_i$  is the begin of the year in which the mainshock occurred. The large triangle denotes the mainshock epicenter, whereas the smaller triangle refer to earthquakes with  $M \geq 5$  in the same year.

**Table 1.** Results of the Likelihood Ratio Test for Individual Mainshocks

Earthquake	$M$	$N_s$ (GSCL)	$N_s$ (AMR)
a. Borrego Mountain (1968)	6.5	36	8
b. San Fernando (1971)	6.6	70	93
c. Coalinga (1983)	6.7	52	11
d. Superstition Hills (1987)	6.6	74	23
e. Loma Prieta (1989)	7.0	100	62
f. Landers (1992)	7.3	98	54
g. Northridge (1994)	6.6	96	67
h. Hector Mine (1999)	7.1	97	60
mean (a-h)		77.9	47.3
$P_{\text{conf}}$ in %		99.7	39.7

$P_{\text{conf}}$  is the probability that the mean of  $\langle N_s \rangle$  is larger than or equal to the mean of eight random numbers between 0 and 100.

between 0 and 100 is 99.7%. In contrast, the results for the AMR patterns is close to random response.

#### 4. Conclusions

[15] In this work, we have defined the critical point hypothesis for large earthquakes in terms of growing spatial correlation length (GSCL) and accelerating moment release (AMR). For both patterns, the correlation with the observed mainshock activity increases, if the magnitude threshold of the target earthquakes  $M_{\text{cut}}$  grows. For  $M_{\text{cut}} \geq 6.5$  the space-time correlation of the GSCL pattern with the target events is significant at greater than 95% confidence. A similar correlation analysis of individual mainshocks leads also to high significances for the largest mainshocks. The result of the AMR analysis is similar but less significant for the space-time correlations and close to a random response for most of the individual earthquakes. We conclude that further refinements of the pattern detection, e.g., the reduction of the number of fit parameters, is very encouraging for a further increase of the significances. This would probably allow to estimate the spatial extensions of the critical point patterns more precisely. In general, our results strengthens the hypothesis that large earthquakes are preceded by observable patterns related to a critical point process.

[16] **Acknowledgments.** This work was supported by the Deutsche Forschungsgemeinschaft (SFB 555 and SCH280/13-1).

#### References

- Allegre, C. J., J. L. Le Mouél, and A. Provost, Scaling rules in rock fracture and possible implications for earthquake predictions, *Nature*, 297, 47–49, 1982.
- Bak, P., and C. Tang, Earthquakes as a self-organized critical phenomenon, *J. Geophys. Res.*, 94, 15,635–15,637, 1989.
- Ben-Zion, Y., and V. Lyakhovskiy, Accelerated seismic release and related aspects of seismicity pattern on earthquake faults, *Pure Appl. Geophys.*, in press, 2001.
- Bowman, D. D., and G. C. P. King, Accelerating seismicity and stress accumulation before large earthquakes, *Geophys. Res. Lett.*, 28, 4039–4042, 2001.
- Bowman, D. D., G. Oullion, C. G. Sammis, A. Sornette, and D. Sornette, An observational test of the critical earthquake concept, *J. Geophys. Res.*, 103, 24,359–24,372, 1998.
- Bufe, C. G., and D. J. Varnes, Predictive modeling of the seismic cycle of the greater San Francisco Bay region, *J. Geophys. Res.*, 98, 9871–9883, 1993.
- Das, S., and C. H. Scholz, Theory of time-dependent rupture in the Earth, *J. Geophys. Res.*, 86, 6039–6051, 1981.
- Geller, R. J., D. D. Jackson, Y. Y. Kagan, and F. Mulargia, Earthquakes cannot be predicted, *Science*, 275, 1616–1617, 1997.
- Gross, S., and J. Rundle, A systematic test of time-to-failure analysis, *Geophys. J. Int.*, 133, 57–64, 1998.
- Hainzl, S., G. Zöller, and J. Kurths, Seismic quiescence as an indicator for large earthquakes in a system of self-organized criticality, *Geophys. Res. Lett.*, 27, 597–600, 2000.
- Jaumé, S. C., and L. R. Sykes, Evolving towards a critical point: A review of accelerating seismic moment/energy release prior to large and great earthquakes, *Pure Appl. Geophys.*, 155, 279–306, 1999.
- Main, I. G., Applicability of time-to-failure analysis to accelerated strain before earthquakes and volcanic eruptions, *Geophys. J. Int.*, 139, F1–F6, 1999.
- Rundle, J. B., W. Klein, and S. Gross, Physical basis for statistical patterns in complex earthquake populations: models, predictions and tests, *Pure Appl. Geophys.*, 155, 575–607, 1999.
- Sornette, D., and C. G. Sammis, Complex critical exponents from renormalization theory group of earthquakes: implications for earthquake predictions, *J. Phys. I France*, 5, 607–619, 1995.
- Sornette, A., and D. Sornette, Earthquake rupture as a critical point: Consequences for telluric precursors, *Tectonophysics*, 179, 327–334, 1990.
- Sykes, L. R., and S. C. Jaumé, Seismic activity on neighboring faults as a long-term precursor to large earthquakes in the San Francisco Bay area, *Nature*, 348, 595–599, 1990.
- Vere-Jones, D., Statistical theories of crack propagation, *Mathematical Geology*, 9, 455–481, 1977.
- Voight, B., A relation to describe rate-dependent material failure, *Science*, 243, 200–203, 1989.
- Zöller, G., and S. Hainzl, Detecting premonitory seismicity patterns based on critical point dynamics, *Natural Hazards and Earth System Sciences*, 1, 93–98, 2001.
- Zöller, G., S. Hainzl, and J. Kurths, Observation of growing correlation length as an indicator for critical point behavior prior to large earthquakes, *J. Geophys. Res.*, 106, 2167–2176, 2001.

S. Hainzl, Institute of Earth Sciences, University of Potsdam, Am Neuen Palais, D-14469 Potsdam, Germany. (hainzl@geo.uni-potsdam.de.)

G. Zöller, Institute of Physics, University of Potsdam, Am Neuen Palais, D-14469 Potsdam, Germany. (gert@agnld.uni-potsdam.de.)



# Appendix H

On increase of earthquake correlation length prior to large earthquakes in California

Autors:	I. Zaliapin, Z. Liu, G. Zöller, V. Keilis-Borok, and D. Turcotte
Journal:	<i>Computational Seimology,</i>
Volume:	<b>33</b>
Pages:	141-161
Year:	2002

УДК 550.341

## ON INCREASE OF EARTHQUAKE CORRELATION LENGTH PRIOR TO LARGE EARTHQUAKES IN CALIFORNIA

I. Zaliapin<sup>1,2</sup>, Z. Liu<sup>3</sup>, G. Zöller<sup>4</sup>, V. Keilis-Borok<sup>1,2,3</sup>, D. Turcotte<sup>5</sup>

<sup>1</sup> International Institute of Earthquake Prediction Theory  
and Mathematical Geophysics, Russian Academy of Sciences, Moscow

<sup>2</sup> Institute of Geophysics and Planetary Physics, UCLA, Los Angeles

<sup>3</sup> Department of Earth and Space Sciences, UCLA, Los Angeles

<sup>4</sup> Institute of Physics and Mathematics, University of Potsdam, Potsdam

<sup>5</sup> Department of Earth and Atmospheric Sciences, Cornell University, Ithaca

It is well established that earthquakes are correlated over distances greatly exceeding their source dimension. Recent studies hypothesize for important associated phenomenon: The area over which earthquake activity is correlated varies in time and might grow prior to a large earthquake. This hypothesis is supported by a wealth of observations, computer simulation, and has theoretical interpretations. Several measures of earthquake correlation lengths were recently suggested by different authors. Here we analyze one of these measures,  $\xi(\mathbf{x}, t)$ , based on single-link cluster analysis of epicenters. Previous studies have shown the growth of  $\xi$  prior to nine large earthquakes in California during 1945-2000. In this paper we study whether the reported growth of the correlation length  $\xi(\mathbf{x}, t)$  can be used for earthquake prediction. Our results show that reasonable retrospective prediction of large earthquakes ( $M \geq 6.5$ ) in California can be achieved by using the increase of  $\xi$  as a signal for the approach of a large earthquake. Extensive variations of numerical parameters demonstrate the stability of this prediction method. Additionally, we compare the distributions of  $\xi(\mathbf{x}, t)$  close and distant in time and space to large earthquakes and find a systematic shift reflecting the increase of the correlation length prior to large earthquakes. Premonitory increases of correlation lengths are seen most clearly in the highly fractured areas near fault junctions. Its predictive power is reduced in more homogeneous regions.

## К ВОПРОСУ ОБ УВЕЛИЧЕНИИ РАДИУСА СЕЙСМИЧЕСКОЙ КОРРЕЛЯЦИИ ПЕРЕД СИЛЬНЫМИ ЗЕМЛЕТРЯСЕНИЯМИ В КАЛИФОРНИИ

И. Заляпин<sup>1,2</sup>, Ж. Лиу<sup>3</sup>, Г. Золлер<sup>4</sup>, В. Кейлис-Борок<sup>1,2,3</sup>,  
Д. Туркотт<sup>5</sup>

<sup>1</sup>Международный институт теории прогноза землетрясений  
и математической геофизики Российской академии наук, Москва

<sup>2</sup>Институт физики Земли и планет, Калифорнийский Университет, Лос-Анджелес

<sup>3</sup>Факультет наук о Земле и космических исследований, Калифорнийский  
Университет, Лос-Анджелес

<sup>4</sup>Институт физики и математики, Потсдамский Университет, Потсдам

<sup>5</sup>Факультет наук о Земле и атмосфере, Корнельский Университет, Итака

Феномен корреляции землетрясений на расстояниях, намного превосходящих размер их очагов (удаленная сейсмическая корреляция), хорошо известен в геофизике. Недавно была высказана гипотеза о том, что размер области удаленной сейсмической корреляции меняется со временем и может увеличиваться перед сильными землетрясениями. Данная гипотеза подтверждается многочисленными наблюдениями, компьютерным моделированием, и может быть теоретически обоснована. В работе анализируется мера  $\xi(t, \mathbf{x})$  радиуса сейсмической корреляции, основанная на кластерном анализе эпицентров землетрясений. Ранее было показано, что  $\xi(t, \mathbf{x})$  растет перед сильными событиями в Калифорнии в период 1945–2000 гг. В работе рассмотрен вопрос о возможности алгоритмического прогноза землетрясений на основе указанного роста. Сформулирован алгоритм, примененный для ретроспективного прогноза событий с магнитудой  $M \geq 6.5$  в Калифорнии. Качество прогноза оценено с помощью диаграммы ошибок, устойчивость проверена вариацией численных параметров алгоритма. В дополнение, распределение значений  $\xi(t, \mathbf{x})$  сопоставлено в областях, близких и удаленных в пространстве–времени от сильных событий. Такой анализ демонстрирует систематическое увеличение радиуса сейсмической корреляции при приближении сильного землетрясения. Предвестниковое увеличение радиуса корреляции наиболее ярко выражено вблизи пересечений основных геологических разломов, в областях, характеризующихся высокой тектонической раздробленностью.

## 1. Introduction

Earthquakes are correlated over the distances far exceeding their source dimension. Among many manifestations of this phenomenon one observes the simultaneous change of seismicity in large areas [1, 2], migration of seismicity along seismic belts [3, 4], global interdependence in the occurrence of major earthquakes [5], etc. Ample evidence of long-range correlations comes from the studies of changes in seismic activity prior to large earthquakes [6–13]. There is growing evidence that earthquake correlation ranges are not only large but also increase with time prior to strong earthquakes. Premonitory patterns based on this phenomenon have been recently found in modeled seismicity and in observations [14–20]. Here, we study one specific measure of earthquake correlation range introduced in [18]. Specifically, we focus on the following questions: Can this measure be used for earthquake prediction? If so, how can it be used?

**1.1. Premonitory long-range correlations.** The area where premonitory patterns can be observed was first estimated by V. Keilis-Borok and L. Malinovskaya [9]. Specifically, it was shown that a) the occurrence rate of moderate-size earthquakes increases years to a decade prior to some large earthquakes, b) the increase, if observed, occurs within a large territory around the approaching earthquake’s rupture zone, and c) the size  $Q$  of that territory scales with the magnitude  $M$  of a large earthquake as

$$\log Q \propto 0.5M. \quad (1)$$

Later studies confirmed these results. Table 1 presents estimates of the linear size of the earthquake preparation area,  $R \approx Q^{1/2}$ , obtained by differ-

TABLE 1. Estimations of the area where premonitory patterns may be observed

Measure	Year	$R(L)$	Reference
Area of faultbreaks	1964	$\sim 10L$	Keilis-Borok and Malinovskaya, 1964
Distant aftershocks	1975	$10L$	Prozoroff, 1975
Earthquake swarms	1977	$5L - 10L$	Caputo et al., 1977
Bursts of aftershocks, area of faultbreaks, swarms	1980	$5L - 10L$	Keilis-Borok et al., 1980
Algorithm CN*	1983	$5L - 10L$	Keilis-Borok and Rotwain, 1990
Algorithm M8*	1985	$5L - 10L$	Keilis-Borok and Kossobokov, 1990
Algorithm SSE*	1992	$\sim 5L$	Vorobieva, 1999
Number of earthquakes	1995	$\sim 100L$	Press and Allen, 1995
Number of earthquakes	1996	$\sim 5L$	Knopoff et al., 1996
Benioff strain release	1989	$\sim 5L$	Varnes, 1989 Bowman et al., 1998 Jaume and Sykes, 1999
Near-simultaneous pairs of earthquakes	2001	$\sim 3L$	Shebalin et al., 2000
Correlation length via Single Link Cluster	2001	$\sim 5L$	Zoller et al., 2001 Zoller and Hainzl, 2001
Simultaneous activation of fault branches	2002	$\sim 10L$	Zaliapin et al., 2002

\* References are given to later comprehensive reviews; not to original work.

ent authors; to make results comparable they are given as relations between  $R$  and the linear dimension  $L$  of the coming earthquake. One can see surprisingly good agreement despite the diversity of applied approaches, data, and regions considered. V. Keilis-Borok and L. Malinovskaya [9] studied the total area of faultbreaks and demonstrated its increase prior to some large earthquakes; A. Prozorov [10] observed that the location of future large earthquake might be depicted years in advance by "distant aftershocks": earthquakes that immediately follow a mainshock at distances 10 times larger than its linear source dimension; study [21] showed that swarms of earthquakes of medium magnitude might occur years prior to large earthquakes. In the wake of these findings the family of algorithmically defined intermediate-term earthquake premonitory seismicity patterns was introduced and tested worldwide during the last 20 years. The latest comprehensive reviews can be found in [12, 22]. These patterns reflect the following changes of seismic-

ity: increase of earthquake activity, clustering, transformations of magnitude distribution (Gutenberg-Richter law), and increase of earthquake correlation range. They have been jointly used in the earthquake prediction algorithms M8 [23], CN [24] and SSE [25]. These algorithms are validated by well-documented advance predictions [12, 25, 26, 27]. Importantly, the relation (1) is used to renormalize the prediction algorithms for different target magnitudes  $M$ . During the past decade, large attention was given to study accelerating seismic moment release prior to large and great earthquakes [13, 28, 29, 30]. Relation (1) was shown to describe the size of the area where seismic activity accelerates prior to a large earthquake. Recently, F. Press and C. Allen extended the frontiers of the long-range-correlation paradigm by demonstrating that "earthquakes in southern California occur within a larger system that includes at least the Great Basin and the Gulf of California" [5]. Particularly, they argue that an earthquake predicted for Parkfield is not likely to occur until activity picks up in one of those distant areas.

Long-range earthquake correlations are observed in modeling [14, 17, 31–34] and explained in the framework of "self-organized criticality", "critical point behavior", and "finite-time singularity" concepts that have reinforced each other during the last decade [35–42].

**1.2. Premonitory increase of earthquake correlation length.** Recent studies hypothesize for important associated phenomena: the area over which earthquake activity is correlated varies in time and might grow prior to a large earthquake. Several explicitly defined measures for the earthquake correlation range were introduced and studied.

Pepke et al. [14] considered a measure AZS (Active Zone Size) for a dynamical model of a fault; it was demonstrated that AZS has a much stronger predictive power comparing to seismic activation and fluctuations of activity in predicting synthetic earthquakes. V. Kossobokov and J. Carlson [15] demonstrated that by using AZS instead of seismic activity in the earthquake prediction algorithm M8 [23], one improves its performance for western United States.

The study of the colliding cascade model of seismicity introduced two earthquake correlation measures: Accord and ROC (Radius of Correlation) [17, 34]. The measure Accord accounts for the geometry of a regional fault network. Its predictive power for observed seismicity of southern California was demonstrated in [20]. Short-term premonitory increases of the measure ROC was found in [16] for observed seismicity of Lesser Antilles.

Study [18] introduced the correlation length measure  $\xi(\mathbf{x}, t)$  based on single-link cluster analyses of epicenters. The  $\xi(\mathbf{x}, t)$  was evaluated for epicenters  $\mathbf{x}_i$  of nine large earthquakes in California for the period preceding each event. It was shown that  $\xi(\mathbf{x}_i, t)$  increases in time prior to each of

the earthquakes considered; the increase lasting for periods from years to decades. In this paper we consider how this measure can be used for earthquake prediction.

**1.3. Verifying premonitory phenomenon.** Is the increase of  $\xi(\mathbf{x}, t)$  observed in [18] a distinctive feature of the area around and the time preceding a large earthquake? More explicitly, can one use the increase of  $\xi(\mathbf{x}, t)$  to predict a large earthquake? Answering this question on the sole basis of observations preceding large earthquakes can be questioned: a trivial analogue is an attempt to predict large earthquakes by the advent of a New Year. It is of course true that one witnesses a New Years celebration a year prior to *any* large earthquake; at the same time a large earthquake cannot be *predicted* this way.

We consider the correlation length  $\xi(\mathbf{x}, t)$  introduced in [18] for California during 1945–2000; it is evaluated over a spatially uniform grid that covers the whole territory. First, we analyze spatio-temporal distributions of  $\xi$  values within areas close and distant in time and space to large ( $M \geq 6.5$ ) earthquakes. Second, we perform a retrospective prediction using the increase of  $\xi(\mathbf{x}, t)$  as a signal of an approaching large earthquake. Quality and stability of the prediction are evaluated. The data and definition of the correlation length are taken unchanged from [18].

## 2. Data

We analyze seismicity of California in the latitude range 32°N–40°N and longitude range 114°W–125°W within the period 1945–2000. The data are taken from Worldwide Earthquake Catalog produced by The Council of the National Seismic System (CNSS) (available at <http://quake.geo.berkeley.edu/cnss>). Only earthquakes with magnitudes  $M \geq 4.0$  are kept for analysis; aftershocks are not excluded. As a result, 3322 earthquakes are considered. Nine of them have magnitude  $M \geq 6.5$ ; they are listed in Table 2 and shown in Fig. 1.

## 3. Correlation length

The correlation length  $\xi(\mathbf{x}, t)$  is defined as the median of the length distribution of links, which form a single-link cluster for epicenters of consecutive  $K$  earthquakes occurred prior to the time  $t$  and within a circle of radius  $R$  centered at the point  $\mathbf{x}$  [18]. The procedure for constructing a single-link cluster connecting  $M$  points in a metric space is the following [43]: 1) Each point of  $M$  is connected with its nearest neighbor;  $M_1 < M$  clusters are pro-

TABLE 2. Large earthquakes considered

	Date	$M$	Longitude, °W	Latitude, °N	Area
a	July 21, 1952	7.5	119.02	35.00	Kern County
b	April 9, 1968	6.5	116.13	33.19	Borrego Mountain
c	February 9, 1971	6.6	118.40	34.41	San Fernando
d	May 2, 1983	6.7	120.32	36.22	Coalinga
e	November 24, 1987	6.6	115.84	33.01	Superstition Hills
f	October 18, 1989	7.0	121.88	37.04	Loma Prieta
g	June 28, 1992	7.3	116.44	34.20	Landers
h	January 17, 1994	6.6	118.54	34.21	Northridge
i	October 16, 1999	7.1	116.27	34.59	Hector Mine

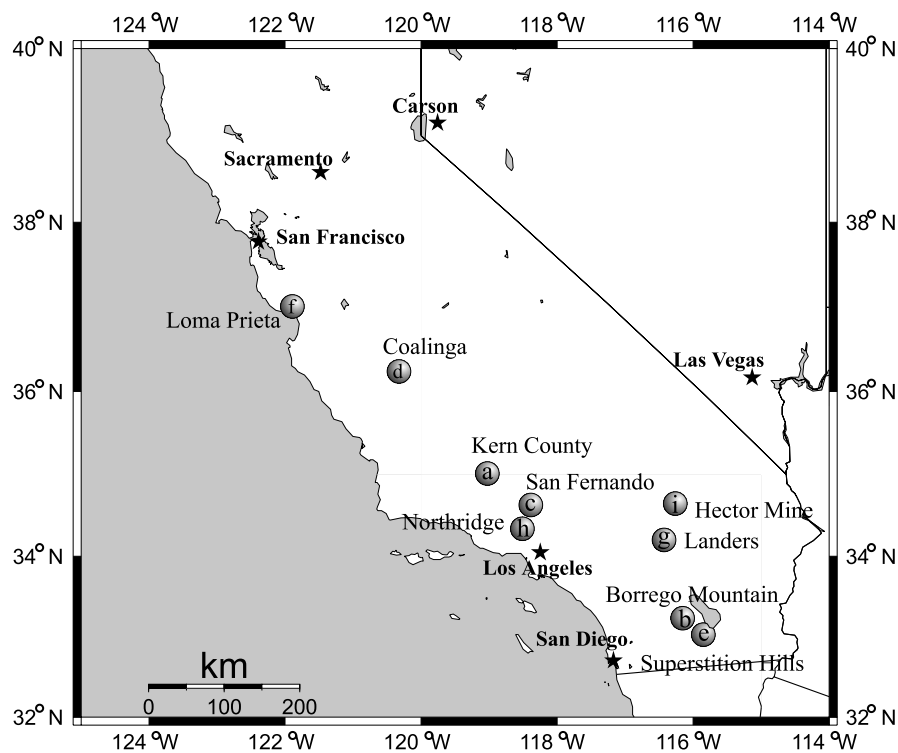


**Fig. 1.** Earthquakes with  $M \geq 6.5$  since 1952 in California: circle (a) Kern County, 1952,  $M = 7.5$ ; (b) Borrego Mountain, 1968,  $M = 6.5$ ; (c) San Fernando, 1971,  $M = 6.6$ ; (d) Coalinga, 1983,  $M = 6.7$ ; (e) Superstition Hills, 1987,  $M = 6.6$ ; (f) Loma Prieta, 1989,  $M = 7.0$ ; (g) Landers, 1992,  $M = 7.3$ ; (h) Northridge, 1994,  $M = 6.6$ ; (i) Hector Mine, 1999,  $M = 7.1$ . After [18]

duced; 2) Each cluster of  $M_1$  is connected with its nearest neighbor; distance between clusters is a minimum distance between points from these clusters;  $M_2 < M_1 < M$  clusters are produced; 3) This procedure is repeated until all points are connected within a single cluster.

The analysis was carried out by considering a spatial grid  $G$  with cell size of  $0.5^\circ \times 0.5^\circ$ . The correlation length  $\xi(\mathbf{x}, t)$  was calculated at each of 247 nodes of the grid for the time period 1945–2000. It was calculated at each node with different sliding event window size  $K$  and circle radii  $R$ :  $K$  was varied from 15 to 25 with step 2;  $R$  was varied from 100 km to 600 km with step 100 km; therefore 36 versions of the correlation length were calculated for each spatial location. Only those circles that contain more than 100 earthquakes during the whole time period are left for further analysis. It is worth mentioning that on average the event window of size  $K = 15$  corresponds to 0.97 yr,  $K = 25$  to 1.51 yr.

The function  $\xi(\mathbf{x}, t)$  for the location  $\mathbf{x} = (34^\circ\text{N}, 116.5^\circ\text{W})$ , close to the epicenter of Landers earthquake (1992,  $M = 7.3$ ), is shown in Fig. 2.

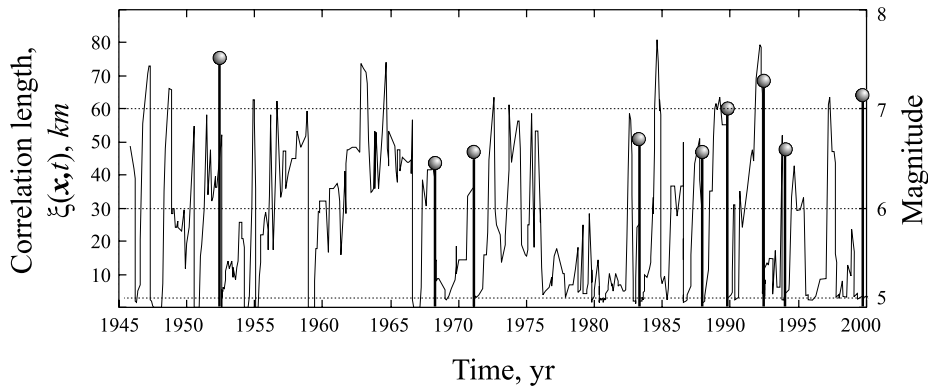


**Fig. 2.** Typical correlation length  $\xi(\mathbf{x}, t)$  evaluated for the location  $x = (34^\circ\text{N}, 116.5^\circ\text{W})$ , close to the epicenter of Landers earthquake (1992,  $M = 7.3$ ). Vertical lines mark occurrence times of large earthquakes. See discussion in Sect. 3

It corresponds to  $K = 25$ ,  $R = 600$  km; vertical lines mark the occurrence time of large ( $M \geq 6.5$ ) earthquakes. There is a sharp increase of the correlation length during 2 years prior to Landers; at the same time the general behavior of the function  $\xi(\mathbf{x}, t)$  is quite irregular and unstable. One observes large spikes over the whole time period; not necessarily preceding a large earthquake. Clearly, this single function does not say too much about large earthquake occurrence. However, what is of interest is to study the collective behavior of  $\xi(\mathbf{x}, t)$  at different spatial locations to check whether its high values can be observed more often prior to a large earthquake.



#### 4. Distribution analysis

In this section we analyze the distributions of  $\xi$  values for two distinct spatio-temporal zones: 1) close in time and space to epicenters of large earthquakes and 2) distant in time and space from the epicenters of large earthquakes. The first zone is called *zone D*, for *dangerous*; the second zone is called *zone N*, for *non-dangerous*. Ideally, one should observe premonitory phenomena within zone **D**, and should not within zone **N**. This simple and straightforward analysis is well known in pattern recognition and was used successfully in many geophysical studies.

Let  $(\mathbf{X}_i, T_i), i = 1, \dots, n_{eq}$  be space and time coordinates of  $n_{eq}$  large earthquakes, which occurred within the analyzed time-space volume. Following are the definitions of zones **A**, **D**, and **N** used in the distribution analyses. Qualitatively, a spatio-temporal point belongs to zone **A** (**D**) if it is close in space and time to one of the large earthquakes and lies after it (prior to it) in time. Formally, point  $(\mathbf{x}, t)$  belongs to zone **A** if and only if the following two conditions hold for at least one index  $k, 1 \leq k \leq n_{eq}$ : 1)  $|\mathbf{X}_k - \mathbf{x}| < r_A$ ; 2)  $0 < t - T_k < T_A$ . Here  $|\cdot|$  denotes a spherical distance. Point  $(\mathbf{x}, t)$  belongs to zone **D** if and only if it does not belong to zone **A** and the following two conditions hold for at least one index  $k$ : 1)  $|\mathbf{X}_k - \mathbf{x}| < r_D$ ; 2)  $0 < T_k - t < T_D$ . Point  $(\mathbf{x}, t)$  belongs to zone **N** if and only if it does not belong neither to zone **A** nor zone **D**.  $r_A, T_A, r_D$ , and  $T_D$  are numerical parameters. Note that each spatio-temporal point belongs to one and only one of zones **A**, **D**, and **N**.

Zone **A** covers the aftermath of a large earthquake; points from this zone are excluded from the analysis. Thus, only the  $\xi$  values evaluated within zones **D** and **N** are considered. This is especially important in our case when aftershocks are not eliminated and dramatically affect the dynamics of the correlation length  $\xi(\mathbf{x}, t)$ . Figures 3a,b show distributions  $H_D$  and  $H_N$  of the correlation length  $\xi(\mathbf{x}, t)$  within zones **D** and **N** respectively; parameters used to construct the distributions are indicated in bold in the first column of Table 3. These distributions are coarsely estimated at three bins each containing 1/3 of the correlation length values observed within zones **D** and **N** together. Clearly, one observes a discrepancy: the distribution  $H_N$  is almost uniform while the distribution  $H_D$  favors high values of the correlation length. To further illustrate this observation we consider the difference of the distributions:  $H_\Delta = H_D - H_N$ , which is shown in Fig. 3 c. Positive values of this difference for the right bin,  $H_\Delta$  ("high"), indicate that high values of the correlation length are observed more often within zone **D**.

Panels d-f of Fig. 3 illustrate the distribution analysis with parameters listed in the third column of Table 3. The qualitative picture is the same

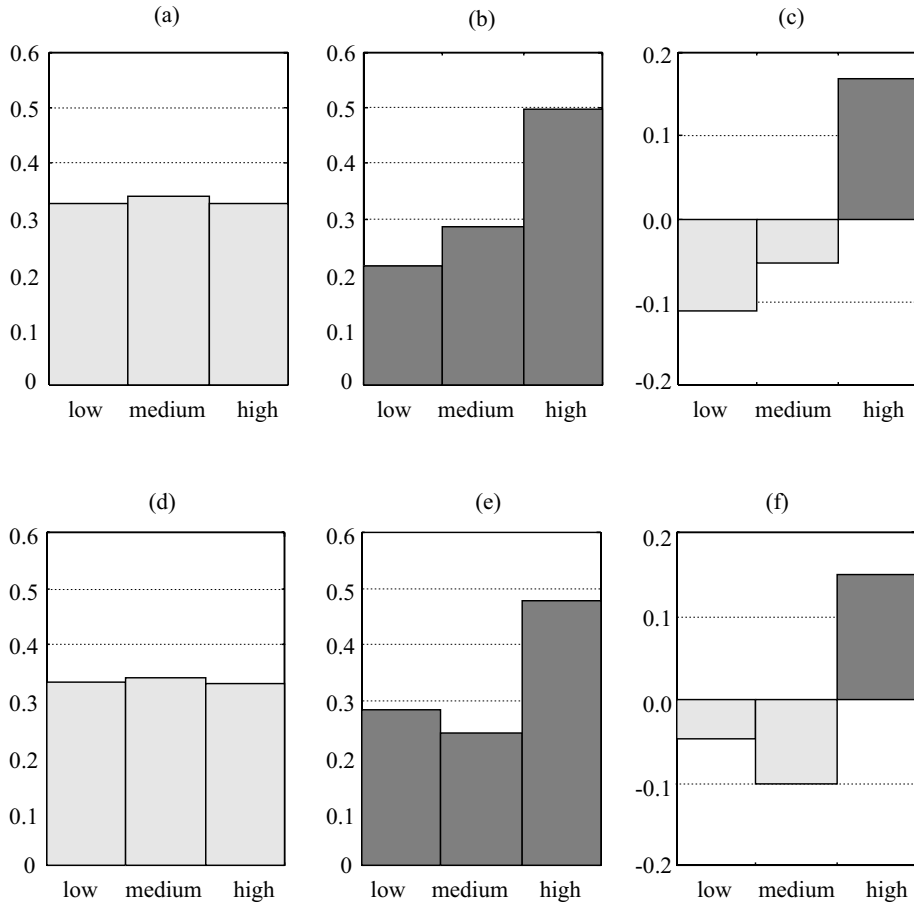


**Fig. 3.** Distribution analysis. Distribution of  $\xi$  is coarsely evaluated at three bins, "low", "medium" and "high", each containing 1/3 of values considered. Panels (a)–(c) correspond to parameters given in the first column of Table 3, (d)–(f) to parameters given in the third column. (a), (d) distribution  $H_N$  within zone N, distant in time and space from large earthquakes; (b), (e) distribution  $H_D$  within zone D, close in time and space to large earthquakes; (c), (f) difference of distributions,  $H_\Delta = H_D - H_N$ . Note the discrepancy of distributions  $H_N$  and  $H_D$ : there is a clear shift toward high values within zone D, which is depicted by positive values of the difference  $H_\Delta$  ("high")

TABLE 3. Distribution analysis (Sect.4). Other parameters are fixed:

$$K = 25, r_A = r_D = 100\text{km}, T_A = 2 \text{ yr}$$

$R$ , km	600*	600	500	500	400	400	300	300	200	200	100	100
$T_D$ , yr	1	5	1	5	1	5	1	5	1	5	1	5
$H_\Delta$ ("high"), %	16	5	15	6	13	5	6	1	4	7	-3	7

\*Sets of parameters given in bold are discussed in the text (Sect.4) and illustrated in Fig.3

as in panels a-c: there is a shift of the distribution toward high values within zone **D**. Results for different parameter values are collected in Table 3. Due to qualitative similarity of analyzed distributions and the obvious relation  $H_{\Delta}(\text{"low"}) + H_{\Delta}(\text{"medium"}) + H_{\Delta}(\text{"high"}) = 0$ , only the differences  $H_{\Delta}(\text{"high"})$  (in %) are shown. The results presented in the table demonstrate that the distribution shift is stable under variations of parameters.

Being calculated with  $T_{\mathbf{D}} = 1$  yr,  $H_{\Delta}(\text{"high"})$  decreases with the radius  $R$  from 16% to 5%; it remains nearly 5% for  $T_{\mathbf{D}} = 5$  yr, i.e., the best statistical separation of zones **D** and **N** are possible within an extended territory,  $R = 600$  km, during the relatively short time period of 1 year; it became worse for improperly long times or small territories.

While the discrepancy between the distributions  $H_{\mathbf{D}}$  and  $H_{\mathbf{N}}$  is evident, it is in fact not too large. The maximum difference between distributions reported in Table 3 is only 16%. Is it enough to distinguish zones **D** and **N** in practice? Is the correlation length a reliable signal of a large earthquake approach? To answer these questions, we analyze retrospective prediction that could be done using the correlation length as a precursor of a large earthquake.

## 5. Retrospective prediction

In this section we consider retrospective predictions targeted at nine large ( $M \geq 6.5$ ) earthquakes in California during 1945–2000; they are listed in Table 2. The predictions are based on the increase of the correlation length defined in Sect. 3.

The prediction methodology that we use here is based on pattern recognition analyses of infrequent events introduced to geophysics by I. M. Gelfand in the early 70-s [44]; it was successfully used for many years in the quest for premonitory seismicity patterns (see review in [12, 22]). The major trait of this approach is its robustness: results are coarse but stable. Prediction is of the yes-no type: we declare precisely outlined alarms and count all successes and errors. Exhaustive variation of the prediction's adjustable elements evaluates its quality and stability. A pivotal tool for such an evaluation is the *error diagram* (Sect. 5.2), which sums up different errors of prediction, allows the comparison of different prediction methods and optimization of prediction strategies. The error diagram was introduced to seismological studies by G. Molchan [45] and became an indispensable tool in earthquake prediction research.

**5.1. Scheme of analysis.** The function  $\xi(\mathbf{x}, t)$  is monitored at each node  $\mathbf{x}_i$  of the grid  $G$ . Once it exceeds the threshold  $C_i$  an *individual alarm* is declared for the time  $\Delta$  within the circle of radius  $r$  centered at  $\mathbf{x}_i$ . Threshold

$C_i$  is defined as  $Q$ -percentile of values  $\xi(\mathbf{x}_i, t)$  observed at the location  $\mathbf{x}_i$ . An *alarm cluster* is defined as a union of alarms that are connected in space and time. This means that two alarms belong to the same cluster if and only if there is a spatio-temporal path, which connects these alarms and is totally covered by these and other alarms (obviously, all alarms that cover this path also belong to the same cluster). If a target earthquake happens to be covered by an alarm cluster it is called a *predicted earthquake*; otherwise it is called an *unpredicted earthquake*. An alarm cluster that covers at least one of the target earthquakes is called a *successful alarm*; otherwise it is called a *false alarm*. Note that the definition of predicted/unpredicted earthquakes would not change if one considered individual alarms instead of alarm clusters; and this is not the case for successful/false alarms.

**5.2. Error diagrams.** Suppose that the prediction was performed during the time interval of length  $T$  (yr) within the area of  $S$  (km<sup>2</sup>) and  $N$  large earthquakes occurred within this period;  $A$  alarm clusters were declared and  $A_f$  of them are false; all the alarms altogether cover the spatio-temporal volume  $V_A$  (yr  $\times$  km<sup>2</sup>);  $N_f$  target earthquakes were unpredicted. Prediction is described by the following dimensionless errors: the fraction of unpredicted earthquakes,  $n = N_f/N$ ; the relative alarm coverage,  $\tau = V_A/(T \times S)$ ; the fraction of false alarms,  $f = A_f/A$ .

The *error diagram* sums up the prediction errors; each particular prediction corresponds to a single point in  $(n, \tau, f)$  space. The error diagram will be used to evaluate the predictive power of our prediction algorithm and its stability.

The evaluation of the correlation length  $\xi(\mathbf{x}, t)$  involves two numerical parameters, event window size  $K$  and data collection radius  $R$ ; a prediction with a particular function  $\xi$  depends on another three parameters, threshold quantile  $Q$ , alarm radius  $r$ , and alarm duration  $\Delta$ . Each combination of these five parameters corresponds to a separate prediction, characterized by three errors:  $n(K, R, Q, r, \Delta)$ ,  $\tau(K, R, Q, r, \Delta)$ ,  $f(K, R, Q, r, \Delta)$ .

**5.3. Prediction.** We performed predictions following the scheme of Sect. 5.1. The parameters are varied as follows:  $K = 15, 17, \dots, 25$ ;  $R = 100, 200, \dots, 600$  km;  $Q = 0.5, 0.6, 0.7, 0.8, 0.9, 0.95, 0.99$ ;  $\Delta = 0.5, 1, \dots, 10$  yr;  $r$  was always fixed at 100 km. Over 5,000 predictions were considered altogether.

An error diagram for predictions with  $R = r = 100$  km is shown in Fig. 4; it brings together 840 individual predictions with different values of parameters  $K, Q$ , and  $\Delta$ . The fact that the fraction of space-time alarm duration is always greater than 15% is due to our prediction scheme. Each node is forced to declare at least one alarm; thus the total space-time area covered by alarms cannot be arbitrary small even for the highest values of

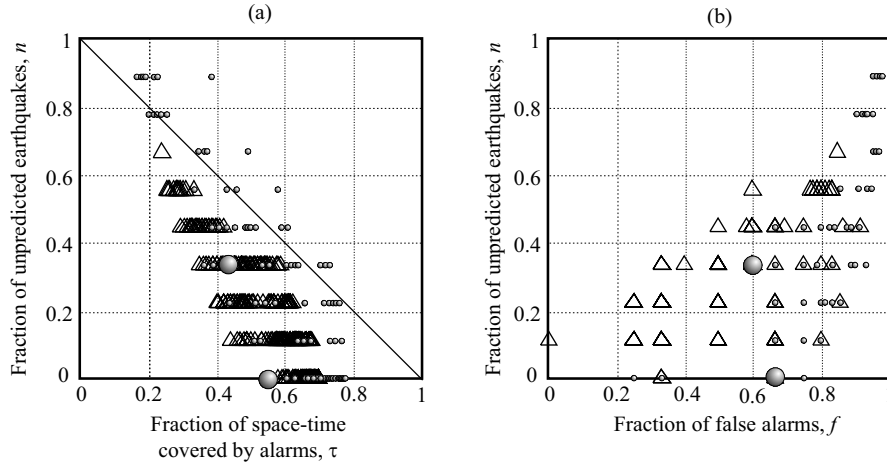


**Fig. 4.** Error diagram for retrospective prediction in California during 1945–2000. Each point corresponds to a fixed set of parameter values. (a) Fraction of space-time covered by alarms,  $\tau$ , vs. fraction of failures to predict,  $n$ . (b) Fraction of false alarms,  $f$ , vs. fraction of failures to predict,  $n$ . Parameters are varied as follows:  $K = 15, 17, \dots, 25$ ;  $R = r = 100$  km;  $Q = 0.5, 0.6, 0.7, 0.8, 0.9, 0.95, 0.99$ ;  $\Delta = 0.5, 1, \dots, 10$  years. Triangles correspond to a narrowed range of parameters:  $Q \geq 0.9, \Delta \geq 2$  years. Large circles mark two versions of predictions that are used for the stability analysis (Sect. 5.4, Fig. 6) and in the analysis of individual predictions (Sect. 5.5, Fig. 7). Diagonal line in panel (a) correspond to a random binomial prediction: alarm is declared at each time with probability  $p = \tau$ , and is not declared with probability  $1 - p = 1 - \tau$ ; deviations from the diagonal line depict predictive power of a precursor [45]

the threshold  $Q$ . Notably, the  $n - \tau$  part of the error diagram is asymmetric relative to the diagonal line of random prediction and most of the points are distanced from this line; thus indicating the predictive power of the considered precursor. Still, some points lie above the diagonal line, implying a prediction worse than "random". Is it an inherent drawback of prediction by the correlation length  $\xi(\mathbf{x}, t)$ ? In fact, we have considered such a broad range of parameter values that it would be too naive to hope that all of them will produce reasonable result. Triangles in Figure 4 mark predictions obtained within the narrowed parameter range:  $Q \geq 0.9, \Delta \geq 2$  yr. All these points are nicely clustered and separated from the random prediction line; the number of false alarms decreases.

Previous studies suggest that premonitory phenomena scale with the size of approaching earthquake. Thus it is natural to expect that the increase of the correlation length should be observed within different spatio-temporal zones for earthquakes of different magnitude. Figure 5 shows separate error diagrams for predictions targeted at earthquakes of magnitude  $M \leq 7.0$  and  $M > 7.0$  (Kern County, Landers, Hector Mine). Panels a, and b correspond to  $M \leq 7.0, R = r = 100$  km,  $Q \geq 0.9, \Delta \geq 2$  yr; panels c, and d to  $M > 7.0, R = 200, r = 100$  km,  $Q \geq 0.95, \Delta \leq 5$  yr. Points on both error

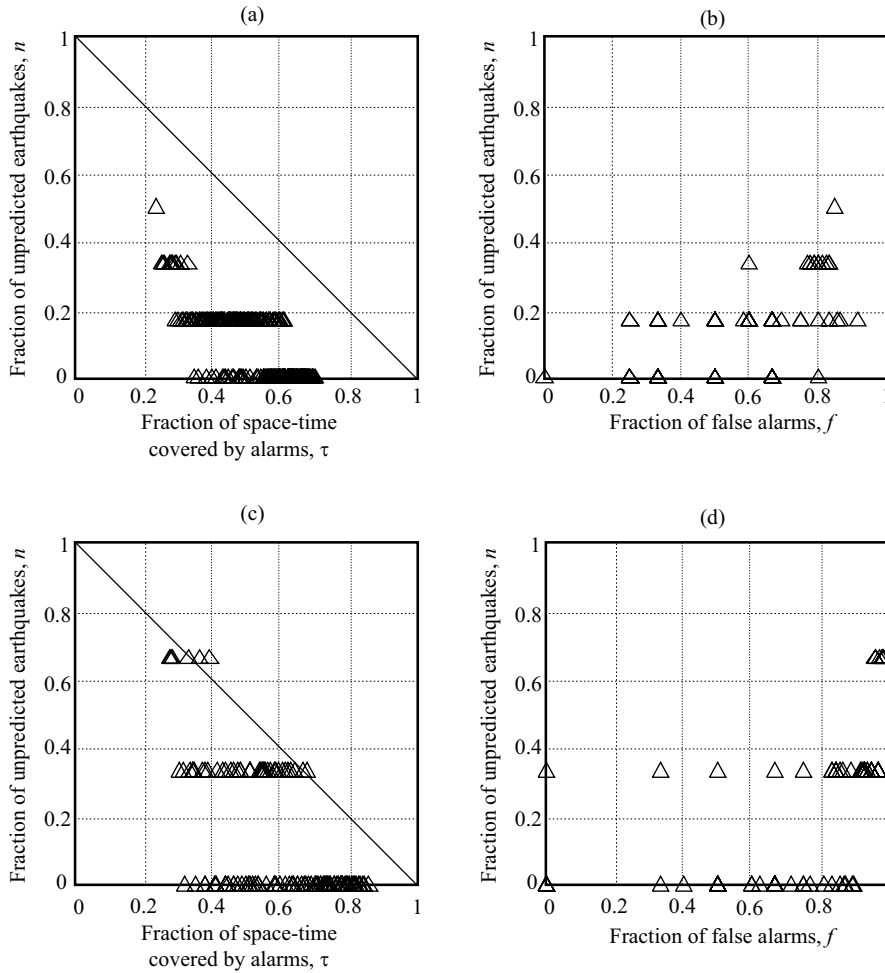


**Fig. 5.** Error diagrams for predictions of different target magnitudes. (a), (b)  $M < 7.0$ ,  $K = 15, 17, \dots, 25$ ,  $R = r = 100$  km,  $Q \geq 0.9$ ,  $\Delta \geq 2$  yr; (c), (d)  $M > 7.0$ ,  $K = 15, 17, \dots, 25$ ,  $R = 200$ ,  $r = 100$  km,  $Q \geq 0.95$ ,  $\Delta \leq 5$  yr. See details in Sect. 5.3

diagrams in Fig. 5 lie closer to the origin,  $n = \tau = f = 0$ , than points in Fig. 4, which means that prediction quality has improved. Noteworthy is the difference in parameters corresponding to the improved predictions. Prediction of earthquakes with  $M > 7.0$  is better with  $\xi(\mathbf{x}, t)$  estimated within an area of  $R = 200$  km; prediction  $M \leq 7.0$  is better with  $\xi(\mathbf{x}, t)$  estimated within a smaller area,  $R = 100$  km. Predictions of  $M > 7.0$  are more precise: The correlation length increases less than 5 years prior to a target earthquake; while for  $M \leq 7.0$  the increase is observed 2–10 years in advance.

**5.4. Stability of prediction.** In the previous section we demonstrated that there is a wide domain of parameters that produce reasonable predictions. But how stable are these predictions? How does a slight variation of parameters affect the prediction outcomes? To answer these questions we single out two predictions marked by large open circles in Fig. 4, slightly change values of numerical parameters corresponding to these versions, and compare our results on the error diagram (Fig. 6).

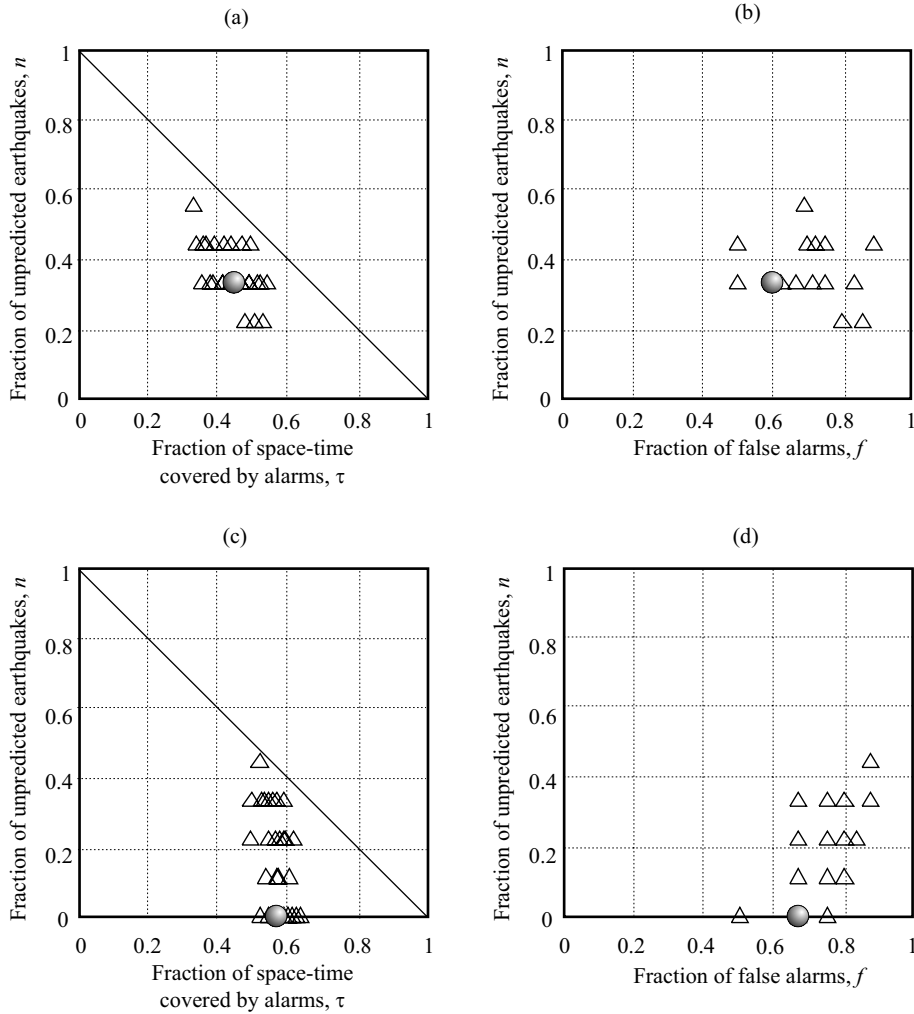


**Fig. 6.** Stability analysis: a particular version of prediction is considered, parameters of this prediction are slightly varied, and results corresponding to these variations are shown in the error diagram. Filled circles: original versions of prediction, triangles – variations. Two versions of prediction are considered:  $K = 25$ ,  $R = r = 100$  km,  $Q = 0.95$ ,  $\Delta = 2$  yr (panels (a), (b)), and  $K = 19$ ,  $R = r = 100$  km,  $Q = 0.9$ ,  $\Delta = 1$  yr (panels (c), (d)). These two versions of prediction are marked by large circles at error diagram in Fig. 4

Parameter values and their variations are given in Table 4. The first row of the table corresponds to panels a, b, and the second to panels c, d.

TABLE 4. Parameters for stability test (Sect. 5.4)

$R$ , km	$K$	$Q$	$r$ , km	$\Delta$ , years
<b>100</b>	21, 23, <b>25</b>	0.9, <b>0.95</b> , 0.99	<b>100</b>	1.5, <b>2</b> , 2.5
<b>100</b>	17, <b>19</b> , 21	0.8, <b>0.9</b> , 0.95	<b>100</b>	0.5, <b>1</b> , 1.5

Stability of prediction is depicted by the clustering of points with regard to the original version of prediction. Obviously, stability is high in panels a, b; and is slightly worse in panels c, d. This is due to our choice of versions for our stability analysis. The original prediction for panels a, b is taken from the center of the point cluster on the error diagram (Fig. 4); as a result it gives not the best but stable and reproducible predictions. On the contrary, the original prediction for panels c, d is taken from the boundary of the cluster. It produces better-than-average but less stable results. Generally, the "best" versions of prediction, taken from the border of the error diagram cluster, outline boundaries of the predictive power of a given method rather than reflect the realistic quality of prediction.

So far we have considered averaged statistics of prediction. Next we focus on individual predictions for specific spatial locations.

**5.5. Individual predictions.** At any given time a particular spatial point may be covered by more than one individual alarm, because an alarm produced at spatial point  $\mathbf{x}$  is declared not only for this point but for an extended circle centered at  $\mathbf{x}$ . In this section we consider the number of alarms that cover a particular spatial location at a given time moment. We focus our attention on three locations: epicenters of Borrego Mountain (1968,  $M = 6.5$ ), San Fernando (1971,  $M = 6.6$ ) and Landers (1999,  $M = 7.3$ ) earthquakes. The number of alarms declared for each of these locations is shown in Fig. 7a. Predictions are made with parameters shown in bold in the first row of Table 4. The top panel corresponds to the Borrego Mountain epicenter, the middle to San Fernando, and the bottom to Landers. Vertical lines mark the occurrence times of these earthquakes. In each panel we additionally show the occurrence times of earthquakes that were within 100 km from the location considered. Thus, we also show Superstition Hills (1988,  $M = 6.6$ ) earthquake in the top panel, Kern County (1952,  $M = 7.5$ ) and Northridge (1994,  $M = 6.6$ ) in the middle panel, and Hector Mine (1999,  $M = 7.1$ ) in the bottom panel. Predictions for the same three locations but with different parameter values are shown in Fig. 7 b; parameters are given in bold in the second row of Table 4.



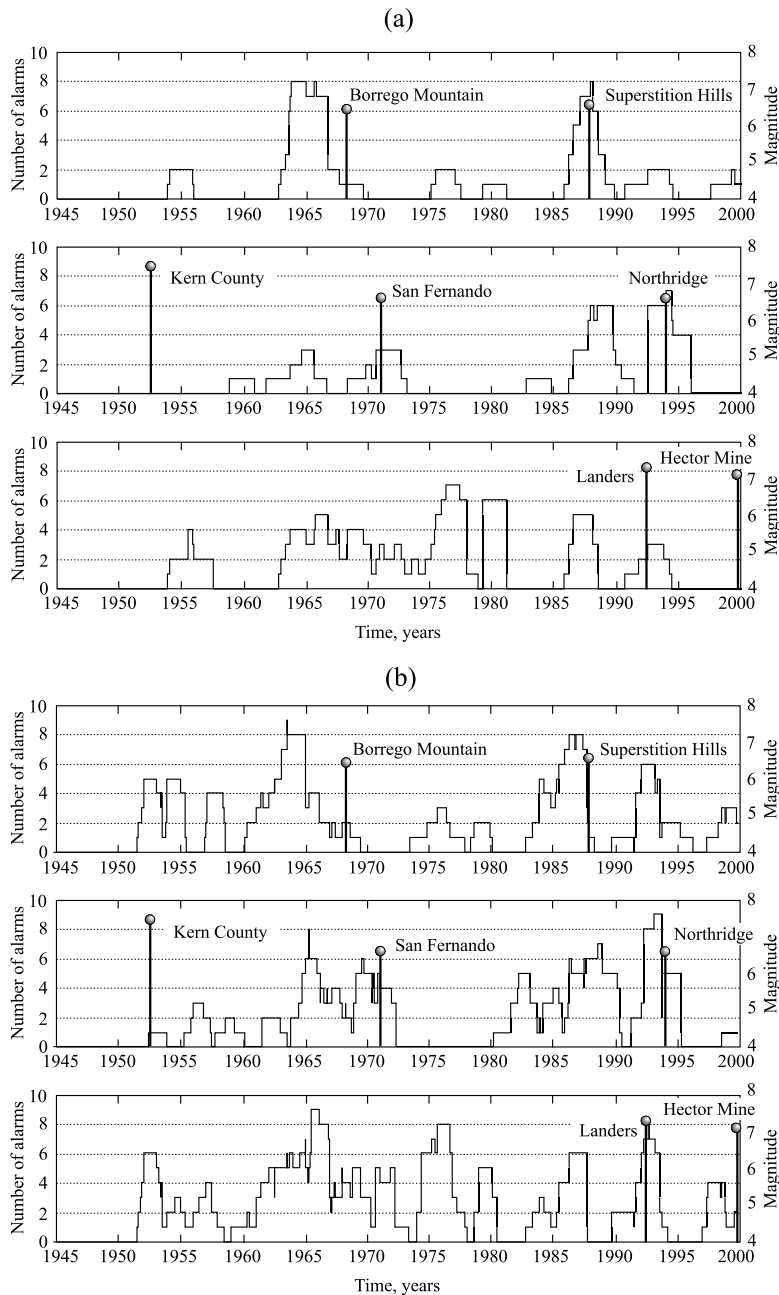


**Fig. 7.** Number of alarms that cover a particular spatial location at time  $t$ . Vertical lines mark occurrence times of large earthquakes that fell within 100 km from the location considered. Top panel corresponds to the epicenters of Borrego Mountain earthquake (1968,  $M = 6.5$ ), middle to San Fernando (1971,  $M = 6.6$ ) and bottom to Landers (1999,  $M = 7.3$ ). (a)  $K = 25$ ,  $R = r = 100$  km,  $Q = 0.95$ ,  $\Delta = 2$  yr, (b)  $K = 19$ ,  $R = r = 100$  km,  $Q = 0.9$ ,  $\Delta = 1$  yr. These two versions of prediction are marked by large circles in the error diagram in Fig. 4

Figures 7 a, b give a typical picture of what happens within the regions considered. Prediction works reasonably for Imperial Valley earthquakes (top panel) and in the area near the San Andreas – Garlock triple junction (middle panel); increases of the correlation length are definitely associated with times preceding large earthquakes. At the same time the prediction fails when it is shifted to the Mojave Desert where a pronounced increase of the correlation length occurred in 1970s but faded away by 1990s when the two largest earthquakes occurred.

Similar analysis shows that Loma Prieta earthquake (1989,  $M = 7.0$ ) is usually predicted with a couple of false alarms within its territory. The Coalinga earthquake (1983,  $M = 6.7$ ) is typically missed. The correlation length significantly increases within its territory only in the late 1990s; 10 years after the event. A notable feature in Fig. 7 is the pronounced clustering of alarms in time.

## 6. Discussion and conclusions

1. We have examined the hypothesis that the earthquake correlation length increases prior to large earthquakes in California and may be used for earthquake prediction. With this aim in view, we analyzed the measure  $\xi(\mathbf{x}, t)$  of correlation length introduced in [18]. First, we considered statistical distribution of the values of the correlation length  $\xi(\mathbf{x}, t)$  and found the shift toward high values within the areas close in space and time to a large earthquake. Second, we performed retrospective predictions of large earthquakes in California during the period 1945–2000, evaluated its performance and found the set of parameters that gave reasonable and stable prediction quality. Finally, we analyzed predictions for territories around epicenters of large earthquakes.

2. Our results imply that the measure  $\xi(\mathbf{x}, t)$  does increase prior to a large earthquake within an extended region around the ensuing epicenter. Importantly, we were able to observe that phenomenon using the *same* fixed set of parameters for *the whole* space and time considered. Moreover, we outlined a large domain of parameters that can be used to reproduce the general result.

3. At the same time, the premonitory increase of the correlation length is weak; e.g. distributions of  $\xi$  values for zones **D** and **N** differ by less than 20% only. This situation is usual for prediction research; it is well known that individual premonitory patterns typically perform not so well and should be considered together within a complex prediction algorithm. This is the case for well-tested prediction algorithms M8, CN, and SSE. Our results suggest that the increase of earthquake correlation range can be considered as a reliable individual precursor.

4. From results in Sect. 4 and 5 we conclude that the best statistical discrimination of zones **D** and **N** corresponds to using a large territory ( $R = 600$  km) to evaluate the correlation length. On the contrary, the best prediction corresponds to a smaller territory,  $R \leq 200$  km. This is caused by a large number of "false" increases of the correlation length evaluated within the large circles. While high values of  $\xi$  are definitely observed prior to large earthquakes (see Fig. 2); they are also frequently seen elsewhere. The number of "false" high values is small enough not to destroy statistics (Sect. 4), but is unacceptable to construct reasonable prediction. This provides a good illustration why statistical difference is not equivalent to the possibility of prediction. Furthermore, this explains why the analysis of only times and spaces around large earthquake (zones **D**) is insufficient to make conclusions about the predictive power of a phenomenon.

5. Results of Sect. 5.5 imply that premonitory increases of the correlation length are best observed for the Imperial Valley and for the area around the San Andreas – Garlock junction. It is not very clear in the Mojave Desert, and along the northern San Andreas fault. These observations suggest a hypothesis that the increase of the correlation length is a phenomenon characteristic for highly fractured regions comprising diverse faults and/or fault systems. Clearly, this hypothesis needs further systematic analysis and cannot be tested by data and methods considered in this paper.

6. Alarms produced by increased correlation length clearly tend to cluster in space and time. It is worth further study to explore how this clustering may be used to improve prediction. Particularly, results of Sect. 5.5 suggest that prediction can be significantly improved using the number of alarms declared for a given spatial point as a precursor.

7. The definition of the earthquake correlation length used in this paper is debatable. The function  $\xi(\mathbf{x}, t)$  does reflect a multitude of seismicity features not necessarily connected with the studied phenomenon. Most obviously, it decreases due to aftershocks and swarms (see Fig. 2). Nevertheless, it demonstrates stable predictive power (Sect. 5.3, 5.4) and allows distinguishing between space and time close and distant from a large earthquake (Sect. 4). Further investigations of the earthquake correlation length dynamics seem promising to improve its definition and explore potential predictive power.

8. The measure  $\xi$  reflects specific features of earthquake clustering depicted by single-link clusters. Noteworthy is an alternative approach to quantitative analysis of premonitory seismicity clustering that was developed by A. Blanter and M. Shnirman in [46] and recently extended to the prediction in a sand-pile model by A. Shapoval and M. Shnirman in [47].

Acknowledgements. The authors sincerely thank V. Pisarenko, G. Molchan and B. Naimark for valuable comments and suggestions. We gratefully acknowledge the financial support from *The 21st Century Collaborative Activity Award for Studying Complex Systems* (James McDonnell Foundation); INTAS, grant 99-00099; and the Deutsche Forschungsgemeinschaft (SFB 555).

## REFERENCES

1. *Mogi K.* Earthquake prediction. Tokyo: Academic Press, 1985.
2. *Press F., Allen C.* Patterns of seismic release in the southern California region // *J. Geophys. Res.* 1995. Vol.100, N 4. P.6421–6430.
3. *Richter C.F.* Elementary seismology. San Francisco: W.H. Freeman and Co. 1958.
4. *Mogi K.* Migration of seismic activity // *Bull. Earthq. Res. Inst., Tokyo Univ.* 1968. Vol.46. P.53–74.
5. *Romanowicz B.* Spatiotemporal patterns in the energy-release of great earthquakes // *Science.* 1993. Vol.260. P.1923–1926.
6. *Willis B.* Earthquake risk in California 8 earthquake districts // *Bull. Seism. Soc. Amer.* 1924. Vol.14. P.9–25.
7. *Imamura A.* Theoretical and applied seismology. Tokyo: Maruzen, 1937.
8. *Gutenberg B., Richter C.F.* Seismicity of the Earth and associated phenomena. N.Y.: Hafner. 1954.
9. *Keilis-Borok V.I., Malinovskaya L.N.* One regularity in the occurrence of strong earthquakes // *J. Geoph. Res.* 1964. Vol.69. P.3019–3024.
10. *Прозоров А.Г.* Изменения сейсмической активности, приуроченные к сильным землетрясениям // *Интерпретация данных сейсмологии и неотектоники.* М.: Наука, 1975. С.71–72. (Вычисл. сейсмология; Вып.8).
11. *Shaw B.E., Carlson J.M., Langer J.S.* Patterns of seismic activity preceding large earthquakes // *J. Geophys. Res.* 1997. Vol.97. P.479.
12. *Keilis-Borok V.I., Shebalin P.N. Eds.* Dynamics of lithosphere and earthquake prediction // *Phys. Earth Planet. Inter., Special Issue.* 1999. Vol.111. P.179–330.
13. *Jaume S.C., Sykes L.R.* Evolving towards a critical point: A review of accelerating seismic moment/Energy release prior to large and great earthquakes // *Pure Appl. Geophys.* 1999. Vol.155. P.279–306.
14. *Pepke G.F., Carlson J.M., Shaw B.E.* Prediction of large events on a dynamical model of fault // *J. Geophys. Res.* 1994. Vol.99. P.6769–6788.
15. *Kossobokov V.G., Carlson J.M.* Active zone size vs. activity: A study of different seismicity patterns in the context of the prediction algorithm M8 // *J. Geophys. Res.* 1995. Vol.100. P.6431–6441.
16. *Shebalin P., Zaliapin I., Keilis-Borok V.I.* Premonitory Rise Of The Earthquakes' Correlation Range: Lesser Antilles // *Phys. Earth Planet. Inter.* 2000. Vol.122. P.241–249.
17. *Gabrielov A.M., Zaliapin I.V., Newman W.I., Keilis-Borok V.I.* Colliding cascades model for earthquake prediction // *Geophys. J. Int.* 2000. Vol.143. P.427–437.
18. *Zöller G., Hainzl S., Kurths J.* Observation of growing correlation length as an indicator for critical point behavior prior to large earthquakes // *J. Geophys. Res.* 2001. Vol.106. P.2167–2176.

19. *Zöller G., Hainzl S.* Detecting premonitory seismicity patterns based on critical point dynamics // *Natural Hazards and Earth System Sciences*. 2001. Vol.1. P.93–98.
20. *Zaliapin I., Keilis-Borok V., Axen G.* Premonitory spreading of seismicity over the fault's network in S. California: precursor accord // *J. Geoph. Res.* 2002 (Accepted).
21. *Caputo M., Gasperini P., Keilis-Borok V.I., Marcelli L., Rotwain I.M.* Earthquakes' swarms as forerunners of strong earthquakes in Italy // *Ann. Geofis. (Roma)*. 1977. Vol.30. P.269–283.
22. *Keilis-Borok V.I.* Earthquake prediction: State-of-the-art and emerging possibilities // *Ann. Rev. Earth Planet. Sci.* 2002. Vol.30. P.1–33.
23. *Keilis-Borok V.I., Kossobokov V.G.* Premonitory activation of earthquake flow: algorithm M8 // *Phys. Earth Planet. Inter.* 1990. Vol.61. P.73–83.
24. *Keilis-Borok V.I., Rotwain I.M.* Diagnosis of time of increased probability of strong earthquakes in different regions of the world: algorithm CN // *Phys. Earth Planet. Inter.* 1990. Vol.61. P.57–72.
25. *Vorobieva I.A.* Prediction of a subsequent large earthquake // *Phys. Earth Planet. Inter.* 1999. Vol.111. P.197–206.
26. *Molchan G.M., Dmitrieva O.E., Rotwain I.M., Dewey J.* Statistical analysis of the results of earthquake prediction, based on bursts of aftershocks // *Phys. Earth Planet. Inter.* 1990. Vol.61. P.128–139.
27. *Kossobokov V.G., Romashkova L.L., Keilis-Borok V.I., Healy J.H.* Testing earthquake prediction algorithms: Statistically significant real-time prediction of the largest earthquakes in the Circum-Pacific, 1992-1997 // *Phys. Earth Planet. Inter.* 1999. Vol.111, N 3-4. P.187–196.
28. *Varnes D.J.* Predicting earthquakes by analyzing accelerating precursory seismic activity // *Pure Appl. Geophys.* 1989. Vol.130. P.661–686.
29. *Bufe C.G., Varnes D.J.* Predictive modeling of the seismic cycle of the great San Francisco bay region // *J. Geophys. Res.* 1993. Vol.98. P.9871–9883.
30. *Bowman D.D., Ouilon G., Sammis C.G., Sornette A., Sornette D.* An observational test of the critical earthquake concept // *J. Geophys. Res.* 1998. Vol.103. P.24359–24372.
31. *Yamashita T., Knopoff L.* Model for intermediate-term precursory clustering of earthquakes // *J. Geophys. Res.* 1992. Vol.97. P.19,873–19,879.
32. *Lyakhovskiy V., Ben-Zion Y., Agnon A.* Earthquake cycle, fault zones and seismicity patterns in a rheologically layered lithosphere // *J. Geophys. Res.* 2001. Vol.106. P.4103–4120.
33. *Soloviev A., Vorobieva I.* Long-range interaction between synthetic earthquakes in the model of block structure dynamics, fifth workshop on non-Linear dynamics and earthquake prediction, 4–22 October 1999. Trieste: ICTP, H4.SMR/1150-4. 18 p.
34. *Zaliapin I., Keilis-Borok V., Ghil M.* A boolean delay model of colliding cascades. II: prediction of critical transitions // *J. Stat. Phys.* 2001 (Submitted).
35. *Sadovsky M.A.* Randomness and instability in geophysical processes (In Russian) // *Fizika Zemli*. 1989. Vol.2. P.3–12.
36. *Knopoff L.* Self-organization and the development of pattern: Implications for earthquake prediction // *Proc. Amer. Philosoph. Soc.* 1993. Vol.137. P.339–349.
37. *Bak P.* How nature works: The science of self-organized criticality. N.Y.: Copernicus, 1996.
38. *Turcotte D.L.* Fractals and chaos in geology and geophysics. Cambridge University Press, 1997.
39. *Sornette D.* Critical phenomena in natural sciences. Chaos, fractals, self-organization and disorder: Concepts & Tools. Springer Ser. Synerg., Heidelberg. 2000. N.Y.: Springer-Verlag. P.432.

40. *Rundle B.J., Turcotte D.L., Klein W. Eds.* Geocomplexity and the physics of earthquakes. Washington, DC: AGU, 2000.
41. *Turcotte D.L., Newman W.I., Gabrielov A.* A statistical physics approach to earthquakes, geocomplexity and the physics of earthquakes. Washington: AGU, 2000.
42. *Kossobokov V.G., Keilis-Borok V.I., Turcotte D.L., Malamud B.D.* Implications of a statistical physics approach to earthquake hazard assessment and forecasting // *Pure Appl. Geophys.* 2002. Vol.157. P.2323–2349.
43. *Frohlich C., Davis S.D.* Single-link cluster analysis as a method to evaluate spatial and temporal properties of earthquake catalogues // *Geophys. J. Int.* 1990. Vol.100. P.19–32.
44. *Gelfand I.M., Guberman Sh.A., Keilis-Borok V.I., Knopoff L., Press F., Ranzman E.Ya., Rotwain I.M., Sadovsky A.M.* Pattern recognition applied to earthquake epicenters in California // *Phys. Earth Planet. Inter.* 1976. Vol.11. P.227–283.
45. *Molchan G.M.* Earthquake prediction as a decision-making problem // *Pure Appl. Geophys.* 1997. Vol.149. P.233–247.
46. *Blanter E.M., Shnirman M.G.* On multifractal theory approach to the clustering of epicenters // *Comput. Seism. and Geodyn.* AGU. 1992. Vol.2. P.37–45.
47. *Шановал А.Б., Шнирман М.Г.* Сценарий сильных событий в модели накопления песка // *Настр. сб.*
48. *Keilis-Borok V.I., Knopoff L., Rotwain I.M.* Bursts of aftershocks, long-term precursors of strong earthquakes // *Nature.* 1980. Vol.283. P.259–263.
49. *Knopoff L., Levshina T., Keilis-Borok V.I., Mattoni C.* Increased long-range intermediate-magnitude earthquake activity prior to strong earthquakes in California // *J. Geophys. Res.* 1996. Vol.101. P.5779–5796.

# Appendix I

**Earthquake clusters resulting from delayed rupture propagation in finite fault segments**

Autors:	S. Hainzl, G. Zöller, and F. Scherbaum
Journal:	Journal of Geophysical Research
Volume (Nr.):	<b>108(B1)</b>
Article/doi:	art. no. 2013, doi 10.1029/2001JB000610
Year:	2003

# Earthquake clusters resulting from delayed rupture propagation in finite fault segments

Sebastian Hainzl

Institute of Earth Sciences and Institute of Physics, University of Potsdam, Potsdam, Germany

Gert Zöller

Institute of Physics, University of Potsdam, Potsdam, Germany

Frank Scherbaum

Institute of Earth Sciences, University of Potsdam, Potsdam, Germany

Received 9 May 2001; revised 25 November 2001; accepted 30 November 2001; published 10 January 2003.

[1] The question whether the preparation process of foreshocks and main shocks is different from other earthquakes is of great interest with regard to earthquake predictability. We show that the most conspicuous properties of earthquake clustering can be explained without assuming any differences in the initiation processes. In particular, the Gutenberg-Richter law as well as the Omori law for foreshock and aftershock sequences can be reproduced by model simulations with the simple assumption that all subsequent events are initiated in the same manner at the edges of the recently ruptured area. In this way, the empirically observed  $b$  and  $p$  values are reproduced naturally without any parameter tuning as well as their differences with regard to foreshock and aftershock activity. These properties are shown to result from the shrinking of the loaded fault region with time. In the model, foreshocks occur in extended and almost compact fault segments, whereas aftershocks are mostly restricted to recesses left unruptured by the main shock. Our investigations lead to the conclusion that the spatial effects rather than the temporal effects of the initiation mechanism are decisive for earthquake clustering. *INDEX TERMS*: 7260 Seismology: Theory and modeling; 7230 Seismology: Seismicity and seismotectonics; 7209 Seismology: Earthquake dynamics and mechanics; 7223 Seismology: Seismic hazard assessment and prediction; *KEYWORDS*: aftershocks, foreshocks, Omori law, seismicity patterns, model simulations

**Citation:** Hainzl, S., G. Zöller, and F. Scherbaum, Earthquake clusters resulting from delayed rupture propagation in finite fault segments, *J. Geophys. Res.*, 108(B1), 2003, doi:10.1029/2001JB000610, 2003.

## 1. Introduction

[2] A current issue of seismology is whether the processes that occur prior to and in the initial stages of foreshock and main shock rupture can be distinguished from other earthquakes [Vidale *et al.*, 2001]. The answer of this question would have important implications with regard to the possibility of earthquake predictions. Because of the complexity of this field we address a more specific question in this paper: Which conclusions can be drawn in this respect from the seismicity patterns conserved in earthquake catalogs?

[3] The occurrence of earthquakes is complex, but not random, neither in the energy release nor in its spatiotemporal correlations. On one hand, this is documented by the patterns of clustering in space and time. Almost all earthquakes are found to trigger aftershocks with a temporal decaying probability. In particular, the occurrence rate of

aftershocks  $R$  can be well described by the modified Omori law

$$R \sim (c + \Delta t)^{-p}, \quad (1)$$

where  $\Delta t$  indicates the time after the main shock and  $c$  is a small constant taking values from 0.01 days to over 1 day with a median of about 0.3 days [Utsu *et al.*, 1995]. The observed values of the power law exponent  $p$  are close to 1. The same law, if  $\Delta t$  indicates the time before the main shock, has been found to describe the foreshock occurrence. This power law behavior has been observed for the much less frequent foreshocks by stacking foreshock activity correlated with different main shocks [Kagan and Knopoff, 1978; Jones and Molnar, 1979]. Likewise the temporal clustering, also the frequency-size distribution of earthquakes is well-defined over a wide range of magnitudes by a specific law, namely, the Gutenberg-Richter law [Gutenberg and Richter, 1956]

$$\log_{10} N = a - bM, \quad (2)$$



where  $N$  defines the number of events with magnitude greater than  $M$  and  $a$  and  $b$  are constants. This relation can be expressed by a power law also for the source size  $S$ :

$$\log_{10} N = S^{-B} \quad (3)$$

with  $B \approx b$  [Kanamori and Anderson, 1975; Purcaru and Berckhemer, 1978]. The observed  $b$  values for regional seismicity are close to 1.

[4] However, the Richter  $b$  value as well as the Omori  $p$  value vary significantly within earthquake clusters. The  $p$  value describing the temporal increase of foreshock activity is significantly smaller than the exponent of the aftershock decay [Maeda, 1999]. Furthermore, the  $b$  value of foreshocks and main shocks has been often found to be much smaller than the  $b$  value of aftershocks [Suyehiro et al., 1964; Papazachos, 1975; Knopoff, 2000], which is also in agreement with the variation of acoustic emissions in fracture experiments [Scholz, 1968; Sammonds et al., 1992; Lei et al., 2000]. It is unknown so far, whether these statistical differences between foreshocks and aftershocks result directly from differences in their initiation processes [Vidale et al., 2001].

[5] The Gutenberg-Richter law (equations (2) and (3)) points to a critical state of the stress field [Main, 1996; Sornette, 2000]. Such critical states self-organizes naturally by repeated earthquakes and tectonic forcing in simulations of the earthquake evolutionary process [Burrige and Knopoff, 1967; Bak and Tang, 1989; Olami et al., 1992; Sornette et al., 1994; Hainzl et al., 1999, 2000b]. Whether the fault system remains always near the critical point or fluctuates back and toward this state depends on the assumptions about dissipation and healing properties [Hainzl and Zöller, 2001]. However, the assumption of a critical stress state is not sufficient to understand the spatiotemporal clustering of earthquakes. Several additional mechanisms have been proposed to underly the earthquake clustering, though their real relevance is unknown so far. In particular, a rate- and state-dependent friction law [Dieterich, 1994], pore fluid flows [Nur and Booker, 1972; Yamashita, 1999], and stress corrosion cracking [Shaw, 1993; Main, 2000] are proposed on the basis of theoretical considerations. Under some restrictions, the nonlinear temporal laws of the proposed mechanism can explain the occurrence of aftershocks according to the Omori law. On the other hand, we have found in previous work [Hainzl et al., 1999] that the introduction of viscoelastic coupling in a fault model can reproduce earthquake clustering as well. However, the underlying reasons for these numerical findings have not been fully understood so far.

[6] In this paper, we will show in detail that the spatial rather than the temporal effects of the triggering mechanisms seem to be crucial for the characteristics of the above mentioned earthquake clustering. For this purpose, we study sequences of earthquakes successively unloading initially prestressed fault patches of finite size. Our cellular automaton model introduced in section 2 is mainly based on the assumption that the earthquakes within a cluster are triggered at the edges of the rupture area of precursory events. The temporal component of the postseismical effect is chosen as simple as possible, namely, state-independent and purely linear. In section 2 we show that simulations based on these

simple assumptions already reproduce the empirical observations. The implications and conclusions which can be drawn from our results are discussed in section 4.

## 2. Model

### 2.1. Assumptions

[7] Our simulations of earthquake ruptures are based on the following assumptions: (1) Ruptures occur at highly stressed fault patches of finite size; (2) the coseismic evolution is dominated by frictional behavior and elastic interactions; (3) a ruptured area remains aseismic (unloaded) within the timescale of the ongoing earthquake clustering, and (4) in response to ruptures, the strength and stress in the rock surrounding the ruptured area is altered postseismically which may result in triggered earthquakes nucleating at the edge of the rupture area.

[8] Several empirical observations seem to justify this simplified picture of the complex processes taking place in fault regions: Assumption 1 is supported, first, by the validity of the Gutenberg-Richter law (equations (2) and (3)) which indicates that earthquakes occur mostly in highly stressed fault patches where ruptures can grow up to all sizes limited only by the fault segment size [Geller et al., 1997; Hainzl and Zöller, 2001]. Second, the time-to-failure analysis of natural seismicity has recovered an underlying critical point behavior [Bufe and Varnes, 1993; Jaumé and Sykes, 1999; Zöller et al., 2001]; and third, in a whole class of models simulating the seismic cycle, the stress field self-organizes into a critical stress state (e.g., [Burrige and Knopoff, 1967; Olami et al., 1992; Main, 1996; Dahmen et al., 1998; Hainzl and Zöller, 2001]). Assumption 2 is justified by the observation that earthquakes occur mostly on preexisting faults, that is, they are a frictional rather than a fracture phenomenon [Scholz, 1998]. Assumptions 3 and 4 are supported by the observation that within earthquake clusters, subsequent events occur next to the rupture area of previous events, in particular, aftershocks are concentrated preferable at the edges of the main shock rupture area and the epicenter of the main shock is situated mostly in the immediate vicinity of the foreshocks [Mendoza and Hartzell, 1988; Ogata et al., 1995]. The timescales of individual ruptures (minutes), earthquake clusters (weeks), and recurrence times of large earthquakes (hundreds to thousands of years) are well separated leading to the conclusion that the mechanism responsible for earthquake clustering is different from that of rupture evolution (elastic interactions) and that of reloading (tectonic plate movement) [Scholz, 1994]. The temporal characteristics of the triggering mechanism will depend on the real underlying process. Different processes have been proposed, e.g., pore fluid flows [Nur and Booker, 1972; Yamashita, 1999] or stress corrosion [Shaw, 1993; Main, 2000]; however, it is not known if one or more of these processes are really underlying the earthquake clustering. Thus, for our investigations we assume the simplest case, that is, a state-independent linear change of the strength (stress) with time.

### 2.2. Algorithm

[9] We implement our model in the form of a continuous cellular automaton by defining a two-dimensional  $L \times L$

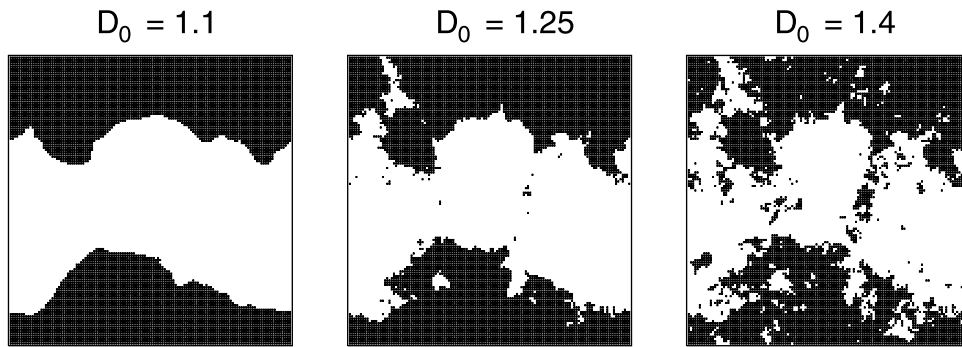


**Figure 1.** Three different types of fault geometry are investigated differing in the smoothness of the transition between seismic (white) and aseismic (black) regions. The surfaces are constructed according to the description in Appendix A and classified by the fractal dimension  $D_0$  of the border line. The analyzed  $128 \times 128$  block systems consist of half black and half white blocks.

array of blocks  $(i, j)$ , where  $i, j$  are integers,  $1 \leq i, j \leq L$ . To account for complex boundary conditions, we produce within this  $L \times L$  array a seismic active patch of  $L^2/2$  sites which is embedded in an aseismic region. The procedure which we use to produce fault geometries of variable geometry is described in Appendix A. We characterize the complexity of the fault geometry by the fractal dimension  $D_0$  of the border line. In Figure 1 one example is shown for each of the three different degrees of fault complexity analyzed in this paper.

[10] The evolution of ruptures within the active fault region is described by the cellular automaton version [Olami *et al.*, 1992] of the two-dimensional spring-block model originally proposed by Burridge and Knopoff [1967]: Stick-slip motion is assumed within the seismic region, where the friction law adopts the Mohr-Coulomb law with a static failure threshold  $\sigma_F$ . If the stress on a block  $(k, l)$  exceeds the static failure threshold,  $\sigma(k, l) \geq \sigma_F$ , sliding is initiated at this block. The moving block slips to the zero-force position and the stress  $\Delta\sigma \equiv \sigma(k, l)$  is partially distributed to the four nearest neighbors  $(k_{\pm}, l_{\pm})$ . The stresses of the nearest neighbors lying within the fault patch are set according to the rule

$$\sigma(k_{\pm}, l_{\pm}) \rightarrow \sigma(k_{\pm}, l_{\pm}) + \frac{g}{4} \Delta\sigma, \quad (4)$$

but the stress transferred to boundary elements is lost. The stress of the sliding site is reset to

$$\sigma(k, l) \rightarrow 0, \quad (5)$$

and this site is set to the aseismic state, that is, it becomes a new boundary element. The coupling constant  $g$  depends on the assumed elastic properties and can vary in the range of  $0 \leq g \leq 1$ . Additionally,  $g$  defines the degree of stress conservation within the fault plane, where  $g = 1$  refers to the conservative case which is a unrealistic limit case because of the elastic coupling to the tectonic plate. The redefined stress on the adjacent blocks  $\sigma(k_{\pm}, l_{\pm})$  may lead to an instability, i.e.,  $\sigma(k_{\pm}, l_{\pm}) \geq \sigma_F(k_{\pm}, l_{\pm})$ , in one or more blocks of the unruptured fault zone. In this case, a chain reaction starts and the stresses at all unstable blocks are distributed according to equations (4)–(5) possibly leading to further

instabilities, and so on, until the earthquake is terminated, i.e., until  $\sigma(i, j) < \sigma_F(i, j)$  for all blocks  $(i, j)$ .

[11] In most models of the earthquake evolutionary process, which aim at simulating main shock occurrence, the earthquake ruptures are initiated on account of the regional stress increase due to the tectonic plate motion. In these models the effect of previous earthquakes is restricted to static stress changes. Such model versions [e.g., Bak and Tang, 1989; Olami *et al.*, 1992] cannot reproduce the empirically observed earthquake clustering. However, we are interested in earthquake clustering rather than in modeling the whole seismic cycle. Thus we neglect tectonic loading, because it is not relevant on the timescale being typical for earthquake clusters, whereas we consider post-seismic processes. That means that the synthetic ruptures do not only lead in adjacent fault regions to a static increase of the Coulomb failure stress or failure function [Beeler *et al.*, 2000], respectively, but also to a further transient increase of the failure function due to pore fluid flows, afterslip, and/or stress corrosion. In particular, we assume that the postseismic effect is mainly localized at the edge of the rupture zone. Thus, in our simulations we assume that the strength of blocks bordering on the rupture area decreases linearly with time which is a first approximation to subcritical crack growth and stress corrosion [Lee and Sornette, 2000]. We have also tested the alternative approach, where a stress increase instead of a strength decrease is assumed. We find that our results do not depend on this specification of the way how the failure function increases postseismically. Therefore we restrict the presentation of the algorithm to the first case: Immediately after an earthquake, the threshold values start to decrease linearly with time until the minimum  $(1 - \tau)\sigma_F$  is reached. The parameter  $\tau \in [0, 1]$  defines the strength of the decrease. When the threshold value at one block equals the local stress level, the next earthquake is initiated and is determined again according to equations (4)–(5). Thus, earthquake sequences are simulated which unload most parts of the fault segment. The timescale is given by the unloading time  $T_0$  which defines the rate of postseismic strength decrease  $-\sigma_F/T_0$ . This timescale is assumed to be much larger than that of individual earthquakes ruptures; that is, the duration of each earthquake is set to be instantaneous. The earthquake sequence is terminated when the whole seismic region is unloaded, or if the

stresses of all blocks bordered on the ruptured area are less than  $(1 - \tau)\sigma_F$ . The data stored for each sequence consist of the occurrence times in units of  $T_0$ , the coordinates of the epicenters and the spatial sizes of all initiated earthquakes.

[12] The ingredients of this model, namely, stress distribution combined with linear strength decrease, are similar to that recently introduced by *Lee and Sornette* [2000] in order to simulate aftershock sequences. However, the mechanism of earthquake triggering is completely different: *Lee and Sornette* [2000] assume a simultaneous strength decrease all over the fault and instantaneous recovering of the original strength value after sliding (i.e., an effective hardening) within ruptured areas. By contrast, our model assumes strength decreases spatially localized at the edge of rupture areas, whereas the rupture areas themselves remain aseismic (no healing on the timescales investigated).

### 3. Numerical Simulations

[13] We have analyzed fault surfaces of size  $128 \times 128$  produced according to the description in Appendix A. For each surface, the initial stress values are randomly distributed in the interval  $[\sigma_0, \sigma_F]$ , where the mean stress level  $\langle \sigma \rangle = (\sigma_0 + \sigma_F)/2$  is set to the critical value. This value defines the minimal stress level, where earthquakes can occur which rupture almost the whole fault segment at once. It is identical to that found in a previous work for the case of a stress concentration factor  $\gamma = 1$  [*Hainzl and Zöller*, 2001]. While all subsequent earthquakes are triggered by previous events, the first earthquake has to be initiated explicitly. We do this by picking one block by chance and setting its stress value to  $\sigma_F$ . Furthermore, we set all threshold values  $\sigma_F$  arbitrarily to 1 at the beginning. Three free parameters are left which have to be fixed for our simulations: the fault roughness  $D_0$ , the coupling constant  $g$ , and the strength of the postseismic effect  $\tau$ . However, by exploring the three-dimensional parameter space, we have found that the main characteristics, namely, the Gutenberg-Richter law and the (inverse) Omori law with its  $b$  value and  $p$  value change due to the main shock occurrence, are reproduced independently of the parameter values. In section 3.3 the robustness of our results with respect to the choice of the parameters and the initial stress state is discussed in more detail.

[14] We simulate many earthquake sequences in different realizations of fault surfaces with a certain  $D_0$ . To characterize our simulations, we use the following notation: The largest event of each sequence is called the main shock, whereas all events occurring before or after the main shock are defined as foreshocks or aftershocks, respectively. One typical example for such a simulated earthquake sequence is shown in Figure 2. Although different earthquake sequences can differ very much in the details of their spatiotemporal rupture histories, we find that all of them share the same universal features: The main shock is preceded by only few, if any foreshocks and followed by much more aftershocks. Furthermore, the rate of aftershocks decreases with time, whereas the foreshock activity, if several foreshocks occur, tends to increase until the main shock occurrence time. These results are in agreement with real earthquake sequences [*Scholz*, 1994], and also with acoustic emissions in laboratory fracture experiments, apart from the fact that the

number of acoustic foreshock emissions is found to be larger than the number of aftershocks [*Sammonds et al.*, 1992].

[15] In terms of our model the observed characteristics can be understood by the following considerations: The probability for triggering aftershocks increases with the number of unbroken blocks bordering on the already ruptured fault patch. In an infinite two-dimensional fault plane this number would increase further and further in response to successive events increasing the ruptured area, and consequently, the seismic activity would accelerate. This is the reason for the observed accelerating foreshock activity. However, for real, i.e., finite, fault sizes the main shock will rupture the main part of the fault which leads to a drastic change of the situation. On the one hand, the probability for subsequent events is suddenly and significantly increased due the sharp rise of the area effected by the postseismic strength decrease. Thus a jump of the seismic rate takes place. On the other hand, the finite size of the fault becomes now significant. In general, the fault area which is left unbroken by the main shock will consist of many disconnected small patches. Each of these patches will rupture at once or by a secondary, much shorter earthquake sequence. Each aftershock leads to a reduction of the number of those unruptured islands and their sizes. Thus, on average, the rate of aftershocks will decrease with time. Note that a small gradual increase of the aftershock zone size occurs as a consequence of our triggering mechanism. In practice, however, this migration of activity is not easily seen in the resulting aftershock sequences (see, e.g., Figure 2). The reason is the complex geometry of the rupture area as well as of the border between seismic and aseismic regions. The aftershocks occurring mostly on islands within the rupture zone and on recesses in the border area.

[16] In the following, we want to characterize the earthquake sequences occurring in finite fault sizes in more detail. At first, we examine the frequency-size distribution of the events in dependence of their occurrence time. In the second part, the averaged temporal characteristics of foreshocks and aftershocks are analyzed.

#### 3.1. Frequency-Size Distribution

[17] Previously, [*Hainzl and Zöller*, 2001] have shown that earthquakes, which are initiated in an infinite two-dimensional critical loaded stress field, have a size distribution reproducing the Gutenberg-Richter law (equations (2) and (3)). However, in comparison to empirical observations, the exponent  $b$  has been found to be unrealistic small, namely,  $b \approx 0.2$ , independent of the model parameters. Now, in the case that a sequence of earthquakes successively rupturing a finite fault segment, the results change because the earthquakes are initiated in fault patches of finite extension limiting the maximum rupture size. In addition, the fault patch sizes depend on the rupture history; in particular, they are shrinking with time. In the first step, we analyze the size distribution of the earthquakes successively triggered in our simulations independently of their occurrence times. Then in a second step, we compare the size distributions of foreshocks and aftershocks.

[18] The overall frequency-size distribution, which is shown in Figure 3 in an incremental form, is found to reproduce very well the Gutenberg-Richter law (equation

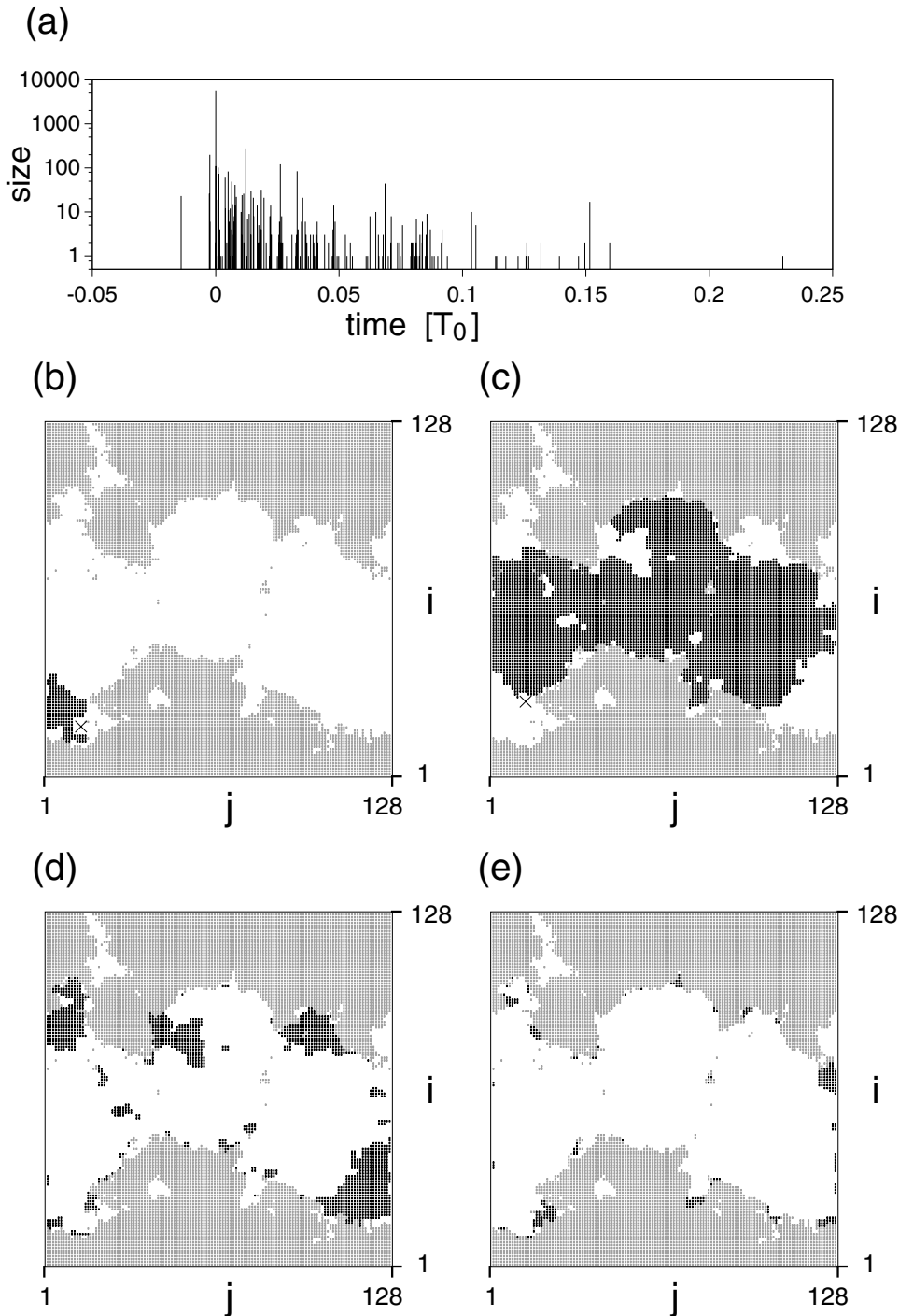


**Figure 2.** A typical example of a simulated earthquake sequence rupturing successively almost the whole prestressed fault segment (here  $\tau = 0.1$ ,  $g = 0.8$ , and  $D_0 = 1.25$ ): (a) the sizes of the events as a function of their occurrence time relative to that of the largest event (main shock); (b) the cumulative rupture area of the five foreshocks (the cross marks the initiation point of the sequence); (c) the main shock rupture area (the cross marks the epicenter); (d) the cumulative rupture area of the first half and (e) of the second half of the subsequently occurring 158 aftershocks.

(3)). In contrast to the earthquakes occurring in infinite two-dimensional fault planes, the  $b$  value ( $\approx 0.9$ ) is now in good agreement with the empirical observed value for the cumulative distribution scattering around 0.9 [Turcotte, 1997]. This value is found independently of the model parameters  $g$ ,  $\tau$ , and the fault geometry referring to the universality of

the underlying critical point physics [Bruce and Wallace, 1989]. Note that the size of the segment which breaks successively by the delayed rupture propagation is set in our investigations. If healing and reloading of the fault system is taken into account, the distribution of fault segment sizes and consequently also the  $b$  value will depend on

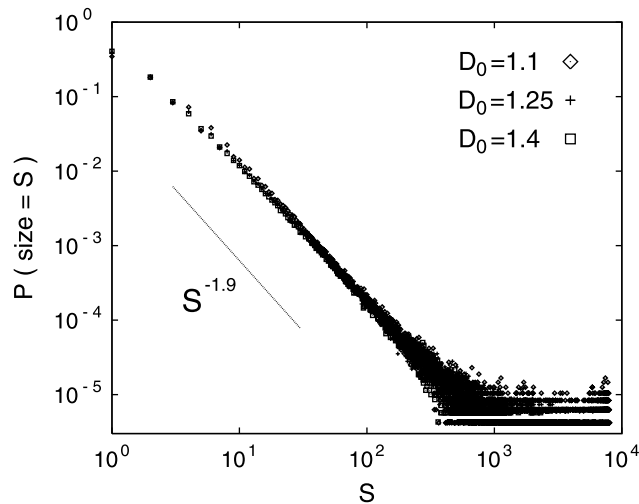


**Figure 3.** The probability of observing an event with source size  $S$  as a function of  $S$  in earthquake sequences rupturing critical loaded faults (here  $\tau = 0.2$  and  $g = 0.8$ ). Independent of the fault geometry  $D_0$ , the distribution can be described very well by a power law  $S^{-(b+1)}$  with  $b = 0.9$ .

the coupling constants  $g$  and  $\tau$  [Hainzl and Zöller, 2001]. The overall frequency-size distribution is built up by the superposition of distributions with cutoffs corresponding to the patch sizes in the stress field. Thus the macroscopic  $b$  value of the overall population is a direct consequence of the fragmentation of the stress field due to precursory events.

[19] Now, in the second step, we compare foreshocks with aftershocks regarding their size distributions. We find that both distributions reproduce the Gutenberg-Richter law; however, they differ significantly with regard to the  $b$  value. Foreshocks can be characterized by a much smaller exponent,  $b \approx 0.6$ , compared to aftershocks,  $b \approx 1$ . This is illustrated in Figure 4. Again, we can explain this result by the different patterns of the stress field before and after the main shock, respectively. Whereas aftershocks occur in a fragmentary stress field being composed of small patches and recesses, foreshocks and main shocks are initiated in a more extended and compact fault segment feeling almost nothing from the finite size of the fault. The increasing relevance of finite size effects with time explains the larger  $b$  value for aftershocks compared to foreshocks and main shocks. A further reason might be the slight tendency that failures occur at weaker blocks with time. However, if we trigger each earthquake in the sequence with the same stress drop, we find the same results. Consequently, this explanation is of minor importance for our observations which are in good agreement with real seismicity and laboratory experiments. Detailed observations of earthquake catalogs have shown that foreshock sequences and main shocks are characterized, on average, by a smaller  $b$  value than aftershocks or other earthquakes [Suyehiro *et al.*, 1964; Papazachos, 1975; Knopoff, 2000]. Furthermore, acoustic emissions from rock fracturing show an analogous jump of the  $b$  value irrespective of pore fluid content and pressure variations [Scholz, 1968; Sammonds *et al.*, 1992]. Previously, the  $b$  value change has been explained to be the result of the stress drop from a high to a low level owing to the

main shock [Scholz, 1968, 1994]. Our simulations suggest that another explanation could be the fragmentation of the stress field due to the precursory earthquakes. Foreshocks as well as aftershocks occur at the same local stress and strength conditions, only differing in the size and geometry of the fault patch where they are initiated. However, both interpretation are equivalent in a macroscopic point of view, if only the mean stress, that is, the stress spatially averaged over the total (broken and unbroken parts of the) fault, is considered.

### 3.2. Temporal Clustering

[20] To extract the general characteristics of temporal clustering, we determine the averaged occurrence rate formed by stacking many simulated earthquake sequences relative to the main shock. In particular, we divide the time in bins of length  $\epsilon$  and calculate the number of earthquakes have occurred in all sequences within each time bin. To obtain the average rate, we normalize each value by  $\epsilon$  and the number of sequences spanning this time bin.

[21] In Figure 5, the averaged seismic activity is illustrated for an intermediate complexity of the fault geometry. The phenomena which we have already observed for individual sequences now become clear: The seismic activity is increasing further and further until the main shock occurs. Then the main shock leads to a pronounced jump of the activity level and to a reversal of the temporal trend; that is, the seismic activity is now decreasing with a rate slowing down with time. To check whether or not our simulations reproduce the Omori law (equation (1)), we redraw the temporal behavior in a double logarithmic plot. This is shown in Figure 6 for three different values of  $D_0$  lightening up two important results: Firstly, the increase of foreshock activity as well as the decrease of aftershock activity can both be described approximately by power laws, where the exponent describing the foreshock increase is found to be significantly smaller than that of the aftershocks. Second, the exponents depend on the fractal dimension  $D_0$ , whereas

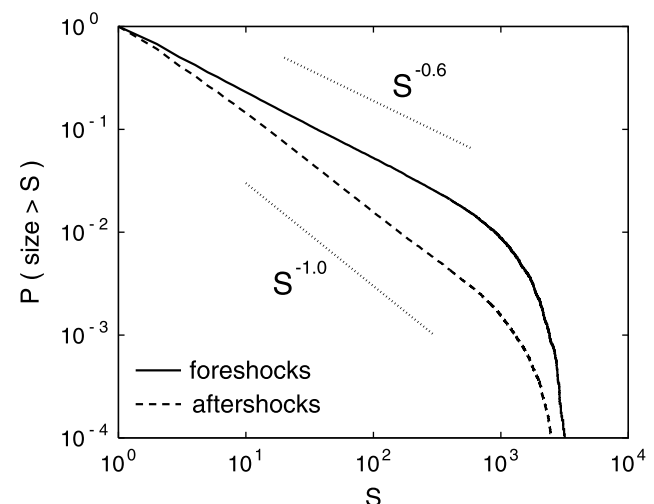


**Figure 4.** Comparison of the cumulative frequency-size distributions of foreshocks with that of the aftershocks (here  $\tau = 0.2$  and  $g = 0.8$ ). The foreshocks are characterized by a significantly smaller power law exponent  $b = 0.6$  compared to  $b = 1$  for aftershocks.

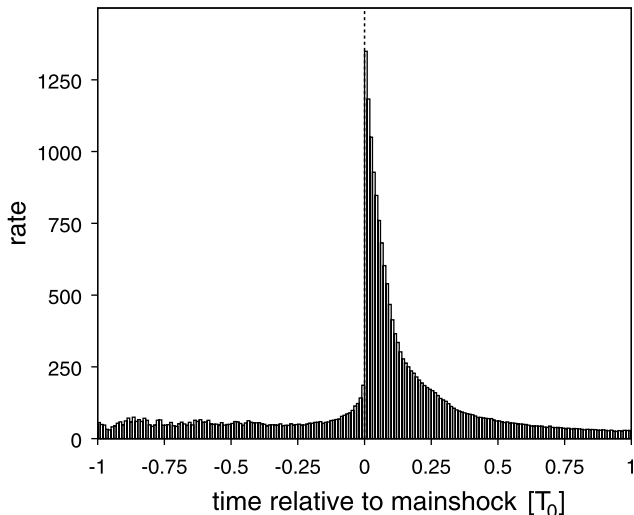


**Figure 5.** The earthquake activity as the function of the time relative to the main shock occurrence time. This curve results from the averaging over 2500 sequences for  $\tau = 0.2$ ,  $g = 0.8$ , and  $D_0 = 1.25$ .

the results are almost insensitive to the other model parameters (see section 3.3). In particular, the exponents are negatively correlated with  $D_0$ . However, the dependence is weak leading only to a variation of the  $p$  value in the vicinity of 1.

[22] These results are in good agreement with the following empirical observations: the validity of the Omori law (equation (1)) for the foreshock increase and the aftershock decay, respectively; the empirical  $p$  values for aftershocks are lying in the same range, namely, between 0.9 and 1.5 [Utsu *et al.*, 1995]; the  $p$  values for foreshocks are found to be smaller than the  $p$  values of the correspondent aftershock sequences [Maeda, 1999]; and the empirical  $p$  values are also found to be negatively correlated to the estimated fractal dimension  $D_0$  of fault systems [Nanjo *et al.*, 1998; Nanjo and Nagahama, 2000]. The only difference is that the empirical observed exponents for foreshocks are mostly in the range from 0.7 to 1.3 [Utsu *et al.*, 1995] and thus generally higher than in our simulations. This difference is manifested also in the smaller gap between the exponents for foreshocks and aftershocks for real seismicity ( $\Delta p \approx 0.2$  [Maeda, 1999]) in comparison to our simulation ( $\Delta p \approx 0.5$ ). However, this apparent inconsistency results probably from the incomplete identification of the earthquake clusters for real earthquake catalogs and the short and varying lengths of the triggered sequences. Especially for larger time gaps to the main shock, foreshocks, and aftershocks cannot be distinguished from background seismicity. Furthermore, the variations of time intervals cannot be considered in real earthquake catalogs because the begin and end of such sequences are not well defined. Both causes are more important for the less frequent foreshocks than for the dominant aftershock activity and lead to an overestimation of the growing rate of the real foreshock activity [Nyffenegger and Frohlich, 1998]. By contrast, we have completely extracted all synthetic foreshocks and we have taken the variable length explicitly into account by averaging at each time bin only over sequences spanning this time. To

confirm our results, we normalize the time scale of each aftershock (foreshock) sequence to the unit time interval before we stack the different sequences together. We find that this representation of our simulations leads to the same results.

[23] The exponents of our simulated foreshock activity,  $0.4 \leq p \leq 0.7$ , are compatible with previous reports on accelerated precursory activity found by time-to-failure analysis of natural seismicity [Bufe and Varnes, 1993; Jaumé and Sykes, 1999]. The cumulative activity is observed to increase with decreasing time distance  $t$  to the main shock according to  $\sim A - Bt^m$  with  $0 < m < 1$  and constants  $A, B > 0$ . The exponent  $m = 1 - p$  is found typically in the interval  $0.2 \leq m \leq 0.6$  [Bowman *et al.*, 1998].

[24] Another way to characterize the temporal behavior of earthquake clusters is to study the waiting time distribution. The waiting times are defined as the time intervals between successive earthquakes within the sequences. For  $D_0 = 1.25$  this distribution is shown in Figure 7 for foreshocks and aftershocks separately. Again, the numerical results can be fit well by power laws, which is in good agreement with empirical findings [Ito, 1995]. Although the waiting time distribution is not completely independent of the Omori law, it gives further evidence for the property of scale invariance, especially with regard to the difference between foreshocks and aftershocks. Again the exponent is found to be smaller for foreshocks than for aftershocks.

### 3.3. Robustness of the Results

[25] Now, we discuss the robustness of our results with respect to the model parameters and the initial stress field in more detail. We have found that the frequency-size distributions and the temporal behavior are independent of the parameter  $g$  characterizing the rupture propagation. Only the

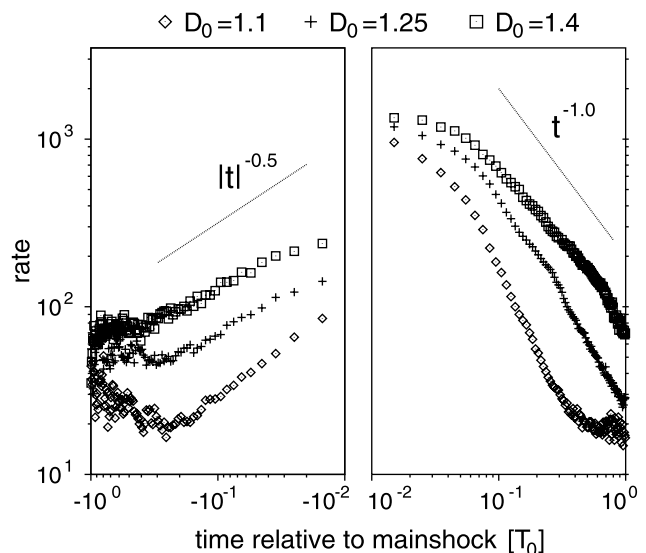


**Figure 6.** The averaged earthquake activity relative to the main shock in double logarithmic plots (here  $\tau = 0.2$  and  $g = 0.8$ ). For three different degrees of fault complexity  $D_0$ , the increase of foreshock activity as well as the decrease of the aftershock rate is found to follow approximately power laws.

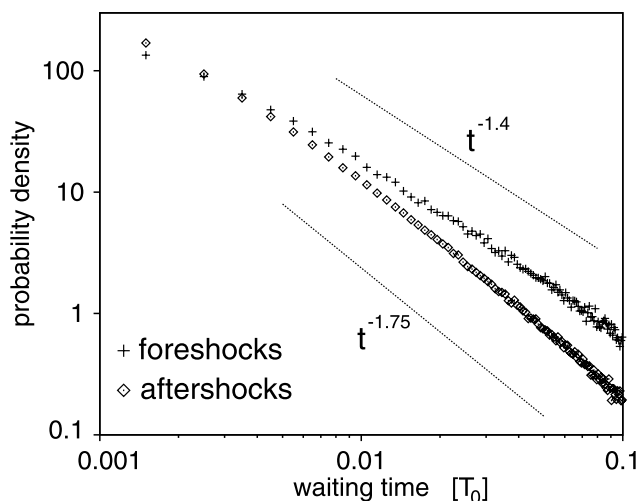


**Figure 7.** The probability density of observing a waiting time  $t$  between two successive foreshocks and aftershocks, respectively. The plot results from a simulation of  $10^4$  sequences with  $\tau = 0.2$ ,  $g = 0.8$ , and  $D_0 = 1.25$ .

initial stress level, i.e., the critical state, depends on this parameter [Hainzl and Zöller, 2001]. Additional investigations of more sophisticated rupture rules have supported our conclusions that the rupture behavior seems to be of minor importance for our results. In particular, we have analyzed model algorithms with more realistic stress concentrations at the rupture front [see Hainzl and Zöller, 2001]. These modifications do not change the characteristics of the earthquake sequences. Our results have also been checked with respect to the parameter  $\tau$  describing the amount of post seismic strength decrease. Most results remain unchanged, only the absolute number of events and the length of the earthquake sequences depend slightly on  $\tau$ : the larger  $\tau$  is, the more earthquakes are triggered on average. Finally, the influence of the spatial fault structure characterized by  $D_0$  has been already discussed in section 3.2: The  $p$  value is negative correlated to  $D_0$ , whereas the  $b$  value does not change significantly.

[26] A purely linear postseismic time dependence of the failure function is only, if at all, a first-order approximation to reality. For example, thermal activation would lead locally to an exponential form [e.g., see Lawn, 1993]. Deviations from linearity will modulate the interevent times and, as a consequence, will probably result in changes of the  $p$  values. However, the mechanism described in this paper is mainly based on spatial effects and on universal critical point physics. Thus the main results can be expected to remain qualitatively independent of nonlinearities which is supported by previous investigations of percolation models [Main, 1999].

[27] Furthermore, we have examined the influence of the initial stress state on the synthetic earthquake clustering. For the simulations shown above, the stress level has been set to the critical state which is the minimum level where the largest events span the whole system. For moderate variations of this initial stress state we find no changes of our results. In particular, for overstressed (supercritical) faults the results are almost robust, although runaway events can

now occur. Such events can be stopped, after growing over a critical size, only at the (aseismic) boundaries in contrast to events occurring in critical or subcritical stress states which are controlled by inherent heterogeneities of the stress field. However, also the stress concentration at the rupture front of runaway events is not enough to rupture all recesses in the fractal boundary region. Analogous to the case of a critical stress state, the postseismic strength decrease leads to successive rupturing of the untouched fault parts and the aftershocks remain distributed according to the Omori law also in the supercritical case. The  $p$  value does not change, whereas the probability for the occurrence of foreshocks becomes much smaller in the case of overstressed faults. By contrast, in the case of a subcritical stress state, the earthquake ruptures are stopped due to inherent stress field heterogeneities and the main part of the fault is ruptured by a whole sequence of earthquakes of comparable size, rather than by an individual main shock at once. As a result, the transition between the increase of seismic activity at the beginning and the decrease at the end of a sequence is much smoother and none of the events within an earthquake sequence is dominating now. In this case, our simulations are visually similar to empirically observed earthquake swarms which cannot be described by the Omori law nor by any other law so far. Thus a comparison of our simulations with earthquake swarms is much more complicated and beyond the scope of this paper. It is an interesting question for future studies whether swarm activity can be explained by a delayed rupture propagation in subcritical stress fields.

[28] In summary, we find that our results shown in sections 2 and 3 are robust with respect to variations of the earthquake mechanism and can be expected for a whole range of stress states.

#### 4. Summary and Conclusions

[29] Our aim is to understand the relevant mechanisms which are responsible for earthquake clustering. For this purpose, we have analyzed earthquake populations initiated in critical stressed fault segments. Such critical states of the stress field are expected for earthquakes on account of theoretical and empirical investigations: Critical stress states have been found to evolve naturally in models simulating the seismic cycle [e.g., Burridge and Knopoff, 1967; Olami et al., 1992; Main, 1996; Dahmen et al., 1998; Hainzl and Zöller, 2001] and in real fault systems which has been recovered by means of the time-to-failure analysis [Bufe and Varnes, 1993; Bowman et al., 1998; Jaumé and Sykes, 1999; Zöller et al., 2001]. On the other hand, the mechanisms being responsible for the observed spatiotemporal clustering of earthquake are not clear so far. In previous investigations [Hainzl et al., 1999, 2000a, 2000b], we have found that postseismic viscoelastic relaxation can explain the observations, however, also other triggering mechanisms, such as state and rate dependent friction [Dieterich, 1994], or stress corrosion cracking [Shaw, 1993; Main, 2000], have been proposed on account of theoretical considerations basing on the nonlinear temporal response of the system due to stress jumps. Although all of these processes will probably occur in real fault systems, it is so far unknown which of them are more relevant. To test our hypothesis that only some basic

assumptions are necessary to explain the empirical observations, we have investigated a very simple triggering mechanism: The postseismic effect is linear in time and concentrates only on the edge of the ruptured area.

[30] Our simulations are in good agreement with empirical observations. Apart from the reproduction of the Gutenberg-Richter law and the Omori law as such, also their differences regarding foreshocks and aftershocks are reproduced. Furthermore, the simulations show the observed negative correlation between the Omori  $p$  value and the fractal dimension of the fault system  $D_0$ . In our model, these characteristics result from the successive shrinking of the loaded fault area size with the continuation of the earthquake sequence. It was neither necessary to introduce any nonlinearity in the temporal initiation process, nor to assume any difference in the nucleation of foreshocks and aftershocks. Although the temporal characteristics of the processes in real fault systems will be more complex, maybe nonlinear, this probably plays only a minor role for the explanation of the most conspicuous properties of spatio-temporal earthquake clusters. Thus our investigations lead to two main conclusions: First, the observation of the Gutenberg-Richter law as well as the Omori law with its empirical exponents alone do not permit to discriminate between several possible mechanisms, because, e.g., pore fluid flows, stress corrosion, or after slip are probably all, in a first approximation, compatible with our basic assumptions. For a discrimination, other observations are needed. Second, the inspected empirical observations, especially the differences in the  $b$  and  $p$  values, do not refer to any differences between the initiation process of foreshocks and that of other events.

## Appendix A: Production of Fault Surfaces

[31] The fault surfaces with complex geometry are produced in the following way: First, we generate surfaces with a fractal distribution of strength according to the detailed description by [Turcotte, 1997]. That is, the Fourier transform of a  $L \times L$  matrix of random numbers  $h_{nm}$  with a Gaussian probability distribution supplies a matrix of complex Fourier coefficients  $H_{st}$  corresponding to radial numbers  $R$  given

$$r = \sqrt{s^2 + t^2}. \quad (\text{A1})$$

The mean power spectral density for each radial wave number  $k_r$  is then filtered according to

$$H_{st}^* = \frac{H_{st}}{k_r^{\frac{\beta+1}{2}}} \quad (\text{A2})$$

The inverse Fourier transform then generates the fractal strength field, where the fractal dimension of this field  $D$  is determined by the parameter  $\beta$ , namely,  $D = (7 - \beta)/2$ .

[32] The fault geometries which are analyzed in this paper result from such strength fields by defining blocks with a strength less (larger) than the mean strength level as seismic active (aseismic). To characterize the complexity of such surfaces, we calculate the fractal box-counting dimension  $D_0$  of the border line separating the seismic active from the a seismic region. The three different types of surfaces

studied in this paper have been produced with a dimension of the strength field  $D = 1.8, 2.4,$  and  $2.8$  yielding  $D_0 = 1.1, 1.25,$  and  $1.4,$  respectively, for the border line.

[33] **Acknowledgments.** We are thankful to Ian Main, Sandy Steacy, and an anonymous reviewer for their recommendations which helped us to improve this paper significantly. This work was supported by the Deutsche Forschungsgemeinschaft (SCH280/13-1 and SFB 555).

## References

- Bak, P., and C. Tang, Earthquakes as a self-organized critical phenomenon, *J. Geophys. Res.*, *94*, 15,635–15,637, 1989.
- Beeler, N. M., R. W. Simpson, S. H. Hickman, and D. A. Lockner, Pore fluid pressure, apparent friction, and Coulomb failure, *J. Geophys. Res.*, *105*, 25,533–25,542, 2000.
- Bowman, D. D., G. Oullion, C. G. Sammis, A. Sornette, and D. Sornette, An observational test of the critical earthquake concept, *J. Geophys. Res.*, *103*, 24,359–24,372, 1998.
- Bruce, A., and D. Wallace, Critical point phenomena: Universal physics at large length scales, in *The New Physics*, edited by P. Davies, pp. 236–267, Cambridge Univ. Press, New York, 1989.
- Bufe, C. G., and D. J. Varnes, Predictive modeling of the seismic cycle of the greater San Francisco bay region, *J. Geophys. Res.*, *98*, 9871–9883, 1993.
- Burridge, R., and L. Knopoff, Model and theoretical seismicity, *Bull. Seismol. Soc. Am.*, *57*, 341–371, 1967.
- Dahmen, K., D. Erta, and Y. Ben-Zion, Gutenberg-Richter and characteristic earthquake behavior in simple mean-field models of heterogeneous faults, *Phys. Rev. E*, *58*, 1494–1501, 1998.
- Dieterich, J. H., A constitutive law for rate of earthquake production and its application to earthquake clustering, *J. Geophys. Res.*, *99*, 2601–2618, 1994.
- Geller, R. J., D. D. Jackson, Y. Y. Kagan, and F. Mulargia, Earthquakes cannot be predicted, *Science*, *275*, 1616–1617, 1997.
- Gutenberg, B., and C. F. Richter, Earthquake magnitude, intensity, energy and acceleration, *Bull. Seismol. Soc. Am.*, *46*, 105–145, 1956.
- Hainzl, S., and G. Zöller, The role of disorder and stress concentration in nonconservative fault systems, *Physica A*, *294*, 67–84, 2001.
- Hainzl, S., G. Zöller, and J. Kurths, Similar power laws for foreshock and aftershock sequences in a spring-block model for earthquakes, *J. Geophys. Res.*, *104*, 7243–7254, 1999.
- Hainzl, S., G. Zöller, J. Kurths, and J. Zschau, Seismic quiescence as an indicator for large earthquakes in a system of self-organized criticality, *Geophys. Res. Lett.*, *27*, 597–600, 2000a.
- Hainzl, S., G. Zöller, and J. Kurths, Self-organization of spatio-temporal earthquake clusters, *Nonlinear Processes Geophys.*, *7*, 21–29, 2000b.
- Ito, K., Punctuated-equilibrium model of biological evolution is also a self-organized-criticality model of earthquakes, *Phys. Rev. E*, *52*, 3232–3233, 1995.
- Jaumé, S. C., and L. R. Sykes, Evolving towards a critical point: A review of accelerating seismic moment/energy release prior to large and great earthquakes, *Pure Appl. Geophys.*, *155*, 279–306, 1999.
- Jones, L. M., and P. Molnar, Some characteristics of foreshocks and their possible relationship to earthquake prediction and premonitory slip on faults, *J. Geophys. Res.*, *84*, 3596–3608, 1979.
- Kagan, Y. Y., and L. Knopoff, Statistical study of the occurrence of shallow earthquakes, *Geophys. J. R. Astron. Soc.*, *55*, 67–86, 1978.
- Kanamori, H., and D. L. Anderson, Theoretical basis of some empirical relations in seismology, *Bull. Seismol. Soc. Am.*, *65*, 1073–1095, 1975.
- Knopoff, L., The magnitude distribution of declustered earthquakes in Southern California, *Proc. Natl. Acad. Sci. U.S.A.*, *97*, 11,880–11,884, 2000.
- Lawn, B., *Fracture of Brittle Solids*, 2nd ed., Cambridge Univ. Press, New York, 1993.
- Lee, M. W., and D. Sornette, Novel mechanism for discrete scale invariance in sandpile models, *Eur. Phys. J. B*, *15*, 193–197, 2000.
- Lei, X.-L., O. Nishizawa, K. Kusunose, A. Cho, T. Satoh, and O. Nishizawa, Compressive failure of mudstone samples containing quartz veins using rapid AE monitoring: The role of asperities, *Tectonophysics*, *328*, 329–340, 2000.
- Maeda, K., Time distribution of immediate foreshocks obtained by a stacking method, *Pure Appl. Geophys.*, *155*, 381–394, 1999.
- Main, I. G., Statistical physics, seismogenesis, and seismic hazard, *Rev. Geophys.*, *34*, 433–462, 1996.
- Main, I. G., Applicability of time-to-failure analysis to accelerated strain before earthquakes and volcanic eruptions, *Geophys. J. Int.*, *139*, F1–F6, 1999.



- Main, I. G., A damage mechanics model for power-law creep and earthquake aftershock and foreshock sequences, *Geophys. J. Int.*, 142, 151–161, 2000.
- Mendoza, C., and S. H. Hartzell, Aftershock patterns and main shock faulting, *Bull. Seismol. Soc. Am.*, 78, 1438–1449, 1988.
- Nanjo, K., and H. Nagahama, Spatial distribution of aftershocks and the fractal structure of active fault systems, *Pure Appl. Geophys.*, 157, 575–588, 2000.
- Nur, A., H. Nagahama, and M. Satomura, Rates of aftershock decay and the fractal structure of active fault systems, *Tectonophysics*, 287, 173–186, 1998.
- Nur, A., and J. R. Booker, Aftershocks caused by pore fluid flow?, *Science*, 175, 885–887, 1972.
- Nyffenegger, P., and C. Frohlich, Recommendations for determining p values for aftershock sequences and catalogs, *Bull. Seismol. Soc. Am.*, 88, 1144–1154, 1998.
- Ogata, Y., T. Utsu, and K. Katsura, Statistical features of foreshocks in comparison with other earthquake clusters, *Geophys. J. Int.*, 121, 233–254, 1995.
- Olami, Z., H. S. Feder, and K. Christensen, Self-organized criticality in a continuous, nonconservative cellular automaton modeling earthquakes, *Phys. Rev. Lett.*, 68, 1244–1247, 1992.
- Papazachos, B. C., Foreshocks and earthquake prediction, *Tectonophysics*, 28, 213–226, 1975.
- Purcaru, G., and H. Berckhemer, A magnitude scale for very large earthquakes, *Tectonophysics*, 49, 189–198, 1978.
- Sammonds, P. R., P. G. Meredith, and I. G. Main, Role of pore fluids in the generation of seismic precursors to shear fracture, *Nature*, 359, 228–230, 1992.
- Scholz, C. H., The frequency-magnitude relation of microfracturing in rock and its relation to earthquakes, *Bull. Seismol. Soc. Am.*, 58, 399–415, 1968.
- Scholz, C. H., *The Mechanics of Earthquakes and Faulting*, Cambridge Univ. Press, New York, 1994.
- Scholz, C. H., Earthquakes and friction laws, *Nature*, 391, 37–42, 1998.
- Shaw, B. E., Generalized Omori law for aftershocks and foreshocks from a simple dynamics, *Geophys. Res. Lett.*, 20, 907–910, 1993.
- Sornette, D., *Critical Phenomena in Natural Sciences*, Springer-Verlag, New York, 2000.
- Sornette, D., P. Miltenberger, and C. Vanneste, Statistical physics of fault patterns self-organized by repeated earthquakes, *Pure Appl. Geophys.*, 142, 491–527, 1994.
- Suyehiro, S., T. Asada, and M. Ohtake, Foreshocks and aftershocks accompanying a perceptible earthquake in central Japan—On a peculiar nature of foreshocks, *Pap. Meteorol. Geophys.*, 15, 71–88, 1964.
- Turcotte, D. L., *Fractals and Chaos in Geology and Geophysics*, Cambridge Univ. Press, New York, 1997.
- Utsu, T., Y. Ogata, and R. S. Matsu'ura, The centenary of the Omori formula for a decay law of aftershock activity, *J. Phys. Earth*, 43, 1–33, 1995.
- Vidale, J., J. Mori, and H. Houston, Something wicked this way comes: Clues from foreshocks and earthquake nucleation, *Eos Trans. AGU*, 82, 68, 2001.
- Zöller, G., S. Hainzl, and J. Kurths, Observation of growing correlation length as an indicator for critical point behavior prior to large earthquakes, *J. Geophys. Res.*, 106, 2167–2176, 2001.
- Yamashita, T., Pore creation due to fault slip in a fluid-permeated fault zone and its effect on seismicity: Generation mechanism of earthquake swarm, *Pure Appl. Geophys.*, 155, 625–647, 1999.

---

S. Hainzl and F. Scherbaum, Institute of Earth Sciences, University of Potsdam, D-14415 Potsdam, Germany. (hainzl@geo.uni-potsdam.de)

G. Zöller, Institute of Physics, University of Potsdam, D-14415 Potsdam, Germany.

# Appendix J

**Emergence of a band-limited power law in the aftershock decay rate of a slider-block model**

Autors:	C. Narteau, P. Shebalin, S. Hainzl, G. Zöller, and M. Holschneider
Journal:	Geophysical Research Letters
Volume (Nr.):	<b>30(11)</b>
Article/doi:	art. no. 1568, doi 10.1029/2003GL017110
Year:	2003

# Emergence of a band-limited power law in the aftershock decay rate of a slider-block model

C. Narteau

School of Geosciences, University of Edinburgh, Grant Institute, Edinburgh, UK.

P. Shebalin

International Institute of Earthquake Prediction and Mathematical Geophysics, Moscow, Russia.

S. Hainzl,<sup>1</sup> G. Zöller,<sup>2</sup> and M. Holschneider<sup>3</sup>

Received 12 February 2003; revised 29 March 2003; accepted 24 April 2003; published 6 June 2003.

[1] In order to elucidate how structural heterogeneities affect the aftershock decay rate, we examine the aftershock sequences produced by a slider-block model of seismicity. In this model, the geometry of the seismic zone is the only free parameter and all aspects of the system are known. The power law aftershock decay rate holds only for smooth faults. A band-limited power law emerges at intermediate fault complexity. For rough faults, only a transient regime toward an exponential decay is observed. In all fault geometries examined, a band-limited power law model fits the synthetic aftershock decay rate better than the Modified Omori Law. Then, as the connected seismic elements form a simpler localised surface, we show that the power law aftershock decay rate extends over longer time, and that the power law exponent increases. These results support the inference that the correlation time of the power law aftershock decay rate increases as the deformation localises along dominant major faults. *INDEX TERMS:* 3299 Mathematical Geophysics: General or miscellaneous; 7230 Seismology: Seismicity and seismotectonics; 7260 Seismology: Theory and modeling. **Citation:** Narteau, C., P. Shebalin, S. Hainzl, G. Zöller, and M. Holschneider, Emergence of a band-limited power law in the aftershock decay rate of a slider-block model, *Geophys. Res. Lett.*, 30(11), 1568, doi:10.1029/2003GL017110, 2003.

## 1. Introduction

[2] Following an earthquake, aftershocks are seismic events of smaller magnitude occurring in the neighbourhood of the rupture. *Omori* [1894] first suggests a hyperbolic aftershock decay rate with respect to the time from the mainshock. This precursory work permits a more general description of the temporal clustering of aftershocks through the modified Omori Law [*Utsu*, 1961],

$$\Lambda(t) = \frac{K}{(t+c)^p}, \quad (1)$$

where  $\Lambda(t)$  is the aftershock rate at time  $t$ ,  $p$  is a positive power law exponent,  $K$  is a constant of proportionality, and

<sup>1</sup>Institute of Earth Sciences and Institute of Physics, Universität Potsdam, Potsdam, Germany.

<sup>2</sup>Institute of Physics, Universität Potsdam, Potsdam, Germany.

<sup>3</sup>Institute of Applied and Industrial Mathematics, Universität Potsdam, Potsdam, Germany.

$c$  is a time constant essential to define a finite aftershock frequency at  $t = 0$ , the mainshock time. This empirical law predicts a power law aftershock decay rate over long time and a constant rate over short time. Later, different models of aftershock decay rate have been tested to improve the fit of natural aftershock sequences [*Gross and Kisslinger*, 1994]. For example, an exponential decay replaces the power law decay to account for an acceleration of the decay rate over long time [*Kisslinger*, 1993].

[3] Following *Scholz* [1968], *Narteau et al.* [2002] develop a model of aftershock decay rate based on a Markov process with stationary transition rates. These transition rates  $\lambda$  vary according to the magnitude of a scalar representing the state of stress, and defined as the overload  $\sigma_0$ . Thus, the aftershock decay rate in the model is a weighted sum of independent exponential decay functions with different characteristic times. From different overload distributions  $N(\sigma_0)$  and different expressions of the transition rates  $\lambda(\sigma_0)$ , it has been shown that the aftershock decay rate can be written as

$$\Lambda(t) = \frac{A(\gamma(q, \lambda_b t) - \gamma(q, \lambda_a t))}{t^q}, \quad (2)$$

where  $\gamma(\rho, x) = \int_0^x \tau^{\rho-1} \exp(-\tau) d\tau$ , is the incomplete Gamma function and where  $q$  and  $A$  can be expressed according to analytical results.  $\lambda_b$  is a characteristic aftershock rate which corresponds to an upper bound of the overload distribution.  $\lambda_a$  is a characteristic aftershock rate which corresponds to a limit of crack growth where the magnitude of the transition rate jumps from 0 to a finite positive value.

[4] The main characteristic of the aftershock decay rate produced by equation 2 is that, if  $\lambda_b \gg \lambda_a$ , three major regimes of the aftershock decay rate emerge: (1) A linear decay is observed for  $t < t_1^\zeta$  where  $t_1^\zeta = x_b/\lambda_b$ . (2) A power law decay is observed for  $t_1^\zeta < t < t_2^\zeta$  where  $t_2^\zeta = x_a/\lambda_a$ . (3) An exponential decay is observed for  $t > t_2^\zeta$ . In this description,  $x_b$  and  $x_a$  are coefficients defined from the  $q$ -value and a threshold of divergence  $\zeta$  between the aftershock decay rate and a permanent power law decay. Thus a band-limited power law aftershock decay rate results from the upper bound of the overload distribution and a limit of crack growth over short and long time respectively. In the framework of this model,  $(q, \lambda_a, \lambda_b)$  are the only free parameters, but sometimes it is more convenient to refer to the temporal limits  $(t_1^\zeta, t_2^\zeta)$  that result from these parameters in order to describe the different types of aftershock decay rate produced by equation 2 (Figure 1).

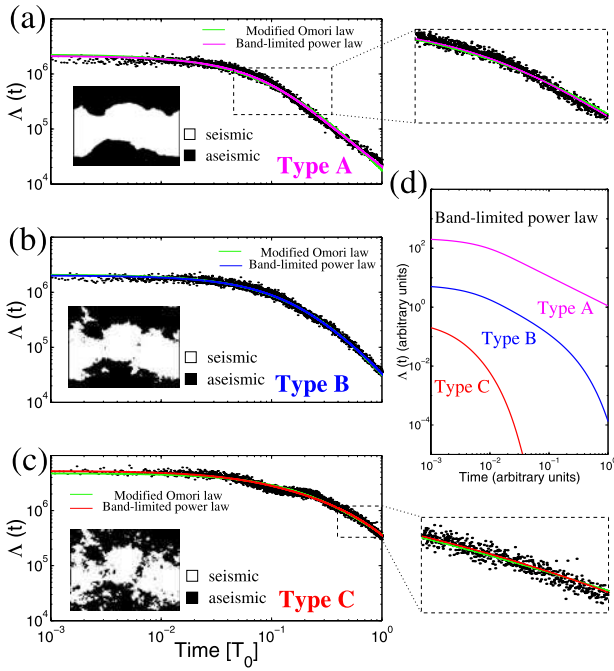


**Figure 1.** Averaged aftershock activity and best-fits of the band-limited power law and the modified Omori law for different fault geometries of the slider-block model. (a)  $D_0 = 1.1$ . (b)  $D_0 = 1.25$ . (c)  $D_0 = 1.4$ . Enlargements show that the band-limited power law is always closer to the data. (d) Generic behaviours of the band-limited power law.  $A$ -values are arbitrary,  $\lambda_b = 200$  and  $q = 1$  (i.e.  $t_2^c = cte/\lambda_a$ ). Type A: power law decay rate over long time ( $1/\lambda_a = 10^0$ ). Type B: band-limited power law ( $1/\lambda_a = 0.2$ ). Type C: transient regime toward an exponential decay rate ( $1/\lambda_a = 10^{-3}$ ).

[5] From several well known aftershock sequences in different geophysical environments, *Narteau et al.* [2002] have suggested that the power law aftershock decay rates extends over longer time according to the concentration of the deformation along dominant major faults. In addition to the limit of crack growth, it has been proposed that structural properties control the time of the transition from a power law to an exponential aftershock decay rate (i.e. correlation time of the power law aftershock decay rate). Such conclusions have now to be confirmed by a systematic analysis of a large number of aftershock sequences. In a preliminary study presented in this paper, we test our hypothesis from aftershock sequences generated by a slider-block model [*Hainzl et al.*, 2003]. In this model, the complexity of the seismic zone is the only free parameter. Thus, modifications of the aftershock decay rate only result from changes in the geometry of the system. On the other hand, all the artifacts coming from data acquisition and data selection are avoided in numerical simulations. Our approach may be therefore visualised as an independent procedure for characterising a relationship between the duration of the power law aftershock decay rate and the faulting complexity.

## 2. The Model

[6] In the modelling of the earthquake phenomenology, slider-block models opened up a variety of new applica-

tions, all based on a standard representation of a frictional behaviour along faults. The model to be presented here retains the simplicity of the conventional slider-block model but specifically accounts for stress corrosion cracking [*Lawn and Wilshaw*, 1975]. Then earthquake clustering and, in particular aftershocks, result from short-range interaction over long time in the neighbourhood of ruptures.

[7] In this model previously described by *Hainzl et al.* [2003], the evolution of individual ‘earthquakes’ is a cellular automaton version [*Olami et al.*, 1992] of the two-dimensional spring-block model originally proposed by *Burridge and Knopoff* [1967]. Elastic interactions are incorporated by nearest neighbour coupling, and the frictional behaviour respects a Mohr-Coulomb criterion with a static failure threshold  $\sigma_F$ . In addition to static stress changes, the strength of the blocks bordering the rupture linearly decreases [*Lee and Sornette*, 2000] to mimic sub-critical crack growth by stress corrosion. Then a characteristic time of a chemical reaction rate can be related to the unloading time  $T_0$  which defines the rate of postseismic strength decrease  $-\sigma_F/T_0$ . Hence the duration of an earthquake is assumed to be few orders of magnitude shorter than  $T_0$ . Under this assumption, from a pre-stressed fault patch and a stochastic nucleation, different parts of the fault segment are unloaded by a succession of individual events. In this sequence of events, it is possible to determine foreshocks, mainshock and aftershocks with respect to the time of the events and their sizes.

[8] The model is implemented in the form of a two-dimensional  $L \times L$  array of blocks. To account for complex boundary conditions, a seismic zone of  $L^2/2$  blocks is embedded within an aseismic region. Practically, different fractal strength fields are generated from different fractal dimensions [*Turcotte*, 1997], and the seismic zone is defined by the blocks with the higher strength. Then we characterise the fault geometry by estimating  $D_0$  the fractal box-counting dimension of the border line between seismic and aseismic zones (i.e. the fault roughness). In addition, we calculate the average number  $N_c$  and the correlation length  $L_0$  of the aseismic regions within the seismic zone [*Stauffer and Aharony*, 1994]. These two parameters are negatively correlated to the degree of localisation of the connected seismic elements. Hence, in the following, we consider that the deformation occurs along simpler localised fault as  $L_0$  and  $N_c$  decrease.

## 3. Results

[9] Different aftershock sequences obtained for a given fault complexity are stacked in a unique catalogue with respect to the time from the mainshock [*Davis and Frohlich*, 1991]. Thus we take advantage of the computing capabilities to reduce the statistical bias associated with individual aftershock sequences. Simultaneously, we verify that the temporal properties of a vast majority of individual sequences are the same as for the stacked catalogue. Each sequence initiates at  $t = 0$  and continues at least until  $t/T_0 = 1$ . Then, we analyse the aftershock decay rate between 0 and  $T_0$  to avoid finite size effects at  $t > T_0$  when individual sequences are more likely to stop. The numerical procedure is the same as in *Narteau et al.* [2002]. We define the parameters of the modified Omori law ( $p$ ,  $c$ ) and the parameter of the band-limited power law ( $q$ ,  $\lambda_a$ ,  $\lambda_b$ ) using state-of-the art statistical

**Table 1.** Simultaneous Comparisons Between the Aftershock Decay Rates of the Slider-Block Model With Different Fault Geometries, and Between the Band-Limited Power Law and the Modified Omori Law

Fault geometry			Mod Omori law		Band-limited power law			Temporal limits				
$D_0$	$L_0$	$N_c$	$N(\times 10^4)$	$p$	$c$	$\lambda_a$	$\lambda_b$	$q$	$\Delta_{AIC} (\times 10^5)$	$t_1^\zeta$	$t_2^\zeta$	Type
1.10	2.50	5	3.41	2.18	0.12	$10^{-3}$	22.8	1.59	-7.04	0.11	394	A
1.25	4.52	24	4.37	2.60	0.25	0.84	15.1	1.41	-9.03	0.14	0.54	B
1.30	5.22	40	4.22	2.02	0.18	0.75	18.1	1.12	-8.61	0.10	0.38	B
1.35	6.89	92	4.97	2.27	0.31	1.28	17.0	0.41	-10.1	0.04	0.012	C
1.40	7.73	185	4.69	1.75	0.30	0.86	22.9	0.15	-9.40	0.008	$2.3 \cdot 10^{-5}$	C

$D_0$  is the fractal box-counting dimension of the border line between seismic and aseismic regions.  $N_c$  and  $L_0$  are the number and the correlation length of aseismic regions within the seismic zone.  $N$  is the number of aftershocks. The time scale is given by the unloading time  $T_0$ .  $\lambda_{a,b}$  have units of frequency.  $t_{1,2}^\zeta$  and  $c$  have units of time, while  $q$  and  $p$  are dimensionless.  $\Delta_{AIC}$  is the difference between the AIC's of the band-limited power law and of the modified Omori law.  $t_{1,2}^\zeta$  are inversely proportional to  $\lambda_{a,b}$  and vary according to the  $q$ -value and a threshold of divergence expressed as a percentage ( $\zeta = 0.8$ ). As in Figure 1, type A corresponds to a power law decay rate over long time  $t_2^\zeta \rightarrow \infty$ , type B corresponds to a band-limited power law  $0 < t_2^\zeta < 1$ , and type C corresponds to a transitional behavior toward an exponential decay rate  $t_2^\zeta \rightarrow 0$ .

measures [Akaike, 1974; Ogata, 1983]. Then we compare the models by calculating the difference  $\Delta_{AIC}$  between the Akaike Information Criterion (AIC) values obtained from both model.  $\Delta_{AIC} < 0$  means that statistically the band-limited power law provides a better fit of the data than the modified Omori law, despite the additional parameter.

[10] Table 1 shows the parameters of the modified Omori law and the parameter of the band-limited power law for five different degrees of fault complexity ( $L = 128$ ). For three of them, Figure 1 shows the aftershock decay rate and the best fits provided by both laws. In Table 1, the  $N_c$ -value and the  $L_0$ -value rapidly decrease as the  $D_0$ -value decreases. Thus we study the transition from a more distributed to a simpler localised seismic zone. In all fault geometries examined, the best-fit of the aftershock sequence is obtained by the band-limited power law.

[11] For the modified Omori law, the  $p$ -value is high and almost constant for the different fault geometries examined. On the other hand, the  $q$ -value continuously decreases from 1.6 to 0.15 as the fault complexity increases. In particular, the  $q$ -value jumps from 1.1 to 0.4 as  $D_0$  moves from 1.3 to 1.35. Small  $t_1^\zeta$ -values suggest a rapid onset of the power-law aftershock decay rate. The  $c$ -value is always higher than the  $t_1^\zeta$ -value, and the ratio  $c/t_1^\zeta$  increases for rougher faults. Thus, the modified Omori law may capture non power law behaviours over long time scales but provides a worst fit to the short-term behaviour.

[12] A rapid decrease of the  $t_2^\zeta$ -value is associated with an increasing complexity of the border line separating seismic and aseismic regions of the model. For a smooth fault ( $D_0 = 1.1$ ),  $t_2^\zeta \rightarrow \infty$  and no transition toward an exponential aftershock decay rate can be observed (Figure 1a). For an intermediate complexity ( $D_0 = 1.25$ ), the  $t_2^\zeta$ -value is less than  $T_0$  and a transition toward an exponential decay rate occurs over long time (Figure 1b). From  $D_0 = 1.1$  to  $D_0 = 1.25$ , we have therefore the emergence of a band-limited power law, and a lower  $\Delta_{AIC}$ -value is obtained. For a more complex fault geometry ( $D_0 = 1.3$ ), the power law aftershock decay rate is still the dominant regime over intermediate time although the smaller  $t_2^\zeta$ -value. For rough faults ( $D_0 \geq 1.35$ ),  $t_2^\zeta \rightarrow 0$  and  $t_2^\zeta < t_1^\zeta$ . It is impossible to observe a power law decay and only a transient regime from a linear decay to an exponential aftershock decay rate occurs (Figure 1c). As shown by the  $\Delta_{AIC}$ -value, the modified Omori law is unable to deal with this decay type. From  $D_0 = 1.35$  to  $D_0 = 1.3$ , we have therefore the emergence of a band-limited power law. As the connected seismic elements form a

simpler localised surface, the power law regime emerges from a linear regime over short time, and extends over longer time to the detriment of the exponential regime.

#### 4. Discussion

[13] In the slider-block model with stress corrosion cracking, the aftershock decay rate results from strength decreases spatially localized at the border of the rupture over a population of blocks with heterogeneous stresses. Hence, the extension of the rupture is essential in determining when aftershocks will be triggered. Aseismic regions included in the seismic zone may inhibit the propagation of an event, and are likely to affect the stress field at the edge of rupture areas. In fact, as the fault becomes smoother, aftershocks are in average triggered at lower stresses, and the macroscopic strength of the fault is decreasing. The controlling properties of the aftershock decay rate in the slider block model and in the model presented by Narteau *et al.* [2002] are therefore the same.

[14] The nature of the heterogeneity that we introduce in the slider block model might not be the same as the heterogeneity in the real Earth. However, the particular mechanism of the heterogeneity is unlikely to be critical to the broadly averaged statistics of aftershock decay, and the huge AIC values resulting from the large numbers of events being fit is a benefit of studying models.

[15] In this paper, we examine how the geometry of the seismic zone affects the temporal properties of the aftershock sequences produced by the slider-block model. In particular, we determine the parameters of a band-limited power model and of the modified Omori law. The band-limited power law predicts a decrease of the exponent of the power law aftershock decay rate with respect to an increasing fault complexity. From real aftershock sequences, Nanjo *et al.* [1998] already suggest such a decrease of the power law exponent with respect to an increase of the fractal dimension of the fault populations. Nevertheless, this analysis suggests that, if the transition toward an exponential regime rate is not taken into account -as in the modified Omori law- such variation may be more difficult to capture because of a worst fit of the aftershock decay rate.

[16] In the model, the power law aftershock decay rate is permanent along smooth faults. For an intermediate fault complexity, a transition toward an exponential decay rate occurs over long time and a band-limited power law emerges. Finally, for the most complex geometries, only a

transient regime toward an exponential aftershock decay rate may be observed. Therefore there is a rapid increase of the correlation time of the power law aftershock decay rate with respect to a decreasing fault complexity.

[17] Without the restrictions applied to seismological and experimental data analysis, these observations are in good agreement with (1) the experimental results of Hirata [1987] that show that an exponential decay is replaced by a power law aftershock decay rate following the advance of the fracturing process, and (2) the inference that have been done from natural sequences [Narteau et al., 2001]. Aftershock sequences produced by the slider-block model along smooth fault correspond to real sequences observed in zones where the strain is concentrated on a major fault and where the aftershocks exhibit a dominant faulting mechanism. In laboratory experiments, they correspond to aftershock sequences observed just before the macroscopic failure (i.e. dynamic stress drop). For an intermediate fault complexity, synthetic aftershock sequences correspond to real sequences observed in zones where the strain is partitioned on smaller faults and where no major structure emerges. Synthetic sequences along rough fault correspond to aftershock sequences observed in zones of distributed damage where the deformation is accommodated by different types of faulting mechanism or where the strain rate is significantly low (i.e. higher crustal strength). In laboratory experiments, such sequences are observed during the preliminary stages of fracture growth.

[18] In the multi-disciplinary science of critical phenomena, a critical behaviour is characterised by an increase of both the correlation time and length in the proximity of a critical point and by a divergence of these parameters at the critical point. During the formation and the evolution of fault populations, individual fault growth, interact, strain localise and structural irregularities are smoothed by the accumulation of the deformation. In a slider-block model, this work suggests that, simultaneously, the correlation time of the power law aftershock decay rate increases. As said above, similar behaviours may have been captured in real sequences and in laboratory experiments. Unfortunately, the selection of only a few aftershock sequences for analysis means that the empirical support provided for such behaviours is still of an anecdotal nature. The statistical analysis presented in this paper is a new and independent contribution about the possible relationship between the correlation time of the power law aftershock decay rate and the faulting. The results support the idea that brittle rocks makes a transition from a subcritical state to a precisely critical state during the localisation process of the deformation.

## 5. Conclusion

[19] Temporal properties of the aftershock sequences produced by a slider-block model depend on the geometry of the seismic zone. Along smooth fault, the power law aftershock decay rate applies at all time scales, but for complex fault geometries, only a transient regime toward an exponential decay may be observed. Between these two end members, a band-limited power law emerges and extends over longer time as the smoothness of the fault increases. In all fault geometries examined, a band-limited power law model fits the synthetic aftershock decay rate better than the

Modified Omori Law, despite the additional parameter. In addition to the duration of the power law aftershock decay rate, we show that the power law exponent increases as the connected seismic elements form a simpler localised surface. Without the usual restrictions applied to geophysical and experimental data analysis, the work presented here supports the inference that the correlation time of the power-law aftershock decay rate increases as the deformation localises along dominant major faults.

[20] **Acknowledgments.** The authors would like to thank Ian Main and two anonymous reviewers for helpful comments. Clément Narteau is supported through a Marie Curie fellowship No HPMFT-2000-00669 from the European Community. This work was partially supported by INTAS (2001-5-748) and by James S. McDonnell Foundation (“Understanding and Prediction of Critical Transitions in Complex Systems”). Sebastian Hainzl and Gert Zöller are supported by the Deutsche Forschungsgemeinschaft (SCH280/13-2 and SFB555, respectively).

## References

- Akaike, H., A new look at the statistical model identification, *IEEE Trans. Autom. Control*, *AC-19*, 716–723, 1974.
- Burridge, R., and L. Knopoff, Model and theoretical seismicity, *Bull. Seismol. Soc. Am.*, *57*, 341–371, 1967.
- Davis, S., and C. Frohlich, Single-link cluster analysis of earthquake aftershocks: Decay laws and regional variations, *J. Geophys. Res.*, *96*, 6335–6350, 1991.
- Gross, S., and C. Kisslinger, Tests of the models of aftershocks rate decay, *Bull. Seismol. Soc. Am.*, *84*, 1571–1579, 1994.
- Hainzl, S., G. Zöller, and F. Scherbaum, Earthquake clusters resulting from delayed rupture propagation in finite fault segments, *J. Geophys. Res.*, *108*(B1), 2013, doi:10.1029/2001JB000610, 2003.
- Hirata, T., Omori’s power law aftershock sequences of microfracturing in rock fracture experiment, *J. Geophys. Res.*, *92*, 6215–6221, 1987.
- Kisslinger, C., The stretched exponential function as an alternative model for aftershock decay rate, *J. Geophys. Res.*, *98*, 1913–1922, 1993.
- Lawn, B., and T. Wilshaw, *Fracture of brittle solids*, Cambridge Univ. Press, New York, 1975.
- Lee, M., and D. Sornette, Novel mechanism for discrete scale invariance in sandpile models, *Eur. Phys. J. B.*, *15*, 193–197, 2000.
- Nanjo, K., H. Nagahama, and M. Satomura, Rates of aftershock decay and the fractal structure of active fault systems, *Tectonophysics*, *287*, 173–186, 1998.
- Narteau, C., P. Shebalin, and M. Holschneider, Temporal limits of the power law aftershock decay rate, *J. Geophys. Res.*, *107*(B12), 2359, doi:10.1029/2002JB001868, 2002.
- Ogata, Y., Estimation of the parameters in the modified Omori formula for aftershocks frequencies by a maximum likelihood procedure, *J. Phys. Earth*, *31*, 115–124, 1983.
- Olami, Z., H. Feder, and K. Christensen, Self-organized criticality in a continuous, nonconservative cellular automaton modeling earthquakes, *Phys. Rev. Lett.*, *68*, 1244–1247, 1992.
- Omori, F., On after-shocks of earthquakes, *J. Coll. Sci. Imp. Univ. Tokyo*, *7*, 111–200, 1894.
- Scholz, C., Microfractures, aftershocks, and seismicity, *Bull. Seismol. Soc. Am.*, *58*, 1117–1130, 1968.
- Stauffer, D., and A. Aharony, *Introduction to Percolation Theory*, Taylor and Francis, Philadelphia, Pa., 1994.
- Turcotte, D. L., *Fractals and Chaos in Geology and Geophysics*, Cambridge Univ. Press, New York, 1997.
- Utsu, T., A statistical study on the occurrence of aftershocks, *Geophys. Mag.*, *30*, 521–605, 1961.

S. Hainzl, Institute of Earth Sciences, Universität Potsdam, POB 601553, D-14115 Potsdam, Germany. (hainzl@geo.uni-potsdam.de)

M. Holschneider, Institute of Applied and Industrial Mathematics, Universität Potsdam, POB 601553, D-14115 Potsdam, Germany. (hols@math.uni-potsdam.de)

C. Narteau, University of Edinburgh, School of Geosciences, Grant Institute, West Mains Road, Edinburgh, EH9 3JW, UK. (Clement.Narteau@glg.ed.ac.uk)

P. Shebalin, International Institute of Earthquake Prediction Theory and Mathematical Geophysics, Shvabovskoye shosse, 79, korp 2, Moscow 113556, Russia. (shebalin@mitp.ru)

G. Zöller, Institute of Physics, Universität Potsdam, POB 601553, D-14115 Potsdam, Germany. (gert@agnld.uni-potsdam.de)

# Appendix K

**Quasi-static and quasi-dynamic modeling of earthquake failure at intermediate scales**

Autors:	G. Zöller, M. Holschneider, and Y. Ben-Zion
Journal:	Pure and Applied Geophysics
Volume (Nr.):	<b>161(9-10)</b>
Pages/doi:	2103-2118, doi 10.1007/s00024-004-2551-0
Year:	2004

## Quasi-static and Quasi-dynamic Modeling of Earthquake Failure at Intermediate Scales

GERT ZÖLLER<sup>1</sup>, MATTHIAS HOLSCHNEIDER<sup>2</sup>, and YEHUDA BEN-ZION<sup>3</sup>

*Abstract*—We present a model for earthquake failure at intermediate scales (space: 100 m–100 km, time:  $100 \text{ m}/v_{\text{shear}}$ - 1000's of years). The model consists of a segmented strike-slip fault embedded in a 3-D elastic solid as in the framework of BEN-ZION and RICE (1993). The model dynamics is governed by realistic boundary conditions consisting of constant velocity motion of the regions around the fault, static/kinetic friction laws with possible gradual healing, and stress transfer based on the solution of CHINNERY (1963) for static dislocations in an elastic half-space. As a new ingredient, we approximate the dynamic rupture on a continuous time scale using a finite stress propagation velocity (quasi-dynamic model) instead of instantaneous stress transfer (quasi-static model). We compare the quasi-dynamic model with the quasi-static version and its mean field approximation, and discuss the conditions for the occurrence of frequency-size statistics of the Gutenberg–Richter type, the characteristic earthquake type, and the possibility of a spontaneous mode switching from one distribution to the other. We find that the ability of the system to undergo a spontaneous mode switching depends on the range of stress transfer interaction, the cell size, and the level of strength heterogeneities. We also introduce time-dependent  $\log(t)$  healing and show that the results can be interpreted in the phase diagram framework. To have a flexible computational environment, we have implemented the model in a modular C++ class library.

**Key words:** Earthquakes, fault models, dynamic properties, seismicity.

### 1. Introduction

In recent years various models of earthquake sequences have been developed. Although the verification of such models is difficult due to limited data, considerable progress has been made with respect to the generation and understanding of various seismicity patterns. An important goal is the development of conceptual models, which are simple enough to allow some analytical understanding of the relevant processes, but also produce seismic dynamics that is to some degree realistic. Such models have in general a set of tuning parameters that should not be too large. For

---

<sup>1</sup> Institute of Physics and Institute of Mathematics, University of Potsdam, Potsdam, Germany.  
E-mail: gert@agnld.uni-potsdam.de

<sup>2</sup> Institute of Mathematics, University of Potsdam, Potsdam, Germany, on leave from CNRS Rennes, France. E-mail: hols@math.uni-potsdam.de

<sup>3</sup> Department of Earth Sciences, University of Southern California, Los Angeles, U.S.A.  
E-mail: benzion@terra.usc.edu



some parameters empirical values are available, while others can be used to tune the model dynamics towards an expected behavior. The model of BEN-ZION and RICE (1993) of a fault in a 3-D elastic half-space appears to meet these criteria. Using this model, several observed frequency-size and temporal statistics could be explained in terms of structural properties of a given fault.

The most striking feature of seismicity is the frequency-size distribution, which follows in regional domains the Gutenberg-Richter power-law relation. On an individual fault, the situation can be different: although power-law scaling is always observed for a certain range of magnitudes, deviations are found for large magnitudes. On one hand, the Gutenberg-Richter scaling can break down; that is, large events may be suppressed. On the other hand, the large magnitude range can be dominated by a frequently occurring “characteristic” earthquake. Using a mean field approximation of the model of BEN-ZION and RICE (1993), it has been shown that different frequency-size distributions can result from different values of a dynamic weakening coefficient controlling the brittle properties of the fault, and a conservation parameter that determines the amount of stress transfer remaining on the fault (DAHMEN *et al.* 1998; FISHER *et al.* 1997). For certain parameter values, the system can spontaneously switch from one state to the other. In HAINZL and ZÖLLER (2001) a cellular automaton model of Burridge-Knopoff type (BURRIDGE and KNOPOFF, 1967; HAINZL *et al.*, 1999) has been analyzed with the result that the degree of disorder and stress concentration can tune the frequency-size statistics. The question whether or not a small earthquake can grow into a system wide event is connected to the degree of smoothness (or roughness) of the stress field. In BEN-ZION (1996) and BEN-ZION *et al.* (2003) it is argued that the smoothing of long wavelength components of stress can be interpreted as a development of long-range correlations or, in terms of critical phenomena, as an increase of the spatial correlation length, which prepares the fault for a large event (SORNETTE and SAMMIS, 1995; ZÖLLER *et al.* 2001; ZÖLLER and HAINZL, 2002). Consequently, all processes that influence the smoothness of the stress field, e.g., the type of stress transfer during a rupture and quenched heterogeneities, are relevant for the dynamics.

Most existing models for earthquake failure are governed by instantaneous stress transfer (quasi-static) during the rupture process, and in part by unrealistic stress transfer functions like nearest-neighbor interaction or homogeneous stress transfer independent of the position on the fault and the rupture dimension (see BEN-ZION, 2001, for a recent summary of fully dynamic earthquake models). As in the present work, the fault is usually discretized into uniform cells. To account for a more realistic rupture process, the quasi-static approach is extended here to a quasi-dynamic one by introducing a finite communication speed (GABRIELOV *et al.*, 1994). Using Chinnery’s solution for a strike-slip fault in a 3-D elastic half-space (CHINNERY, 1963), realistic boundary conditions, dynamic weakening, and optionally a gradual time-dependent healing, provides a realistic, but still relatively simple earthquake model on the intra- and the inter-event time scale.

The results indicate that the quasi-dynamic model favors for certain parameter values the occurrence of large events. In particular, the truncation of the Gutenberg-Richter law in the quasi-static approach vanishes. We further show that the ability of a system to undergo a mode switching between the Gutenberg-Richter law and a characteristic earthquake distribution depends on the range of the stress transfer interaction, the cell size, and the strength heterogeneities. If  $\log(t)$  healing is included, the time-dependence can be absorbed in an effective dynamic friction and stress loss in the model without healing.

## 2. Model Framework

We assume conceptually a hierarchical model that consists of three hierarchies: the system (top level) as a whole contains a set of faults (middle level); each fault is composed of an array of cells (bottom level). The system is embedded in a three-dimensional elastic half-space. At the system level, the interaction between the faults is accounted for. The fault controls the interaction of the cells during an event, while the accumulation and the release of stress takes place on the cell level.

At the present state of model development, only a single rectangular fault is considered. Unless stated otherwise, a fault of 70-km length and 17.5-km depth is covered by a computational grid, divided into  $128 \times 32$  uniform cells, where deformational processes are calculated. As discussed in BEN-ZION and RICE (1993), this geometry corresponds approximately to the San Andreas fault near Parkfield, CA. Tectonic loading is imposed by a motion with constant velocity  $v_{pl} = 35$  mm/year of the regions around the computational grid. The space-dependent loading rate provides realistic boundary conditions. Using the static stress transfer function  $K(i, j; k, l)$  from CHINNERY (1963), the tectonic loading for each cell  $(i, j)$  is a linear function of time  $t$  and plate velocity  $v_{p/l}$ :

$$\Delta\tau(i, j; t) = (-v_{pl} \cdot t) \cdot \sum_{k, l \in \text{fault}} K(i, j; k, l), \quad (1)$$

where the minus sign stems from the fact that forward (right-lateral) slip of regions around a locked fault segment is equivalent to back (left-lateral) slip of the locked fault segment. The grid of cells is governed by a static/kinetic friction law, i.e., a cell slips initially if the static friction  $\tau_s$  is exceeded. The threshold decreases instantaneously to the dynamic friction  $\tau_d < \tau_s$  and remains there until the earthquake is terminated (model without healing during events). The stress itself drops to the arrest stress  $\tau_a < \tau_d$ . This process of dynamic weakening can be parameterized by the dynamic overshoot coefficient  $D = (\tau_s - \tau_a)/(\tau_s - \tau_d)$ . Following the description in DAHMEN *et al.* (1998), we set  $\tau_s = 1$  and  $\tau_a = 0$  and use the dynamic weakening coefficient  $\varepsilon = (\tau_s - \tau_d)/\tau_s = 1 - \tau_d$  to connect static/kinetic friction and arrest stress. Consequently, the dynamic weakening parameter

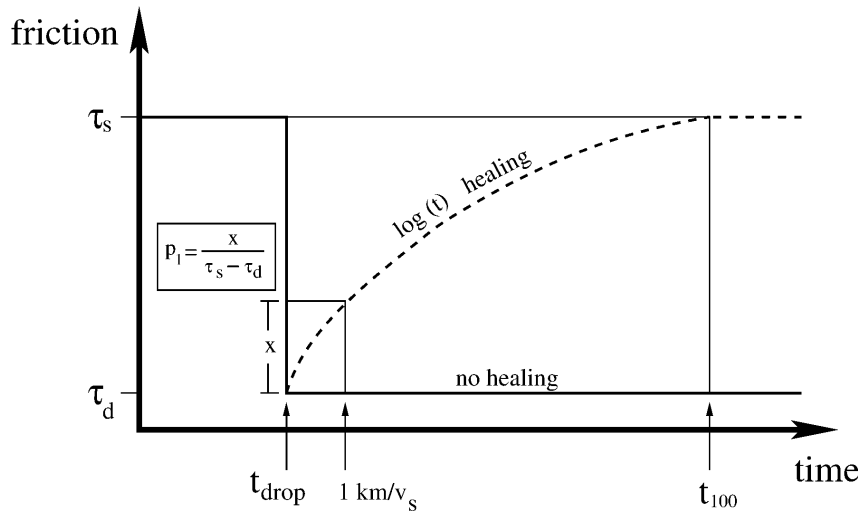


Figure 1

Sketch of frictional processes: in the model without healing during events (solid line), the friction drops from  $\tau_s$  to  $\tau_d$  and remains there until the earthquake is terminated, at which time there is instantaneous healing. In the model with healing during events (dashed line) the friction increases as  $\log(t)$  after the stress drop. The shape of the healing curve is parameterized by the values of  $p_1$  and  $t_{100}$ .

$\varepsilon = 1 - \tau_d$  is bounded between 0 and 1. The case  $\varepsilon = 0$  represents the unrealistic case of static friction equals kinetic friction, or instantaneous healing. To account for heterogeneities in the brittle properties, some uniformly distributed noise  $\in [-0.5; 0.5]$  is added to  $\tau_d$ .

As yet, the frictional properties of the fault are strongly simplified; the strength envelope, which describes the change of the friction coefficient by means of static and dynamic frictions, is a piecewise constant function (see solid line in Fig. 1). It is, however, known from laboratory experiments that ruptures are governed by more complicated friction laws (DIETERICH, 1972; 1978). Most of the experimental results are described by the rate- and state-dependent constitutive law (RUINA, 1983; SCHOLZ, 1998). Within this law, the response to a sudden change of the sliding velocity is an instantaneous effect on the friction coefficient followed by a more gradual evolution.

As a first step towards a more realistic friction law, we introduce a gradual time-dependent healing of the form (see dashed line in Fig. 1)

$$\tau_d(t) = \tau_{d,0} + C \log(1 + (t/t_0)), \quad (2)$$

where  $\tau_{d,0}$  is the initial dynamic friction coefficient,  $t_0$  is a reference time and  $C$  is a free parameter. The healing begins after the instantaneous drop of the friction from  $\tau_s$  to  $\tau_{d,0}$ . For our numerical simulations, we parameterize the healing with two parameters  $p_1$  and  $t_{100}$ , instead of  $C$  and  $t_0$ . The value of  $p_1$  gives the fraction of  $\tau_s - \tau_{d,0}$  that has healed after a time of  $1 \text{ km}/v_s$ , and the value  $t_{100}$  gives the time interval required for complete healing,  $\tau_d(t_{100}) = \tau_s$ .

The stress transfer during an earthquake is calculated by means of the three-dimensional solution of CHINNERY (1963) for static dislocations on rectangular patches in an elastic Poisson solid with rigidity  $\mu = 30\text{GPa}$ . In particular, we approximate the 3 + 1 dimensional space-time stress transfer by

$$\Delta\tau(i, j; t) = (1 - \gamma) \cdot \sum_{k, l \in \text{fault}} K(i, j; k, l) \Delta u(k, l; t - r/v_s), \quad (3)$$

where  $\Delta u$  is the slip,  $r$  is the spatial distance between the cells  $(i, j)$  and  $(k, l)$ , and  $v_s$  is the shear-wave velocity. The factor  $1 - \gamma \in (0; 1]$  corresponds to a given ratio of rigidities governing during instabilities the self-stiffness of a slipping cell (diagonal elements of the stiffness matrix) and the stress transfer to the surrounding domain (off-diagonal elements). A ratio smaller than 1 represents stress loss during rapid slip on the fault to internal free surfaces in the solid associated with porosity and cracks. We refer to  $\gamma$  and  $1 - \gamma$  the stress loss parameter and stress conservation parameter, respectively. The slip  $\Delta u(i, j)$  of a cell at a position  $(i, j)$  is related to the stress drop  $\Delta\tau(i, j)$  at the same position through the self-stiffness:  $\Delta u(i, j) = \Delta\tau(i, j)/K(i, j; i, j)$ . The size of an earthquake is measured with two quantities: 1. the area, which is proportional to the number of cells that participated in the earthquake failure, and the potency, which is the integral of the slip over the rupture area. This approach extends the model of BEN-ZION and RICE (1993) to a quasi-dynamic procedure with a finite communication speed  $v_s$  for stress transfer and a related causal rupture process. In one version of the model, the quasi-dynamic rupture process is calculated on a continuous time scale. This may, however, lead to a numerical explosion during the simulation, for certain parameter values. Therefore, we also study simplifications of the continuous time process, e.g., by discretizing the time scale for the stress transfer during an earthquake.

At the present state, the model is characterized by two separate time scales: the inter-event time scale during which the fault is loaded between two events, and the intra-event time scale defined by the travel time of a shear wave along the fault, where coseismic stress redistribution takes place. During the event, the tectonic loading is neglected. The stress conservation parameter  $1 - \gamma$ , which controls the amount of stress remaining on the computational grid, is varied between  $\gamma \approx 1$  (no stress redistribution) and the conservative case  $\gamma = 0$  (stress drop  $\tau - \tau_a$  is completely redistributed). In general,  $\gamma$  controls the size of the generated earthquakes: for high values of  $\gamma$ , small amounts of stress are redistributed and the evolution of cascading failure events stops earlier than in corresponding cases of small  $\gamma$ , for which large earthquakes can develop. In the latter case, numerical problems may occur, because large runaway events that cover the entire fault and have multiple slip episodes of each cell, result in a memory exhaustion on the continuous intra-event time scale. Therefore, we also study a simplification of the quasi-dynamic rupture: the intra-event time scale is discretized into  $N$  time intervals. Each slip of a cell is assigned to one of the time intervals. Note that the case  $N = 1$  represents the quasi-static model

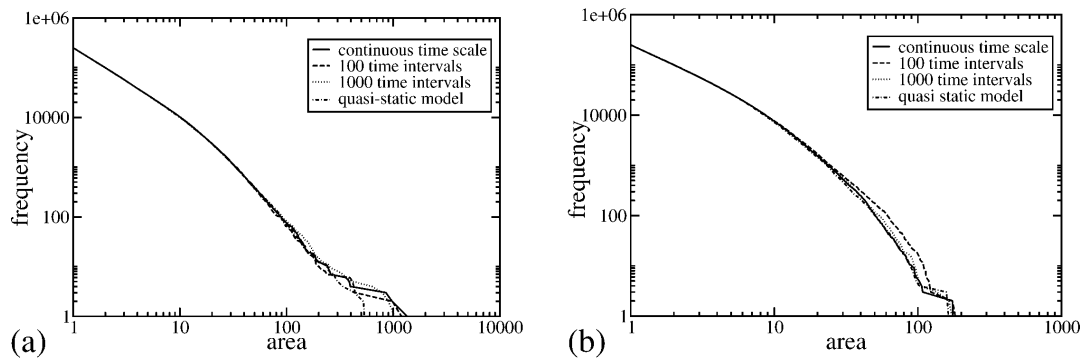


Figure 2

Frequency-size distribution for different model versions (without healing during events) employing  $\gamma = 0.3$  with  $\varepsilon = 0.8$  (Figure (a)) and  $\varepsilon = 0.0$  (Figure (b)). The solid line refers to the continuous intra-event time scale; the dashed and the dotted line refer to discretized time scales with the 100 and 1000 time intervals, respectively. The dash-dotted line refers to the quasi-static model of BEN-ZION and RICE (1993). The area is given in units of the used cell size.

used in BEN-ZION and RICE (1993). Although it is mathematically not clear that the limit  $N \rightarrow \infty$  converges to the continuous time scale, we assume that a value of  $N$  exists, which approximates the continuous case with a reasonable accuracy. In our simulations we used  $N = 1000$ . Given the dimensions of our grid, a stress signal may travel ten times along the fault before the time error becomes comparable to the travel time between neighboring cells. The model simulations are started with a random distribution of initial stress. To account for transient effects in the dynamics, the first 50,000 earthquakes are neglected in each simulation.

### 3. Model Simulations

#### 3.1. Influence of Intra-event Dynamic

Figure 2 gives the frequency-size distribution for different versions of the intra-event time scale. Figure 2(a) shows results calculated with  $\gamma = 0.3$  and a realistic value of the dynamic weakening coefficient  $\varepsilon = 0.8$  corresponding to a dynamic overshoot coefficient  $D = 1.25$  (MADARIAGA, 1975). Figure 2(b) shows the same calculation for the unrealistic case of  $\varepsilon = 0$  and instantaneous healing ( $\tau_d = \tau_s$ ), where the frequency-size statistics is a truncated power law. The results indicate that the continuous time scale (solid line) can be approximated quite well by the discretized time scale with 1000 intervals (dotted line). In the case without large earthquakes, there is no significant difference between the quasi-dynamic model and the quasi-static model (dash-dotted line). In contrast, Figure 2(a) shows a clear fall-off for large events in the quasi-static case. This difference is a stable feature; that is, it is also present for a broad range of parameter values  $\varepsilon$  and  $\gamma$  that allow large earthquakes to occur. Consequently, the quasi-static approximation seems to

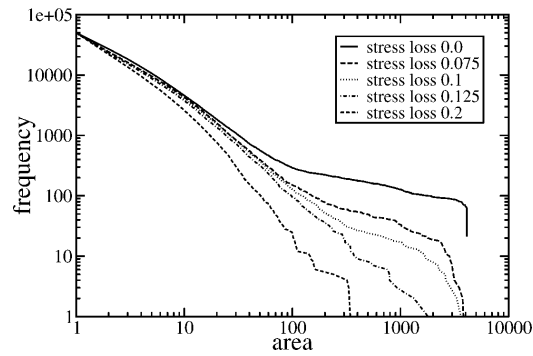


Figure 3

Frequency-size statistics for different values of the stress loss factor  $\gamma$  with  $\varepsilon = 0.6$  (no healing during events). The transition from the Gutenberg-Richter distribution to the characteristic earthquake distribution takes place at  $\gamma \approx 0.125$ .

suppress large earthquakes leading to a truncation in the frequency-size statistics. For large earthquakes, the propagation of stress with finite communications speed  $v_s$  is obviously a relevant feature.

### 3.2. The Phase Diagram Framework

In DAHMEN *et al.* (1998) a simplified two parameter mean field version of the quasi-static model of BEN-ZION and RICE (1993) has been analyzed. A “conservation parameter”  $c$  (similar to our  $1 - \gamma$ ) has been introduced, and an infinite-range mean-field stress transfer function  $G \sim c/N$  ( $N =$  total number of cells) was used instead of Chinnery’s solution for the 3-D elastic stress transfer. For this model, a phase diagram spanned by  $c$  and the dynamic weakening coefficient  $\varepsilon$  contains two distinct phases: one phase where the frequency-size distribution follows the Gutenberg-Richter law, and a second phase governed by a spontaneous mode switching between Gutenberg-Richter statistics and the characteristic earthquake distribution. In particular, it is hypothesized that these phases are generic for more realistic stress transfer functions. In the first part of this study, we analyze this claim for various types of interactions. We observe in agreement with WEATHERLEY *et al.* (2002) that with coarse cell size there is a threshold of the interaction range, below which no mode-switching occurs. However, with small enough cells and strong heterogeneities, mode-switching also occurs for the realistic case of elastic stress transfer. In the second part, we consider the influence of time-dependent  $\log(t)$  healing. The results show that the model can be mapped onto the same phase diagram if the net effect of healing is absorbed in effective dynamic threshold and stress loss.

#### 3.2.1. The phase diagram for the quasi-dynamic and elastic model.

Figure 3 shows frequency-size statistics for a fixed dynamic weakening coefficient  $\varepsilon = 0.6$  as a function of the stress loss factor  $\gamma$ . High values of  $\gamma$  prevent the occurrence of large earthquakes, in that stress that is needed to bring cells to failure is

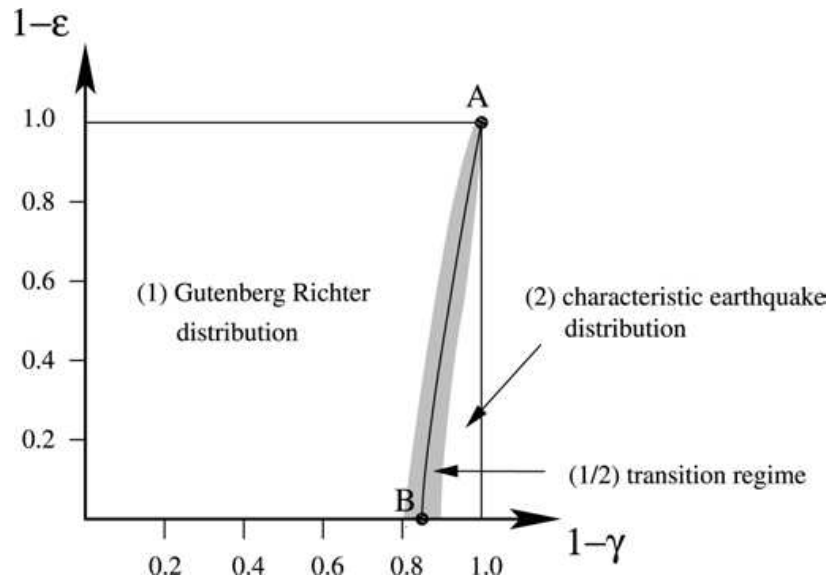


Figure 4

Schematic phase diagram for a fault with  $N = 128 \times 32$  cells as a function of the dynamic weakening parameter  $\varepsilon$  and the stress loss factor  $\gamma$  (model without healing during events). The line AB separates the Gutenberg-Richter phase and the phase where large characteristic earthquakes occur.

lost and earthquakes are stopped earlier. Furthermore, the figure shows a transition from a truncated Gutenberg-Richter distribution ( $\gamma = 0.2$ ) to a characteristic earthquake distribution ( $\gamma = 0$ ). For  $\gamma \approx 0.125$ , the system bifurcates to the two regimes.

Our calculations with the quasi-dynamic elastic model lead (Fig. 4) to a large Gutenberg-Richter regime with small earthquake sizes, and a regime governed by a characteristic earthquake distribution with some short time fluctuations. Note that the factor  $c$  in DAHMEN *et al.* (1998) is now replaced by  $1 - \gamma$ . The characteristic earthquake regime is smaller than the mode switching phase in DAHMEN *et al.* (1998), because in the elastic model a small fraction of the stress drop is lost even for  $\gamma = 0$  due to the finite fault size. We have estimated that on average 80% of the stress drop remains on the fault for the employed 70 km and 17.5 km dimensions with  $\gamma = 0$ . Consequently, the case  $\gamma = 0$  for the elastic model corresponds to  $c = 0.8$  of the mean field model. This is approximately confirmed by a comparison of Figure 4 with the phase diagram in DAHMEN *et al.* (1998).

### 3.2.2. Mode-switching between Gutenberg-Richter and characteristic earthquake statistics.

To address the question of a possible mode switching, long simulations are required. Therefore, we use for the following analysis a fault of 10.9-km length and 2.7-km depth divided into  $20 \times 5$  uniform cells. Figure 5 shows a typical earthquake sequence (rupture area vs. time) from a catalog representing the characteristic earthquake regime. The quasi-periodically occurring characteristic earthquakes are

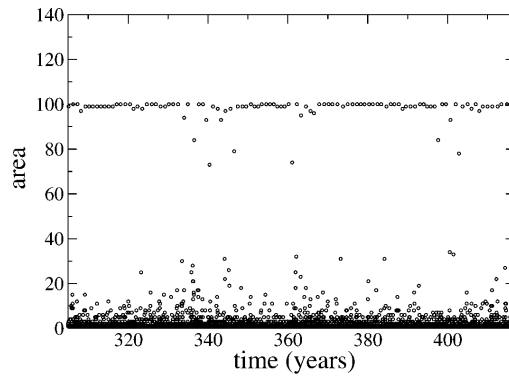


Figure 5

Earthquake area as a function of time for the quasi-static model ( $N = 20 \times 5$ ,  $\epsilon = 0.6$ ,  $\gamma = 0.03$ , no healing during events). The sequence follows the characteristic earthquake distribution, although the system attempts to switch to a Gutenberg-Richter phase, e.g., at  $t \approx 361$ .

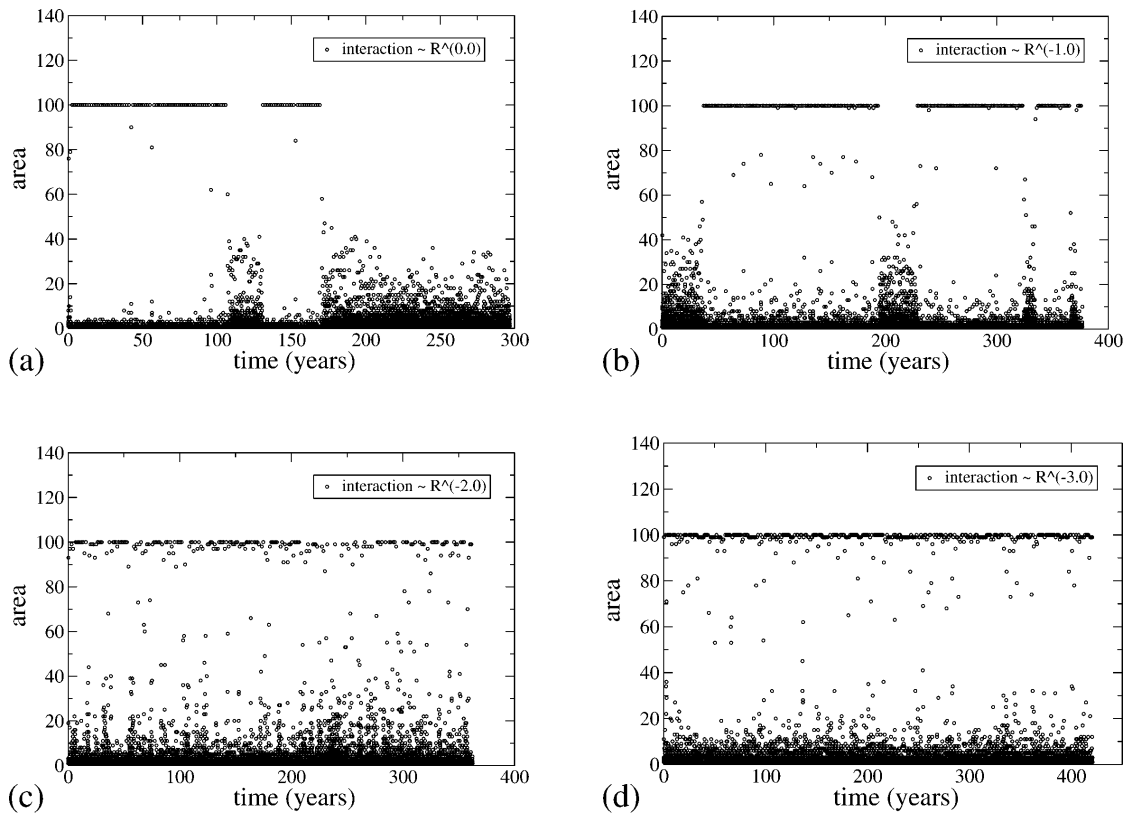


Figure 6

Earthquake area as a function of time for the quasi-static model ( $N = 20 \times 5$ ,  $\epsilon = 0.6$ , no healing during events) and different types of interaction  $\sim r^{-x}$ . The stress loss factor  $\gamma$  has been adjusted in order to bring the system into the transition regime between Gutenberg-Richter and characteristic earthquake distributions. The case  $x = 0$  represents the mean field approximation [DAHMEN *et al.*, 1998], while  $x = 3$  corresponds to the elastic solution of CHINNERY [1963].

interrupted for short time by clusters of small and intermediate earthquakes. It seems as if the system attempts to switch into the other regime and flips back after a short time, e.g., for  $t = 361$  in Figure 5. In Figure 6 we show that the ability of the system



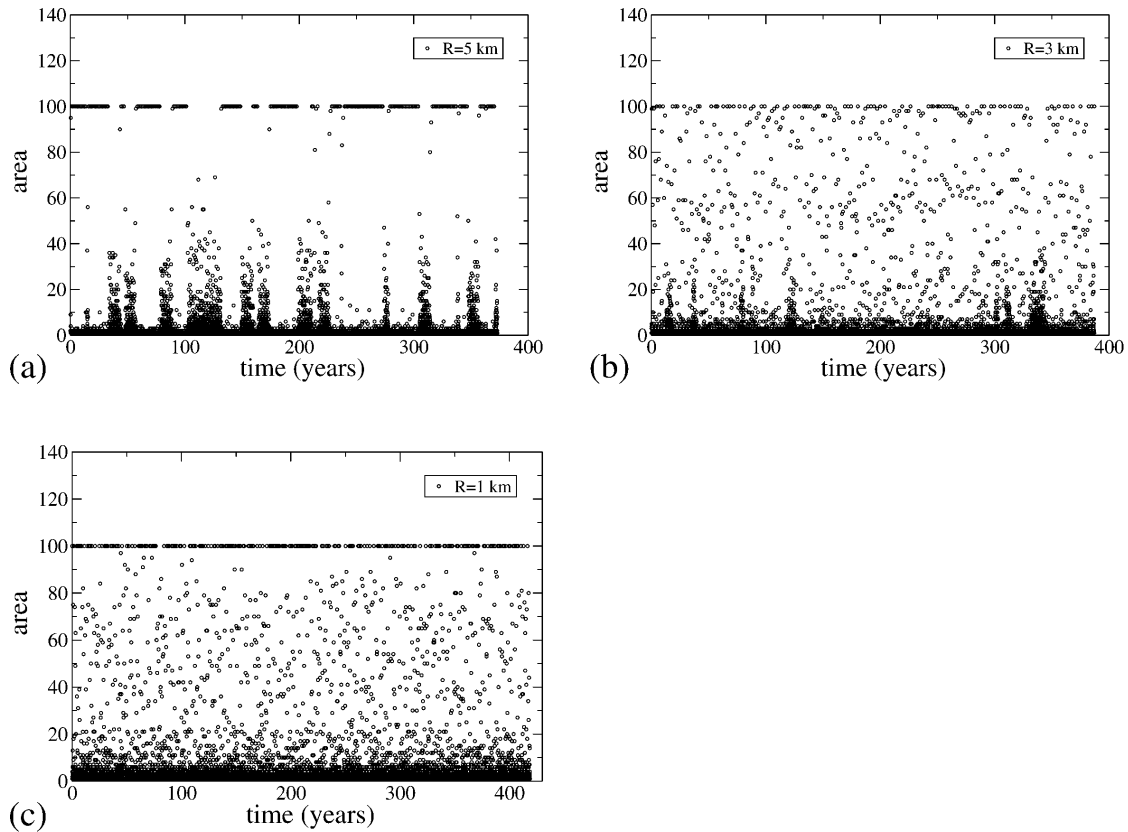


Figure 7

Earthquake area as a function of time for the quasi-static model ( $N = 20 \times 5$ ,  $\varepsilon = 0.6$ , no healing during events) as in Fig. 6, with stress transfer on a compact support with a radius  $R$ .

to undergo a mode-switching depends significantly on the kind of stress transfer. We consider interactions between the limit cases of mean field interaction ( $\Delta\tau \sim r^0$ , where  $r$  is the distance from the slipped cell) and the elastic solution of CHINNERY (1963),  $\Delta\tau \sim r^{-3}$ . These simulations are performed on a  $20 \times 5$  grid with dynamic weakening  $\varepsilon = 0.6$ . Since mode-switching most likely occurs in the transition regime between Gutenberg-Richter and characteristic event distribution, we adjust the stress loss factor  $\gamma$  to be in this part of the parameter space. Each plot in Figure 6 gives results for 10,000 simulated events with stress transfer  $\Delta\tau \sim r^{-x}$  and a certain value of the exponent  $x$ . The plots show clearly that in simulations with coarse cells, the mode-switching in the mean field approximation degenerates with increasing exponent  $x$  to the short-term fluctuations described above. We also performed similar calculations for a uniform stress transfer on a compact support (circle with radius  $R$ ),  $\Delta\tau = \tau_0 \cdot \Theta(r - R)$ . Figure 7 shows earthquake sequences as in Figure 6 for this kind of interaction. Again, the mode-switching behavior, which is clearly visible for large radii, degenerates to short-term fluctuations for small radii. Although we did not observe mode-switching of the type described in DAHMEN *et al.* (1998) in earthquake catalogs up to 20,000,000 events, it cannot be ruled out that this behavior may occur with a very large persistence time in one mode.

In sum, we have found that the ability of the system to undergo a mode-switching from the Gutenberg-Richter distribution to the characteristic earthquake distribution with coarse cell size depends on the range of the stress transfer interaction. Similar results were found in (WEATHERLEY *et al.*, 2002). While mode-switching occurs quite frequently for the infinite range mean field interaction, this behavior could not be observed for the more realistic long-range 3-D elastic interaction, although the system attempts to switch from time to time. In this case, the transition from the Gutenberg-Richter regime to the characteristic earthquake regime with coarse grid is continuous; that is, a decrease of  $\gamma$  leads to the growth of the average magnitude. The limit case ( $\gamma \rightarrow 0$ ) is the characteristic earthquake distribution with quasi-periodically occurring earthquakes that rupture the entire fault. It is also visible that in contrast to the mean field approximation, intermediate size earthquakes are also present in the characteristic earthquake regime. These observations also hold for the quasi-dynamic model.

Until now we have kept the cell size fixed and have varied only the range of stress transfer interaction. It is, however, possible that smaller numerical cells will produce mode-switching, since such will lead to larger stress concentrations near failure areas and larger stress fluctuations. To investigate this hypothesis we have to consider a grid with numerous cells. Note that a change of the fault dimension in terms of total length and depth produces the same earthquake sequences with a rescaled time axis. Such an analysis requires very time-consuming numerical simulations due to two reasons: 1. A new phase diagram corresponding to Figure 4 must be calculated; 2. the transition between both phases must be scanned with a very high resolution in order to extract the range of parameters within which mode-switching is expected in reasonable short simulations. In this context it is important to note that the persistence time in a certain mode depends not only sensitively on  $\gamma$  and  $\varepsilon$ , but also on the number of cells  $N$ . In the mean field model, the persistence time increases according to  $\exp(N)$  (DAHMEN *et al.*, 1998).

In Figure 8 we show two simulations using the elastic stress transfer on a  $128 \times 50$  grid and values for  $\tau_d$  which are uniformly distributed between 0.15 and 0.35 ( $\langle \varepsilon \rangle = 1 - \langle \tau_d \rangle = 0.75$ ), resulting in a more heterogeneous distribution of the brittle properties. The two plots refer to different values of the stress loss  $\gamma$ . The results clearly show a tendency towards mode-switching behavior, e.g., for  $t \in [6.4; 9.0]$  in Figure 8(a). We can thus conclude that mode-switching also depends on the degree of heterogeneity in a system, determined by the cell size and the distribution of the brittle properties. While in the constant mean-field interaction, a large fraction of the parameter-space is governed by mode-switching. This phenomenon seems to occur with the more realistic  $1/r^3$  elastic interaction in considerably smaller ranges of parameters. However, the region in parameter space producing mode-switching in the case of  $1/r^3$  interaction is expected to increase with further decreasing of cell size and increasing of heterogeneities.

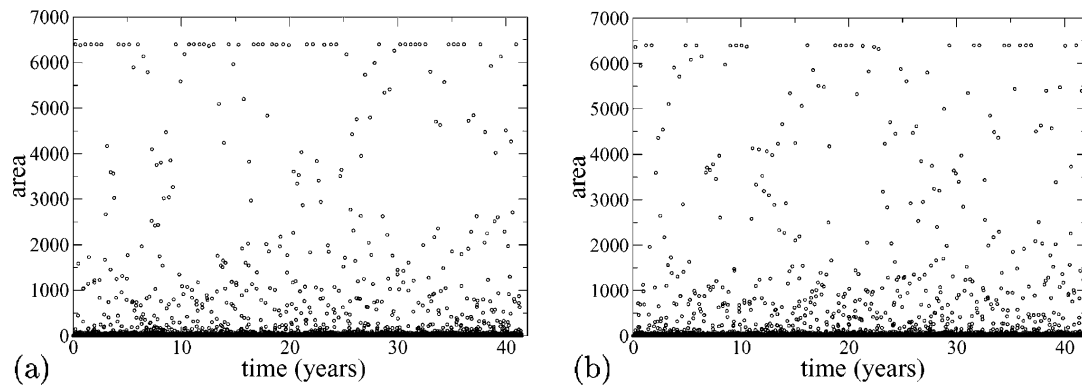


Figure 8

Earthquake area as a function of time for simulations of the quasi-static model (without healing during events) on a fault with  $N = 128 \times 50$  cells. The stress loss parameter is  $\gamma = 0.01$  in (a) and  $\gamma = 0.015$  in (b). The dynamic weakening coefficients for the cells are drawn from a uniform distribution  $\varepsilon \in [0.65; 0.85]$ .

### 3.2.3 Time-dependent healing.

The introduction of time-dependent healing according to Eq. (2) replaces the piecewise constant strength envelope by a function consisting of a strength drop followed by a  $\log(t)$  increase of the strength. This kind of healing requires three parameters: the value of  $p_1$  (healing rate after  $1 \text{ km}/v_s$  stress propagation, the value  $t_{100}$  (time when healing is complete) and the values  $\tau_{d,0}$  to which the strength drops when a cells begins to slide. For the present analysis we keep  $t_{100}$  fixed ( $t_{100} = 100 \text{ km}/v_s$ ) and tune the shape of the healing curve by means of  $p_1$  and  $\tau_{d,0}$ . The stress loss  $\gamma$  is an additional parameter independent of the healing.

It is a reasonable assumption that in the case of healing, effective values of  $\tau_{d,0}$  and  $\gamma$  exist that correspond to  $\tau_d$  in the case without healing. To investigate this hypothesis we determine for different values of  $p_1$  and  $\gamma$  the dynamic threshold  $\tau_{d,0}^*$ , where the transition between the Gutenberg-Richter law and the characteristic earthquake distribution occurs. The value  $\tau_{d,0}^*$  as a function of  $p_1$  and  $\gamma$  is then compared with the corresponding dynamic threshold  $\tau_d^*$  in the system without healing.

Figure 9 shows for the  $20 \times 5$  grid the dependence of  $\tau_{d,0}^*$  on  $p_1$  for different values of  $\gamma$  (Fig. 9(a)) and the dependence of  $\tau_{d,0}^*$  on  $\gamma$  for different values of  $p_1$  (Fig. 9(b)). The curves for the model with healing ( $p_1 > 0$ ) are normalized to the model without healing ( $p_1 = 0$ ). In particular, the vertical axis gives  $\tau_{d,0}^*(p_1)/\tau_{d,0}^*(p_1 = 0)$ . Note that  $\tau_{d,0}^*(p_1 = 0) = \tau_d^*$  describes the model without healing. In Figure 9(b) the curves are normalized to the horizontal line  $\tau_{d,0}^*(p_1)/\tau_{d,0}^*(p_1 = 0) \equiv 1$ . Figure 9(a) shows clearly a systematic decrease of  $\tau_{d,0}^*$  for growing values of  $p_1$ . Moreover,  $\tau_{d,0}^*$  also decreases as a function of  $p_1$ , although this decrease is less significant. The dependence of  $\tau_{d,0}^*$  on  $p_1$  and  $\gamma$  can be described by the formula

$$\tau_{d,0}^*(p_1, \gamma) = \tau_d^* \cdot (1 - s(p_1, \gamma)), \quad (4)$$

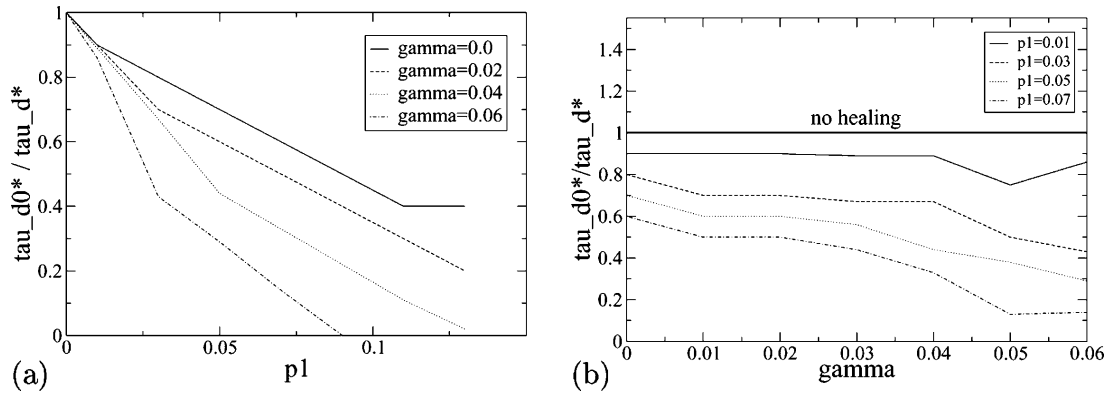


Figure 9

Model with healing: dynamical threshold  $\tau_{d,0}^*$  at the transition between Gutenberg-Richter law and characteristic earthquake distribution (a) as a function of  $p_1$  for different values of the stress loss  $\gamma$  and (b) as a function of  $\gamma$  for different values of  $p_1$ . The vertical axis in (a) is normalized to 1 at  $p_1 = 0$ ; in (b) the curves for  $p_1 > 0$  are normalized to the model without healing ( $p_1 = 0$ , horizontal line).

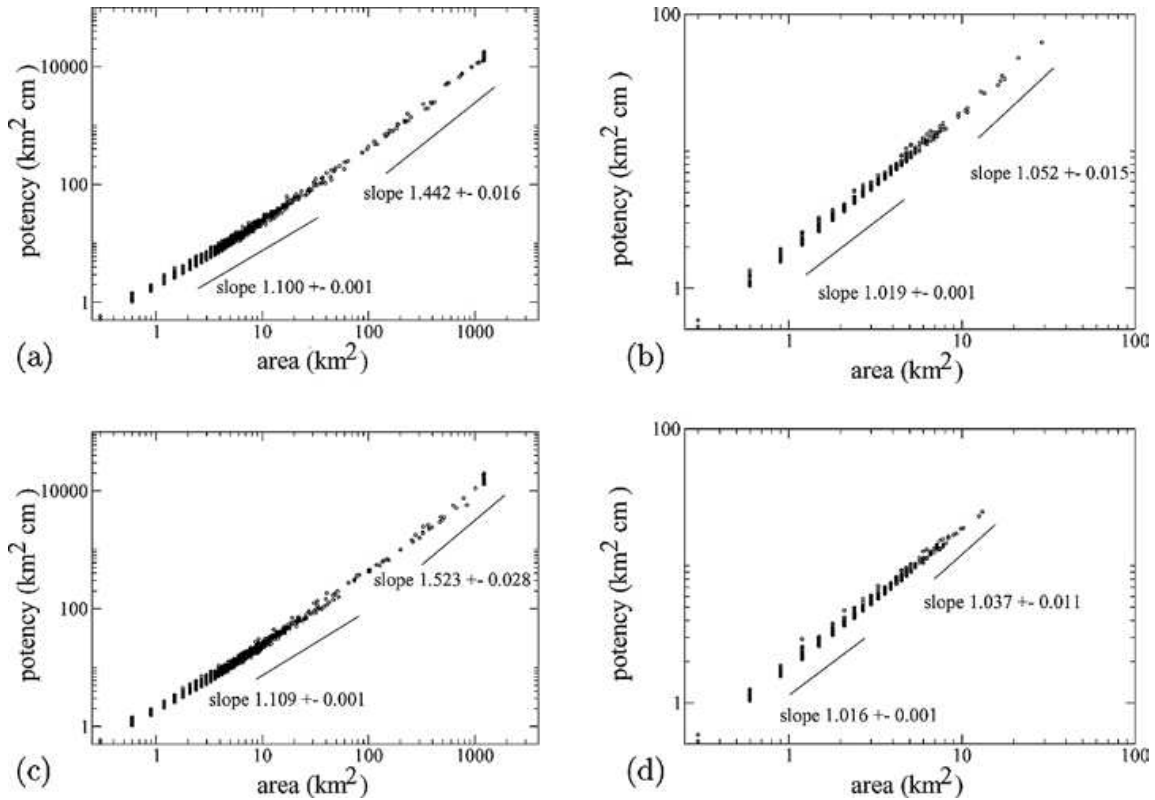


Figure 10

Relation between potency and rupture area in a model realization with  $\epsilon = 0.8$  and (a)  $\gamma = 0.0$  or (b)  $\gamma = 0.3$  (model without healing during events). Panels (c) and (d) show the corresponding results for the quasi-static model.

where  $s(p_1, \gamma)$  is given by the curves in Figure 9. This rule connects the model with healing ( $p_1 > 0$ ) and the model without healing ( $p_1 = 0$ ). Consequently,  $p_1$  is not an independent parameter like  $\tau_d$  and  $\gamma$ . Rather, the model with healing can be obtained

from the model without healing by a shift in the phase diagram according to Eq. (4). The observation that the dependence of  $s(p_1, \gamma)$  on  $p_1$  is more pronounced than the dependence on  $\gamma$  arises from the origin of  $p_1$ : this parameter defines the rate of healing; in other words, the rate of increase of  $\tau_d$ . It is, therefore, reasonable that an effective dynamic threshold (in the model without healing) exists that can to some degree absorb the time-dependence in the model with healing.

In general, it is an interesting task to also map other models systematically onto the present one with respect to the phase diagram. This would, however, require two independent state variables that allow positioning a given catalog in the phase diagram without pre-knowledge of the parameters. This work is left for the future.

### 3.3. Area-potency Relations

Finally, we investigate the area-potency relation. Figure 10 shows calculations for  $\varepsilon = 0.8$  and  $\gamma = 0.0$  and  $\gamma = 0.3$ , for both the quasi-dynamic and the quasi-static models. The change of slope for the transition from small to large earthquakes is in agreement with the quasi-static simulations in BEN-ZION and RICE (1993) and the data analysis in BEN-ZION and ZHU (2002). The slope for the large earthquakes is close to the exponent in the classical crack relation  $a \sim p^{2/3}$  (KANAMORI and ANDERSON, 1975).

## 4. Conclusions

We have developed a model for earthquake failure at intermediate scales that is based on the framework of BEN-ZION and RICE (1993). The model is implemented in a flexible C++ class library and therefore allows the incorporation of additional processes and structural fault properties in a straightforward manner. In this study we extended the model of BEN-ZION and RICE (1993) by two important features. First, the stress propagation is modeled on a continuous intra-event time scale using a finite communication speed. This quasi-dynamic model results in more realistic behavior of the stress propagation. Second, we have introduced a gradual time-dependent healing after a cell has slipped. This mechanism modifies the frictional properties from the simple static/kinetic friction towards the rate- and state-dependent constitutive law.

The results indicate that the finite stress propagation velocity is a relevant feature even for the frequency-size statistics. The quasi-dynamic model produces larger events compared to the quasi-static model in which the occurrence of large events is suppressed. This is in agreement with the fully dynamic 2-D calculations of BEN-ZION and RICE (1997). Future activities with the quasi-dynamic version of the model include analysis of slip histories and possible calculations of synthetic seismograms. In another research direction we examined the ability of the model to undergo a spontaneous mode-switching between the Gutenberg-Richter law and the charac-

teristic earthquake distribution. While the mean field model, which is characterized by a constant stress transfer function, exhibits clear mode-switching behavior, this is not the case in the model with the coarse grid and 3-D elastic stress transfer function. Instead, it is found that in the characteristic earthquake regime, the system attempts to switch into the Gutenberg-Richter regime, but flips back after a very short time. However, if the cell size is decreased and the degree of strength heterogeneity is increased, mode-switching behavior is observed, even for the  $1/r^3$  elastic stress transfer function. This is in agreement with similar studies in more complex models (BEN-ZION *et al.*, 1999; LYAKHOVSKY *et al.*, 2001). Remaining important questions are which mechanisms are responsible for this behavior and whether these mechanisms are relevant for real faults.

The incorporation of time-dependent healing leads to a modification of the phase diagram shown in Figure 4. As we have shown, the frequency-size event distribution for a model with a  $\log(t)$  healing can be reproduced by a model without healing and with different values of  $\gamma$  and  $\tau_d$ . It is desirable to find two independent state variables that will allow quantification of a catalog and assignment of unique values of  $\gamma$  and  $\tau_d$ . With such state variables one could map other model classes onto the present model.

Due to the modular design of our model code, it is easy to include more structural features and mechanisms into the model, e.g., a more refined frictional behavior and heterogeneities in the distribution of the arrest stress. A detailed analysis of statistical properties and seismicity patterns with various model versions and ranges of parameters will result in a deeper understanding of natural seismicity.

### *Acknowledgments*

We are grateful to Karin Dahmen and Sebastian Hainzl for stimulating discussions. The reviews of Yaolin Shi and Yongxian Zhang aided our improvement of the manuscript. This work was supported by the ‘‘Sonderforschungsbereich 555’’ of the ‘‘Deutsche Forschungsgemeinschaft’’ and the USGS grant 02HQGR0047.

### REFERENCES

- BEN-ZION, Y. (1996), *Stress, Slip, and Earthquakes in Models of Complex Single-fault Systems Incorporating Brittle and Creep Deformations*, J. Geophys. Res. 101, 5677–5706.
- BEN-ZION, Y. (2001), *Dynamic Ruptures in Recent Models of Earthquake Faults*, J. Mech Phys. Sol. 49, 2209–2244.
- BEN-ZION, Y., DAHMEN, K., LYAKHOVSKY, V., ERTAS, D., and AGNON, A. (1999), *Self-driven Mode-switching of Earthquake Activity on a Fault System*, Earth and Plan. Sci. Lett. 172, 11–21.
- BEN-ZION, Y., M. ENEVA, and LIU, Y. (2003), *Large Earthquake Cycles and Intermittent Criticality on Heterogeneous Faults due to Evolving Stress and Seismicity*, 108, 10.1029/2002JB002121 J. Geophys. Res.

- BEN-ZION, Y. and RICE, J. R. (1993), *Earthquake Failure Sequences along a Cellular Fault Zone in a Three-dimensional Elastic Solid Containing Asperity and Nonasperity Regions*, J. Geophys. Res. 98, 14, 109–14, 131.
- BEN-ZION, Y. and RICE J. R. (1997), *Dynamic Simulations of Slip on a Smooth Fault in an Elastic Solid*, J. Geophys. Res. 102, 17, 771–17, 784.
- BEN-ZION, Y. and ZHU, L. (2002), *Potency-magnitude Scaling Relations for Southern California Earthquakes with  $1.0 \leq M_L \leq 7.0$* , Geophys. J. Int. 148, F1–F5.
- BURRIDGE, R. and KNOPOFF, L. (1967), *Model and Theoretical Seismicity*, Bull. Seimol. Soc. Am. 57, 341–371.
- CHINNERY, M. (1963), *The Stress Changes that Accompany Strike-slip Faulting*, Bull. Seimol. Soc. Am. 53, 921–932.
- DAHMEN, K., ERTAS, D., and BEN-ZION, R. (1998), *Gutenberg-Richter and Characteristic Earthquake Behavior in Simple Mean-field Models of Heterogeneous Faults*, Phys. Rev. E 58, 1494–1501.
- DIETERICH, J. (1972), *Time-dependent Friction in Rocks*, J. Geophys. Res. 77, 3690–3697.
- DIETERICH, J. (1978), *Time-dependent Friction and the Mechanics of Stick-slip*, Pure Appl. Geophys. 116, 790–806.
- FISHER, D. S., DAHMEN, K., RAMANATHAN, S., and BEN-ZION, Y. (1997), *Statistics of Earthquakes in Simple Models of Heterogeneous Faults*, Phys. Rev. Lett. 78, 4885–4888.
- GABRIELOV, A., NEWMAN, W. I., and KNOPOFF, L. (1994), *Lattice Models of Failure: Sensitivity to the Local Dynamics*, Phys. Rev. E 50, 188–197.
- HAINZL, S. and ZÖLLER, G. (2001), *The Role of Disorder and Stress Concentration in Nonconservative Fault Systems*, Physica A 294, 67–84.
- HAINZL, S., ZÖLLER, G., and KURTHS, J. (1999), *Similar Power Laws for Fore- and Aftershock Sequences in a Spring-block Model for Earthquakes*, J. Geophys. Res. 104, 7243–7253.
- KANAMORI, H. and ANDERSON, D. L. (1975), *Theoretical Basis of Some Empirical Relations in Seismology*, Bull. Seimol. Soc. Am. 65, 1073–1095.
- LYAKHOVSKY, V., BEN-ZION, Y., and AGNON, A. (2001), *Earthquake Cycle, Fault Zones, and Seismicity Patterns in a Rheologically Layered Lithosphere*, J. Geophys. Res. 106, 4103–4120.
- MADARIAGA, R. (1975), *Dynamics of an Expanding Circular Fault*, Bull. Seimol. Soc. Am. 66, 639–666.
- RUINA, A.L. (1983), *Slip Instability and State Variable Friction Laws*, J. Geophys. Res. 88, 10,359–10,370.
- SCHOLZ, C. H. (1998), *Earthquakes and Friction Laws*, Nature 391, 37–42.
- SORNETTE, D. and SAMMIS, C. G. (1995), *Complex Critical Exponents from Renormalization Theory Group of Earthquakes: Implications for Earthquake Predictions*, J. Phys. I France 5, 607–619.
- WEATHERLEY, D., MORA, P., and XIA, M. F. (2002), *Long-range Automaton Models of Earthquakes: Power-law Accelerations, Correlation Evolution, and Mode-switching*, Pure Appl. Geophys. 159, 2469–2490.
- ZÖLLER, G. and HAINZL, S. (2002), *A Systematic Spatio-temporal Test of the Critical Point Hypothesis for Large Earthquakes*, Geophys. Res. Lett. 29, 10.1029/2002GL014856.
- ZÖLLER, G., HAINZL, S., and KURTHS, J. (2001), *Observation of Growing Correlation Length as an Indicator for Critical Point Behavior prior to Large Earthquakes*, J. Geophys. Res. 106, 2167–2176.

(Received September 27, 2003, revised March 20, 2004, accepted March 30, 2004)

---

To access this journal online:  
<http://www.birkhauser.ch>

---

# Appendix L

The role of heterogeneities as a tuning parameter of earthquake dynamics

Autors:	G. Zöller, M. Holschneider, and Y. Ben-Zion
Journal:	Pure and Applied Geophysics
Volume (Nr.):	<b>162(6-7)</b>
Pages/doi:	1027-1049, doi 10.1007/s00024-004-2660-9
Year:	2005



## The Role of Heterogeneities as a Tuning Parameter of Earthquake Dynamics

GERT ZÖLLER,<sup>1</sup> MATTHIAS HOLSCHNEIDER<sup>2</sup> and YEHUDA BEN-ZION<sup>3</sup>

*Abstract*—We investigate the influence of spatial heterogeneities on various aspects of brittle failure and seismicity in a model of a large strike-slip fault. The model dynamics is governed by realistic boundary conditions consisting of constant velocity motion of regions around the fault, static/kinetic friction laws, creep with depth-dependent coefficients, and 3-D elastic stress transfer. The dynamic rupture is approximated on a continuous time scale using a finite stress propagation velocity (“quasidynamic model”). The model produces a “brittle-ductile” transition at a depth of about 12.5 km, realistic hypocenter distributions, and other features of seismicity compatible with observations. Previous work suggested that the range of size scales in the distribution of strength-stress heterogeneities acts as a tuning parameter of the dynamics. Here we test this hypothesis by performing a systematic parameter-space study with different forms of heterogeneities. In particular, we analyze spatial heterogeneities that can be tuned by a single parameter in two distributions: (1) high stress drop barriers in near-vertical directions and (2) spatial heterogeneities with fractal properties and variable fractal dimension. The results indicate that the first form of heterogeneities provides an effective means of tuning the behavior while the second does not. In relatively homogeneous cases, the fault self-organizes to large-scale patches and big events are associated with inward failure of individual patches and sequential failures of different patches. The frequency-size event statistics in such cases are compatible with the characteristic earthquake distribution and large events are quasi-periodic in time. In strongly heterogeneous or near-critical cases, the rupture histories are highly discontinuous and consist of complex migration patterns of slip on the fault. In such cases, the frequency-size and temporal statistics follow approximately power-law relations.

**Key words:** Earthquake dynamics, fault models, seismicity, ruptures, heterogeneities, criticality.

### 1. Introduction

Theoretical parameter-space studies of earthquake models aim to provide a physical basis for understanding seismicity. Such studies complement observational efforts to collect better and larger data sets, and statistical efforts to establish better estimation procedures. In this context, the main goal of the fault model studies is to

---

<sup>1</sup> Institute of Physics and Institute of Mathematics, University of Potsdam, Potsdam, Germany (e-mail: gert@agnld.uni-potsdam.de)

<sup>2</sup> Institute of Mathematics, University of Potsdam, Potsdam, Germany; on leave from CNRS Rennes, France (e-mail: hols@math.uni-potsdam.de)

<sup>3</sup> Department of Earth Sciences, University of Southern California, Los Angeles, USA (e-mail: benzion@usc.edu)

identify different physical regimes that may be present in the data. This can provide guidelines for separating the observations to different corresponding populations, thereby allowing higher-resolution (i.e., more space-time specific) information to be extracted from the available data. In this work we attempt to provide a better understanding of the role of heterogeneities on earthquake dynamics. Toward this goal we first develop a description of heterogeneities that is likely to be physically relevant and has a small number of parameters. We then perform a systematic parameter-space study using that form of heterogeneities and a model of a segmented strike-slip fault in elastic half space.

Important unresolved questions are the dependencies of the frequency-size and temporal statistics of earthquakes on the physical properties and parameters of the fault. The most general feature of seismicity is probably the Gutenberg-Richter (GR) law (GUTENBERG and RICHTER, 1956) for the frequency of earthquake occurrence,  $\log N = a - bm$ , where  $a$  and  $b$  are constants and  $N$  is the number of earthquakes with magnitudes greater than or equal to  $m$ . When phrased in terms of seismic potency (average slip times rupture area) or moment (rigidity times potency), the GR relation follows a power-law distribution (e.g., TURCOTTE, 1997; BEN-ZION, 2003). It has been observed that the GR law is valid over a broad range of magnitudes for data collected in large regions of space (e.g., UTSU, 2002). However, on individual fault zones the situation is different: although power-law behavior is in general present, certain ranges of earthquake magnitudes are characterized by clear deviations from power-law scaling. Observed frequency-size statistics on individual faults are found to exist between two end-member cases: (1) a Gutenberg-Richter law with a fall-off for large magnitudes, and (2) a power law for small earthquakes followed by a gap for intermediate earthquakes and a peak for frequently-occurring characteristic events.

Several explanations for the occurrence of the different frequency-size distributions have been derived from fault models. Here it is crucial to distinguish whether or not an earthquake can rupture large parts of the fault (critical or supercritical behavior), or is stopped after short propagation due to spatial barriers or stress loss during rupture (subcritical behavior). BEN-ZION and RICE (1993, 1995) and BEN-ZION (1996) examined this issue in terms of stress concentration and strength heterogeneities in elastic solids. LOMNITZ-ADLER (1999), STEACY and MCCLOSKEY (1999) and others studied the same with cellular automata models. HAINZL and ZÖLLER (2001) studied this question in terms of stress concentration and spatial disorder in a spring-block model. FISHER *et al.* (1997) and DAHMEN *et al.* (1998) have shown that coseismic dynamic weakening and stress loss in a mean field version of the elastic half-space model of BEN-ZION and RICE (1993) can produce the different end-member frequency-size statistics and spontaneous transitions between them. ZÖLLER *et al.* (2004) generalized the phase diagram of DAHMEN *et al.* (1998) to a more realistic model with (non-mean field) elastic Green's function for the coseismic stress transfer and several other features (e.g., gradual strength healing and causal propagation of stress).

It is widely accepted that spatial disorder, or heterogeneities, significantly influence rupture propagation and thus the frequency-size statistics and other aspects of earthquake behavior. Such heterogeneities may have various forms. The locations of large asperities (e.g., the Parkfield asperity) are known from seismological and other studies (WYSS *et al.*, 2000) and can be implemented easily in fault models. In contrast, small-scale heterogeneities are in general unknown with respect to their sizes, forms and positions. Therefore, heterogeneities in model simulations are often based on simple assumptions, e.g., uniformly distributed random numbers with a certain range, or power-law distributions characterized by range of values and fractal dimensions. Both types of heterogeneities produce stress fluctuations that may be associated with smoothness or roughness of the fault. The results of such studies indicate that large (characteristic) earthquakes can evolve on smooth faults, whereas the growth of a rupture is terminated earlier on a rough fault. A natural example for a smooth fault is the San Andreas fault, which is characterized by a Gutenberg-Richter law for small events and quasiperiodic occurring “characteristic” large events. In contrast, the San Jacinto fault with its numerous offsets and branches has a highly irregular geometry and is governed by Gutenberg-Richter distributed seismicity over the entire range of magnitudes (WESNOUSKY 1994; STIRLING *et al.*, 1996). In this paper, we examine whether the degree of spatial heterogeneity can be tuned by one or two parameters in a fault model between these two extreme cases. This would allow a description of the heterogeneity in terms of the phase diagram approach of DAHMEN *et al.* (1998) and ZÖLLER *et al.* (2004).

BEN-ZION and RICE (1993, 1995, 1997) studied evolutionary seismicity on homogeneous and heterogeneous fault systems using several types of calculations ranging from quasi-static to fully-dynamic. The results from these and related analytical and numerical studies (BEN-ZION *et al.*, 1999; DAHMEN *et al.*, 1998; BEN-ZION, 2001; FISHER *et al.*, 1997; ZÖLLER *et al.*, 2004; MEHTA *et al.*, 2005) indicate that the essential long-term properties of earthquake statistics, and overall aspects of additional dynamic quantities such as moment-rate functions and slip distributions, remain the same when the models share certain key features. These include the physical dimension, range of interaction, overall class of heterogeneities (e.g., continuum vs. inherently discrete cases), and the existence of dynamic weakening and dissipation. Such models are referred to as belonging to the same universality class and they share the same coarse-grained properties that govern the behavior on large space-time scales (e.g., WILSON 1979; BINNEY *et al.*, 1993).

The goal of the present work is to study phenomena associated with large-scale ruptures in realistic heterogeneous fault structures. As discussed by BEN-ZION and RICE (1993, 1995, 1996), the successful propagation of rupture in such systems involves stresses that operate at finite distances from the rupture front, where slip can nucleate at non-contiguous locations across fault offsets and other strong barriers. Thus the large-scale growth of slip instabilities in realistic segmented fault systems is governed by length scales that are much larger than those associated with crack-tip

processes such as strength degradation with slip. We therefore neglect detailed small-scale crack-tip processes and fully dynamic calculations, and focus on large-scale fault interactions given approximately by macroscopic static/kinetic friction and creep property values (BEN-ZION, 1996). The assumed properties are assigned to a system of numerical cells representing quasi-independent fault segments, each behaving uniformly in the adopted modeling approximation. Our investigations are done with quasi-dynamic calculations (ZÖLLER *et al.*, 2004) that incorporate causal spatio-temporal propagation of stress during an earthquake failure. This allows us to discuss basic differences of rupture histories on smooth and rough faults.

Power-law distribution of fault properties may be used to tune the smoothness of a fault by two parameters, the fractal dimension  $D$  and standard deviation of values. It is, however, unlikely that the active structure of large faults or fault systems is characterized by fractal properties over tens or hundreds of kilometers (BEN-ZION and SAMMIS, 2003). Instead, it is more realistic to use heterogeneities that model large-scale offsets and branches superimposed on a relatively smooth fault. BEN-ZION and RICE (1995) and BEN-ZION (1996) used such a form of heterogeneities consisting of strong (high stress drop) barriers separating weaker (low stress drop) fault segments. To model realistic structures, the barriers were assumed to be strongly correlated with depth and essentially uncorrelated in the strike direction. In the following sections we perform a systematic study of frequency-size statistics and other aspects of earthquake dynamics using such nearly-vertical barriers embedded in an overall smooth fault, as well as power-law distributions, and discuss the results in terms of the phase diagram approach.

## 2. Model Framework

Our model includes a single rectangular fault embedded in a 3-D elastic half space (Fig. 1). A fault region of 70 km length and 17.5 km depth is covered by a computational grid, divided into  $128 \times 32$  uniform cells, where deformational processes are calculated. Tectonic loading is imposed by a motion with constant velocity  $v_{\text{pl}} = 35$  mm/year of the regions around the computational grid. The space-dependent loading rate provides realistic boundary conditions. Using the static stress transfer function  $K(x, z; x', z')$  from CHINNERY (1963), the continuous tectonic loading for each cell  $(x, z)$  on the computational grid is a linear function of time  $t$  and plate velocity  $v_{\text{pl}}$ :

$$\Delta\tau(x, z; t) = (-v_{\text{pl}} \cdot t) \cdot \sum_{x', z' \in \text{grid}} K(x, z; x', z'), \quad (1)$$

where the minus sign stems from the fact that forward (right-lateral) slip of regions around a locked fault segment is equivalent to back (left-lateral) slip of the locked fault segment. Additional loadings on a given cell occur due to brittle and creep failures on the fault.

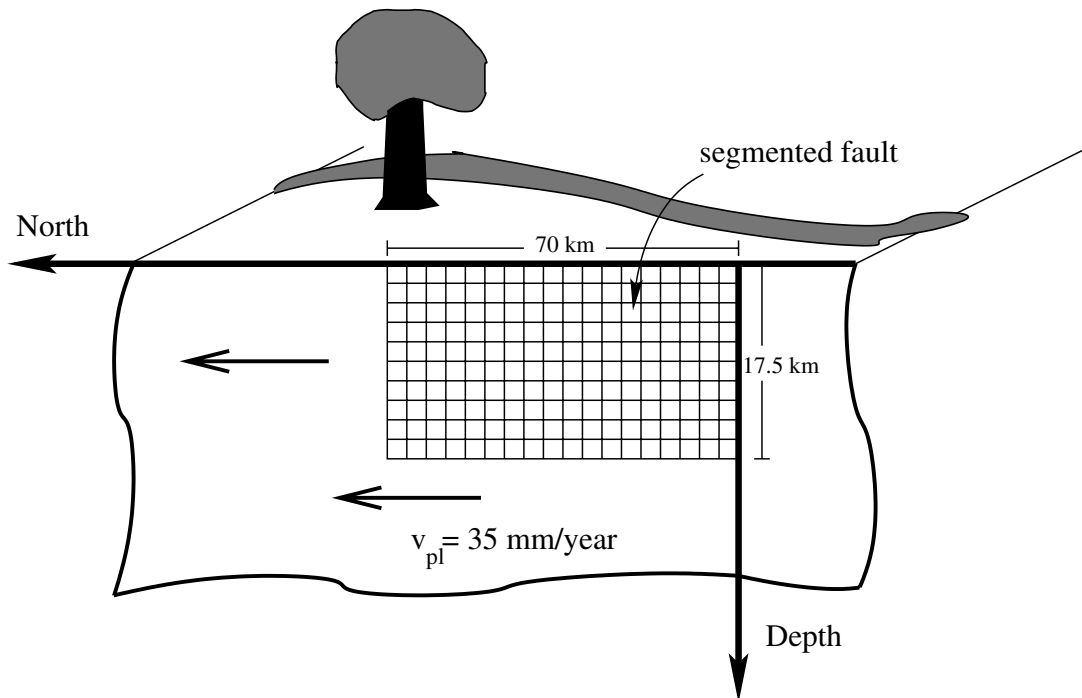


Figure 1

A sketch of a 2-D strike-slip fault in a 3-D elastic half space.

While the loadings produce an increase of stress on the fault, the local stress may be reduced by creep and brittle failure processes operating “in series.”

### 2.1. The Creep Process

The ongoing creep motion on the fault is implemented as in BEN-ZION (1996). The space- and time-dependent creep rate follows the formula

$$\dot{u}_{\text{creep}}(x, z, t) = c(x, z)\tau(x, z, t)^3, \quad (2)$$

where  $c(x, z)$  are time-independent coefficients and  $\tau$  is the local stress.

Equation (2) corresponds to dislocation creep observed in laboratory experiments with a coefficient  $c$  that increases with temperature and pressure. Following BEN-ZION (1996), we choose a distribution  $c(x, z)$  that simulates “brittle-ductile” transitions in the vertical and horizontal directions:

$$c(x, z) = A \exp(B \cdot \text{Max}((x - x_{BD}), (z - z_{BD}))) + \text{ran}(x, z), \quad (3)$$

where  $A$  and  $B$  are constants and  $x_{BD} = 62.5$  km,  $z_{BD} = 10.0$  km are the horizontal and vertical positions of the “brittle-ductile” transition zones. The transition in depth models the occurrence of ductile deformation with increasing temperature and pressure, while the transition along strike is based on the assumption that an essentially brittle fault segment is connected with a creeping fault section. At  $x_{BD}$  and  $z_{BD}$ , the creep rates equal approximately the tectonic loading rate, the stress increase

due to the plate motion is released mostly by aseismic creep, and consequently hypocenters do not nucleate. The values  $ran(x, z)$  simulate a certain mixing between the two zones which are dominated by different brittle and ductile properties. Details about the calculation of  $A$  and  $B$  and the values of  $ran(x, z)$  are given in BEN-ZION (1996). We point out that this choice of creep coefficients represents a certain type of quenched spatial heterogeneities, which are, however, constant in all simulations. The gradual creep motion results in realistic depth profiles of the simulated hypocenter distribution, which follow approximately a Gaussian function in agreement with observations.

Taking into account the relation between stress and displacement on the computational grid

$$\Delta\tau(x, z) = \sum_{x', z' \in \text{grid}} K(x, z, x', z') \Delta u(x', z'). \quad (4)$$

Equations (2)–(4) result in a system of  $128 \times 32$  coupled ordinary differential equations, which is solved numerically using a Runge-Kutta scheme. However, in order to increase numerical efficiency we use the decay of the elastic Green's function to reduce the interaction during the creep to a local neighborhood.

## 2.2. The Brittle Process

The brittle process is governed by a static/kinetic friction law and dynamic overshoot. A brittle failure is initiated on a cell if the static friction  $\tau_s$  is exceeded. We assume that the static threshold increases with depth  $z$ :

$$\tau_s(z) = \Delta\tau_{\max} + f \cdot z, \quad (5)$$

where  $f = 13.5$  MPa/km and  $\Delta\tau_{\max}$  is the maximum allowed brittle stress drop (BEN-ZION, 1996). If a cell slips, the stress drops to an arrest stress  $\tau_a = \tau_s - \Delta\tau$ , where the stress drop  $\Delta\tau$  is the parameter that defines the heterogeneity, e.g.,  $\Delta\tau$  can be drawn from a power-law distribution or from a set of two values representing high stress drop and low stress drop regions.

Following an initial failure during an earthquake, the brittle threshold drops from the static value  $\tau_s$  to a dynamic value  $\tau_d$ , which is calculated in relation to a dynamic overshoot coefficient  $DOS$ :

$$\tau_d = \tau_s - \frac{\tau_s - \tau_a}{DOS}. \quad (6)$$

In our study, we use the value  $DOS = 1.25$  for the dynamic overshoot (BEN-ZION and RICE, 1993; MADARIAGA, 1976).

An important aspect of the brittle process is the dynamic weakening coefficient  $\varepsilon$ :

$$\varepsilon = \frac{\tau_s - \tau_d}{\tau_s}, \quad (7)$$

which becomes space-dependent if  $\Delta\tau$  is a function of space and  $DOS$  is a constant number.

The coseismic stress transfer is calculated by means of the three-dimensional solution of CHINNERY (1963) for static dislocations on rectangular patches in an elastic Poisson solid with rigidity  $\mu = 30$  GPa. In particular, we approximate the 3 + 1 dimensional space-time stress transfer by

$$\Delta\tau(x, z; t) = (1 - \gamma) \cdot \sum_{(x', z') \in \text{grid}} K(x, z; x', z') \Delta u(x', z'; t - r/v_s), \quad (8)$$

where  $\Delta u$  is the slip,  $r$  is the spatial distance between the cells  $(x, z)$  and  $(x', z')$ , and  $v_s$  is the shear wave velocity.

The factor  $(1 - \gamma)$  is in the range  $(0; 1]$  and corresponds to a given ratio of rigidities governing during instabilities the self-stiffness of a slipping cell (diagonal elements of the stiffness matrix  $K$ ) and the stress transfer to the surrounding domain (off-diagonal elements). A ratio smaller than 1 represents stress loss during rapid slip on the fault to internal free surfaces in the solid associated with porosity and cracks. We refer to  $\gamma$  and  $1 - \gamma$  as the stress loss parameter and stress conservation parameter, respectively. FISHER *et al.* (1997) and DAHMEN *et al.* (1998) showed analytically that at  $\varepsilon = 0$  and  $\gamma = 0$  the model has a critical point of phase transition.

The slip  $\Delta u(x, z)$  of a cell at position  $(x, z)$  is related to the stress drop  $\Delta\tau(x, z)$  at the same position through the self-stiffness:  $\Delta u(x, z) = \Delta\tau(x, z)/K(x, z; x, z)$ . The size of an earthquake is measured by the potency (e.g., BEN-ZION, 2003), which is the integral of the slip  $\Delta u$  over the rupture area  $A$ ,

$$P = \int_A \Delta u(x, z) \, dx dz. \quad (9)$$

We note that Equation (8) corresponds to the quasi-dynamic model of ZÖLLER *et al.* (2004), which reduces for  $\gamma = 0$  and  $v_s \rightarrow \infty$  to the quasi-static model of BEN-ZION (1996). The quasi-dynamic model has the advantage that the spatio-temporal evolution of stress transfer during an earthquake can be analyzed, whereas the rupture in the quasi-static model occurs instantaneously. This allows us to study rupture properties in model realizations characterized by different degrees of heterogeneity. Similar quasi-dynamic procedures were used by ROBINSON and BENITES (2001) and HEIMPEL (2003).

### 2.3. Heterogeneities

In this study we consider two different types of heterogeneities that can be tuned with a single parameter: (1) near-vertical barriers of high stress drop embedded in regions of low stress drop, and (2) continuous power-law distributions of the stress drop with a fixed standard deviation.

The first type of heterogeneities, hereinafter referred to as RW, represents near-vertical offsets that produce, as discussed by BEN-ZION and RICE (1995) and BEN-ZION (1996), large-scale fault segmentation. To generate the stress drop distribution, we fix randomly a certain number  $k$  of cells along the free surface that act as initiators of the barriers. The continuation of the barriers with depth is determined by a quasi-2-D random walk, where with each depth increment the barrier may move one unit to the left or right. Using different values of  $k$  results in different degrees of complexity, e.g., for  $k = 1$  two continuous patches with low brittle stress drop are separated by one high stress drop barrier representing an overall relatively smooth fault. The roughness or segmentation of the fault increases if more barriers are added. The degree of heterogeneity is quantified by means of a tuning parameter  $h$  which is calculated in the following way: Each cell with a low stress drop is surrounded by the circle of maximum area  $A_i$  which includes only cells with low stress drop. The circle size  $\sqrt{A_i}$  is a measure for the distance to the nearest high stress drop barrier or to a fault boundary. The standard deviation of the distribution of the circle sizes gives a measure for the range of size scales. To remove boundary effects, we define the heterogeneity parameter by

$$h = \text{std} \left( \sqrt{|A_i - A_i^0|} \right), \quad (10)$$

where  $A_i^0$  is the corresponding circle area on an “empty” fault (fault without barriers). The dimension of  $h$  is km. For a fixed fault,  $h$  may be transformed to a dimensionless value,  $h_n = h/h_{\max}$ .

We point out that  $h$  is determined only by the distribution of the stress drops  $\Delta\tau$ . The stress drop values themselves are fixed for all simulations of model RW:  $\Delta\tau_h + R$  is the high stress drop value,  $\Delta\tau_l + R$  denotes the low stress drop value.  $\Delta\tau_{h,l}$  are constant numbers, while  $R = \sigma \cdot rn$  is additive noise with a width  $\sigma$  and a random number  $rn$  in the range  $[0; 1]$ .

For finite faults,  $h$  always has a positive value even if no barrier is present. BEN-ZION and RICE (1995) and BEN-ZION (1996) pointed out that the simulated earthquake dynamics depend on the range of size scales of the heterogeneities, and distinguished between wide range of size scales (WROSS) and narrow range of size scales (NROSS). In terms of this concept,  $h$  tunes range of size scales represented by the range of radii of the circles discussed above. Specifically, small values of  $h$  correspond to NROSS and large values correspond to WROSS.

For the fractal heterogeneities (F), we generate a power-law distribution (see e.g., TURCOTTE, 1997) of stress drops between  $\Delta\tau_{\min}$  and  $\Delta\tau_{\max}$  with a given fractal dimension  $D$ . Although the fractal dimension allows some tuning of the range of size scales in the distribution of stress drops, model F belongs to the class associated with NROSS (BEN-ZION, 1996). This is because the power-law distribution has a continuous range of stress drop values leading to an overall higher degree of smoothness. In particular, despite the presence of heterogeneities with a range of size



scales, a rupture can easily overcome such heterogeneities since the stress drops fluctuations at the cell boundaries are relatively small. This is in contrast to model RW, which has a bimodal distribution of stress drop (“high” and “low”) with high fluctuations at the barrier boundaries. Model F can be somewhat tuned towards WROSS by increasing the standard deviation of the stress drop distribution. As will be shown, however, we find that power-law distributions do not provide an effective way of tuning the heterogeneities.

### 3. Model Simulations

In the first part of this section, we discuss frequency-size and temporal distributions of seismicity in simulated earthquake catalogs. In the second part, we present the main characteristics of individual ruptures for different ranges of model parameters.

#### 3.1. Analysis of Earthquake Catalogs

We generate heterogeneities for the quasi-dynamic model as described in Section 3. The first type of heterogeneities consists of near-vertical high stress drop barriers embedded in a fault with low stress drops. The brittle stress drop in the barriers is  $\Delta\tau_h = 100 \pm 5 \cdot rn$  and the stress drop in the other cells is  $\Delta\tau_l = 10 \pm 5 \cdot rn$ , where  $rn$  is a uniformly distributed random number between 0 and 1. The degree of complexity is essentially controlled by the density of barriers. We point out that the total number of points with high/low stress drops does not effect the form of the frequency-size distribution. If this number is changed, the average stress on the fault and inter-patch distances will be modified resulting in a rescaling of the time and magnitude axes. The form of the frequency-size distribution depends only on the distribution of the different brittle properties. Three different RW type distributions of stress drops with different values of  $h$  from Eq. (10) are used in our study (Fig. 2). A comparison of the distributions in Figures 2(a) to (c) suggests that  $h$  may provide an effective measure for the complexity of the distribution.

The second type of heterogeneities is based on a power-law distribution of brittle stress drops; three employed examples are given in Figure 3. Although the distributions represent smooth and rough surfaces like the RW heterogeneities, the power-law distributions are structurally different: while the RW heterogeneities are characterized by strong localized stress drop gradients which produce high stress fluctuations at these positions on the fault, the power-law distributions are smoother even for high fractal dimensions.

Figure 4(a) shows the cumulative frequency-size distribution for a purely elastic model without stress loss ( $\gamma = 0$ ) and the three stress drop distributions of Figure 2. The results indicate that  $h$  acts as a tuning parameter for the frequency-size

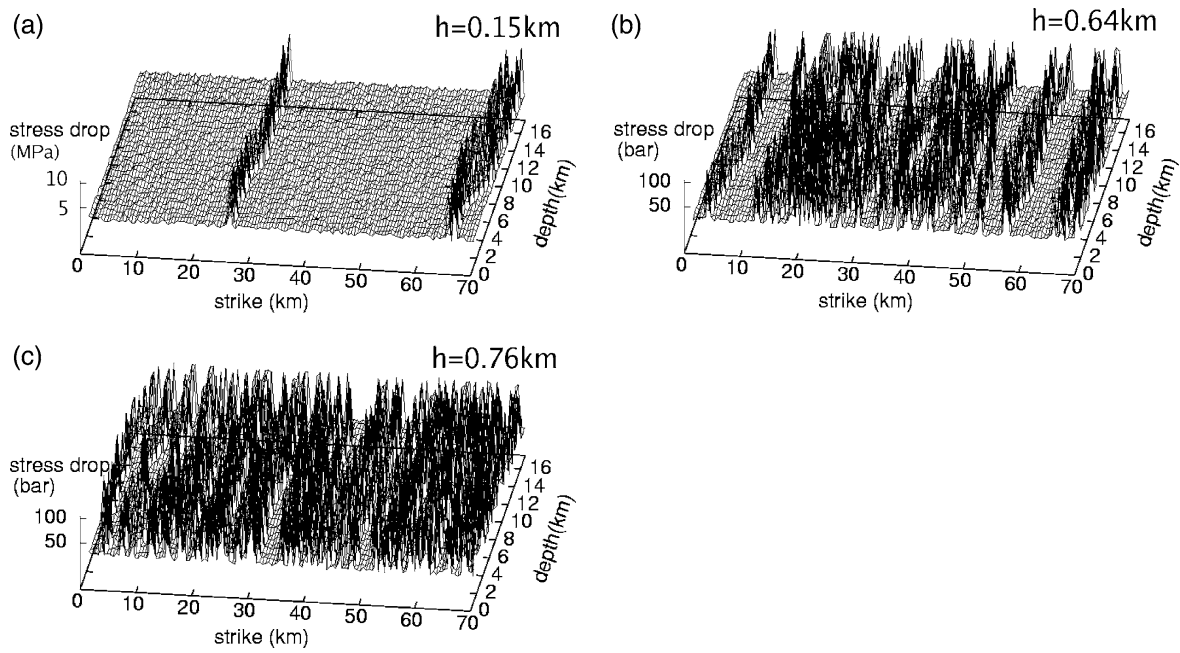


Figure 2

Heterogeneities of the quasi-2D random walk type (RW): The distribution of brittle stress drops consists of high stress drop barriers in a near-vertical direction embedded in a low stress drop environment. The tuning parameter  $h$  (Eq. (10)) measures the degree of heterogeneity in units of km.

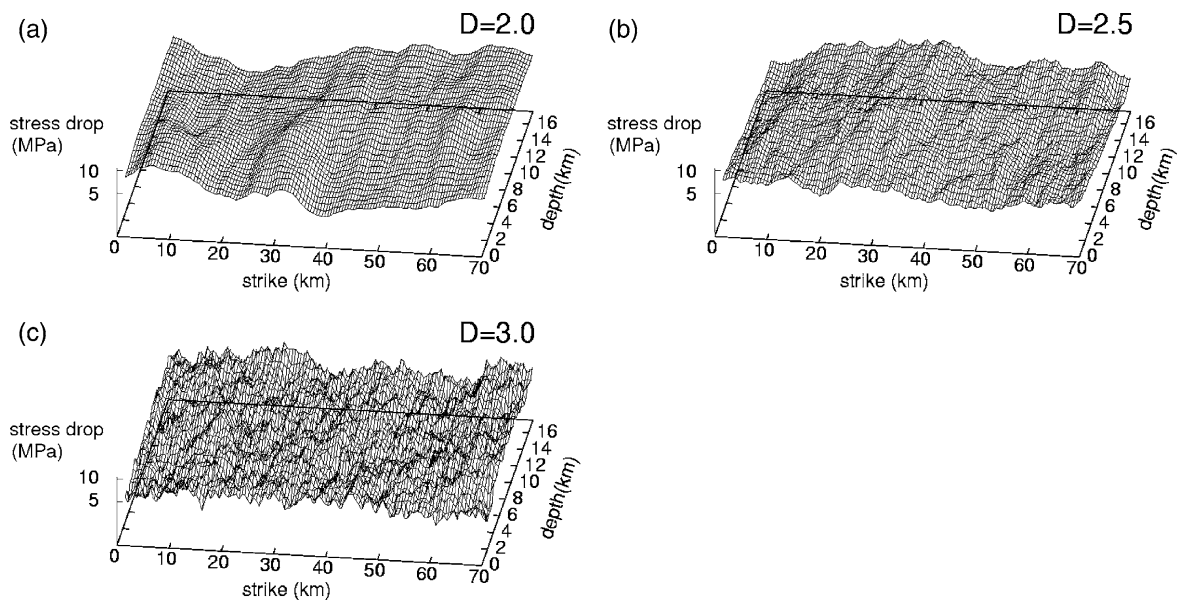


Figure 3

Power-law distributions of the brittle stress drops with three fractal dimensions  $D$  and values between 1 MPa and 9 MPa.

distribution. If  $h$  is small, the fault is characterized by a NROSS and a few low stress drop patches with relatively uniform size. Only a few ruptures are effected by the high stress drop barriers leading to a characteristic earthquake behavior. In contrast, high

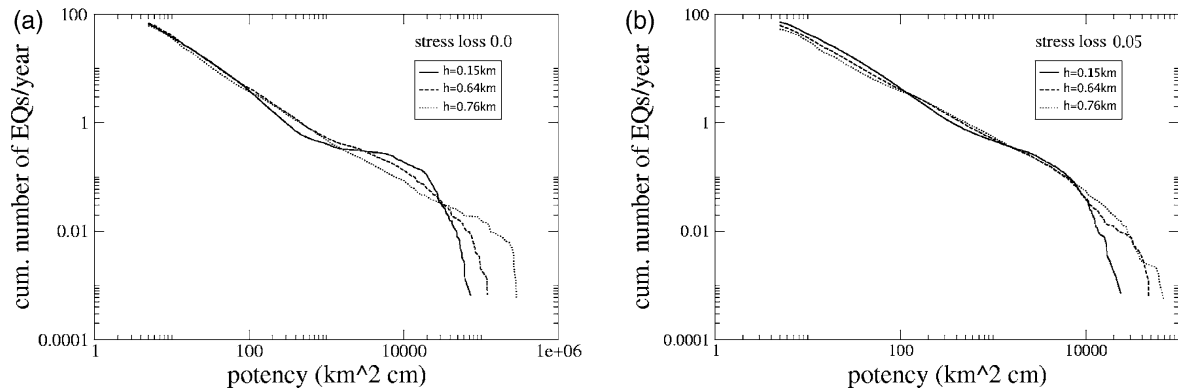


Figure 4

Cumulative frequency-size distributions for RW heterogeneities with different values of  $h$  (Eq. (10)) given in Figure 2.

$h$ -values representing many low stress drop patches on a fault which has a WROSS, lead to a Gutenberg-Richter distribution with a broader region of power-law scaling. If the number of barriers is increased further, the frequency-size distribution will again show a tendency towards characteristic earthquake behavior, because the barriers will begin to form continuous patches. Consequently, the roles of barriers and surrounding environment will be exchanged and the fault will consist of low stress drop barriers in a high stress drop environment. For physical cases with a finite size, the parameter  $h$  can only be considered in certain parts of the interval  $[0; h_{\max}]$ . The fault with the dimensions shown in Figure 1 and  $128 \times 32$  cells has a value of  $h_{\max} \approx 0.76$  km, while for a fault with  $256 \times 32$  cells and  $140 \text{ km} \times 17.5 \text{ km}$   $h_{\max} \approx 0.84$  km. The frequency-size distribution for the latter case (Figure 5) is qualitatively similar to the distribution of the smaller fault, with the difference that a broader range of heterogeneities is covered. The results for  $h = 0.84$  km show power-law statistics over the entire range of event sizes.

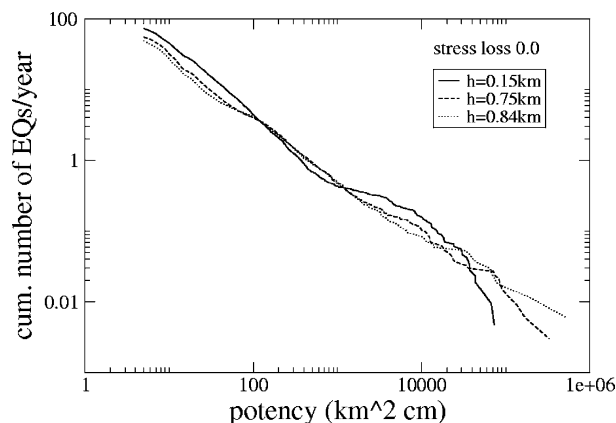


Figure 5

Cumulative frequency-size distributions for RW heterogeneities with different degrees of disorder on a large fault ( $256 \times 32$  cells corresponding to a fault of  $140 \text{ km}$  length and  $17.5 \text{ km}$  depth).

If a stress loss  $\gamma > 0$  is introduced, the frequency-size distributions for different values of  $h$  become more similar to each other (Fig. 4(b)) in agreement with previous observations of DAHMEN *et al.* (1998) and ZÖLLER *et al.* (2004).

The frequency-size distributions for the different cases with fractal dimensions and  $\gamma = 0$  are shown in Figure 6(a). It is seen that the fractal dimension does not provide an effective tuning parameter for the frequency-size distribution. The effect of positive  $\gamma$  is again to make the frequency-size distributions more Gutenberg-Richter like and more similar to each other (Fig. 6(b)).

Figures 7(a) and 7(b) show earthquake sequences (rupture area vs. time) for two realizations of model RW, while Figures 7(c) and 7(d) give similar results for model F. The time series suggest that model RW allows a greater variability of the temporal behavior in terms of the tuning parameter  $h$ . The results for model F show an increased occurrence rate for earthquakes with area  $A \approx 700$  cells. We note again that model F represents a smoother fault than model RW, and it has a continuous distribution of stress drops in the range  $1 \text{ MPa} \leq \Delta\tau \leq 9 \text{ MPa}$ . This leads to large-scale patches which have their own “characteristic events.”

The clustering properties of the simulation results can be quantified with the ratio  $\mu/\sigma$  of interevent times between large events, where  $\mu$  and  $\sigma$  are the mean value and standard deviation, respectively. For clustered seismicity  $\mu/\sigma < 1$ , whereas for quasi-periodic occurrence of events  $\mu/\sigma > 1$ . The case  $\mu/\sigma = 1$  corresponds to a Poisson process. Table 1 shows  $\mu/\sigma$  values for the  $N$  largest earthquakes in models RW and F with  $\gamma = 0$  and different values of the degree of spatial disorder measured by  $h$  and  $D$ . Each value of  $N$  corresponds to a magnitude condition  $M \geq M_{\text{cut}}$ , where  $M_{\text{cut}}$  varies slightly for different values of  $h$  and  $D$ . The approximate value of  $M_{\text{cut}}$  is also given in the table. The relation between potency  $P$  and magnitude  $M$  is given by  $M = (2/3) \log P + 3.6$  (BEN-ZION and RICE, 1993). For  $N = 100 (M_{\text{cut}} \approx 6.5)$  and  $N = 1000 (M_{\text{cut}} \approx 5.6)$ , model RW shows a decrease of  $\mu/\sigma$  with increasing  $h$ . In other

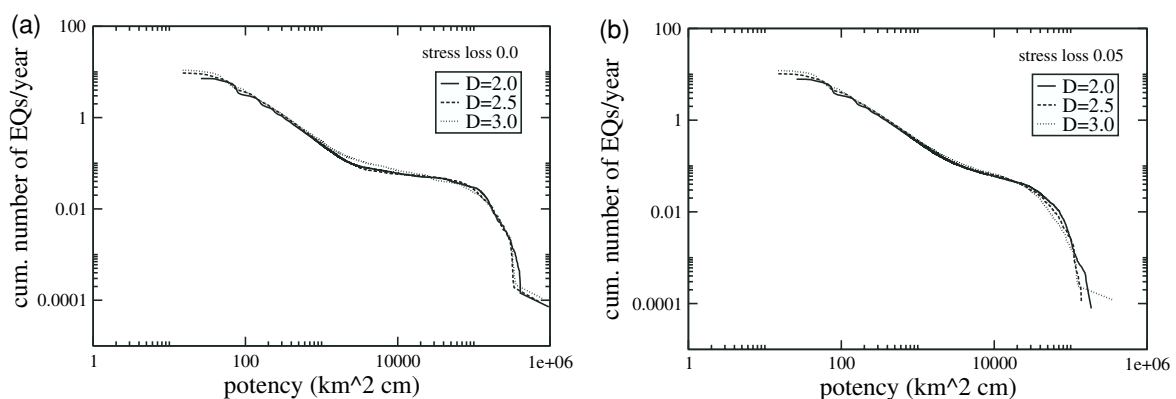


Figure 6  
Cumulative frequency-size distributions for fractal heterogeneities with different fractal dimensions  $D$  given in Figure 3.

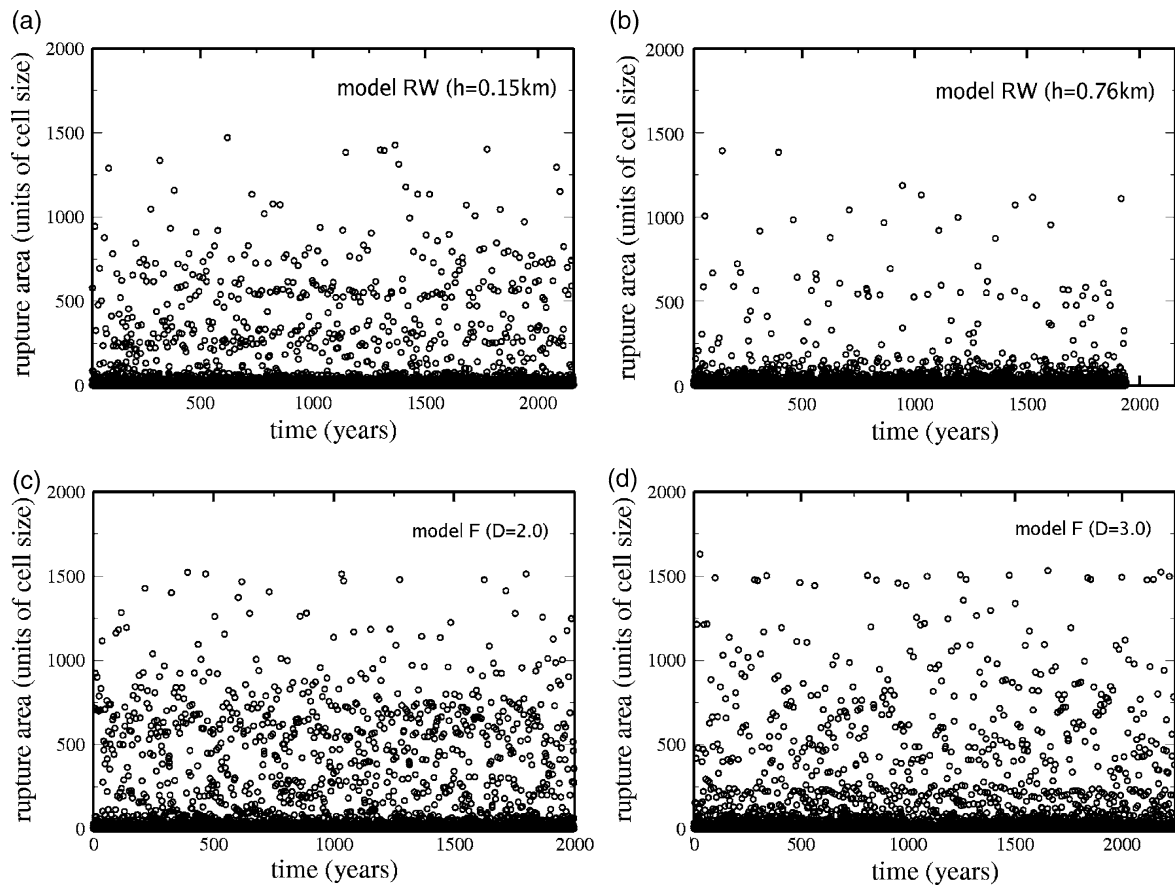


Figure 7

Earthquake sequences (rupture area vs. time) for four simulations with  $10^6$  events. Panels (a) and (b) correspond to model RW (Figs. 2(a) and (c)); panels (c) and (d) correspond to model F (Figs. 3(a) and (c)).

words, for cases with RW heterogeneities and increasing range of size scales, the temporal behavior changes from a quasi-periodic occurrence of large events toward a random/clustered behavior. For smaller values of  $M_{\text{cut}}$ ,  $\mu/\sigma$  is almost constant and corresponds to random/clustered statistics. This result is supported by the values of  $\mu/\sigma$  for the highest degree of disorder ( $h = 0.84$  km) on the large fault ( $140 \text{ km} \times 17.5 \text{ km}$ ), which are also given in Tab. 1. In contrast, model F has no systematic dependence of  $\mu/\sigma$  on the fractal dimension  $D$ . These observations support our assertion that the distribution type RW is more efficient for tuning the dynamics with a single heterogeneity parameter.

ZÖLLER *et al.* (2004) have shown that high stress fluctuations occurring along cell boundaries on a heterogeneous fault can cause a spontaneous mode-switching between a Gutenberg-Richter and a characteristic earthquake distribution (DAHMEN *et al.*, 1998; BEN-ZION *et al.*, 1999; WEATHERLEY *et al.*, 2002). Although the type of distribution does not change in the simulations leading to Figure 7, the results (especially those for model RW) have time periods with clearly different maximum magnitudes. This has a similar origin to the mode-switching: strong stress fluctuations sometimes lead to a spontaneous synchronization or desynchronization

Table 1

The ratio  $\mu/\sigma$  for different model realizations with  $\gamma = 0$ , where  $\mu$  is the mean value of interevent times calculated for earthquakes with magnitudes  $M \geq M_{\text{cut}}$  and  $\sigma$  is the corresponding standard deviation. For statistical reasons, a fixed number  $N$  of earthquakes with  $M \geq M_{\text{cut}}$  is used. The approximate value of  $M_{\text{cut}}$  corresponding to  $N$  is given in parentheses. The case RWL represents the large fault (140 km  $\times$  17.5 km) with the highest degree of disorder. In this case, the catalog contains only 16,000 events. Therefore, the value in the last line is given in parentheses

model  $N$	RW			RWL		F	
	$h = 0.15$ km	$h = 0.64$ km	$h = 0.76$ km	$h = 0.84$ km	$D = 2.0$	$D = 2.5$	$D = 3.0$
100 ( $M_{\text{cut}} \approx 6.5$ )	1.664	1.566	1.402	1.200	1.508	1.232	1.845
1000 ( $M_{\text{cut}} \approx 5.6$ )	1.480	1.180	0.990	1.005	0.869	0.790	0.826
10000 ( $M_{\text{cut}} \approx 4.9$ )	0.907	0.989	0.968	0.948	0.883	0.832	0.911
100000 ( $M_{\text{cut}} \approx 4.0$ )	0.960	0.970	0.969	(0.938)	0.882	0.835	0.911

of a large number of cells resulting in an increase or decrease of the maximum magnitude.

The observations discussed above indicate that the relevant parameter of the heterogeneities is the range of size scales (ROSS) introduced in Section 2.3, which is measured by  $h$ . The patches that contribute to different ROSS have to be separated by strong localized barriers, otherwise the rupture can easily jump the barriers. This is the case for fractal heterogeneities with small standard deviation. Therefore, model F requires two parameters to tune the fault towards NROSS or WROSS, as discussed in Section 2.3. Model RW needs only one parameter to control the ROSS, and it is probably also closer to natural faults due to the existence of near-vertical fault offsets. We conclude that model RW gives a better performance of both the ability to tune effectively the level of fault heterogeneities and the relation between model simulations and natural seismicity.

The results of the simulations with heterogeneous faults can be summarized in a phase diagram. According to the results of Figures 4–7, the parameter  $h$  represents a third dimension in addition to the stress loss  $\gamma$  and the dynamic weakening  $\varepsilon$ . Figure 8(a) shows a projection of the 3-D phase diagram onto the plane  $\gamma = 0$  and Figure 8(b) gives a similar projection for  $\varepsilon = \text{constant}$ . As discussed by BEN-ZION *et al.* (1999), DAHMEN *et al.* (1998), and FISHER *et al.* (1997), cases with  $\varepsilon = 0$  and  $\gamma = 0$  represent a critical point of a phase transition in the 2-D phase diagram. To illustrate the difference between purely static friction ( $\varepsilon = 0$ ) and the static-kinetic friction ( $\varepsilon > 0$ ), two frequency-size distributions are shown in Figure 9, one for  $\varepsilon = 0$  (for all cells) and another for  $\langle \varepsilon \rangle = 0.02$ . Both are calculated on a fault with heterogeneities according to Figure 2(a). As discussed in Section 2.2, a heterogeneous fault includes space-dependent dynamic weakening coefficients  $\varepsilon$ , because of varying stress drops  $\Delta\tau$  and constant dynamic overshoot  $DOS$ . Therefore, the value of  $\varepsilon$  in the phase diagram (Fig. 8) should be understood as a mean value. The frequency-size distribution for  $\varepsilon = 0$  follows a Gutenberg-Richter behavior tapered by finite-size

effects, while  $\varepsilon > 0$  leads to a characteristic earthquake distribution. The precise structure of the phase diagrams of Figure 8 should be clarified in a future work.

### 3.2. Investigation of Rupture Histories

In contrast to the earlier quasi-static version of the model (e.g., BEN-ZION, 1996), the present quasi-dynamic model simulates the spatio-temporal evolution of stress and slip with a finite propagation velocity  $v_s$ . This allows us to study general properties of rupture histories for single earthquakes, in particular events which rupture large parts of the fault. It can be expected that quenched heterogeneities significantly influence the stress propagation, especially if high stress drop barriers are included. As pointed out in Section 2.1, the creep mechanism already creates some quenched spatial heterogeneities, because the mixture of brittle and ductile processes produces heterogeneous effective rheology. Therefore, we compare rupture histories of two extreme cases in this section: (1) A fault *without* creep motion and uniformly distributed brittle properties:  $\tau_s = 10$  MPa,  $\Delta\tau = 1$  MPa +  $ran \cdot 8$  MPa, where  $ran$  is a uniformly distributed random number between 0 and 1. (2) A fault with creep motion and heterogeneous brittle properties according to Figure 2(b). Both simulations start with randomly distributed initial stresses  $\tau \in [\tau_a; \tau_s]$ .

Figures 10 and 11 show snapshots from rupture histories of mainshocks in both models described above. While Figure 10 corresponds to a system-wide event with area  $A = 4096$  cells, the rupture area in Figure 11 is smaller having  $A = 2093$  cells. Both events were recorded after the model had evolved for some 1000's of years. The gray scaled boxes show the dimensionless stress  $\hat{\tau} = (\tau - \tau_a)/(\tau_s - \tau_a)$ , which is 1 for

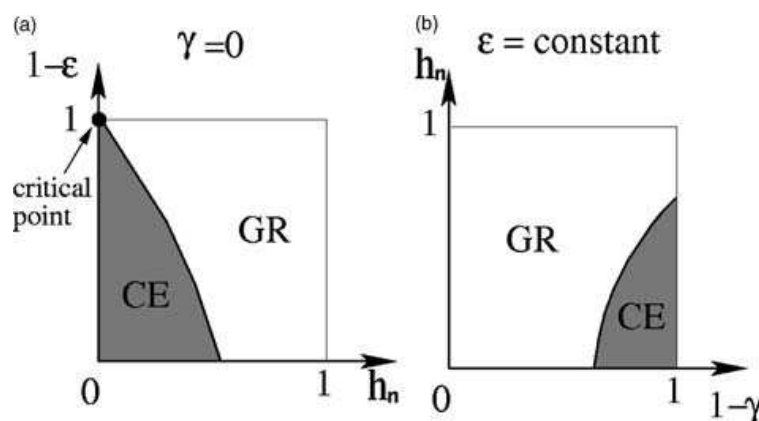


Figure 8

Projections of the 3-D schematic phase diagrams for  $\gamma = 0$  (panel (a)) and  $\varepsilon = \text{constant}$  (panel (b)). The value  $h_n = h/h_{\max}$  denotes the heterogeneity parameter normalized to the interval  $[0; 1]$ . CE denotes the characteristic earthquake distribution and GR the Gutenberg-Richter distribution. Note that  $\varepsilon$  represents the mean value of the dynamic weakening coefficient over the fault; due to a constant dynamic overshoot  $DOS = 1.25$  and space-dependent stress drops (see Figs. 2 and 3),  $\varepsilon$  is also space-dependent. The finite-size effects at  $h_n \approx 1$  (see text) are not taken into account here; that is, the phase diagram is assumed to represent a fault of infinite size.

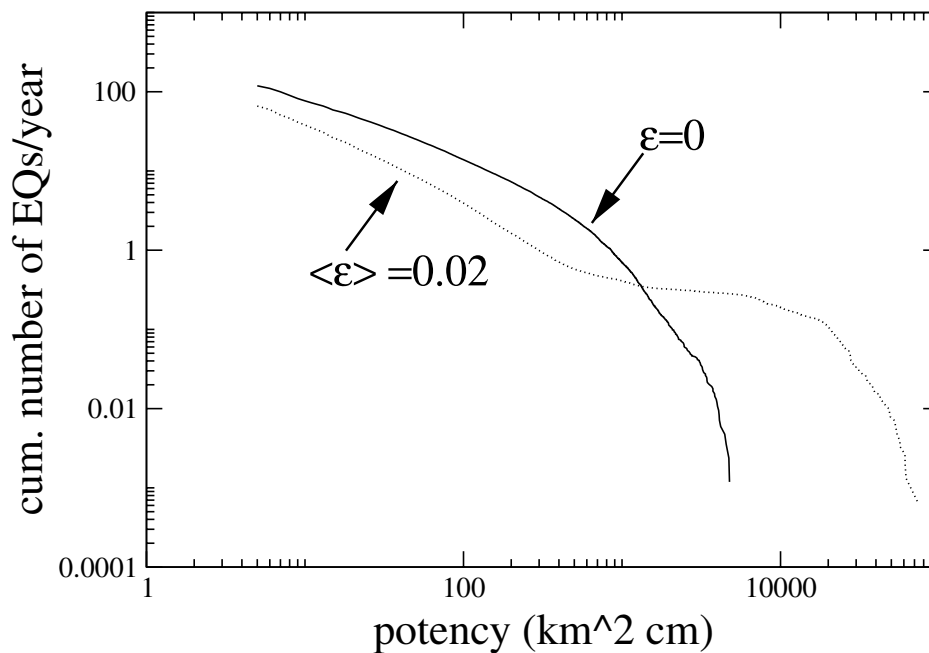


Figure 9

Comparison of frequency-size distributions for a model at the critical point  $C$  ( $\gamma = \varepsilon = 0$ , solid line) and a noncritical model realization with finite  $\varepsilon$  (dashed line). Note that the presence of heterogeneities (here according to Figure 2(a)) leads to space-dependent dynamic weakening.

a critical cell (light color) and 0 for a the lowest stress value  $\tau_a$  (dark color). It is remarkable that the situation on the homogeneous fault before the occurrence of a large earthquake has evolved to clearly defined patches with highly loaded boundaries (Fig. 10). The mainshock is initiated at a boundary of a patch and propagates from the boundary inward. After the system-wide event, the plate motion reloads the fault and the stress evolves to form new similar spatial patterns. In an intermediate size earthquake, not all patches are ruptured. This behavior is similar to a rupture scenario of “double encircling pincers,” which have been found by DAS and KOSTROV (1983) in a dynamic fault model with a circular asperity. However, DAS and KOSTROV (1983) observe an almost isotropic propagation inward, while the patches in our model are mostly ruptured from a preferred direction.

A completely different scenario is observed in the highly heterogeneous model with creep motion. The stress field before a mainshock has no obvious regularity, except the brittle-ductile transition (here at about 15 km depth), which is responsible for the stable sliding of the deep cells. After the first large self-organized patch is ruptured from the hypocenter in Figures 11(a) and 11(b), a barrier at about 15 km along strike is jumped and the next patch is ruptured. Due to the irregular stress field and long-range interaction, different regions of the fault can be ruptured simultaneously, e.g., in Figure 11(c) a new patch at the right boundary of the fault is created while the rupture adjacent to the hypocenter continues to evolve. This is in contrast to the smooth fault, where most of the patches are ruptured almost sequentially. The



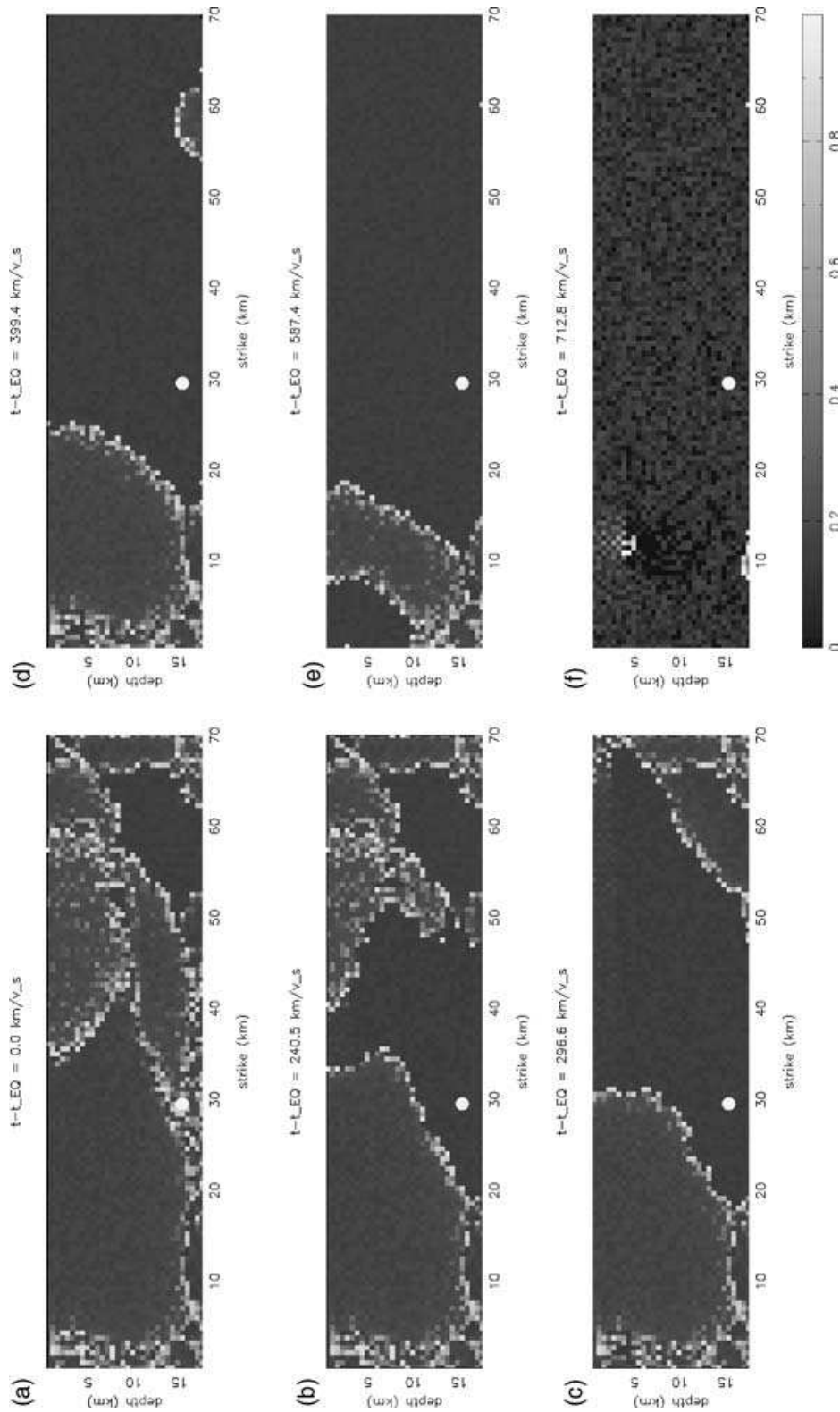


Figure 10

Snapshots of rupture evolution for a system-wide event on a smooth fault without creep motion.  $t - t_{EO}$  denotes the time after the rupture initiation and depends on the choice of the shear wave velocity  $v_s$ . The filled white circle is the hypocenter of the event. The figure shows the dimensionless stress state  $\hat{\tau} = \frac{\tau - \tau_a}{\tau_s - \tau_a}$  of the cells.

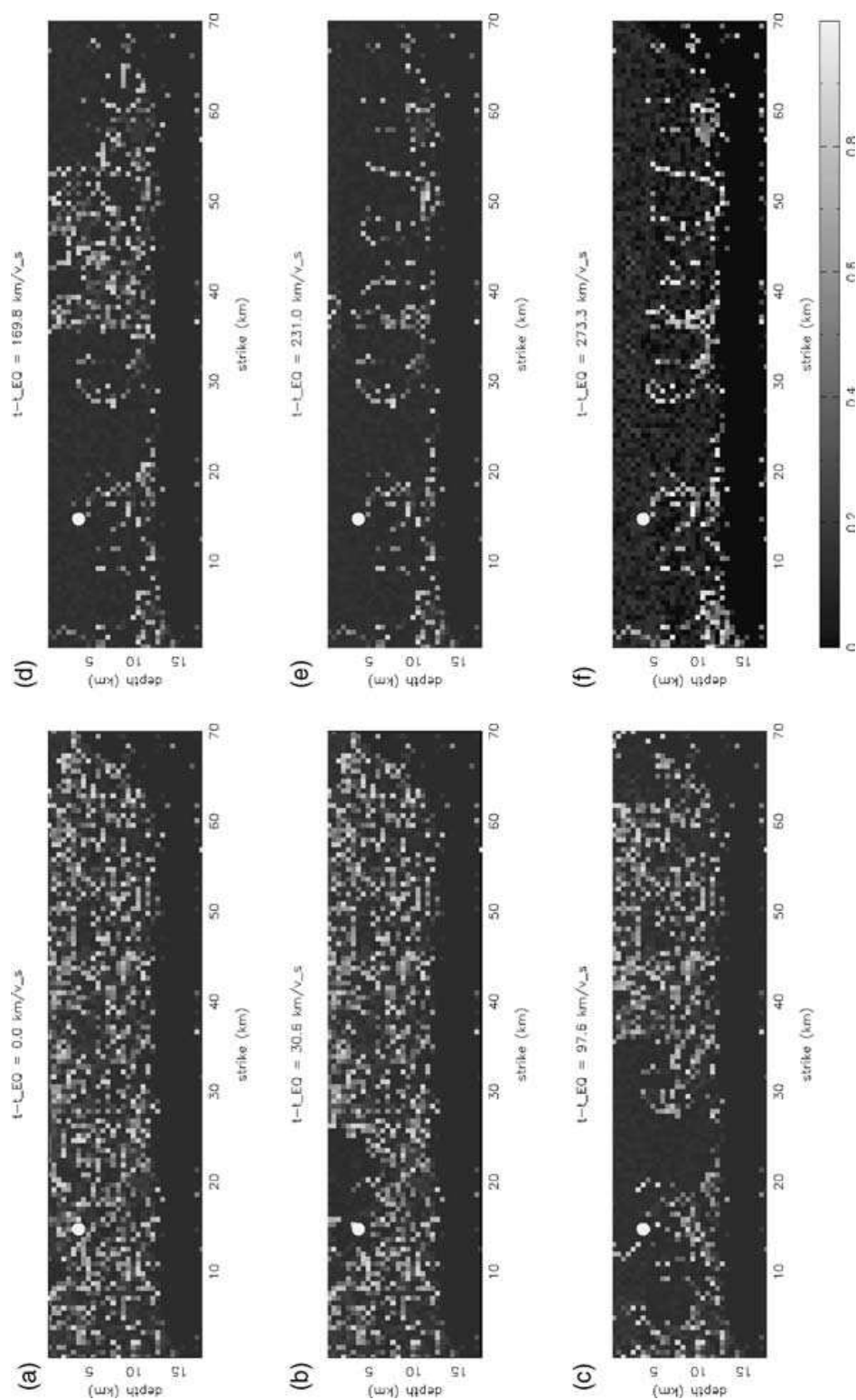


Figure 11

Same as Figure 10 for a fault with heterogeneities according to 2(b) with a brittle-ductile transition at about 15 km depth.

overall rupture propagation on the heterogeneous fault is relatively slow, because some cells undergo multiple slips due to the heterogeneous distribution of stress drops and slow the rupture process. During the rupture and especially at the end, quasi-vertical stress patterns are created from time to time, e.g. in Figure 11(e) and 11(f). These patterns reflect the high stress drop barriers in Figure 2(b). At the end of the mainshock, the fault is almost unloaded between these near-vertical barriers. A highly irregular rupture history similar in some respects to the results of Figure 11, was observed during the Chi-Chi (Taiwan) earthquake on September 21, 1999 ( $M_w = 7.6$ ) (SHIN and TENG, 2001).

Finally, we show in Figure 12 three snapshots of a model at the critical point  $\varepsilon = 0$ ,  $\gamma = 0$  (see Fig. 8(a)). The snapshots were taken before, during and after a large event with area  $A = 2199$  cells. The only difference from the smooth model leading to Figure 10 is the choice of a purely static friction ( $\tau_d = \tau_s$ ) instead of static-kinetic friction. Despite the high degree of smoothness of brittle parameters, the stress field has no obvious structure and the rupture consists of a sequence of almost uncorrelated cell slips. This is in agreement with the analytical results of FISHER

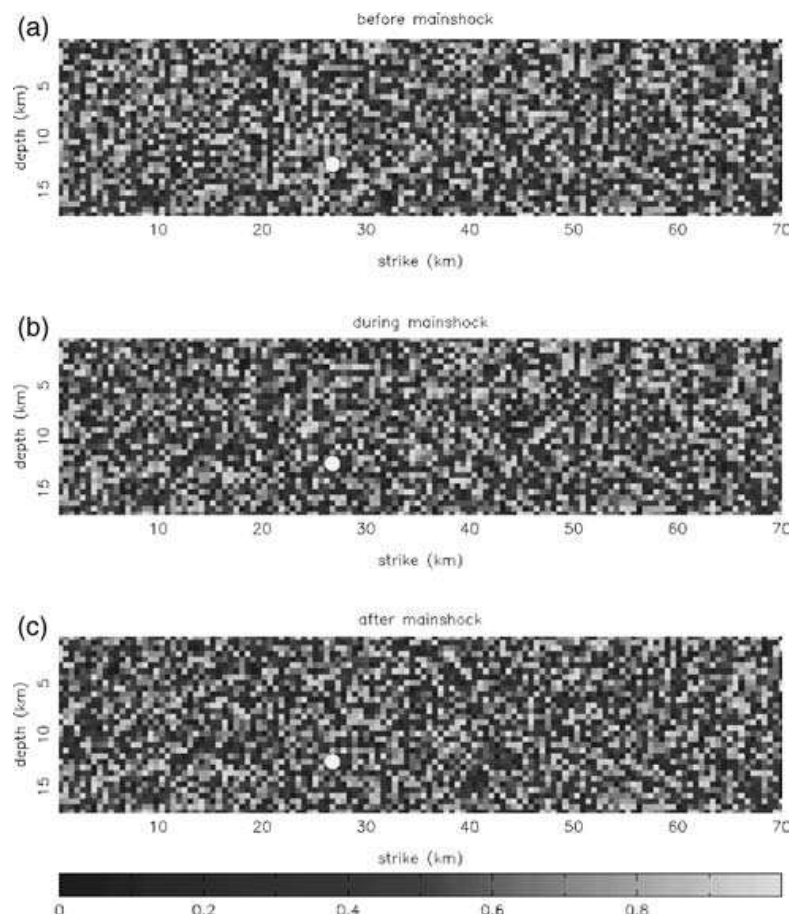


Figure 12

Same as Figure 10 for purely static friction ( $\tau_s = \tau_d$ ) corresponding to the critical point in Figure 8(a): normalized stress field before (panel (a)), during (panel (b)), and after (panel (c)) a mainshock with area  $A = 2199$  cells).

*et al.* (1997) and similar in some respects to the simulations of Figure 11. As shown in Figure 9, the frequency-size statistics for  $\varepsilon = 0$ ,  $\gamma = 0$  follow the Gutenberg-Richter law without the enhanced occurrence of large events.

#### 4. Discussion and Conclusions

We have investigated the effect of quenched spatial heterogeneities in a quasi-dynamic version of a discrete strike-slip fault in a 3-D elastic half space (BEN-ZION, 1996, BEN-ZION and RICE, 1993; ZÖLLER *et al.*, 2004). The calculations employed two types of heterogeneities: 1. near-vertical barriers of high brittle stress drop embedded in a fault with low brittle stress drop (RW) and 2. power-law stress drop distributions (F). The former type probably provides a closer representation of natural faults because it simulates fault offsets which are common geological features (WESNOUSKY 1994; BEN-ZION and SAMMIS, 2003). Both types of heterogeneities can be tuned with respect to the degree of spatial complexity between the two end-member cases of a smooth fault (few barriers/low fractal dimension) and a rough fault (many barriers/high fractal dimension). However, large variations in the parameters of model F produce a small effect on the obtained earthquake behavior.

The results indicate that the degree of spatial disorder can act as a tuning parameter for the earthquake dynamics. Smooth faults are governed by characteristic earthquake behavior, connected slip areas and cyclic components in various time histories like potency release. In contrast, seismicity on rough faults is characterized by a Gutenberg-Richter law, disconnected slip areas and fractal-like time histories. FISHER *et al.* (1997), DAHMEN *et al.* (1998), and BEN-ZION *et al.* (2003) showed with related quasi-static models that similar differences exist on these and other earthquake quantities as the dynamic weakening parameter  $\varepsilon$  moves toward or away from a critical values ( $\varepsilon = 0$ ).

Although  $h$  may act as a tuning parameter for the heterogeneities, the results suggest that the basic underlying physical quantity is the range of size scales (ROSS) that characterizes the heterogeneities. This is clear in the case of the RW heterogeneities. If an earthquake is initiated in a cell with a low brittle stress drop, the rupture can propagate easily until a high stress drop barrier is reached. Then the barrier can overcome the stress concentration at the rupture front with some probability. On the other hand, if an earthquake starts in one of the barriers, it is likely that the adjacent low stress drop regions will be ruptured, resulting in a large event. Therefore, the low and intermediate events will organize in the patches between the barriers. Consequently, a large range of size scales of such patches will result in a Gutenberg-Richter law, and a narrow range will favor characteristic events. Thus the ROSS of the heterogeneities is the key property controlling the frequency-size distribution as suggested by BEN-ZION and RICE (1995), BEN-ZION

(1996), and BEN-ZION *et al.* (2003). A narrow range of size scales (NROSS) leads to characteristic earthquake behavior, while a wide range of size scales (WROSS) results in a Gutenberg-Richter distribution.

This behavior is also somewhat valid in a weaker form for the power-law stress drop distribution, where in this case the fault is overall smoother due to the continuous distribution of stress drops in contrast to the sharp bimodal distribution of the RW heterogeneities. The comparison of the two types of heterogeneities unveils the relevance of an additional tuning parameter in model F, the standard deviation of the stress drops. If this range of values is small, a rupture can easily jump heterogeneities, although the degree of spatial disorder may be high. This occurs for power-law distributions of the stress drop due to the continuous range of values. Therefore power-law distributions require two tuning parameters, the fractal dimension and the standard deviation in order to tune the heterogeneities between NROSS and WROSS. The RW model needs only the tuning parameter  $h$  for this aim, because the almost discontinuous shape of the barriers defines the patches where ruptures can propagate.

A qualitative analysis of rupture histories of mainshocks in the case of faults with low and high degrees of disorder reveals clear differences in the spatio-temporal evolution of stress. On smooth faults, the stress field organizes itself into large patches with highly loaded boundaries. A mainshock starts at one of the boundaries and ruptures a patch in the inward direction. For a system-wide event all patches are ruptured more-or-less in series. This highly organized pattern formation vanishes if the static-kinetic friction is replaced by a purely static friction ( $\tau_d = \tau_s$ ). Assuming full stress conservation during rupture ( $\gamma = 0$ ), this case represents a critical point in the phase diagram Figure 8(a), where no system-wide event occurs. If dynamic weakening is switched on ( $\varepsilon > 0$ ), earthquakes bigger than a certain size become unstoppable (BEN-ZION and RICE, 1993; DAHMEN *et al.*, 1998), unless the fault heterogeneities have a WROSS. In the latter case, the stress field before a mainshock is highly irregular also for a finite dynamic weakening ( $\varepsilon > 0$ ) without large self-organized patches. The rupture propagates simultaneously in several regions and is slowed down or terminated if a barrier is reached.

A shortcoming of our simulations that should be addressed in future studies is the effect of finite size of the fault, which limits the range of  $h$  values. A more efficient design of the computer code will provide a possibility perform parameter space studies on a larger fault and quantify more clearly the role of the heterogeneities on earthquake dynamics. The results of this paper indicate that heterogeneities have dramatic effects on the spatio-temporal evolution of rupture histories and earthquake statistics. These effects should be clarified further with more detailed analyses, e.g., by using stress and seismicity functions of the type employed by BEN-ZION *et al.* (2003). Another interesting problem for future studies is a joint theoretical-observational work involving tuning the model parameters to specific fault zones (e.g., the Parkfield section of the San Andreas fault). Large

statistically-complete data sets of simulated slip histories and events statistics for various cases of such tuned models may provide important input for models of seismic hazard assessment.

### *Acknowledgments*

This work was supported by the collaborative research center “Complex Nonlinear Processes” (SFB555) of the “German Research Society” (DFG). YBZ acknowledges support from a Mercator fellowship of the DFG. The manuscript benefited from comments by two anonymous referees and Ramón Zúñiga.

### REFERENCES

- BEN-ZION, Y. (1996), *Stress, slip, and Earthquakes in Models of Complex Single-fault Systems Incorporating Brittle and Creep Deformations*, J. Geophys. Res. 101, 5677–5706.
- BEN-ZION, Y. (2001), *Dynamic Rupture in Recent Models of Earthquake Faults*, J. Mech. Phys. Solids 49, 2209–2244.
- BEN-ZION, Y. (2003), *Key Formulas in Earthquake Seismology*, International Handbook of Earthquake and Engineering Seismology, Part B, 1857–1875.
- BEN-ZION, Y., DAHMEN, K., LYAKHOVSKY, V., ERTAS, D., and AGNON, A. (1999), *Self-driven Mode Switching of earthquake activity on a fault system*, Earth and Plan. Sci. Lett., 172, 11–21.
- BEN-ZION, Y., M. ENEVA, and LIU, Y. (2003), *Large Earthquake Cycles and Intermittent Criticality on Heterogeneous Faults due to Evolving Stress and Seismicity*, J. Geophys. Res. 108, doi 10.292002JB002121.
- BEN-ZION, Y. and RICE, J. R. (1993), *Earthquake Failure Sequences along a Cellular Fault Zone in a Three-dimensional Elastic Solid Containing Asperity and Nonasperity Regions*, J. Geophys. Res. 98, 14,109–14,131.
- BEN-ZION, Y. and RICE, J. R. (1995), *Slip Patterns and Earthquake Populations along Different Classes of Faults in Elastic Solids*, J. Geophys. Res. 100, 12,959–12,983.
- BEN-ZION, Y. and RICE, J. R. (1997), *Dynamic Simulations of Slip on a Smooth Fault in an Elastic Solid*, J. Geophys. Res. 102, 17,771–17,784.
- BEN-ZION, Y. and SAMMIS, C. G. (2003), *Characterization of fault zones*, Pure Appl. Geophys, 160, 677–715.
- BINNEY, J. J., DOWRICK, N. J., FISHER, A. J., and NEWMAN, M. E. J. *The Theory of Critical Phenomena* (Oxford University Press 1993).
- CHINNERY, M. (1963), *The Stress Changes that Accompany Strike-slip Faulting*, Bull. Seismol. Soc. Am. 53, 921–932.
- DAHMEN, K., ERTAS, D., and BEN-ZION, R. (1998), *Gutenberg-Richter and Characteristic Earthquake Behavior in Simple Mean-field Models of Heterogeneous Faults*, Phys. Rev. E 58, 1494–1501.
- DAS, S. and KOSTROV, B. V. (1983), *Breaking of a Single Asperity-rupture Process and Seismic Radiation*, J. Geophys. Res. 88, 4277–4288.
- FISHER, D. S., DAHMEN, K., RAMANATHAN, S., and BEN-ZION, Y. (1997), *Statistics of Earthquakes in Simple Models of Heterogeneous Faults*, Phys. Rev. Lett. 78, 4885–4888.
- GUTENBERG, G. and RICHTER, C. F. (1956), *Earthquake Magnitude, Intensity, Energy and Acceleration*, Bull. Seismol. Soc. Am. 46, 105–145.
- HAINZL, S. and ZÖLLER, G. (2001), *The Role of Disorder and Stress Concentration in Nonconservative Fault Systems*, Physica A 294, 67–84.
- HAINZL, S., ZÖLLER, G., and KURTHS, J. (1999), *Similar Power Laws for Fore- and Aftershock Sequences in a Spring-block Model for Earthquakes*, J. Geophys. Res. 104, 7243–7253.

- HEIMPEL, M. H. (2003), *Characteristic Scales of Earthquake Rupture from Numerical Models*, *Nonlin. Proc. Geophys.* 10, 573–584.
- LOMNITZ-ADLER, J. (1999), *Automaton Models of Seismic Fracture: Constraints Imposed by the Magnitude-frequency Relation*, *J. Geophys. Res.* 98, 17,745–17,756.
- MADARIAGA, R. (1976), *Dynamics of an Expanding Circular Fault*, *Bull. Seismol. Soc. Am.* 66 639–666.
- MEHTA, A. P., DAHMEN, K. A., and BEN-ZION, Y. (2005), *From Magnets to Earthquakes: Universal Mean Moment Rate Profiles of Earthquake Ruptures*, submitted to *Phys. Rev. Lett.*
- ROBINSON, R., and BENITES, R. (2001), *Upgrading a Synthetic Seismicity Model for More Realistic Fault Ruptures*, *Geophys. Res. Lett.* 28, 1843–1846.
- SHIN T.C., TENG T.L. (2001), *An Overview of the 1999 Chi-Chi, Taiwan, Earthquake*, *Bull. Seismol. Soc. Am.* 91, 895–913.
- STEACY, S. J. and MCCLOSKEY, J. (1999), *Heterogeneity and the Earthquake Magnitude-frequency Distribution*, *Geophys. Res. Lett.* 26, 899–902.
- STIRLING, M. W., WESNOUSKY, S. G., and SHIMAZAKI, K. (1996), *Fault Trace Complexity, Cumulative Slip, and the Shape of the Magnitude-frequency Distribution for Strike-slip Faults: A Global Survey*, *Geophys. J. Int.* 126, 301–301.
- TURCOTTE, D. L. *Fractals and Chaos in Geology and geophysics* (Cambridge University Press, New York 1997).
- UTSU, T. (2002), *Statistical Features of Seismicity*, *International Handbook of Earthquake and Engineering Seismology, Part B*, 719–732.
- WEATHERLEY, D., MORA, P., and XIA, M. F. (2002), *Long-range Automaton Models of Earthquakes: Power-law Accelerations, Correlation Evolution, and Mode-switching*, *Pure Appl. Geophys.* 159, 2469–2490.
- WEASNOUSKY, S. G. (1994), *The Gutenberg-Richter or Characteristic Earthquake Distribution, which is it?*, *Bull. Seismol. Soc. Am.* 84, 1940–1959.
- WILSON, K. G. (1979), *Problems in Physics with Many Scales of Length*, *Scientific American* 241, 158–179.
- WYSS, M., SCHORLEMMER, D., and WIEMER, S. (2000), *Mapping Asperities by Minima of Local Recurrence Time: San Jacinto-Elsinore Fault Zones*, *J. Geophys. Res.* 105, 7829–7844.
- ZÖLLER, G., HOLSCHNEIDER, M., and BEN-ZION, Y. (2004), *Quasi-static and Quasi-dynamic Modeling of Earthquake Failure at Intermediate Scales*, *Pure Appl. Geophys.* 161, 2103–2118.

(Received December 12, 2003, accepted August 14, 2004)



To access this journal online:  
<http://www.birkhauser.ch>

---

# Appendix M

## Aftershocks resulting from creeping sections in a heterogeneous fault

Autors: G. Zöller, S. Hainzl, M. Holschneider, and Y. Ben-Zion  
Journal: Geophysical Research Letters  
Volume (Nr.): **32(3)**  
Article/doi: art. no. L03308, doi 10.1029/2004GL021871  
Year: 2005



## Aftershocks resulting from creeping sections in a heterogeneous fault

G. Zöller,<sup>1</sup> S. Hainzl,<sup>2</sup> M. Holschneider,<sup>3</sup> and Y. Ben-Zion<sup>4</sup>

Received 29 October 2004; revised 6 January 2005; accepted 11 January 2005; published 10 February 2005.

[1] We show that realistic aftershock sequences with space-time characteristics compatible with observations are generated by a model consisting of brittle fault segments separated by creeping zones. The dynamics of the brittle regions is governed by static/kinetic friction, 3D elastic stress transfer and small creep deformation. The creeping parts are characterized by high ongoing creep velocities. These regions store stress during earthquake failures and then release it in the interseismic periods. The resulting postseismic deformation leads to aftershock sequences following the modified Omori law. The ratio of creep coefficients in the brittle and creeping sections determines the duration of the postseismic transients and the exponent  $p$  of the modified Omori law. **Citation:** Zöller, G., S. Hainzl, M. Holschneider, and Y. Ben-Zion (2005), Aftershocks resulting from creeping sections in a heterogeneous fault, *Geophys. Res. Lett.*, 32, L03308, doi:10.1029/2004GL021871.

### 1. Introduction

[2] The occurrence of aftershock sequences is one of the most general patterns of observed seismicity. The temporal decay rate  $\dot{n}(t)$  of the number of aftershocks is found to follow the modified Omori law [Omori, 1894; Utsu *et al.*, 1995]

$$\dot{n}(t) = (c + t - t_M)^{-p}, \quad (1)$$

where  $t_M$  is the occurrence time of the mainshock and the exponent  $p$  is close to 1 for observed seismicity.

[3] Many models were used to explain the frequency-magnitude distribution of observed seismicity [e.g., Burridge and Knopoff, 1967; Bak and Tang, 1989; Dahmen *et al.*, 1998]. In these models dealing solely with coseismic stress transfers and tectonic loading, aftershocks are not observed, unless the stress transfer on the fault becomes very weak. However, in such a case, the  $p$  value of the Omori law is unrealistically low [Hergarten and Neugebauer, 2002].

[4] Various mechanisms were proposed to explain the generation of aftershock sequences. These include viscoelastic relaxation in the fault zone [Dieterich, 1972; Hainzl *et al.*, 1999], fault strengthening or weakening after a block slips [Ito and Matsuzaki, 1990], pore fluid flow [Nur and Booker, 1972], rate-state friction [Dieterich, 1994], and damage

rheology [Ben-Zion and Lyakhovskiy, 2003; Shcherbakov and Turcotte, 2004]. While these mechanisms are based on time-dependent processes, Hainzl *et al.* [2003] have shown that foreshocks and aftershocks can also be explained by spatial effects, namely a decrease of strength localized at the edges of the rupture area. Some of the proposed models are, however, conceptual and it remains an open question whether these mechanisms can explain detailed observations of space-time earthquake clustering in natural fault systems.

[5] Empirical observations show that aftershocks are concentrated near the margin of fault areas where large coseismic displacements occur [Utsu, 2002], and partly on adjacent segments. A full numerical treatment of systems of segmented faults with realistic stress transfer requires very large computational effort. In the present work, we overcome this difficulty by using a fault plane that is divided by near-vertical aseismic barriers into separate segments. The aseismic barriers can undergo postseismic creep deformation and thus transfer stress from one fault segment to another. The presence of coseismic, postseismic and interseismic creep is now commonly observed by means of InSAR and other geodetic measurements [e.g., Lyons and Sandwell, 2003]. Numerous studies show that fault segments, e.g., along the San Andreas fault, can store stress and remain locked for certain periods, while other less brittle segments undergo a steady creep deformation [Bürgmann *et al.*, 2000].

[6] The model used in the present work is based on earlier works of Ben-Zion [1996] and Zöller *et al.* [2004, 2005] with a heterogeneous strike-slip fault in an elastic half-space. Various model ingredients, including the laws for brittle and creep deformation, stress transfer, and boundary conditions, are compatible with empirical knowledge. The simulations cover hundreds of years and allow us to reproduce brittle deformation as well as postseismic and interseismic creep deformation. The results indicate that a spatially heterogeneous distribution of brittle and creeping fault sections leads to realistic aftershock sequences compatible with observed data. We note that the assumed creeping barriers provide an effective way of parameterizing macroscopically a variety of physical processes including viscous relaxation, fluid migration, rate-state friction and damage.

### 2. Model

[7] In the first part of this section, we give a brief summary of the employed fault model following Ben-Zion [1996] and Zöller *et al.* [2004, 2005]. In the second part, we describe how the assumed brittle and creep mechanisms are implemented.

#### 2.1. Model Framework

[8] The model includes a strike-slip fault region of 70 km length and 17.5 km depth, covered by a computational grid,

<sup>1</sup>Institute of Physics and Institute of Mathematics, University of Potsdam, Potsdam, Germany.

<sup>2</sup>Institute of Earth Sciences, University of Potsdam, Potsdam, Germany.

<sup>3</sup>Institute of Mathematics, University of Potsdam, Potsdam, Germany.

<sup>4</sup>Department of Earth Sciences, University of Southern California, Los Angeles, USA.

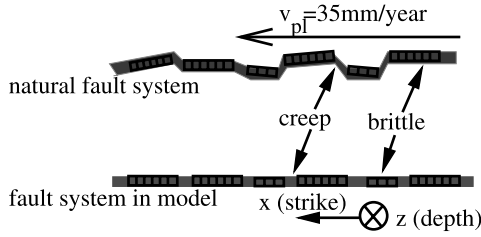


**Figure 1.** Sketch of a natural fault system and the linear approximation of the assumed fault model.

divided into  $128 \times 32$  uniform cells, where deformational processes are calculated [Ben-Zion and Rice, 1993].

[9] Tectonic loading is imposed by a motion with constant velocity  $v_{pl} = 35$  mm/year of the regions around the computational grid. The space-dependent loading rate provides realistic boundary conditions. Using the static stress transfer function for slip in elastic solid, the continuous tectonic loading for each cell on the computational grid is a linear function of time  $t$ . While the loading produces an increase of stress on the fault, the local stress may be reduced by creep and brittle failure processes.

[10] The ongoing creep motion on the computational grid is governed by a local constitutive law corresponding to lab-based dislocation creep. Specifically, we assume that the creep velocity is given by

$$\dot{u}_c(x, z; t) = c(x, z)(\tau(x, z; t))^3, \quad (2)$$

where  $x$  and  $z$  denote coordinates along strike and depth,  $c(x, z)$  are time-independent coefficients,  $\tau$  is the local stress and  $\dot{u}$  is the creep velocity [Ben-Zion, 1996]. Equation (2) results in a system of  $128 \times 32$  coupled ordinary differential equations, which is solved numerically using a Runge-Kutta scheme.

[11] An earthquake is initiated if the local stress  $\tau(x, z; t)$  exceeds the static friction  $\tau_s(x, z)$ . Then the stress drops in cell  $(x, z)$  to the arrest stress  $\tau_a(x, z)$  and the strength drops to a dynamic friction value  $\tau_d(x, z)$  for the remainder of the event. At the end of the earthquake, the strength recovers back to the static level. The dynamic friction is calculated from the static and arrest stress levels in relation to a dynamic overshoot coefficient  $D$ :

$$\tau_d = \tau_s - \frac{\tau_s - \tau_a}{D}. \quad (3)$$

Following Ben-Zion and Rice [1993] and Madariaga [1976], we use  $D = 1.25$ . The static strength is constant,  $\tau_s(x, z) \equiv 10$  MPa, and the arrest stress is chosen randomly from the interval  $\tau_a(x, z) \in [0; 1$  MPa].

[12] The stress transfer due to coseismic slip and creep motion is calculated by means of the three-dimensional solution  $K(x, z; x', z')$  of Chinnery [1963] for static dislocations on rectangular patches in an elastic Poisson solid with rigidity  $\mu = 30$  GPa:

$$\Delta\tau(x, z; t) = \sum_{(x', z') \in \text{fault}} K(x, z; x', z') \Delta u(x', z'; t - r/v_s) \quad (4)$$

where  $\Delta u$  is the slip,  $r$  is the spatial distance between the cells  $(x, z)$  and  $(x', z')$ ,  $v_s$  is a constant shear wave velocity,

and the kernel  $K$  decays like  $1/r^3$ . The value of  $v_s$  defines the event time scale and has no influence on the earthquake catalogs. A finite value of  $v_s$  corresponds to the quasi-dynamic approximation of Zöller *et al.* [2004], whereas  $v_s \rightarrow \infty$  reduces to the quasi-static procedure of Ben-Zion and Rice [1993] and Ben-Zion [1996]. The calculations below are done for a finite value of  $v_s$ , but the statistical aspects of the results remain the same for the quasi-static case.

## 2.2. Brittle and Creep Parameters

[13] Each cell of the computational grid is either a “brittle” or a “creep” cell. A brittle cell can undergo slip during an earthquake (coseismic) and small creep motion between two earthquakes (interseismic). A creep cell can only perform interseismic creep. Figure 1 shows a sketch of the distribution of brittle and creep cells. The creep barriers are generated by near-vertical random walks from various along-strike positions at the free surface to depth [Ben-Zion, 1996]. As shown below, the assumed barriers provide a simple way of simulating non-brittle deformation processes near segment boundaries (e.g., step-over regions) of a large strike-slip fault. The material surrounding the computational grid moves with a constant velocity  $v_{pl}$ . The model has two imposed timescales: A long time scale associated with the tectonic loading and a short earthquake timescale. In addition, there is a third emergent timescale generated by the interplay between the processes occurring on the brittle fault patches and creeping barriers.

[14] The creep coefficients for the brittle cells  $c_b(x, z)$  in equation (2) are chosen similar to the values by Ben-Zion [1996] and Zöller *et al.* [2005]:  $c_b(x, z)$  is randomly distributed in  $[0.9\langle c_b \rangle; 1.1\langle c_b \rangle]$ , where  $\langle c_b \rangle = 10^{-7} \text{ m s}^{-1} \text{ MPa}^{-3}$ . The coefficients for the creep cells  $c_{cr}(x, z)$  are varied in different model simulations as follows: Model A:  $\langle c_{cr} \rangle = 10^{-2} \text{ m s}^{-1} \text{ MPa}^{-3}$ , Model B:  $\langle c_{cr} \rangle = 5 \cdot 10^{-3} \text{ m s}^{-1} \text{ MPa}^{-3}$ , and Model C:  $\langle c_{cr} \rangle = 10^{-3} \text{ m s}^{-1} \text{ MPa}^{-3}$ . Noise is added to the mean values as for  $c_b(x, z)$ .

## 3. Model Simulations and Results

[15] For each model introduced at the end of the previous section, we perform a simulation with random initial stresses. After the stress field has reached a steady state, we produce an earthquake catalog containing 20,000 events and covering about 500 years. Figure 2 shows that the frequency-size distributions for all models include a scaling region followed by a characteristic earthquake at  $M \approx 6.6$ .

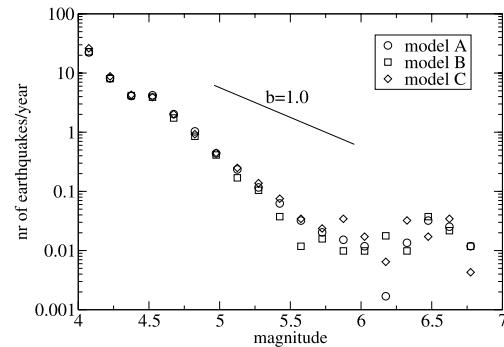


**Figure 2.** Frequency-size distributions for different model simulations.

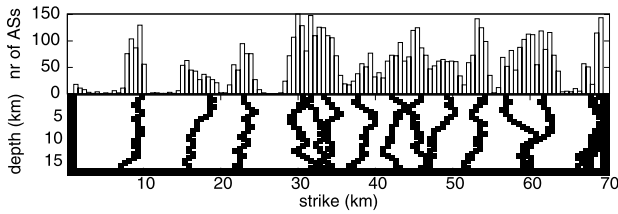


**Figure 3.** Model A: Hypocenter distribution of aftershocks (for a definition see text) along strike (top). Bottom: Distribution of brittle cells (white boxes) and creeping cells (black boxes) in the fault region.

Similar frequency-size distributions have been observed by *Ben-Zion* [1996] for a fault with uniform brittle properties. The fact that no earthquakes with  $M < 4.0$  occur, stems from the discretization of the computational grid. Because the magnitude is derived from the cumulative slip during an event [Ben-Zion, 1996], the size of a cell determines the minimum magnitude. The bump at  $M = 4.5$  is associated with the sizes of the brittle patches produced by the employed spatial realization of the creeping barriers.

[16] Figure 3 (bottom) shows the spatial distribution of creep and brittle cells in the fault region and the number of aftershocks along strike. Here, aftershocks are earthquakes occurring up to one year after a  $M \geq 6.2$  mainshock. The aftershocks are mostly concentrated close to the near-vertical creep barriers (margins of the fault segments), which become highly loaded during mainshocks that transfer stress from the rupturing cells into the creeping parts of the fault. Because these parts do not fail in rapid brittle fashion, they store stress until each mainshock is terminated. After the mainshock they creep, thereby transferring stress back to the entire fault region. This leads to aftershocks, which occur preferentially close to creeping parts and in high stress fault patches that have not ruptured during the large event.

[17] Figure 4 (bottom) shows a typical aftershock sequence following a mainshock with magnitude  $M = 6.6$ . Immediately after the mainshock, the sequence is strongly clustered and becomes less concentrated some months later.

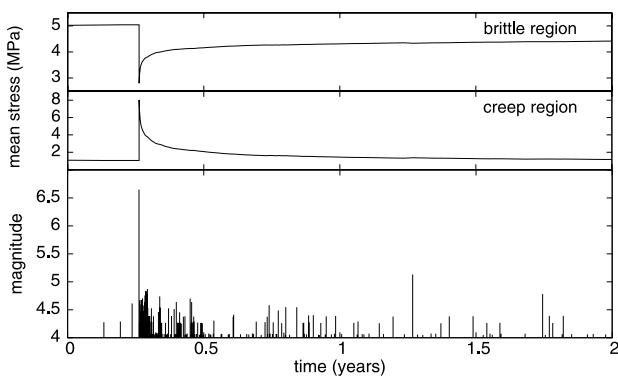


**Figure 4.** Example for a typical aftershock sequence in Model A: Mean stress as a function of time in the brittle region (top) and in the creeping region (middle panel) for a period of two years. The bottom panel shows earthquake magnitudes as a function of time.

The evolution of stress during this period in the brittle and creep regions is shown in the top and middle panel of Figure 4. The mean stress in the creeping regions grows rapidly during the occurrence of mainshocks and then relaxes. The mean stress in the brittle region drops at the time of the mainshock and then increases due to the stress transfer from the creeping cells. It is clear that the time scale of the stress relaxation in the creep regions depends on the average creep rate  $\langle c_{cr} \rangle$ . If this value grows, the creep velocity will increase according to equation (2). Thus, the relaxation becomes faster and aftershocks will occur in a shorter period after the main event. Comparing the bottom panel of Figure 4 with typical features of observed seismicity, we conclude that Model A represents a realistic scenario of aftershock activity.

[18] Figure 5 shows the mean earthquake rate after a mainshock in Models A, B, and C. The rate is stacked for all mainshocks with  $M \geq 6.6$ . The estimated  $p$  exponent of the modified Omori law and the level of background seismicity are indicated in each plot. The deviation of the aftershock activity from the background level can be measured by the ratio of earthquakes occurring up to three months after and before the main event. This ratio is about 10 for Models A and B, and about 6 for Model C. It is clearly visible that a high ratio of  $\langle c_{cr} \rangle / \langle c_b \rangle$  (Model A) leads to aftershock sequences on short time scales characterized by relatively high exponents. A smaller ratio results in a slower stress transfer from creeping cells and thus leads to less clustered aftershock sequences (Model C). It is conspicuous that in Model C the maximum number of aftershocks is not observed directly after the mainshock. This is similar to the relative quiescence in the model without creep [Ben-Zion and Rice, 1993; Zöller et al., 2004], which is due to the relative slow recovery of the stress field after the fault region has been unloaded by the mainshock. In particular,

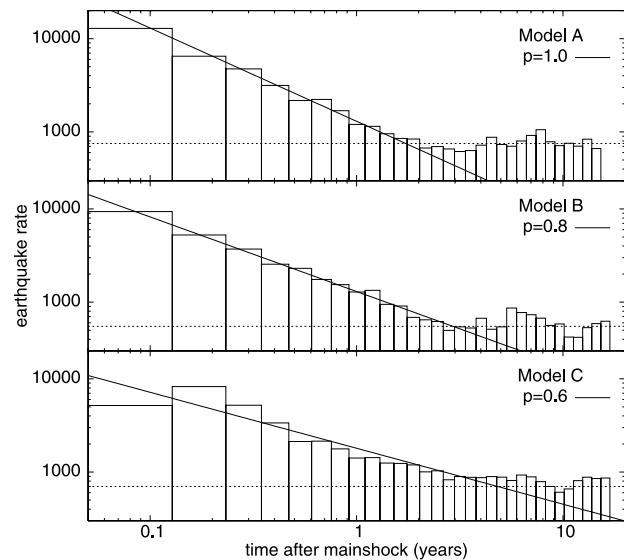


**Figure 5.** Earthquake rate as a function of time for different models. The solid lines give estimates of the modified Omori law and the dotted lines mark the background level of seismicity. Each plot is based on a simulation with 20,000 earthquakes covering about 500 years; the earthquake rates are averaged over about 30 mainshock cycles.

the amount of stress resulting from afterslip in Model C is too small to compensate the unloading of the fault due to the mainshock immediately after the mainshock. If the ratio  $\langle c_{cr} \rangle / \langle c_b \rangle$  is close to 1, the loading of each brittle cell will be approximately linear. The results of Figure 5 indicate that Model A with  $p = 1.0$  represents the most realistic case of aftershock sequences.

#### 4. Discussion and Conclusions

[19] We study the behavior of a fault consisting of seismic segments separated by creeping regions that do not fail on the short earthquake timescale. Aseismic creep is known as an important process in fault zones [Wesson, 1988]. This is obvious for deep sections with ductile characteristics, but geodetic measurements as well as studies of seismic data indicate that creep plays also an important role in shallow parts of crust. It is interesting to note that the creep deformation of a fault may be of the same order of magnitude or even higher than the coseismic change. This has been observed, e.g., for the postseismic creep response of the 1984 Morgan Hill earthquake that occurred on the Calaveras fault in California [Schaff *et al.*, 1998].

[20] In our model, the interplay of brittle and creep deformation produces significant afterslip on creeping regions following large events. As a consequence, aftershocks are triggered on highly stressed fault patches that did not rupture during the mainshock. The occurrence of afterslip following large earthquakes has been documented in observational studies [e.g., Bürgmann *et al.*, 2002], and analyzed in laboratory experiments and numerical models [Marone *et al.*, 1991]. The  $p$  exponent of the modified Omori law and the time scale of aftershocks depend only on the coefficients of the imposed creep law (equation (2)). If the ratio of creep coefficients in the creeping and the brittle regions  $\langle c_{cr} \rangle / \langle c_b \rangle$  is of the order  $10^5$ , realistic aftershock sequences with  $p \approx 1$  are observed. A study of foreshocks, which occur less frequent than aftershocks, requires a large number of mainshocks in various realizations. This is beyond the ability of our current computational method and is left for a future work.

[21] Summarizing, we have developed a fault model based on dislocation theory and empirical knowledge. The mixing of brittle and creep properties leads to postseismic effects, which are in agreement with numerous experiments and observational studies, and produce aftershock sequences following the modified Omori law. The high correspondence of the results to observations indicates that the model provides an effective parameterization of the key physical process that govern seismicity on large strike-slip faults.

[22] **Acknowledgments.** G. Z. acknowledges support from the collaborative research center "Complex Nonlinear Processes" (SFB555) of the German Research Society (DFG). We thank Ilya Zaliapin and anonymous reviewer for useful comments.

#### References

Bak, P., and C. Tang (1989), Earthquakes as a self-organized critical phenomenon, *Geophys. Res. Lett.*, *94*, 15,635–15,637.  
 Ben-Zion, Y. (1996), Stress, slip, and earthquakes in models of complex single-fault systems incorporating brittle and creep deformations, *J. Geophys. Res.*, *101*, 5677–5706.

Ben-Zion, Y., and V. Lyakhovsky (2003), A generalized law for aftershock rates in a damage rheology model, *Eos Trans. AGU*, *84*(46), Fall Meet. Suppl., Abstract NG12C-02.  
 Ben-Zion, Y., and J. R. Rice (1993), Earthquake failure sequences along a cellular fault zone in a three-dimensional elastic solid containing asperity and nonasperity regions, *J. Geophys. Res.*, *98*, 14,109–14,131.  
 Bürgmann, R., D. Schmidt, R. M. Nadeau, M. d'Alessio, E. Fielding, D. Manaker, T. V. McEvilly, and M. H. Murray (2000), Earthquake potential along the northern Hayward fault, California, *Science*, *289*, 1178–1182.  
 Bürgmann, R., S. Ergintav, P. Segall, E. H. Hearn, S. McClusky, R. E. Reilinger, H. Woith, and J. Zschau (2002), Time-dependent distributed afterslip on and deep below the Izmit earthquake rupture, *Bull. Seismol. Soc. Am.*, *92*, 126–137.  
 Burridge, R., and L. Knopoff (1967), Model and theoretical seismicity, *Bull. Seismol. Soc. Am.*, *57*, 341–371.  
 Chinnery, M. (1963), The stress changes that accompany strike-slip faulting, *Bull. Seismol. Soc. Am.*, *53*, 921–932.  
 Dahmen, K., D. Ertas, and Y. Ben-Zion (1998), Gutenberg-Richter and characteristic earthquake behavior in simple mean-field models of heterogeneous faults, *Phys. Rev. E*, *58*, 1494–1501.  
 Dieterich, J. H. (1972), Time-dependent friction as a possible mechanism for aftershocks, *J. Geophys. Res.*, *77*, 3771–3781.  
 Dieterich, J. H. (1994), A constitutive law for earthquake production and its application to earthquake clustering, *J. Geophys. Res.*, *99*, 2601–2618.  
 Hainzl, S., G. Zöller, and J. Kurths (1999), Similar power laws for fore- and aftershock sequences in a spring-block model for earthquakes, *J. Geophys. Res.*, *104*, 7243–7253.  
 Hainzl, S., G. Zöller, and F. Scherbaum (2003), Earthquake clusters resulting from delayed rupture propagation in finite fault segments, *J. Geophys. Res.*, *108*(B1), 2013, doi:10.1029/2001JB000610.  
 Hergarten, S., and H. J. Neugebauer (2002), Foreshocks and aftershocks in the Olami-Feder-Christensen model, *Phys. Rev. Lett.*, *88*, 238501, doi:10.1103/PhysRevLett.88.238501.  
 Ito, K., and M. Matsuzaki (1990), Earthquakes as self-organized critical phenomena, *J. Geophys. Res.*, *95*, 6853–6860.  
 Lyons, S., and D. Sandwell (2003), Fault creep along the southern San Andreas from interferometric synthetic aperture radar, permanent scatterers, and stacking, *J. Geophys. Res.*, *108*(B1), 2047, doi:10.1029/2002JB001831.  
 Madariaga, R. (1976), Dynamics of an expanding circular fault, *Bull. Seismol. Soc. Am.*, *66*, 639–666.  
 Marone, C. J., C. H. Scholz, and R. Bilham (1991), On the mechanisms of earthquake afterslip, *J. Geophys. Res.*, *96*, 8441–8452.  
 Nur, A., and J. R. Booker (1972), Aftershocks caused by pore fluid flow?, *Science*, *175*, 885–887.  
 Omori, F. (1894), On the aftershocks of earthquakes, *J. Coll. Sci. Imp. Univ. Tokyo*, *7*, 111–200.  
 Schaff, D. P., G. C. Beroza, and B. E. Shaw (1998), Postseismic response on repeating aftershocks, *Geophys. Res. Lett.*, *25*, 4549–4552.  
 Shcherbakov, R., and D. L. Turcotte (2004), A damage mechanics model for aftershocks, *Pure Appl. Geophys.*, *161*, 2379, doi:10.1007/s00024-004-2570-x.  
 Utsu, T. (2002), Statistical features of seismicity, in *International Handbook of Earthquake and Engineering Seismology*, Int. Geophys. Ser., vol. 81A, edited by W. H. K. Lee *et al.*, pp. 719–732, Elsevier, New York.  
 Utsu, T., Y. Ogata, and R. S. Matsu'ura (1995), The centenary of the Omori formula for a decay law of aftershock activity, *J. Phys. Earth*, *43*, 1–33.  
 Wesson, R. L. (1988), Dynamics of fault creep, *J. Geophys. Res.*, *93*, 8929–8951.  
 Zöller, G., M. Holschneider, and Y. Ben-Zion (2004), Quasi-static and quasi-dynamic modeling of earthquake failure at intermediate scales, *Pure Appl. Geophys.*, *161*, 2103, doi:10.1007/s00024-004-2551-0.  
 Zöller, G., M. Holschneider, and Y. Ben-Zion (2005), The role of heterogeneities as a tuning parameter of earthquake dynamics, *Pure Appl. Geophys.*, in press.

Y. Ben-Zion, Department of Earth Sciences, University of Southern California, Los Angeles, Los Angeles, CA 90089–0740, USA. (benzion@usc.edu)

S. Hainzl, Institute of Earth Sciences, University of Potsdam, POB 60 15 53, D-14415 Potsdam, Germany. (hainzl@geo.uni-potsdam.de)

M. Holschneider, Institute of Mathematics, University of Potsdam, POB 60 15 53, D-14415 Potsdam, Germany. (hols@math.uni-potsdam.de)

G. Zöller, Institute of Physics and Institute of Mathematics, University of Potsdam, POB 60 15 53, D-14415 Potsdam, Germany. (gert@agnld.uni-potsdam.de)

# Appendix N

**Earthquake activity related to seismic cycles in a model for a heterogeneous strike-slip fault**

Autors:	G. Zöller, S. Hainzl, Y. Ben-Zion, and M. Holschneider
Journal:	Tectonophysics
Volume:	submitted
Year:	2005

## **Earthquake activity related to seismic cycles in a model for a heterogeneous strike-slip fault**

Gert Zöller<sup>1</sup>

Sebastian Hainzl<sup>2</sup>

Yehuda Ben-Zion<sup>3</sup>

Matthias Holschneider<sup>4</sup>

Short title:

---

<sup>1</sup>Institute of Mathematics and Institute of Physics, University of Potsdam, Potsdam, Germany  
(email: gert@agnld.uni-potsdam.de, phone: +49-331 977 1175, fax: +49-331 977 1142)

<sup>2</sup>Institute of Earth Sciences University of Potsdam, Potsdam, Germany  
(email: hainzl@agnld.uni-potsdam.de, phone: +49-331 977 5078, fax: +49-331 977 5060)

<sup>3</sup>Department of Earth Sciences, University of Southern California, Los Angeles, USA  
(email: benzion@usc.edu, phone: +1-213 740 6734, fax: +1-213 740 8801)

<sup>4</sup>Institute of Mathematics, University of Potsdam, Potsdam, Germany  
(email: hols@math.uni-potsdam.de, phone: +49-331 977 1663, fax: +49-331 977 1578)

**Abstract.** We investigate the evolution of the seismicity within seismic cycles in a model of a discrete large strike-slip fault in elastic solid. The model dynamics is governed by realistic boundary conditions consisting of constant velocity motion of regions around the fault, static/kinetic friction and dislocation creep along the fault, and 3D elastic stress transfer. The fault consists of brittle parts which fail during earthquakes and undergo small creep deformation between events, and aseismic creep cells which are characterized by high ongoing creep motion. This mixture of brittle and creep cells is found to generate realistic aftershock sequences which follow the modified Omori law and scale with the mainshock size. Furthermore, we find that the distribution of interevent times of the simulated earthquakes is in good agreement with observations. The temporal occurrence, however, is magnitude-dependent; in particular, the small events are clustered in time, whereas the largest earthquakes occur quasiperiodically. Averaging the seismicity before several large earthquakes, we observe an increase of activity and a broadening scaling range of magnitudes when the time of the next mainshock is approached. These results are characteristics of a critical point behavior. The presence of critical point dynamics is further supported by the evolution of the stress field in the model, which is compatible with the observation of accelerating moment release in natural fault systems.

**Keywords:** earthquake dynamics; fault models; seismicity; ruptures; heterogeneities; criticality

## 1. Introduction

The complexity of spatiotemporal earthquake occurrence on natural fault systems has been discussed and quantified in numerous studies (for an overview see [RUNDLE *et al.*, 2000B]). While some seismicity patterns show an almost universal behavior, others are observed less frequently and follow no obvious law. For example, aftershocks according to the modified Omori law are observed after almost all large earthquakes [UTSU *et al.*, 1995], whereas foreshocks are a rare phenomenon [WYSS, 1997; UTSU, 2002]. However, the Parkfield experiment in California [ROELOFFS AND LANGBEIN, 1994] demonstrates that even if a fault segment shows regular behavior over several decades, a prediction of future activity can fail drastically. One reason for this is that the given data sets are too limited to provide enough information for the understanding of the complex relationships between the various physical mechanisms in the earth's crust. This emphasizes the importance of model simulations which cover several seismic cycles and allow to study the dependences of seismicity on the underlying parameters and evolving stress field.

Several conceptual models have been proposed to describe properties of observed seismicity, e.g. the first generation of spring-block models and cellular automata, which reproduce the frequency-size distribution of earthquakes. These models are mainly based on tectonic loading and the coseismic stress transfer [BURRIDGE AND KNOPOFF, 1967; BAK AND TANG, 1989]. Others have implemented additional mechanisms, like viscoelastic relaxation in the fault zone [DIETERICH, 1972; HAINZL *et al.*, 1999], fault strengthening or weakening after a block slip [ITO AND MATSUZAKI, 1990], pore fluid flow [NUR AND BOOKER, 1972], rate-state friction [DIETERICH, 1994], and damage rheology [BEN-ZION AND LYAKHOVSKY, 2005; SHCHERBAKOV AND TURCOTTE, *et al.*, 2004]. Although most of these models reproduce certain observed phenomena, the underlying frameworks are often abstract and the application to an actual fault system with its spatiotemporal complexity of earthquake occurrence remains questionable.

In this study, we analyze earthquake catalogs generated by the model of [ZÖLLER *et al.*, 2005] for a large heterogeneous strike-slip fault. The model develops further the framework of [BEN-ZION AND RICE, 1993] and [BEN-ZION, 1996] for a discrete fault in a surrounding elastic solid, and it combines computational efficiency with realistic physical properties. The simulations cover 1000s of years and allow us to reproduce brittle as well as postseismic and interseismic creep deformation. The model ingredients, including laws for brittle and creep deformation, stress transfer, and boundary conditions, are compatible with empirical knowledge. Several relationships between imposed model parameters (e.g., frictional parameters, creep velocities, spatial heterogeneities) and observed seismicity quantities like frequency-size distributions and aftershock clustering,



have been previously quantified [ZÖLLER *et al.*, 2005]. In this paper, we will focus on the temporal evolution of seismicity during seismic cycles. Many observational and theoretical studies have shown that seismicity is largely time-dependent. In particular, the seismic moment release is found to accelerate prior to large earthquakes [BUFE AND VARNES, 1993; BOWMAN *et al.*, 1998; JAUME AND SYKES, 1999]. This phenomenon indicates that seismicity is a process that may be characterized by critical point behavior in terms of upcoming long-range correlations prior to a large earthquake [SORNETTE AND SORNETTE, 1990; ZÖLLER *et al.*, 2001; ZÖLLER AND HAINZL, 2002]. Analyzing stress and seismicity functions over several seismic cycles, [BEN-ZION *et al.*, 2003] conclude that mainshock occurrence is associated with a period where the stress-field evolves toward a critical level of disorder. In this state, the stress field heterogeneities are characterized by many size scales and a brittle failure can evolve into a large earthquake. It is, therefore, an important question, whether the evolution of stress and seismicity in our model reflects such critical point behavior.

## 2. Model

In this section, we give a brief description of the fault model. Further details can be found in [ZÖLLER *et al.*, 2005] and references therein.

Our model includes a single rectangular fault embedded in a 3D elastic half space (Fig. 1). A fault region of 70 km length and 17.5 km depth is covered by a computational grid, divided into  $128 \times 32$  uniform cells, where deformational processes are calculated. Tectonic loading is imposed by a motion with constant velocity  $v_p=35$  mm/year of the regions around the computational grid. The space-dependent loading rate provides realistic boundary conditions. Using the static stress transfer function for slip in elastic solid, the continuous tectonic loading for each cell on the computational grid is a linear function of time and plate velocity  $v_p$ . Additional loadings on a given cell occur due to brittle and creep failures on the fault. While the loading produces an increase of stress on the fault, the local stress may be reduced by interseismic creep and coseismic brittle processes. As in [ZÖLLER *et al.*, 2005], all cells on the computational grid undergo creep deformation, while brittle deformation during an earthquake is only possible for “brittle cells” (white cells in Fig. 1). The aseismic “creep cells” (black cells in Fig. 1) are generated by near-vertical random walks from the free surface to depth accounting for offsets and step-over regions in the fault zone.

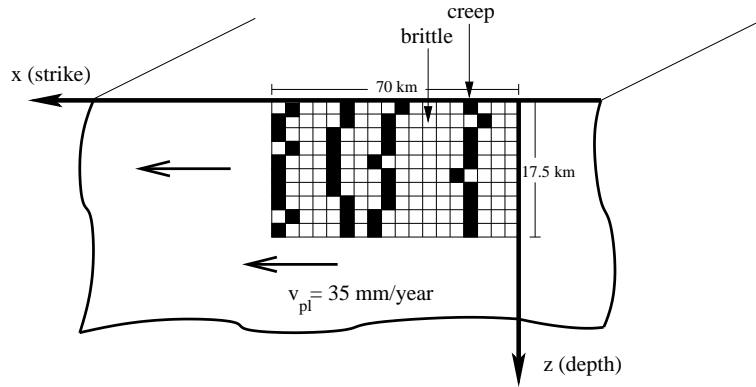


**Figure 1.** A sketch of a 2D strike-slip fault in a 3D elastic half space

The ongoing creep motion on the grid is implemented by a local constitutive law corresponding to lab-based dislocation creep [BEN-ZION, 1996]:

$$\dot{u}_{creep}(x, z, t) = c(x, z)\tau(x, z, t)^3, \quad (1)$$

where  $\dot{u}_{creep}(x, z, t)$  is the creep velocity of the cell with coordinates  $(x, z)$ ;  $\tau(x, z, t)$  is the local stress at time  $t$ , and  $c(x, z)$  are time-independent coefficients, which are different for the creep cells and the brittle cells. As shown in [ZÖLLER *et al.*, 2005], this design can produce aftershock sequences, where the ratio of the mean creep coefficients in the creep cells and in the brittle cells  $\langle c_{cr} \rangle / \langle c_b \rangle$  determines the exponent  $p$  of the modified Omori law for the rate  $\dot{n}(t)$  of aftershocks:

$$\dot{n}(t) = \frac{c_1}{(c_2 + t - t_M)^p}. \quad (2)$$

Here,  $c_1$  and  $c_2$  are time-independent numbers, and  $t_M$  is the mainshock occurrence time. For this work, we choose the creep coefficients leading to  $p = 1$ : The creep parameters for the brittle cells  $c_b$  are randomly distributed in the interval  $[0.9\langle c_b \rangle; 1.1\langle c_b \rangle]$ , where  $\langle c_b \rangle = 10^{-7} ms^{-1} MPa^{-3}$ . The values for the brittle cells  $c_{cr}$  are calculated accordingly with  $\langle c_{cr} \rangle = 10^{-2} ms^{-1} MPa^{-3}$ . This choice corresponds to model A in [ZÖLLER *et al.*, 2005]. Equation (1) results in a system of  $128 \times 32$  coupled ordinary differential equations, which is solved numerically using a Runge-Kutta scheme.

The coseismic processes are governed by static/kinetic friction. An earthquake is initiated if the local stress  $\tau(x, z; t)$  exceeds the static friction  $\tau_s(x, z)$ . Then the stress drops in cell  $(x, z)$  to the arrest stress  $\tau_a(x, z)$  and

the strength follows a piecewise constant failure envelope  $\tau_f(x, z, t)$  during an earthquake:

$$\tau_f(x, z; t) = \begin{cases} \tau_d(x, z) & : \text{ cell } (x, z) \text{ already failed during this event} \\ \tau_s(x, z) & : \text{ cell } (x, z) \text{ failed not during this event.} \end{cases} \quad (3)$$

If  $\tau(x, z; t) < \tau_f(x, z; t)$  for all cells on the grid, the earthquake is terminated. Then, the strength recovers back to the static level for all cells:  $\tau_f(x, z; t) = \tau_s(x, z)$ . The dynamic friction is calculated from the static and arrest stress levels in relation to a dynamic overshoot coefficient  $D$ :

$$\tau_d = \tau_s - \frac{\tau_s - \tau_a}{D}. \quad (4)$$

Following [MADARIAGA, 1976], we use  $D = 1.25$ . The static strength is constant,  $\tau_s(x, z) \equiv 10MPa$ , and the arrest stress is chosen randomly from the interval  $\tau_a(x, z) \in [0; 1MPa]$ .

The stress transfer due to coseismic slip and creep motion is calculated by means of the three-dimensional solution  $K(x, z; x', z')$  of [CHINNERY, 1963] for static dislocations on rectangular patches in an elastic Poisson solid with rigidity  $\mu = 30GPa$ :

$$\Delta\tau(x, z; t) = \sum_{(x', z') \in \text{grid}} K(x, z; x', z') \Delta u(x', z'; t - r/v_s), \quad (5)$$

where  $\Delta u$  is the slip,  $r$  is the spatial distance between the cells  $(x, z)$  and  $(x', z')$ ,  $v_s$  is a constant shear wave velocity, and the kernel  $K$  decays like  $1/r^3$ . The value of  $v_s$  defines the event time scale and has no influence on the earthquake catalogs.

### 3. Results

We analyze an earthquake catalog covering about 5000 years, which contains 200,000 earthquakes with moment magnitudes  $M$  between 4.0 and 6.8. The seismic potency  $P_0$  (moment  $M_0$  divided by rigidity  $\mu$ ) is calculated as the integral of slip over the rupture area during an earthquake. The range of magnitudes depends on the segmentation of the grid into computational cells, e.g. smaller cells would allow to simulate smaller earthquakes. On the other hand, a larger fault would result in a higher maximum magnitude. Figure 2 shows an earthquake sequence (magnitude vs. time) from the catalog over a period of 60 years.

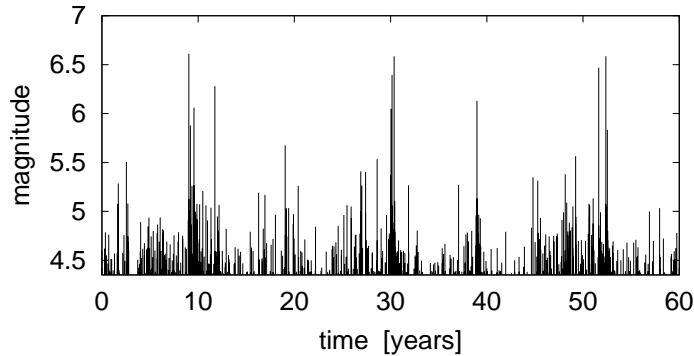


**Figure 2.** Example of the model seismicity in a time span of 60 years.

### 3.1. Aftershocks

The most obvious feature in Fig. 2 is the aftershock clustering following the largest events. As mentioned above, the aftershock decay is compatible with the modified Omori law, Eq. (2), with an exponent  $p = 1$ . Furthermore, it has been demonstrated that the aftershocks are predominantly concentrated at the margins of the fault segments [ZÖLLER *et al.*, 2005], which is in good agreement with observational studies.

An important question is the dependence of the aftershock sequences on the mainshock magnitude  $M_{\text{main}}$ , expressed by the value of  $c_1$  in Eq. (2). The exponent  $p$  is found to be almost independent of  $M_{\text{main}}$  in agreement with [UTSU, 1962; UTSU, 2002]. For the rate of aftershocks, [REASENBERG, 1985] assumes the relation

$$c_1 \propto 10^{\frac{2}{3} \cdot M_{\text{main}}}. \quad (6)$$

The number of aftershocks as a function of the mainshock magnitude is given in Fig. 3a. It is clearly visible that the scaling law Eq. (6) is fulfilled in our model. A second scaling relation is observed, if the number of aftershocks is plotted as a function of the mainshock rupture area, leading to  $N_A \propto A^{1/2}$  and thus to  $N_A \propto R$ , where  $R$  is the rupture length (Fig. 3b). Combining both scaling laws, results in a relation  $P_0$  (or  $M_0$ )  $\propto A^{9/8}$  between seismic potency (or moment) and rupture area  $A$ . In sum, we note that the aftershock sequences in our model govern the main properties of observed aftershock activity with respect to frequency and spatiotemporal occurrence.

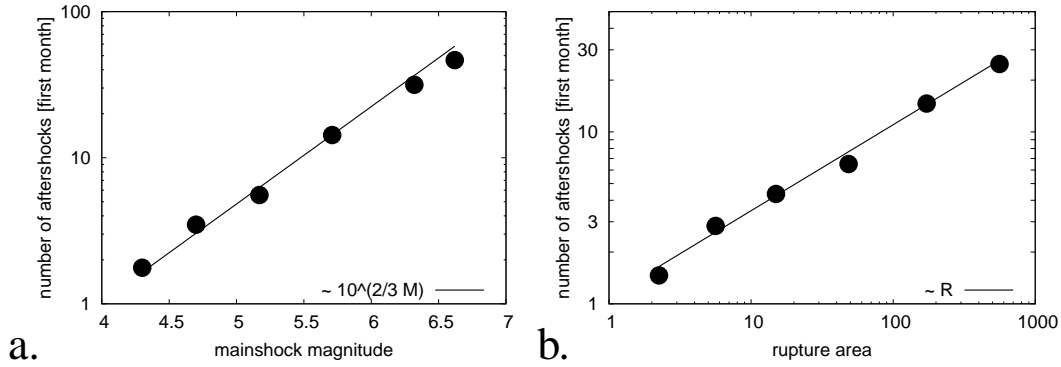


**Figure 3.** The number of aftershocks in the first month after a mainshock as a function of the mainshock magnitude. Here, an earthquake is defined to be a mainshock if it is the largest event within  $\pm 1$  month. The aftershock productivity is found to scale with  $10^{\frac{2}{3}M_{main}}$  (panel a) and with the rupture length  $R \propto \sqrt{A}$  (panel b).

### 3.2. Interevent times

In recent studies, it has been shown that the distribution of interevent times can be described by a universal law. In particular, the distributions from different tectonic environments, different spatial scales (from worldwide to local seismicity) and different magnitude ranges collapse, if the time  $\tau$  is rescaled with the rate  $R_{xy}$  of seismic occurrence in a region denoted by  $(x, y)$  [CORRAL, 2004]:

$$D_{xy}(\tau) = R_{xy} \cdot f(R_{xy}\tau), \quad (7)$$

where  $D_{xy}$  is the probability density for the interevent time  $\tau$ , and  $f$  can be expressed by a generalized gamma distribution

$$f(\theta) = C \frac{1}{\theta^{\gamma-1}} \exp\left(-\frac{\theta^\delta}{B}\right) \quad (8)$$

with parameters  $C$ ,  $\gamma$ ,  $\delta$ , and  $B$ , which have been determined by a fit to several observational catalogs [CORRAL, 2004].

In Fig. 4, we compare  $D_{xy}(\tau)$  from Eq. (7) with two earthquake catalogs: 1. The ANSS catalog of California (catalog ranges are given in the caption) and 2. the model catalog. We note that due to the numerical procedure, especially the Runge-Kutta integration of the creep law (Eq. (1)), the interevent times in the model have a finite lower limit. However, in the region where the interevent times are calculated, the agreement of the three curves is remarkable. For small values of  $\tau$ , Eq. (7) deviates from the California data; for high values the model has a slightly better correspondence with the observational data than Eq. (7). Thus the interevent time

distribution is in excellent agreement with observational results.

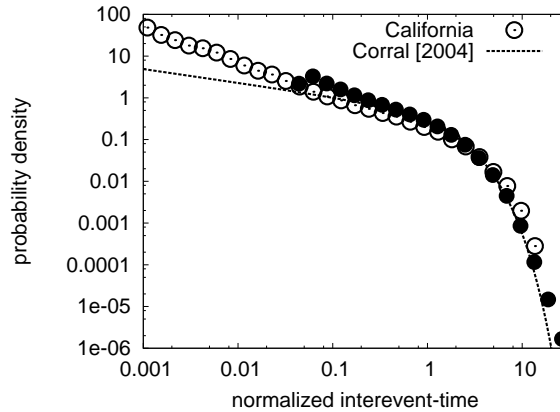


**Figure 4.** The normalized interevent time distribution of the model simulations (black dots) compared with the result of [CORRAL, 2004] and the distribution of earthquakes in California (ANSS catalog of  $M > 3$  earthquakes occurred between 1970 and 2004 within  $29^\circ$  and  $43^\circ$  latitude and  $-113^\circ$  and  $-123^\circ$  longitude).

The degree of temporal clustering of earthquakes can be estimated by the coefficient of variation  $CV$  of the interevent time distribution.

$$CV = \sigma/\mu, \quad (9)$$

where  $\sigma$  is the standard deviation and  $\mu$  the mean value of the interevent time distribution. High values of  $CV$  denote clustered activity, while low values represent quasiperiodic occurrence of events. The case  $CV = 1$  corresponds to a random Poisson process. [BEN-ZION, 1996] and [ZÖLLER *et al.*, 2004] have found that the clustering properties of the large events depend on the degree of quenched spatial disorder of the fault. Here we show that  $CV$  as a function of the lower magnitude cutoff has a characteristic shape (Fig. 5). The values of  $CV$  are higher than 1 (clustered) for small and intermediate earthquakes ( $M \leq 5.4$ ) and smaller than 1 (quasiperiodic) for larger earthquakes. This corresponds to the case of a low degree of disorder in [ZÖLLER *et al.*, 2004], because the brittle cells which participate in an earthquake have no significant spatial disorder. We note that this behavior resembles the seismicity on the Parkfield segment of the San Andreas fault, which is characterized by a quasiperiodic occurrence of mainshocks. The fact that the dependence of  $CV$  on the magnitude cutoff is not monotonic for the small magnitude cutoffs, is again due to the time discretization as a consequence of the numerical procedure.

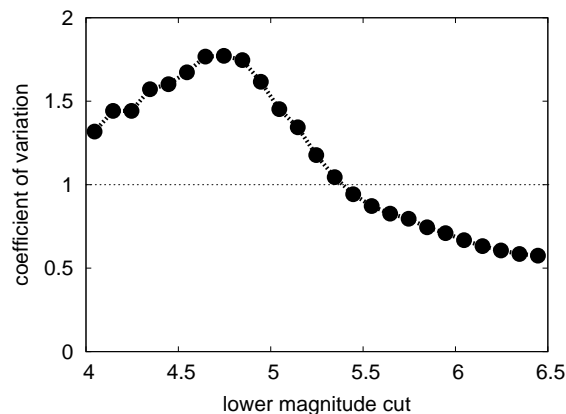


**Figure 5.** The temporal earthquake occurrence quantified by the coefficient of variation as a function of the lower magnitude cutoff. Values larger than 1 indicate clustering, whereas lower values point to quasiperiodic behavior.

### 3.3. Foreshocks

In [ZÖLLER *et al.*, 2005] and in Section 3.1, it is shown that our model produces aftershocks sequences which are quantitatively in very good agreement with observed aftershock activity. Foreshock activity is, however, less present in observed data. Although it is documented that the increase of activity prior to a mainshock follows an “inverse Omori law”  $\dot{n}(t) \sim (c + t_M - t)^{-q}$  with an exponent  $q \approx 1$  [HAINZL *et al.*, 1999], the overall smaller number of foreshocks requires very long data sets including many mainshocks to detect a clear foreshock signal. Stacking the activity before 225 mainshocks with  $M \geq 6$ , shows a moderate but clearly visible increase of the earthquake rate before a mainshock (see Fig. 6). The exponent  $q$  of foreshock activity is, however, difficult to estimate, because it is not clear how to distinguish the small number of extra events from the background activity. The observation of an increasing precursory rate is encouraging for the applicability of the model to real fault zones.

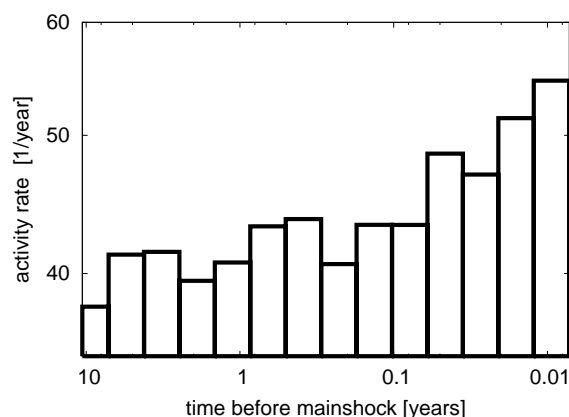


**Figure 6.** The stacked and averaged activity prior to mainshocks (225 sequences). Here, mainshocks are  $M > 6$  events which are the largest earthquakes within  $\pm 10$  years.

### 3.4. Critical point behavior

The interpretation of seismicity in terms of critical point dynamics has opened new perspectives for the analysis and the understanding of earthquake data. These include self-organized criticality [BAK AND TANG, 1989; HAINZL *et al.*, 1999], growing spatial correlation length [ZÖLLER *et al.*, 2001; ZÖLLER AND HAINZL, 2002] and accelerating moment release [BUFE AND VARNES, 1993; JAUME AND SYKES, 1999]. A key question is whether the approach to the critical point can be measured by stress or seismicity functions as addressed by [BEN-ZION *et al.*, 2003]. Their analysis of catalogs from three end-member models leads to the conclusion, that large earthquakes are preceded by a period of criticality characterized by a highly disordered stress field with a broad range of size scales. In this section, we search for signals of criticality in our more realistic model.

Figure 7 (bottom) shows the average earthquake rate before and after a large event as a function of time. This figure is again based on a stacking of 225 large events ( $M \geq 6$ ). The top panel of Figure 7 is the corresponding mean stress (normalized) on the computational grid. The mainshock itself is characterized by a significant stress drop. In the following period of aftershocks, lasting for about 1.2 years, the mean stress still decreases before it recovers and increases again. This stress increase is almost linear and lasts until the next mainshock occurs.

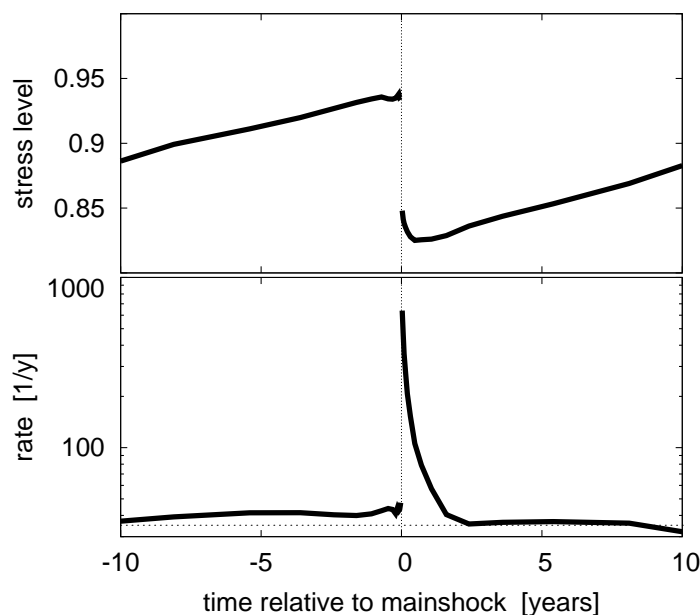


**Figure 7.** The averaged activity and stress evolution relative to mainshocks ( $M > 6$  events which are the largest earthquakes within  $\pm 10$  years).



In previous studies [BEN-ZION, 1996; BEN-ZION *et al.*, 2003; ZÖLLER *et al.*, 2005], it has been demonstrated that the degree of disorder of the stress field is correlated with the frequency-size distribution of the seismicity: a smooth stress field produces characteristic earthquake distributions with a frequently occurring characteristic event, almost no intermediate earthquakes and small events following a truncated Gutenberg-Richter distribution; in contrast, the seismicity from a disordered stress field is characterized by a Gutenberg-Richter distribution over a broad range of magnitudes. Therefore, we expect that the frequency-size distribution before a mainshock has a broad scaling region, whereas the overall seismicity follows a characteristic earthquake distribution. Figure 8 shows the cumulative frequency-size distributions for foreshocks, aftershocks, and all earthquakes in our model. Due to the small number of foreshocks, the corresponding curve is less smooth than the curves for aftershocks and all events. However, it is clearly visible that the foreshock activity shows the smallest deviations from a scaling law (denoted as solid lines) compared to the other curves. Although the overall frequency-size distribution of earthquakes follows a characteristic earthquake law, the periods before mainshocks are characterized by a scaling law of Gutenberg-Richter type with a broad scaling range pointing to a disordered stress field with a wide range of spatial size scales.

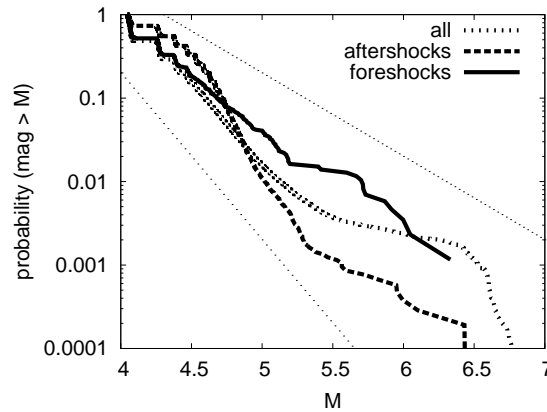


**Figure 8.** The frequency-magnitude distribution of all earthquakes, foreshocks and aftershocks, respectively. Foreshocks and aftershocks are defined to be earthquakes occurring within one month before and after a mainshock, where the mainshock definition is the same way as before. The dotted lines refer to  $b$ -values of 1 and 2.

The second indication for critical point behavior is the the acceleration of seismic moment release, which is assumed to follow the power law

$$(\Sigma\Omega)(t) = A + B(t_f - t)^m, \quad (10)$$

where the cumulative Benioff strain  $(\Sigma\Omega)(t)$  is calculated from the energy releases  $E(\tau)$  of earthquakes at times

$\tau \leq t$  by  $(\Sigma\Omega)(t) = \int_0^t \sqrt{E(\tau)} d\tau$ . The time  $t_f$  is the mainshock occurrence time,  $A$ ,  $B$ , and  $m$  are parameters. Analyzing eight large earthquakes in California, [BOWMAN *et al.*, 1998] find values of the exponent  $m$  in the range  $0.1 \leq m \leq 0.55$ . The theoretical analysis of [RUNDLE *et al.*, 2000A] of a critical point process leads to  $m = 0.25$ . The observational study of [BUFE AND VARNES, 1993] and the theoretical damage model of [BEN-ZION AND LYAKHOVSKY, 2002] suggest the value  $m = 0.3$ .

Due to the noisy character of single earthquake sequences, it is difficult to detect accelerating moment release before individual mainshocks. Instead, we use a more robust representation by plotting the release of potency  $P_0$  as a function of the (normalized) stress level on the fault. We note that the stress increase on the fault is linear (see Fig. 7). Consequently, the abscissa represents effectively the time between two mainshocks. The curve shows a clear power law dependence of the (non-cumulative) potency release on the stress level with an exponent of  $s = -1.5$ . This results in a power law for the cumulative Benioff strain according to Eq. (10) with  $m = 0.5 \cdot s + 1 = 0.25$ , which is in good agreement with empirical and theoretical findings [BUFE AND VARNES, 1993; BOWMAN *et al.*, 1998; RUNDLE *et al.*, 2000A; BEN-ZION AND LYAKHOVSKY, 2002]. In sum, our results are compatible with the hypothesis of accelerating moment release and provide further support for the presence of critical point dynamics in the simulated seismicity.

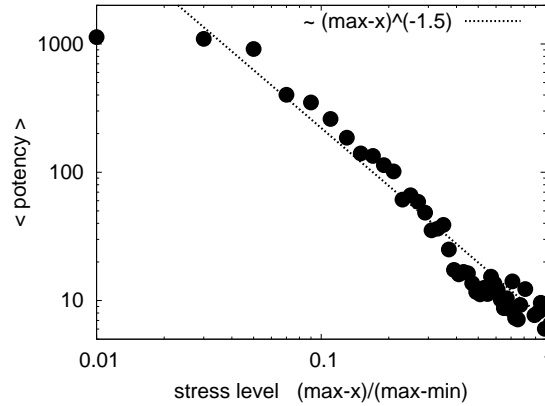


**Figure 9.** The mean potency of earthquakes as a function of the stress level  $\tau$ . The stress level is normalized to the maximum (max) and minimum (min) observed stress. The potency is found to increase according to a power law  $\Delta\tau^{-1.5}$ , if stress approaches the maximum.

#### 4. Discussion and conclusions

In the present work, we have analyzed an earthquake catalog from a recently developed model for a large heterogeneous strike-slip fault. As shown in a previous work, this model reproduces various characteristics of observed seismicity [ZÖLLER *et al.*, 2005]. Using different parameters, like frictional values and creep rates, the model can be tuned towards observed cases, e.g. a fault which produces clustered seismicity obeying

Gutenberg-Richter statistics or a fault with quasiperiodically occurring mainshocks following the characteristic earthquake distribution. Here, we have analyzed an earthquake catalog from the latter situation, which resembles many features of seismicity on the Parkfield segment of the San Andreas fault in California, including quasiperiodically occurring mainshocks, which are followed by aftershock sequences. In contrast to short observational data sets covering some years or decades, we consider an observational period of about 5000 years of simulated seismicity. This allows us to use a stacking procedure in order to unveil properties, which are not visible in short and noisy data sets.

The stacking of many aftershock sequences shows a scaling relation between the mainshock magnitude and the number of aftershocks. This gives in combination with the modified Omori law an excellent explanation of aftershock activity. In addition, the less frequently occurring foreshock activity is also visible in our model. The temporal occurrence of earthquakes is quasiperiodic for large events and clustered for intermediate and small events with an overall interevent time distribution that follows a recently proposed universal law and is very similar to the interevent time distribution of California seismicity. While these results demonstrate a high correspondence of the model output with observed seismicity, we also find support for the hypothesis that seismicity is characterized by critical point dynamics. In particular, we have shown that the scaling range of the frequency-size distribution becomes broader, when the time of a mainshock is approached. This indicates that the stress field has reached a certain degree of disorder, where a single failure can evolve into a large event. Furthermore, the moment release accelerates in the interseismic periods in good agreement with observational and theoretical results.

In sum, we have demonstrated that our model provides a very good performance of natural earthquake activity and gives new insights to various aspects of the so-called “critical earthquake concept”. Therefore, we believe that it will have impact on the problem of earthquake predictability in certain fault zones.

## **Acknowledgments**

G.Z. acknowledges support from the collaborative research center “Complex Nonlinear Processes” (SFB555) of the “German Research Society” (DFG).

## References

- BAK, P., AND TANG, C. (1989), *Earthquakes as a self-organized critical phenomenon*, *Geophys. Res. Lett.* **94**, 15,635-15,637.
- BEN-ZION, Y. (1996), *Stress, slip, and earthquakes in models of complex single-fault systems incorporating brittle and creep deformations*, *J. Geophys. Res.*, **101**, 5677-5706.
- BEN-ZION, Y., M. ENEVA, AND LIU, Y. (2003), *Large earthquake cycles and intermittent criticality on heterogeneous faults due to evolving stress and seismicity*, *J. Geophys. Res.* **108**, doi 1029.2002JB002121.
- BEN-ZION, Y. AND LYAKHOVSKY, V. (2002), *Accelerated Seismic Release and Related Aspects of Seismicity Patterns on Earthquake Faults*, *Pure Appl. Geophys.*, **159**, 2385-2412.
- BEN-ZION, Y. AND LYAKHOVSKY, V. (2005), *Analysis of aftershocks in a lithospheric model with seismogenic zone governed by damage rheology*, submitted to *Geophys. J. Int.*
- BEN-ZION, Y. AND RICE, J. R.. (1993), *Earthquake failure sequences along a cellular fault zone in a three-dimensional elastic solid containing asperity and nonasperity regions*, *J. Geophys. Res.* **98**, 14,109-14,131.
- BOWMAN, D. D., OULLION, G., SAMMIS, C. G., SORNETTE, A., AND SORNETTE, D., (1998), *An observational test of the critical earthquake concept*, *J. Geophys. Res.*, **103**, 24,359-24,372.
- BUFE, C. G., AND VARNES, D. J. (1993), *Predictive modeling of the seismic cycle in the greater San Francisco Bay area*, *J. Geophys. Res.*, **98**, 9871-9883.
- BURRIDGE, R., AND KNOPOFF, L. (1967), *Model and theoretical seismicity*, *Bull. Seism. Soc. Am.*, **57**, 341-371.
- CHINNERY, M. (1963), *The stress changes that accompany strike-slip faulting*, *Bull. Seim. Soc. Am.*, **53**, 921-932.
- CORRAL, Á. (2004), *Long-term clustering, scaling, and universality in the temporal occurrence of earthquakes*, *Phys. Rev. Lett.*, **92**, doi 10.1103/PhysRevLett.92.108501.
- DIETERICH, J. H. (1972), *Time-dependent friction as a possible mechanism for aftershocks*, *J. Geophys. Res.*, **77**, 3771-3781.
- DIETERICH, J. H. (1994), *A constitutive law for earthquake production and its application to earthquake clustering*, *J. Geophys. Res.*, **99**, 2601-2618.
- HAINZL, S., ZÖLLER, G., AND KURTHS, J. (1999), *Similar power laws for fore- and aftershock sequences in a spring-block model for earthquakes*, *J. Geophys. Res.*, **104**, 7243-7253.

- ITO, K., AND MATSUZAKI, M. (1990), *Earthquakes as self-organized critical phenomena*, J. Geophys. Res., 95, 6853-6860.
- JAUMÉ, S. C., AND SYKES, L. R.. (1999), *Evolving towards a critical point: A review of accelerating moment/energy release prior to large and great earthquakes*, Pure Appl. Geophys, 155, 279-306.
- MADARIAGA, R. (1976), *Dynamics of an expanding circular fault*, Bull. Seim. Soc. Am., 66, 639-666.
- NUR, A., AND BOOKER, J. R. (1972), *Aftershocks caused by pore fluid flow?*, Science, 175, 885-887.
- REASENBERG, P. (1985), *Second-order moment of Central California Seismicity*, J. Geophys. Res., 90, 5479-5495.
- ROELOFFS, E., AND LANGBEIN J. (1994), *The earthquake prediction experiment at Parkfield, California*, Rev. Geophys., 32, 315-336.
- RUNDLE, J. B., KLEIN, W., TURCOTTE D. L., AND MALAMUD, B. D. (2000A), *Precursory seismic activation and critical point phenomena*, Pure Appl. Geophys, 157, 2165-2182.
- RUNDLE, J. B., TURCOTTE D. L., AND KLEIN, W. (2000B), *Geocomplexity and the physics of earthquakes*, Geophysical Monograph 120, American Geophysical Union, Washington, DC.
- SHCHERBAKOV, R., AND TURCOTTE, D. L. (2004), *A damage mechanics model for aftershocks*, Pure and Applied Geophysics, 161, 2379, doi 10.1007/s00024-004-2570-x.
- SORNETTE, A., AND SORNETTE, D. (1990), *Earthquake rupture as a critical point: consequences for telluric precursors*, Tectonophysics, 179, 327-334.
- UTSU, T. (1962), *On the nature of three Alaskan aftershock sequences of 1957 and 1958*, Bull Seism. Soc. Am. 52, 279-297
- UTSU, T. (2002), *Statistical features of seismicity*, International handbook of earthquake and engineering seismology, Part B, 719-732
- UTSU, T., Y. OGATA, AND MATSU'URA, R. S. (1995), *The centenary of the Omori formula for a decay law of aftershock activity*, J. Phys. Earth, 43, 1-33.
- WYSS, M. (1997), *Cannot earthquakes be predicted?*, Science, 278, 487
- ZÖLLER, G., AND HAINZL, S. (2002), *A systematic spatiotemporal test of the critical point hypothesis for large earthquakes*, Geophys. Res. Lett., 29, doi 10.1029/2002GL014856.
- ZÖLLER, G., HAINZL, AND KURTHS, J. (2001), *Observation of growing correlation length as an indicator for critical point behavior prior to large earthquakes*, J. Geophys.Res., 106, 2167-2175.

ZÖLLER, G., HAINZL, S., HOLSCHEIDER, M., AND BEN-ZION, Y. (2005), *Aftershocks resulting from creeping sections in a heterogeneous fault*, Geophys. Res. Lett., 32, L03308, doi 10.1029/2004GL021871.

ZÖLLER, G., HOLSCHEIDER, M., AND BEN-ZION, Y. (2004), *Quasi-static and quasi-dynamic modeling of earthquake failure at intermediate scales*, Pure Appl. Geophys., 161, doi 10.1007/s00024-004-2551-0.

ZÖLLER, G., HOLSCHEIDER, M., AND BEN-ZION, Y. (2005), *The role of heterogeneities as a tuning parameter of earthquake dynamics*, Pure Appl. Geophys., 162, doi 10.1007/s00024-004-2660-9.

Received \_\_\_\_\_